DEVCOM DAC-TR-2024-030
March 2024

The Impact and Injury Response of Female and Male PMHS, Hybrid III 50th and 5th Percentile ATDs, and WIAMan under Blast-Induced Accelerative Loading

by Danielle M. Cristino, Kerry A. Danelson, Warren N. Hardy, John H. Bolte IV, Dawn Crawford, and Kathryn L. Loftis

DISCLAIMER

The findings in this report are not to be construed as an official Department of the Army position unless so specified by other official documentation.

WARNING

Information and data contained in this document are based on the input available at the time of preparation.

TRADE NAMES

The use of trade names in this report does not constitute an official endorsement or approval of the use of such commercial hardware or software. The report may not be cited for purposes of advertisement.

DEVCOM DAC-TR-2024-030
March 2024

The Impact and Injury Response of Female and Male PMHS, Hybrid III 50th and 5th Percentile ATDs, and WIAMan under Blast-Induced Accelerative Loading

by Danielle M. Cristino, Kerry A. Danelson, and Warren N. Hardy
Center for Injury Biomechanics, Virginia Tech

John H. Bolte IV
Injury Biomechanics Research Center, The Ohio State University

Dawn Crawford
DEVCOM Army Research Laboratory

Kathryn L. Loftis
DEVCOM Analysis Center

REPORT DOCUMENTATION PAGE

1. REPORT DATE	2. REPORT TYPE	3. DATES COVERED	
		START DATE	END DATE
March 2024	Technical Report	May 2016	May 2018

4. TITLE AND SUBTITLE

The Impact and Injury Response of Female and Male PMHS, Hybrid III 50th and 5th Percentile ATDs, and WIAMan under Blast-Induced Accelerative Loading

5a. CONTRACT NUMBER	5b. GRANT NUMBER	5c. PROGRAM ELEMENT NUMBER
5d. PROJECT NUMBER	**5e. TASK NUMBER**	**5f. WORK UNIT NUMBER**

6. AUTHOR(S)

Danielle M. Cristino, Kerry A. Danelson, Warren N. Hardy, John H. Bolte IV, Dawn Crawford, and Kathryn L. Loftis

7. PERFORMING ORGANIZATION NAME(S) AND ADDRESS(ES)

Director
DEVCOM Analysis Center
6896 Mauchly Street
Aberdeen Proving Ground, MD 21005

8. PERFORMING ORGANIZATION REPORT NUMBER

DEVCOM DAC-TR-2024-030

9. SPONSORING/MONITORING AGENCY NAME(S) AND ADDRESS(ES)	10. SPONSOR/MONITOR'S ACRONYM(S)	11. SPONSOR/MONITOR'S REPORT NUMBER(S)

12. DISTRIBUTION/AVAILABILITY STATEMENT

DISTRIBUTION STATEMENT A. Approved for public release: distribution unlimited.

13. SUPPLEMENTARY NOTES

14. ABSTRACT

The Warrior Injury Assessment Manikin (WIAMan), which is representative of a 50th percentile male, is the only anthropomorphic test device (ATD) that is designed to evaluate injury patterns in underbody blast (UBB) conditions. The WIAMan ATD will aid in predicting the injuries sustained by Warfighters in theater, and it will enable the development and implementation of improved vehicle systems and personal protective equipment. This work is being conducted in support of an Analysis of Alternatives to inform future decisions regarding implementation of a valid injury assessment capability for female Soldiers in the UBB environment (i.e., a separate female UBB ATD or the collection of the female biomechanics data needed to map the performance and injury prediction of the existing male ATD to that of the female). This work will determine the path forward for injury prediction and mitigation for the female Warfighter.

15. SUBJECT TERMS

WIAMan, female, injury risk, under-body blast, injury biomechanics

16. SECURITY CLASSIFICATION OF:			17. LIMITATION OF ABSTRACT	18. NUMBER OF PAGES
a. REPORT	b. ABSTRACT	C. THIS PAGE		
UNCLASSIFIED	UNCLASSIFIED	UNCLASSIFIED	UU	263

19a. NAME OF RESPONSIBLE PERSON	19b. PHONE NUMBER *(Include area code)*
Kathryn L. Loftis	(410) 306-0344

STANDARD FORM 298 (REV. 5/2020)

Prescribed by ANSI Std. Z39.18

(U) Table of Contents

(U) Table of Contents

List of Figures

List of Figures

List of Figures

List of Figures

List of Figures

List of Figures

List of Figures

List of Figures

List of Figures

List of Figures

List of Figures

List of Figures

List of Figures

List of Figures

List of Tables

Executive Summary

This effort has collected data regarding the accelerative loading responses of female and male postmortem human surrogates (PMHS) under various underbody blast (UBB) scenarios, and it has begun to examine the differences between female and male responses to high-rate vertical loading. This has increasing importance because women in the Armed Forces are serving in direct combat military operational specialties that were previously closed to women. The goals of this research effort are being accomplished through testing of 5th and 75th percentile female and 50th percentile male PMHS using the Accelerative Loading Fixture installation at Aberdeen Proving Ground, Maryland. Female and male PMHS results from the current effort are also compared to data previously generated for the midsized male PMHS (CORALS). To further elucidate damage thresholds and damage mechanisms observed during the whole-body PMHS work, supplemental structural-level testing is planned for isolated regions of the body that are at high risk for severe injuries during UBB (i.e., pelvis, lumbar spine, and ankle). The proposed test rig will impart displacement-controlled linear impacts to component specimens via a cam-driven energy source.

The Warrior Injury Assessment Manikin (WIAMan), which is representative of a 50th percentile male, is the only anthropomorphic test device (ATD) that is designed to evaluate injury patterns in UBB conditions. The WIAMan ATD will aid in predicting the injuries sustained by Warfighters in theater, and it will enable the development and implementation of improved vehicle systems and personal protective equipment. This work is being conducted in support of an Analysis of Alternatives to inform future decisions regarding implementation of a valid injury assessment capability for female Soldiers in the UBB environment (i.e., a separate female UBB ATD or the collection of the female biomechanics data needed to map the performance and injury prediction of the existing male ATD to that of the female). This work will determine the path forward for injury prediction and mitigation for the female Warfighter.

1. INTRODUCTION

The overall purpose of these tests is to collect responses of both female and male postmortem human surrogates (PMHS) in relevant, lower extremity postures under various high-rate, vertical-loading conditions using a blast buck-testing apparatus. The objective of the current phase of the research effort is to fill in knowledge gaps related to the biomechanical responses of female and male PMHS and to define response envelopes for females in the underbody blast (UBB) environment. This is accomplished by conducting female and male whole-body PMHS and anthropomorphic test device (ATD) tests in both subdamage and damaging test conditions and drawing comparisons to existing data. These comparisons, in combination with upcoming structural testing, will inform decisions regarding the need for a new, separate, female ATD for use in the UBB environment versus the potential ability to map female injury prediction to the response of the male Warrior Injury Assessment Manikin (WIAMan). The objectives covered in this report include the following:

- Collect whole-body kinematics and response data for female and male PMHS
- Characterize the kinematics response of the lower extremities, pelvis, and lumbar spine using a nominal posture (90° at the knee)
- Determine the extent of, and timing associated with, any damage sustained by the PMHS
- Determine whether any differences in response are as a result of size, shape, anatomy, and/or tolerance
- Finite element modeling in support of the WIAMan ATD development (Appendix A)

2. TECHNICAL PROGRESS

2.1 Test Apparatus

The study was conducted on a simplified representation of a military vehicle, called the Accelerative Loading Fixture (ALF) (Figure 1). The ALF is designed to generate floor and seat loading conditions representative of the loading level, rate, location, direction, and extent seen in UBB. Modifications were made to stiffen the fixture and reinforce the seats for the desired loading in the current study. The ALF consists of an occupant platform that is driven upward within a surrounding superstructure by the detonation of an explosive charge placed beneath the deck. The occupant platform is subsequently captured by a rope and cleat braking system after it passes through the apex of its travel. The occupant platform supports two rigid seats having five-point harnesses. Seat height is incrementally adjustable to allow the angle of the knees to be set to 90° for the variety of PMHS sizes in the study. Similarly, the seats are incrementally adjustable fore-aft to maintain similar foot placement with respect to the floor plate for the various PMHS sizes. The seat bottoms are 46 cm wide and 46 cm deep. The floor plate, which is made of rolled homogeneous armor, undergoes plastic deformation and is replaced between each test. The floor and seat performance can be modulated independently and are symmetric, predictable, and repeatable. A set of accelerometers and angular rate sensors is attached to the seats and floor of the ALF to characterize the structural response.

This study was performed in cooperation with the U.S. Army Combat Capabilities Development Command (DEVCOM) Army Research Laboratory (ARL) (now DEVCOM Analysis Center) and Aberdeen Test Center (ATC) personnel at the Aberdeen Proving Grounds (APG) in Aberdeen, Maryland. The ARL provided some equipment, including ATDs, personal protective equipment (PPE), high-speed video cameras, structure-mounted transducers, a stationary data acquisition system, overhead digital image correlation cameras, and overall test infrastructure.

Figure 1. Accelerative loading fixture

2.2 Test Matrix

Twenty unembalmed PMHS were tested during 11 UBB tests (Table 1). The PMHS in the study included eight 50th percentile males, six 75th percentile females, and six 5th percentile females, which were tested in pairs or paired with a Hybrid III 5th female ATD. Each test event is referred to as a "Shot" and test occupants are designated Crew 1 or Crew 2, with Crew 1 always being the heavier surrogate. Series 1 combines the previous CORALS tests, which consisted of two shots that included two 50th percentile male PMHS each (M1 and M2), with four shots that introduced 5th and 75th percentile female PMHS (F1–F4). Shots F2 and F4 used the Hybrid III 5th percentile female ATD in the Crew 2 position. The ATD responses are not included in the current analyses. Test Series 2, which was set to include PPE, was not conducted in favor of testing at higher floor deformation rates. Test Series 3 and 4 each consisted of three shots that included 5th and 75th percentile females as well as 50th percentile males (F5–F9). The average age of the PMHS tested was 54 years, ranging from 26 to 75 years old. The average conventional body mass index (BMI) was 23.8 kg/m^2.

The performance of the ALF is described by target peak speed and the time taken to reach the specified peak speed at both the seats and the floor. During Test Series 1, a lower energy floor condition was implemented to collect kinematics data in the absence of substantive damage to the lower extremities. Test Series 3 and 4 introduced a higher energy floor condition to produce damaging test conditions for the lower extremities.

Series 4 imposed higher speeds at the seat, initially. The test matrix is described in Table 2.

Table 1. PMHS characteristics

Shot	Crew	PMHS	Size	Sex	Age	Mass (kg)	Stature (cm)
M1	1	SM117	50th	Male	58	95.1	182.9
	2	SM118	50th	Male	54	82.5	174.5
M2	1	SM120	50th	Male	69	81.8	188.0
	2	SM119	50th	Male	73	65.0	181.8
F1	1	SF127	75th	Female	57	69.2	170.9
	2	SF126	5th	Female	54	47.1	159.2
F2	1	SF128	75th	Female	45	66.1	161.5
	2	ATD	5th	…	…	48.9	150.1
F3	1	SF131	75th	Female	55	68.5	165.1
	2	SF132	5th	Female	66	66.4	165.1
F4	1	SF133	5th	Female	57	57.4	162.6
	2	ATD	5th	…	…	48.9	150.1
F5	1	SF138	75th	Female	50	74.7	166.6
	2	SF134	5th	Female	53	60.6	171.6
F6	1	SM140	50th	Male	50	68.7	186.9
	2	SF135	5th	Female	36	56.9	160.3
F7	1	SM141	50th	Male	55	93.8	168.5
	2	SF142	75th	Female	75	88.1	164.3
F8	1	SM145	50th	Male	68	75.3	178.0
	2	SF148	75th	Female	56	69.3	162.9
F9	1	SM150	50th	Male	26	78.0	181.6
	2	SF151	5th	Female	28	36.5	159.0

Table 2. Test matrix

Test series	Shot	Target peak floor speed	Target floor time-to-peak	Target peak seat speed	Target seat time-to-peak
1	M1, M2, F1, F2, F3, F4	8 m/s	2 ms	5 m/s	4 ms
3 and 4	F5, F6, F7, F8, F9	20 m/s	2 ms	4 m/s	7 ms

2.3 Specimen Selection

The PMHS are tested following the procedures outlined in the Annual Program Plan 2. Authorization for the testing is demonstrated in USAMRMC ORP Log Number A-18968.1a. The PMHS are selected within a specified range of mass and stature for a given sex and percentile (Table 3). The upper and lower bounds of the mass and stature were determined by a detailed anthropometric survey of U.S. Army Soldiers (ANSUR II) that was performed by the Natick Soldier Research, Development and

Engineering Center.[1] Selecting PMHS within the acceptable mass range is prioritized over selecting within the acceptable height range. The accepted BMI is between 18 and 35. The accepted age range is 18 to 80 years old. Specimens are required to have a T-score between −1.0 and +2.5. The T-score, which serves as an estimate of bone quality, is the number of standard deviations that the bone mass density (BMD) of the specimen is away from the average adult. Osteoporosis is associated with a T-score of −2.5 or lower, as arbitrarily defined by the World Health Organization. The BMD used to determine T-score is the average BMD value calculated from quantitative CT scans of the second, third, and fourth lumbar vertebrae.

Table 3 Accepted mass and stature range

PMHS	Stature (cm)	Mass (kg)
50th Male	165–186	64–106
75th Female	160.9–173.7	64–89
5th Female	145.6–158.4	39–63

Further screening of the specimens includes a review of medical history and cause of death, a radiological examination, and serologic testing for human immunodeficiency virus, hepatitis B, and hepatitis C. Exclusion criteria include communicable diseases, pre-existing skeletal injuries, existing damage or trauma to any important anatomical region (i.e., spine, pelvis, lower extremity), appreciable bone metastases or some advanced or aggressive forms of cancer (e.g., melanoma), some surgeries such as lower extremity amputations, unhealed orthopedic procedures, spinal fixation and/or arthroplasty, joint replacement, some disease states such as sepsis, or extreme cases of the following: disc degeneration; scoliosis; stenosis or osteophytic growths; rheumatoid arthritis, osteomyelitis, etc.; congenital joint malformations or developmental anomalies (talipes equinovarus, dysplasia, etc.); spina bifida; amyotrophic lateral sclerosis; muscular dystrophy; polio; and severely limited range of motion at joints or in the spine.

2.4 Specimen Preparation

Pretest preparations require 1 to 2 weeks and are performed at the Virginia Tech Center for Injury Biomechanics Crash Sled Laboratory. Preparation of the specimens includes collection of full-body CT images, full-body X-ray images, and standard anthropomorphic measurements, as well as application and troubleshooting of instrumentation, and the collection of additional full-body CT imaging after instrumentation is installed. Anthropomorphic measurements, modeled after the National Highway Traffic Safety Administration guidelines,[2] are defined in the document titled *Signal Conversion Tiger Team [ScoTT] Recommendations for Anatomical Reference, Rev. 0.6.*[3]

2.5 Specimen Instrumentation

2.5.1 Coordinate System

The SAE-J211 coordinate system described in the document Instrumentation for Impact Test is used for all occupant measurements and calculations.[4] Positive X is posterior to anterior, positive Y is left to right, and positive Z is superior to inferior. This coordinate system is based on a standing occupant, so repositioning to the seated posture on the ALF causes a corresponding change in axes orientation with respect to global coordinates for the femurs.

2.5.2 Kinematics Instrumentation

Several types of instrumentation are mounted to the specimens. The instrumentation mounting is summarized in Table 4. Six-degrees-of-freedom (6-DoF) “motion blocks” with three mutually orthogonal linear accelerometers (Endevco 7264, 7264B, or 7264C) and three orthogonal angular rate sensors (DTS ARS Pro or HG) are rigidly attached to specific bones of interest to collect kinematics of body segments in all three planes of motion. The 6-DoF motion blocks are mounted to the following locations: the anterior aspect of the body of the fourth cervical vertebra (Figure 2) and third lumbar vertebra; the iliac fossa of the ilia of the pelvis bilaterally; and the anterior aspect of the distal femura (Figure 3) and tibia (Figure 4), bilaterally. The 6-DoF motion blocks of the lower extremities are positioned at the center of incisions that are made at specified distances from anatomical landmarks per the SCoTT document guidelines. Three-degrees-of-freedom motion blocks are rigidly mounted to other relevant bones. These consist of one accelerometer oriented in the x-direction, one accelerometer oriented in the z-direction, and one ARS oriented about the y-axis. They are mounted to the anterior aspect of the sternum at its midpoint, as well as the posterior aspect of the 1st, 5th, 8th, and 12th thoracic vertebrae.

Table 4. Kinematics instrumentation mounting

Location	Sensors	Blocks	Interface
Head	DTS 6DF	None	Aluminum plate
C4	3 Accels, 3 ARS	Aluminum block	Delrin block
Sternum	2 Accels, 1 ARS	Aluminum block	Aluminum plate
Thoracic spine (T1, T5, T8, T12)	2 Accels, 1 ARS	Aluminum block	Aluminum block
L3	3 Accels, 3 ARS	Aluminum block	Delrin block
Sacrum	DTS 6DF	None	Aluminum channel
Pelvis (right and left)	3 Accels, 3 ARS	Aluminum block	Delrin block
Distal femur (right and left)	3 Accels, 3 ARS	Aluminum block	Delrin block
Distal tibia (right and left)	3 Accels, 3 ARS	Aluminum block	Delrin block
Calcaneus (right and left)	1 Accel	Aluminum block	Cyanoacrylate

Figure 2. Cervical spine instrumentation locations

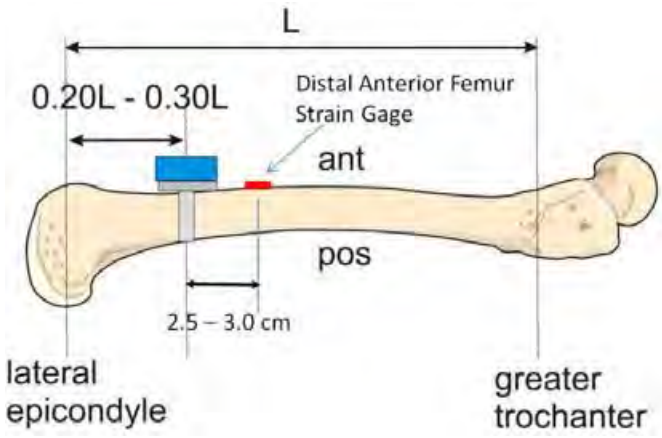

Figure 3. Femur instrumentation location

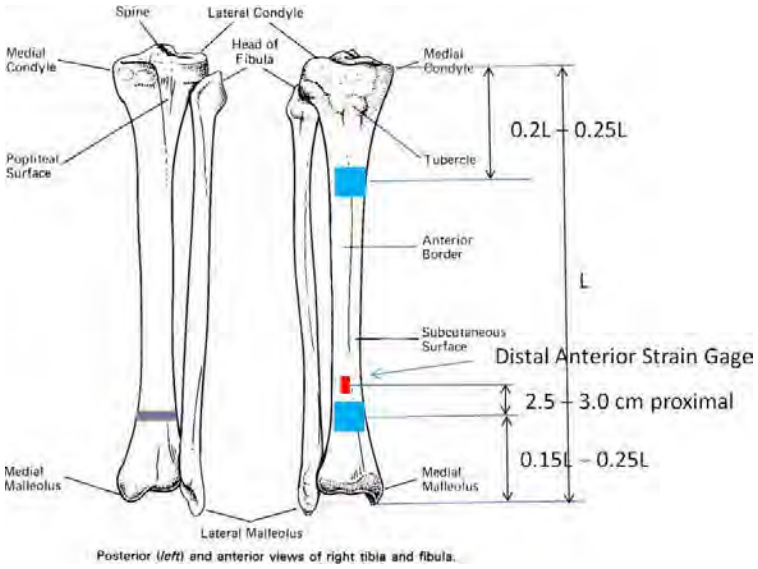

Figure 4. Tibia instrumentation locations

Each motion block comprises an aluminum block to which the transducers are attached. All of the 6-DoF motion blocks have an associated Delrin block that interfaces between the aluminum and the bone. The aluminum blocks are bolted to the Delrin blocks. Friction between the Delrin block and the bone is increased by a serrated interface at the base of the Delrin. Sections of 80-grit sandpaper are adhered to the bone beneath the Delrin blocks mounted to the femur and tibia to further prevent slipping. Metal hose clamps or screws are used to secure the motion blocks to the various bones. A single metal hose clamp is used for the femur, whereas both a metal hose clamp (proximally) and a 300-lb tensile strength cable tie (distally) are used for the tibia. These are passed between the aluminum and Delrin components of the motion blocks and around the diaphysis of the bone. The motion blocks on the pelvis are attached with two bolts passed through each ilium. For the motion blocks on the lumbar and cervical spine, a hose clamp is passed through the motion block and around the vertebral body. Each motion block on the thoracic spine is attached by passing two screws through an omega-shaped aluminum block into the pedicles. A Pi-shaped aluminum block to which the transducers are fixed is then bolted to each omega block. The motion block on the sternum is attached with two screws that pass through the aluminum plate and into the bone.

Additional 6-DoF accelerometers (DTS 6DX PRO) are rigidly attached to the left side of the skull (Figure 5) and the posterior aspect of S1 of the sacrum (Figure 6). The head array is attached to a thin aluminum plate mounted to the skull using two screws. The sacrum array is attached to a channel fixture that bridges over the median sacral crest. Two screws are used to fix this channel to the sacrum, avoiding the sacral foramina. Individual accelerometers (Endevco 7264D) are mounted to both calcanei with the

sensing axes aligned with the z-axis (Figure 7). These accelerometers are fixed to aluminum blocks with cyanoacrylate. The aluminum blocks have one face that is engraved with a series of grooves. Glue is injected into the grooves of the block, and the block is pressed firmly to the bone until the glue cures. Additional cyanoacrylate is added as needed.

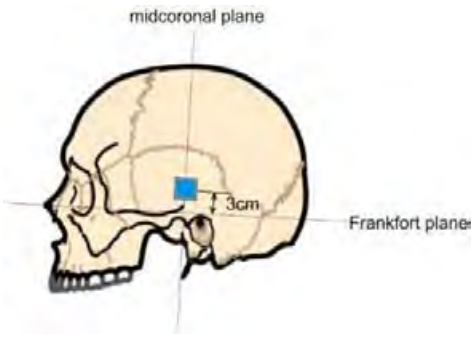

Figure 5. Head instrumentation location

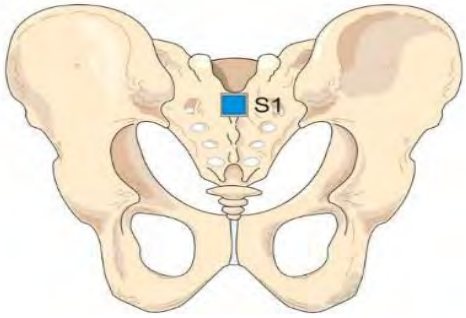

Figure 6. Sacrum instrumentation location

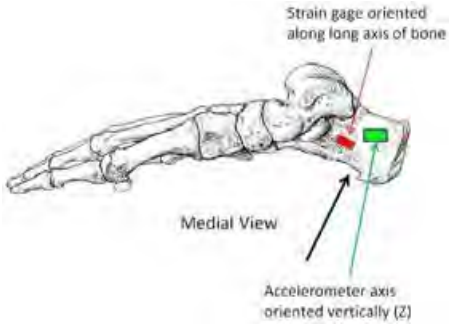

Figure 7. Foot instrumentation locations

2.5.3 Strain

Single-axis strain gages are adhered to the lumbar spine and lower extremities (Figure 4) and pelvis (Figure 8). The strain gages on the pelvis (cea-13-125un-350) are placed in the following locations: the anterior superior iliac spine (ASIS), bilaterally, with the sensing axes oriented along the direction of input loading from the seatbelt; the anterior aspect of the pubic ramus, bilaterally, with the sensing axes oriented laterally in line with the bone bridge; and the ischial tuberosities inferior to the ischial spines, bilaterally, with the sensing axes oriented along the direction of loading from the seat bottom input. The strain gages on the lumbar spine (Micro-Measurements cea-13-062uw-350) are adhered to the lateral aspect of the fourth lumbar vertebral body, bilaterally, with the sensing axes aligned from superior to inferior. The strain gages on the lower extremity (Micro-Measurements cea-06-250uw-350) are adhered to the anterior aspect of the proximal and distal femura and tibiae, bilaterally, with the sensing axes aligned with the long axes of the bones, as well as the medial or lateral aspect of the calcaneus (Micro-Measurements cea-13-062uw-350), with the axes oriented perpendicular to the floor.

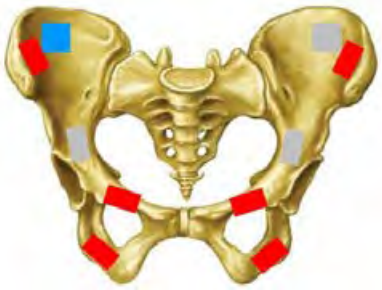

Figure 8. Strain gage (red) and motion block (blue/gray) locations on the pelvis

To prepare the bone surface for strain gage, tissue is removed from the bone surface using a scalpel. The 80-grit sandpaper is used to lightly abrade the bone surface. Acetone is used to remove fatty residue and moisture. The bone is cleaned and dried with isopropyl alcohol before applying a thin layer of cyanoacrylate. After the adhesive layer cures, it is softly sanded with 120-grit sandpaper and cleaned again with alcohol to prepare for another layer of glue. These steps are repeated until a smooth layer of glue has sealed off any moisture from the bone. The strain gages are prepared for application by attaching lead wires to the solder tabs. A small amount of glue is applied to the back of the strain gage. The strain gage is gently pressed in place to fix the entire surface to the bone. The strain gage is cleaned and dried with isopropyl alcohol, and at least two layers of a protective acrylic coating are applied to seal out moisture. The lead wires are soldered to the extension wire and tethered to nearby tissue within the incision. The strain gages are connected to the signal conditioning using a three-wire

configuration, with one bridge completion resistor being external to the data acquisition system and two being internal.

2.5.4 Additional Instrumentation

A calibrated tilt sensor is rigidly attached to the right ilium of the pelvis. During pretest preparations, the angle of the pelvis is determined by placing a digital angle finder on a rigid plate pressed firmly against the pubic symphysis and the right and left ASIS. The voltage output of the tilt sensor that corresponds to a pelvis angle of 45° is recorded. The tilt sensor is used during positioning of the specimen on the ALF to set the pelvis at the desired angle without the need for external measurement tools. During each test, the PMHS are outfitted with boots that have been prepared with foil contact pads. When the PMHS are positioned on the ALF, the bottom of the boots complete a circuit with foil contact pads on the floor. This provides information regarding contact timing between the boot and the floor plate throughout test. Four seatbelt load cells per specimen are used during each test (eight total). They are attached to the shoulder and lap belts, bilaterally.

2.5.5 Instrumentation Packaging

All cables from instrumentation are passed through passageways (tunnels) made on the lateral aspect of the body between the skin/fat and muscle and exit the body at the acromion process, bilaterally. The wire bundles are tethered to tissue at the shoulder. Tunnels on the posterior aspect of the rib cage connect the posterior instrumentation to the main tunnels. Wires exiting transducers are sutured to nearby tissue structures. Wherever possible, motion blocks are covered with dental dam that is secured with a rubber band. All incisions made for the application of instrumentation are stitched closed. The feet, distal tibiae, distal femura, and head are wrapped in self-adherent elastic wrap to protect protruding instrumentation blocks. The PMHS are dressed in spandex bodysuits. The transducers are connected to the data acquisition system and their functionality is checked in the laboratory.

Pretest CT scans are used to document the position and orientation of the instrumentation. The data acquisition hardware for each specimen is shock mounted within a hardened case that is secured to the top of the pedestal behind the seat during each test. A thin layer of rubber is placed between the case and the pedestal to provide additional shock absorption. The wire bundle running from the PMHS to portable case is lashed to the structures that reinforce the seat.

2.6 Test Procedure

2.6.1 Specimen Logistics and Schedule

After specimen preparation, a 4-day procedure is followed for performing the test. First, the specimens are transported from Virginia Tech to APG in a temperature-controlled morgue within a secure trailer. Upon arrival at APG, the PMHS are stored at an onsite preparation facility located in ARL space at an APG Experimental Facility. The next day, final preparation takes place. After final specimen preparation, the PMHS are moved from the experimental facility to the test site and positioned on the ALF. The PMHS are attended overnight. The test is conducted the following day. After the test, the PMHS are transported back to the experimental facility and the ALF is decontaminated. The next day, the PMHS are transported back to Virginia Tech for posttest procedures such as scanning, deinstrumenting, polarity checks, and autopsy. The PMHS are then processed for final disposition per the donors' wishes. If weather interferes with the ability to safely perform the test, the testing schedule may be extended by one day.

2.6.2 Specimen Imaging

PMHS are imaged using DeXa and CT prior to acceptance. Full-body CTs are taken upon procurement at Ohio State University (before PMHS are stored in the freezer), after instrumentation is installed at Virginia Tech, and after the test is conducted. The X-rays of all body regions are collected at Virginia Tech before instrumentation is installed. An additional X-ray of the lower extremities is taken on the ALF after final positioning of the PMHS. Photos of the final setup on the ALF are taken before the test is conducted. Video is recorded using four Vision Research Phantom 9.1v CMOS video cameras operating at 1 kfps, as well as four backup Photron FASTCAM SA1.1 cameras operating at 10 kfps. The cameras are positioned within protected enclosures. The camera views include the frontal and lateral plane views of the PMHS. Platforms are positioned along the edges of the ALF to prevent soil ejecta from blocking the camera view of the occupant platform.

Video tracking markers are applied to various anatomical landmarks and to the harness, seat, and test apparatus following the procedure defined in the document titled WIAMan Bio PT PMHS Positioning Procedure guidelines, Rev. 0.7.[5] To track body segment motion, white sport tape is wrapped around the limb on either side of joint centers, and cross-hairs are drawn onto the medial, anterior, and lateral aspect of the tape with black paint pens. Target stickers are also placed on palpable bony landmarks of the limbs and head (Figures 9–11). Motion tracking software (TEMA Motion 3D, Image Systems, Linkoping, Sweden) is used to track the targets throughout the event.

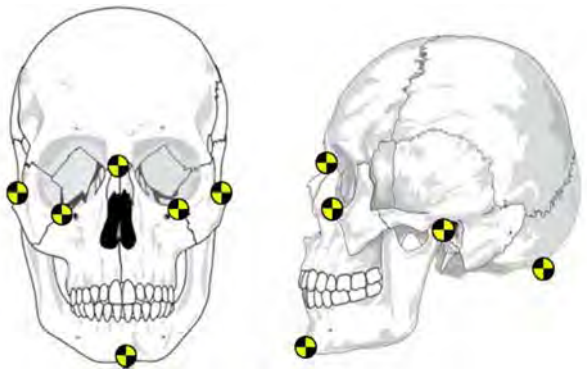

Figure 9. Video tracking markers of the head

Figure 10. Video tracking markers of the upper extremity

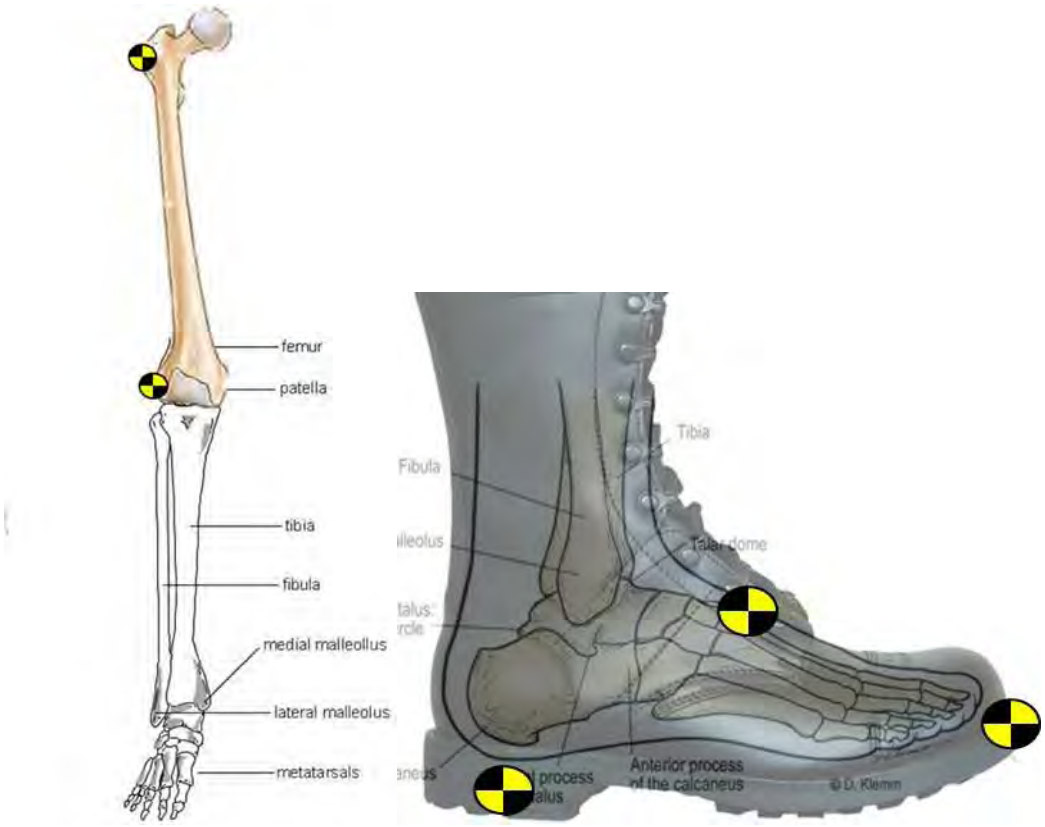

Figure 11. Video tracking markers of the lower extremity

2.6.3 Specimen Positioning

The specimen-positioning procedure follows the guidelines presented in the WIAMan Bio PT PMHS Positioning Procedure guidelines, Rev. 0.7.[5] A nominal posture was chosen for all PMHS, meaning that the ankle and knee joints are set to 90°, and the hands are placed on the thighs with the arms resting at the sides of the chest. The heels and toes are aligned in the median plane, and the limbs are positioned equidistant from the midsagittal plane. The heels are positioned using 295-mm spacing for males and 266-mm spacing for females (±10 mm for both), which consequently sets the knees at the same distance. String is looped around the thighs to keep the knees from splaying open. The pelvis is set with a posterior tilt measuring 40 ± 5° from the vertical. The only PPE includes standard boots, which are fitted to each specimen based on the anthropometry of the feet. The boots are laced and tightened per the prescribed donning procedure for all tests. The five-point harnesses are replaced between tests. The height of the shoulder belts is adjusted by feeding them through the appropriate slot in the seatback such that they are at the level of the top of the shoulder or slightly higher.

To pre-position the adjustable seat on the ALF for a given specimen geometry, measurements are taken in the laboratory with the specimen seated in the approximate

position for testing on the ALF. On the day of the test, the specimen is seated on the ALF and moved to the approximately correct position with the torso upright against the seatback and the pelvis centered between the left and right edges of the seat. The five-point harness is used to loosely secure the torso in place. The pelvis is shifted until the tilt sensor indicates that the desired pelvis angle of 40 ± 5° from vertical is achieved. Once the pelvis is in place, the harness is fully tightened. The legs are positioned perpendicular to the floor as indicated by the position of the lateral malleolus of the fibula and the lateral epicondyle of the femur. This sets the angle at the ankle to 90°. The predetermined seat height consequently sets the femur parallel to the floor as indicated by the H-point of the pelvis and the lateral epicondyle of the femur, which sets the angle at the knee to 90°.

A coordinate measurement machine (FARO) is used to verify that various anatomical landmarks are positioned at specified distances relative to one another within specified tolerances. The hands are loosely secured onto the tops of the thighs with the palms down and the fingers in line with the thighs using breakaway tape. The head is positioned using a frangible hanging system that is fashioned to remain undisturbed until the test event. An example of a small female cadaver position is shown with the corresponding small female ATD in Figure 12.

Figure 12. PMHS (left) and Hybrid III 5th percentile female ATD (right) positioned on the ALF

2.6.4 Data Processing and Analysis

There are two data acquisition systems for each PMHS. The first is a 32-channel DTS G5 sampling using 100 kHz, with a 30-kHz cutoff frequency, 8th-order Butterworth profile, low-pass filter. The second is a 64-channel DTS TDAS Pro sampling using 20 kHz with a 4,300-Hz cutoff, 8th-order Butterworth profile, antialiasing filter. The data from the TDAS

Pro were interpolated to 100,000 samples per second using a cubic spline algorithm. Large spikes that were unrelated to the test were removed. The data are corrected for polarity then zeroed, truncated, and filtered. Linear acceleration is filtered using a cutoff frequency of 3 kHz, and angular rate is filtered using a cutoff frequency of 1.65 kHz. Angular acceleration is calculated by differentiating filtered angular speed and filtered using 0.5-kHz cutoff. The strain gage data are adjusted to a baseline of zero and filtered with a 4,950-Hz cutoff frequency. All digital filters are 4^{th}-order Butterworth profiles. The data are not normalized so that raw differences between the sexes and sizes can be examined. The acceleration traces are integrated using Simpson's rule to determine speed. All data acquisition and video systems are synchronized.

Coordinate system transformations of the transducer data are performed to align the signals with the anatomical axes and then transform the signals to coincide with defined anatomical origins. Local motion block coordinate systems and bone coordinate systems are defined within the global CT space. Points are chosen to define the motion block and bone coordinate systems and are determined from CT scans. The motion block coordinates are transformed to align with the prescribed bone coordinate systems' locations and orientations.

After each test, detailed autopsies are performed to assess damage to joints and load-bearing bones. CT segmentation is used to estimate the mass of the thigh, shank, and foot of each specimen.

3. MAJOR TECHNICAL DEVELOPMENTS

3.1 Impact Response

Response envelopes are generated to illustrate natural variance in the kinematic responses for the three surrogate types (50th percentile male, 75th percentile female, and 5th percentile female) in both the lower energy floor condition (CORALS and Series 1) and higher energy floor conditions (Series 3 and 4). The plots discussed in the current analysis include vertical speed, vertical acceleration, and angular speed in the sagittal plane (along the y-axis) for the distal tibia, distal femur, pelvis, and lumbar spine. The envelopes are defined by the minimum value and maximum value at each time point for a given surrogate type. No scaling or shifting is applied. Response envelops are shown for the right side of the body wherever applicable; however, the left side of the body as well as additional envelops that are not discussed in the body of the report are included in Appendix A. Appendix B provides individual traces that are organized by body region and floor energy level.

3.1.1 Transducer Response

3.1.1.1 Tibia

The kinematic responses are similar in shape and duration between the right and left tibiae but differ in magnitude. In male CORALS and Series 1, both the general shape and duration of the speed responses of the tibiae in the vertical (z) direction are similar between the female and male PMHS (Figure 13); however, the tibiae of the female PMHS reach higher peak vertical speeds, and they reach those speeds earlier in the event. In Series 3 and 4, the general shape and duration of the speed responses of the tibiae in the vertical (z) direction are again similar between the female and male PMHS; however, the tibiae of the male PMHS are reaching higher peak speeds than those of the females at a later time in the event (Figure 14). The values of speed in Series 3 and 4 are approximately twice those of Series 1. In male CORALS and Series 1, the tibiae of the female PMHS reach greater peak accelerations than those of the males (Figure 15). During Series 3 and 4, the tibiae of the female PMHS undergo greater initial acceleration than those of the males (Figure 16). During all tests, the shape and duration of the angular speed response tibiae is similar between female and male PMHS (Figures 17 and 18).

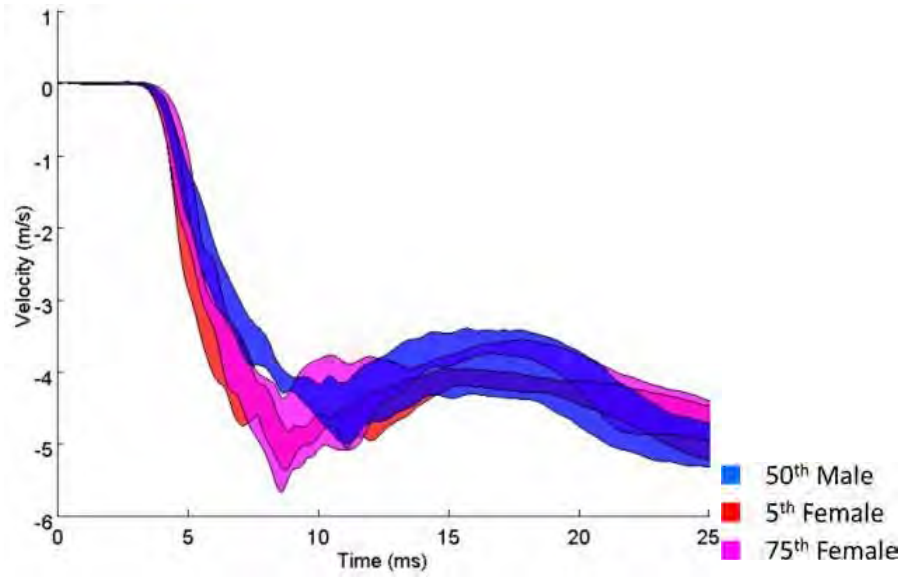

Figure 13. Male CORALS and Series 1 right distal tibia vertical speed (z-direction)

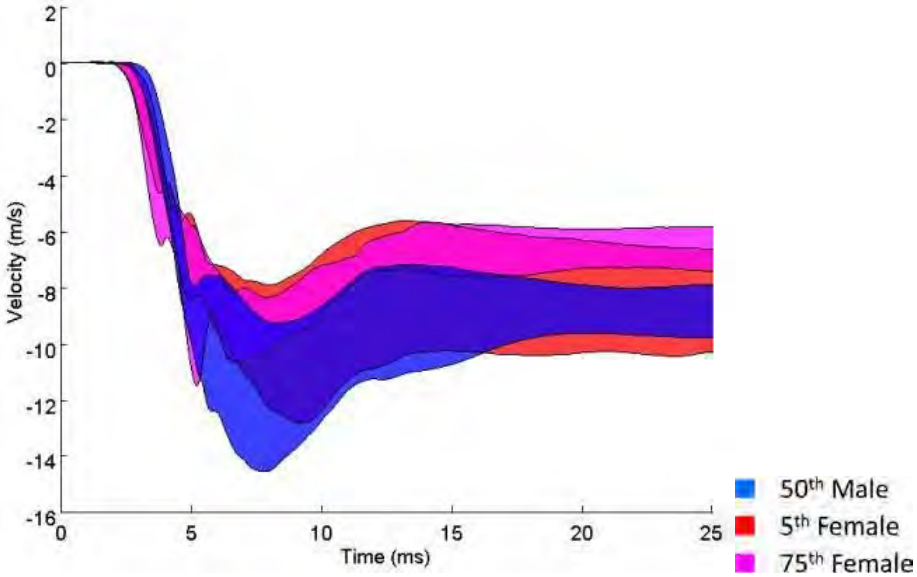

Figure 14. Series 3 and 4 right distal tibia vertical speed (z-direction)

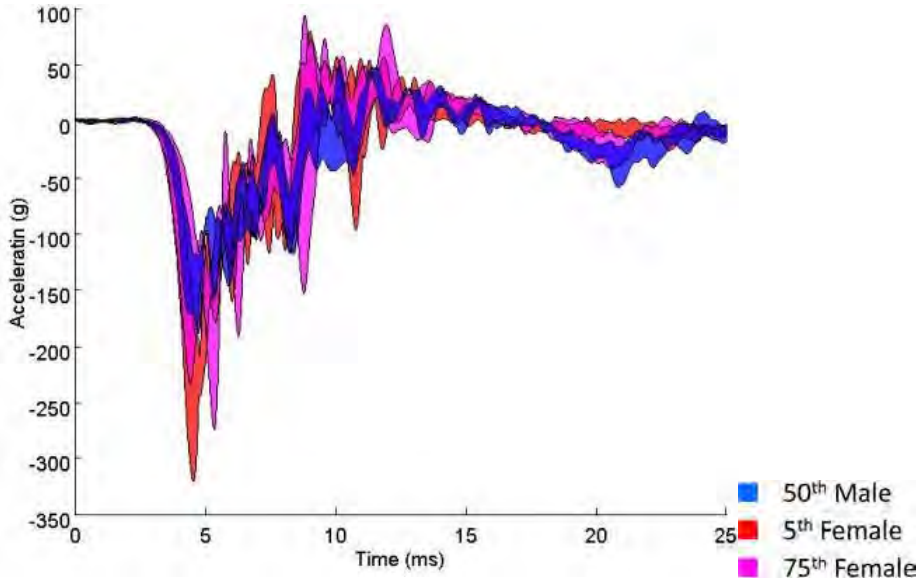

Figure 15. Male CORALS and Series 1 right distal tibia vertical acceleration (z-direction)

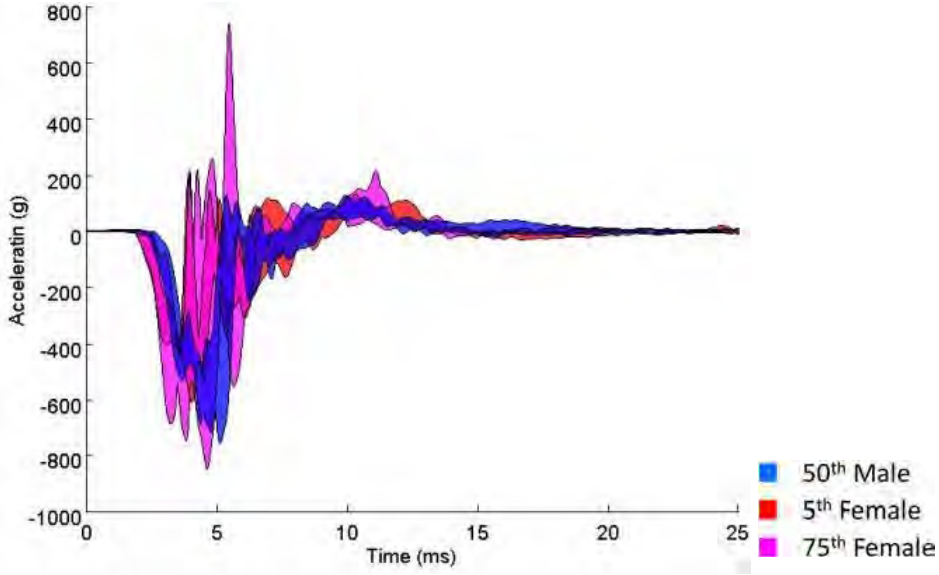

Figure 16. Series 3 and 4 right distal tibia vertical acceleration (z-direction)

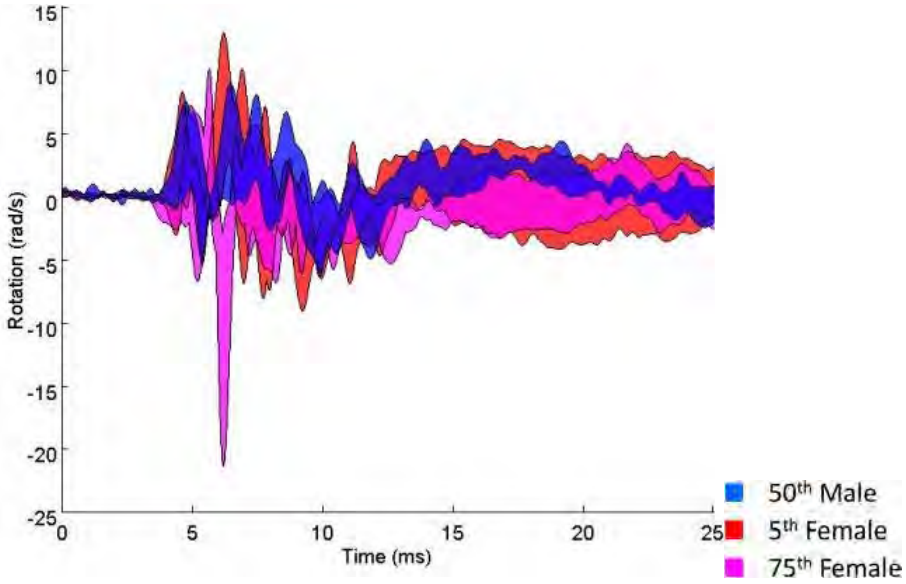

Figure 17. Male CORALS and Series 1 right distal tibia angular speed in the sagittal plane (along the y-axis)

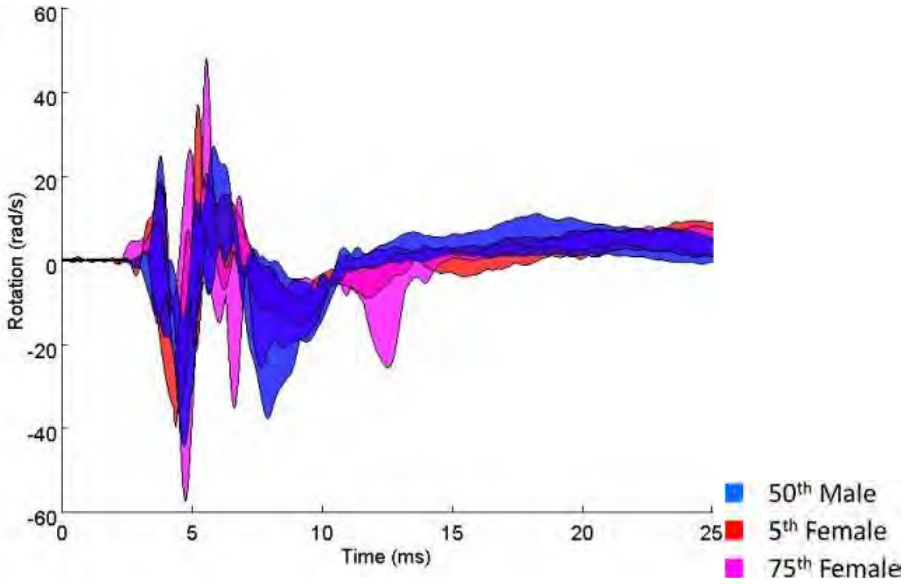

Figure 18. Series 3 and 4 right distal tibia angular speed in the sagittal plane (along the y-axis)

3.1.1.2 Femur

The kinematic responses are similar between the right and left femura. In male CORALS and Series 1, the general shape of the speed responses of the femura in the vertical (x) direction are similar between the female and male PMHS, but the femura of the females attain greater peak speeds earlier in the event (Figure 19). This is not observed in Series 3 and 4, where the femura of the female PMHS attain greater initial speed that is eventually surpassed by the femura of the male PMHS (Figure 20). Similar

to the tibiae, the femura of the females also attain greater peak accelerations in male CORALS and Series 1 (Figure 21) as well as greater initial acceleration in Series 3 and 4 (Figure 22). Due to the increased floor energy in Series 3 and 4, a more pronounced second-order effect is observed in the vertical speed response of the femura of the females. This is illustrated by the acceleration response envelopes for Series 3 and 4, which are more bimodal in nature for the female PMHS. The acceleration response of the femura in male CORALS and Series 1 exhibits a unimodal response for both sexes. In all tests, the rotation of the femura in the sagittal plane is similar between female and male PMHS; however, the females initially rotate faster and more often than the males (Figures 23 and 24). The femura of the female PMHS reach greater angular speeds in male CORALS and Series 1 than those of the male PMHS.

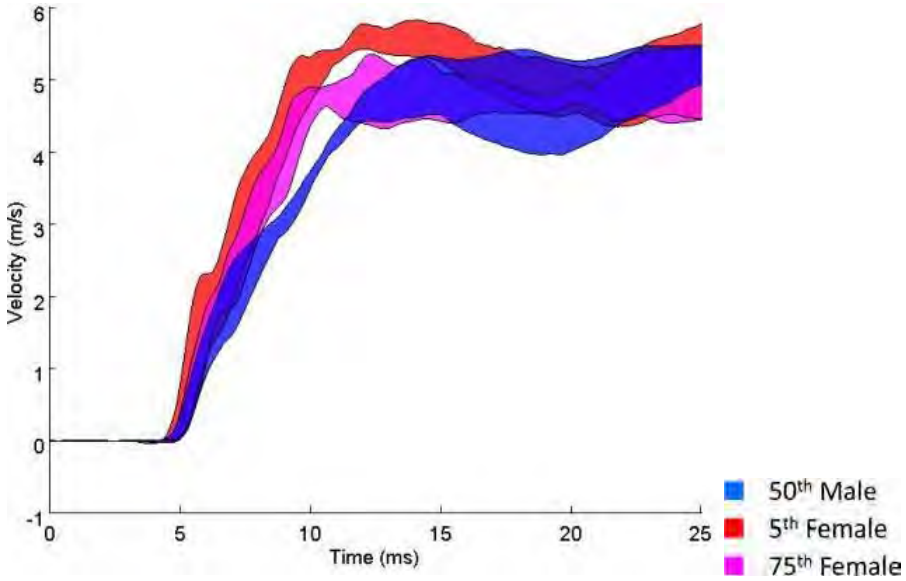

Figure 19. Male CORALS and Series 1 right distal femur vertical speed (x-direction)

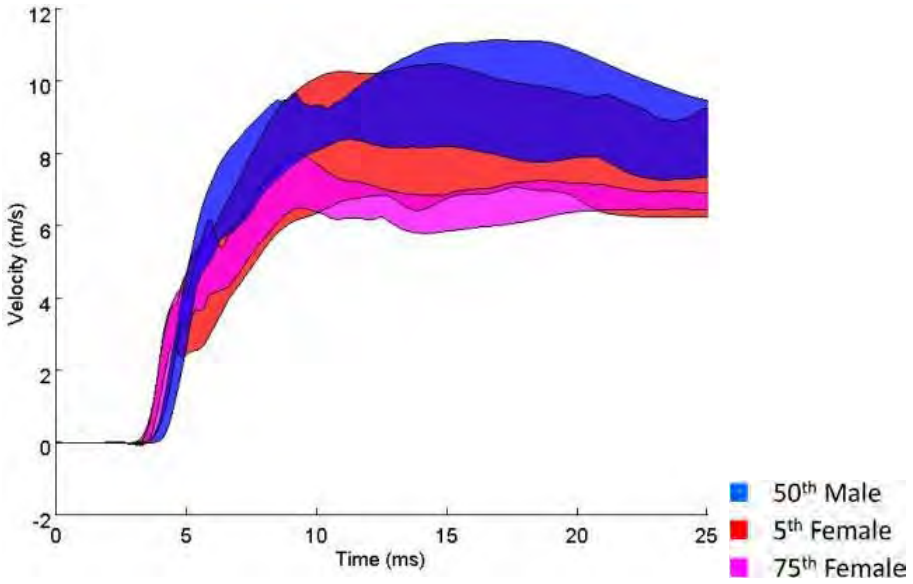

Figure 20. Series 3 and 4 right distal femur vertical speed (x-direction)

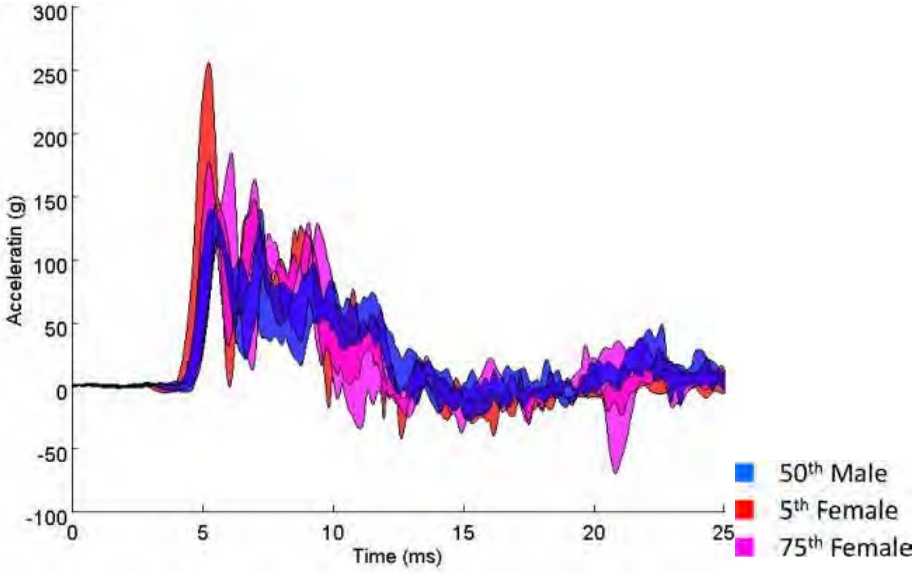

Figure 21. Male CORALS and Series 1 right distal femur vertical acceleration (x-direction)

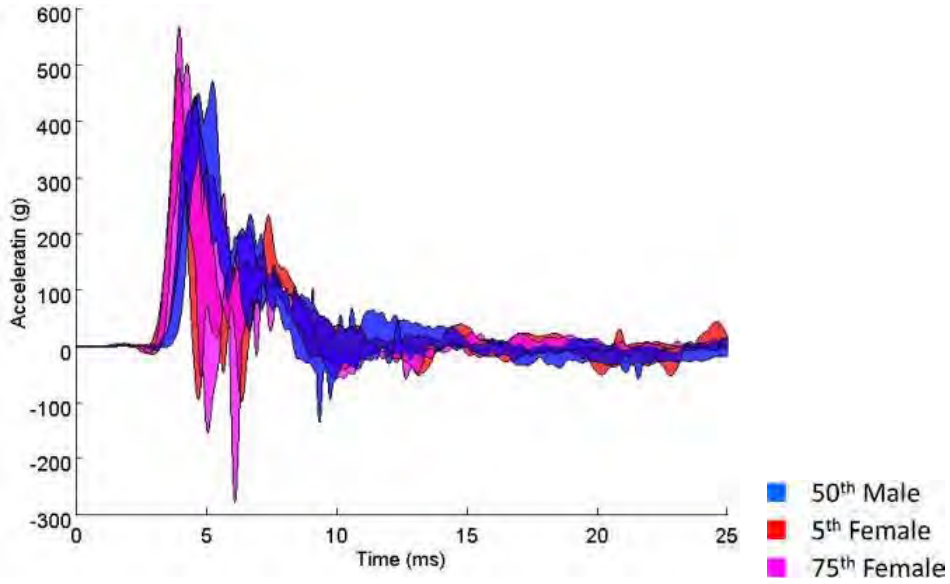

Figure 22. Series 3 and 4 right distal femur vertical acceleration (x-direction)

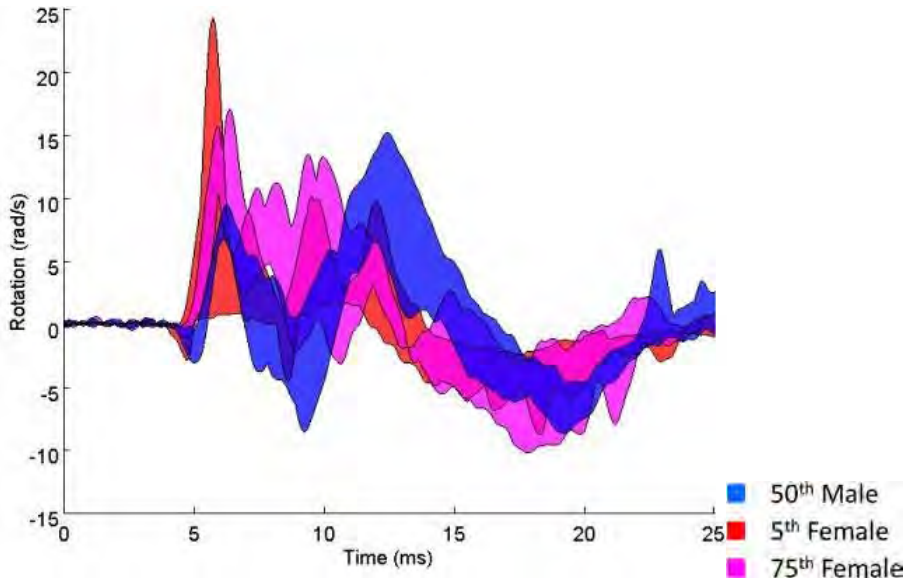

Figure 23. Male CORALS and Series 1 right distal femur angular speed in the sagittal plane (along the y-axis)

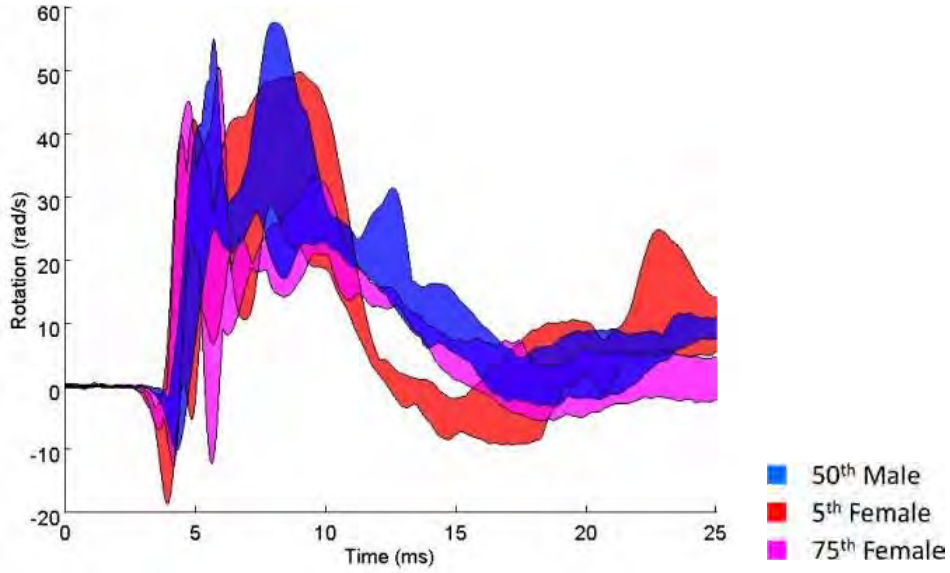

Figure 24. Series 3 and 4 right distal femur angular speed in the sagittal plane (along the y-axis)

3.1.1.3 Pelvis

The kinematic responses are similar between the right and left side of the pelvis. In male CORALS and Series 1, the speed responses of the pelves of the female and male PMHS exhibit similar shapes (Figure 25). In Series 3 and 4, the pelves of the 75th percentile female PMHS maintain greater speed throughout the event than those of the other surrogates (Figure 26). The vertical acceleration responses of the pelves are similar in shape between all surrogates in male CORALS and Series 1 (Figure 27); however, in Series 3 and 4, the pelves of the 75th percentile females attain greater acceleration peaks throughout the event (Figure 28). The angular speed response of the pelvis in male CORALS and Series 1 is similar in shape between the female and male PMHS (Figure 29). This is repeated in Series 3 and 4; however, the pelves of the 5th percentile females exhibit a shorter response (Figure 30).

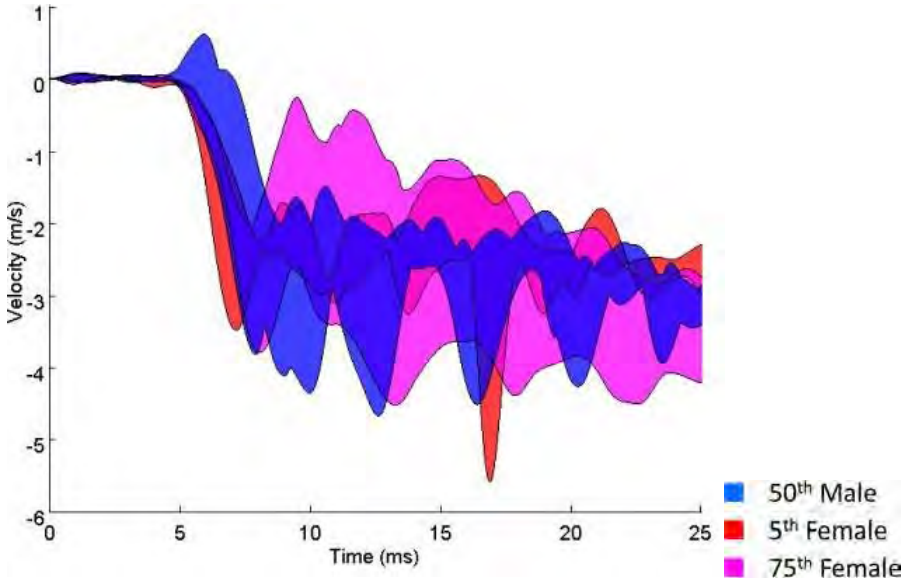

Figure 25. Male CORALS and Series 1 right-side pelvis vertical speed (z-direction)

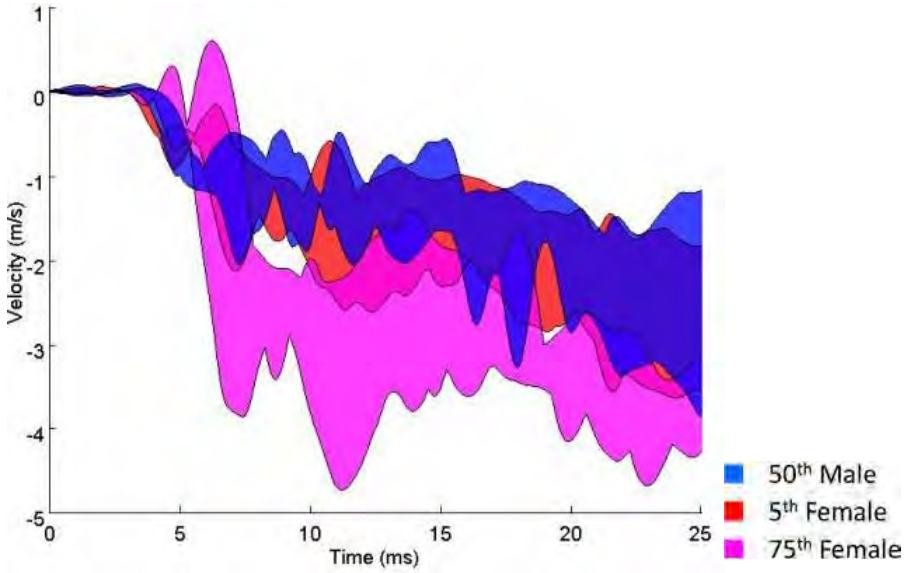

Figure 26. Series 3 and 4 right-side pelvis vertical speed (z-direction)

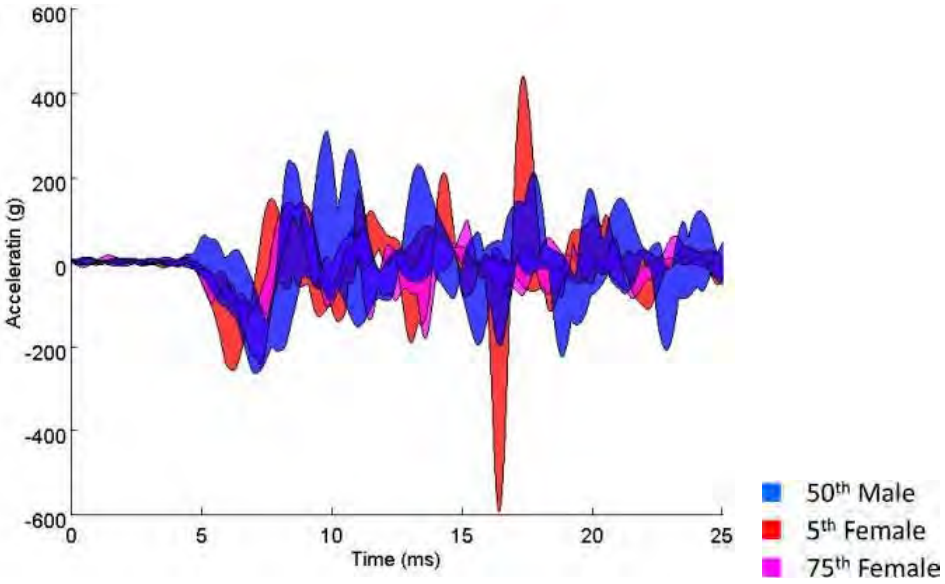

Figure 27. Male CORALS and Series 1 right-side pelvis vertical acceleration (z-direction)

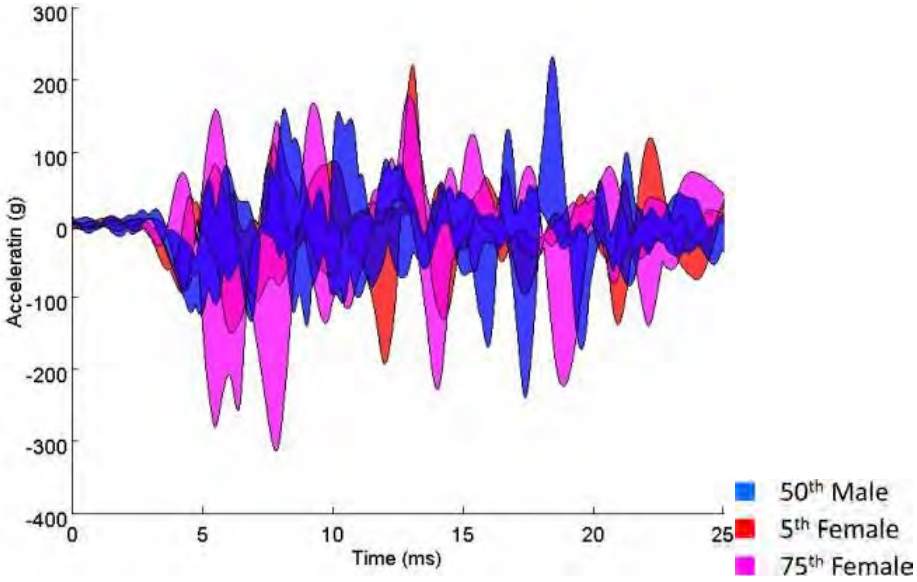

Figure 28. Series 3 and 4 right-side pelvis vertical acceleration (z-direction)

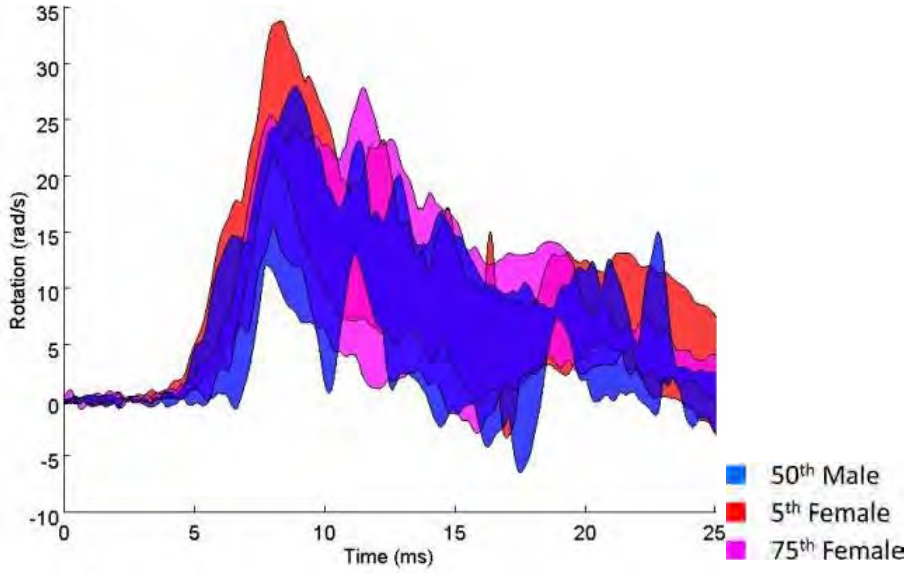

Figure 29. Male CORALS and Series 1 right-side pelvis angular speed in the sagittal plane (about the y-axis)

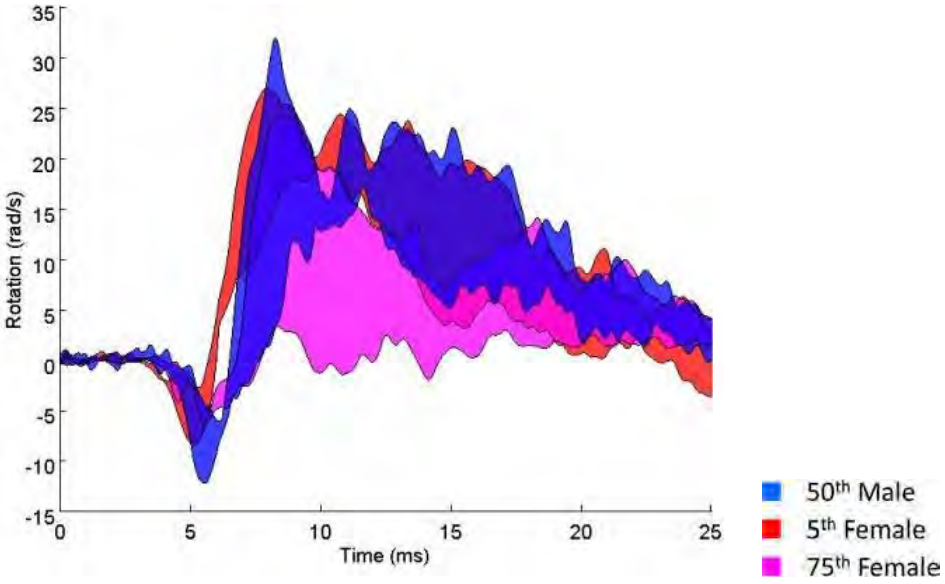

Figure 30. Series 3 and 4 right-side pelvis angular speed in the sagittal plane (along the y-axis)

3.1.1.4 Lumbar Spine

During all test series, the lumbar spine vertical-speed responses are similar in shape between the female and male PMHS, with the females maintaining higher speeds throughout the event (Figures 31 and 32). In male CORALS and Series 1, the lumbar spines of the male PMHS attain greater peak vertical accelerations throughout the event (Figure 33). In Series 3 and 4, the vertical acceleration responses of the males and 75th percentile females include higher peaks throughout the event than those of the 5th

percentile females (Figure 34). Similarly, in all test series, the 50th percentile males and 75th percentile females reach higher angular speeds of the lumbar spine in the sagittal plane (Figures 35 and 36).

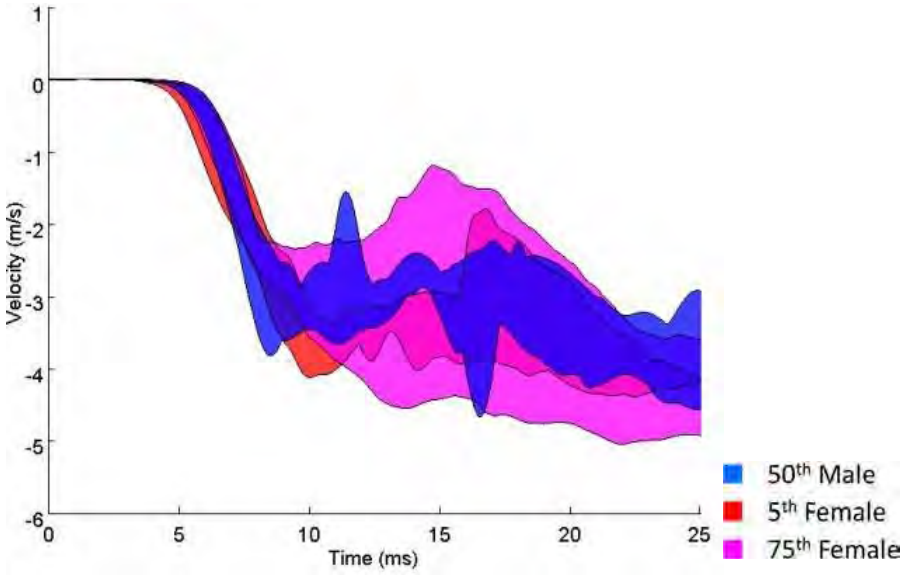

Figure 31. Male CORALS and Series 1 lumbar spine vertical speed (z-axis)

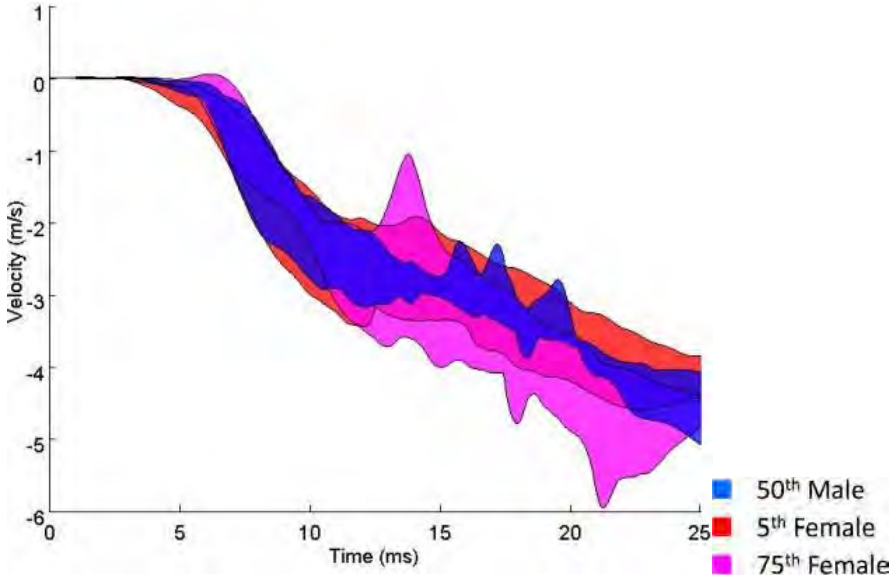

Figure 32. Series 4 and 4 lumbar spine vertical speed (z-axis)

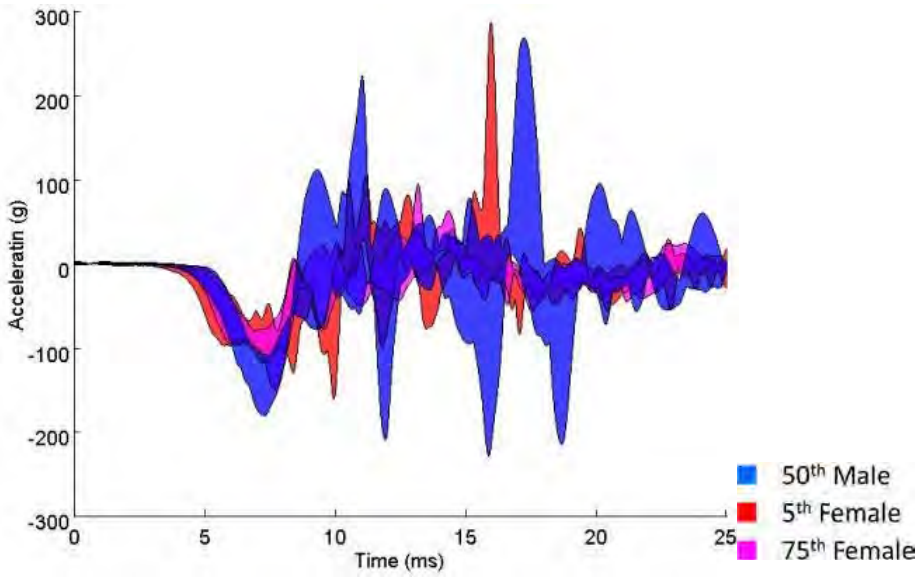

Figure 33. Male CORALS and Series 1 lumbar spine vertical acceleration (z-axis)

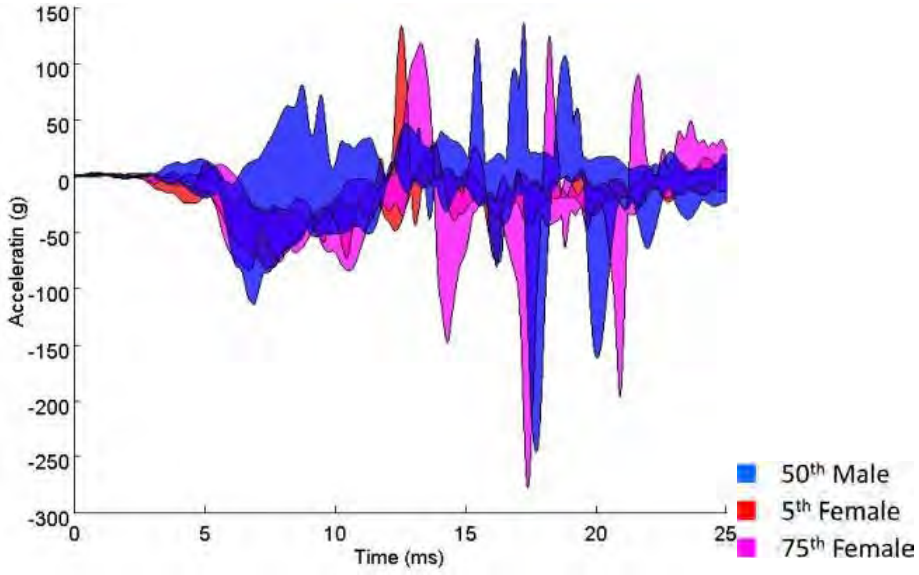

Figure 34. Series 3 and 4 lumbar spine vertical acceleration (z-axis)

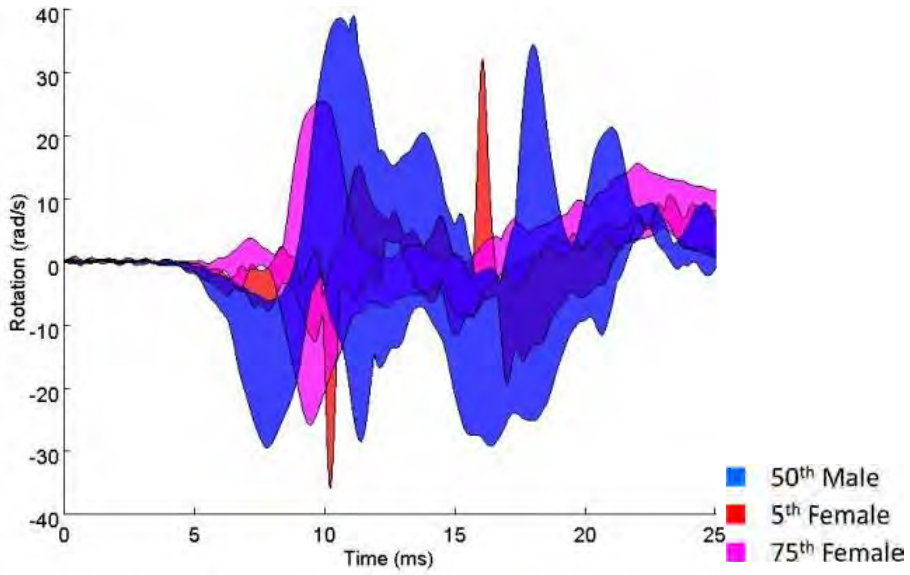

Figure 35. Male CORALS and Series 1 lumbar spine angular speed in the sagittal plane (about the y-axis)

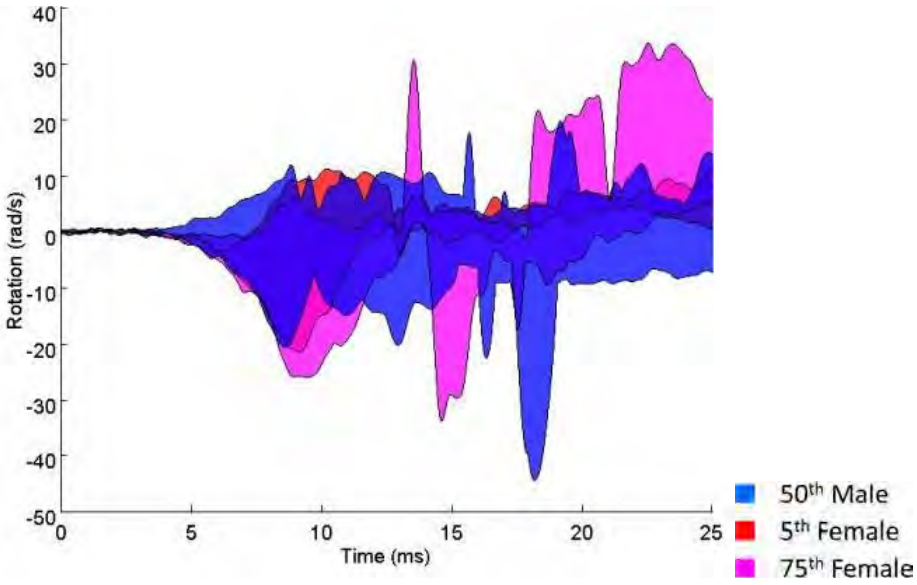

Figure 36. Series 3 and 4 lumbar spine angular speed in the sagittal plane (about the y-axis)

3.1.2 Video Response

Still frames are presented from video captured during the tests to illustrate the movement of the surrogates throughout the test event. Lateral and frontal views are shown for each crew member for all shots. Figures 37 through 58 show representative still frames from the loading phase of each test for each crew. Frames are shown for 0, 4, 8, 12, and 16 ms for CORALS and Series 1 and 0, 2, 4, 6, 8 ms for Series 3 and 4. Appendix C

includes a frame showing the surrogate position at mid-event (150 ms for CORALS and Series 1; 75 ms for Series 3 and 4) as well as a frame showing the apex of limb motion (300 ms for CORALS and Series 1; 150 ms for Series 3 and 4).

There are no gross kinematics differences observed between the surrogate groups in the video data. It is notable that images from female shots 2 and 4 demonstrate that it is physically impossible to position the Hybrid III 5th percentile female ATD in an upright, seated position on the ALF. In addition, Appendix C illustrates the smaller range of motion exhibited by the ATD. As expected, the center of the floor undergoes greater deformation due to the central location of the charge. This causes greater vertical displacement of the inboard (left) lower extremity than the outboard (right) lower extremity. This is more noticeable in the high-energy floor condition (Series 3 and 4), which exhibits greater floor deformation sooner in the event. Differences in floor input between the inboard and outboard lower extremities (e.g., variations in displacement, rate of displacement, and/or energy level) may be responsible for the observed differences in injury pattern. Video data revealed variation in joint behavior among the surrogates. Table 5 shows the initial anatomical motions observed at the ankle and hip in the frontal and lateral views. The hip typically remains neutral, with a natural splaying of the knees towards the end of the event. External rotation of the hip at an earlier time was noted in two female PMHS. Inversion and eversion at the ankle are common.

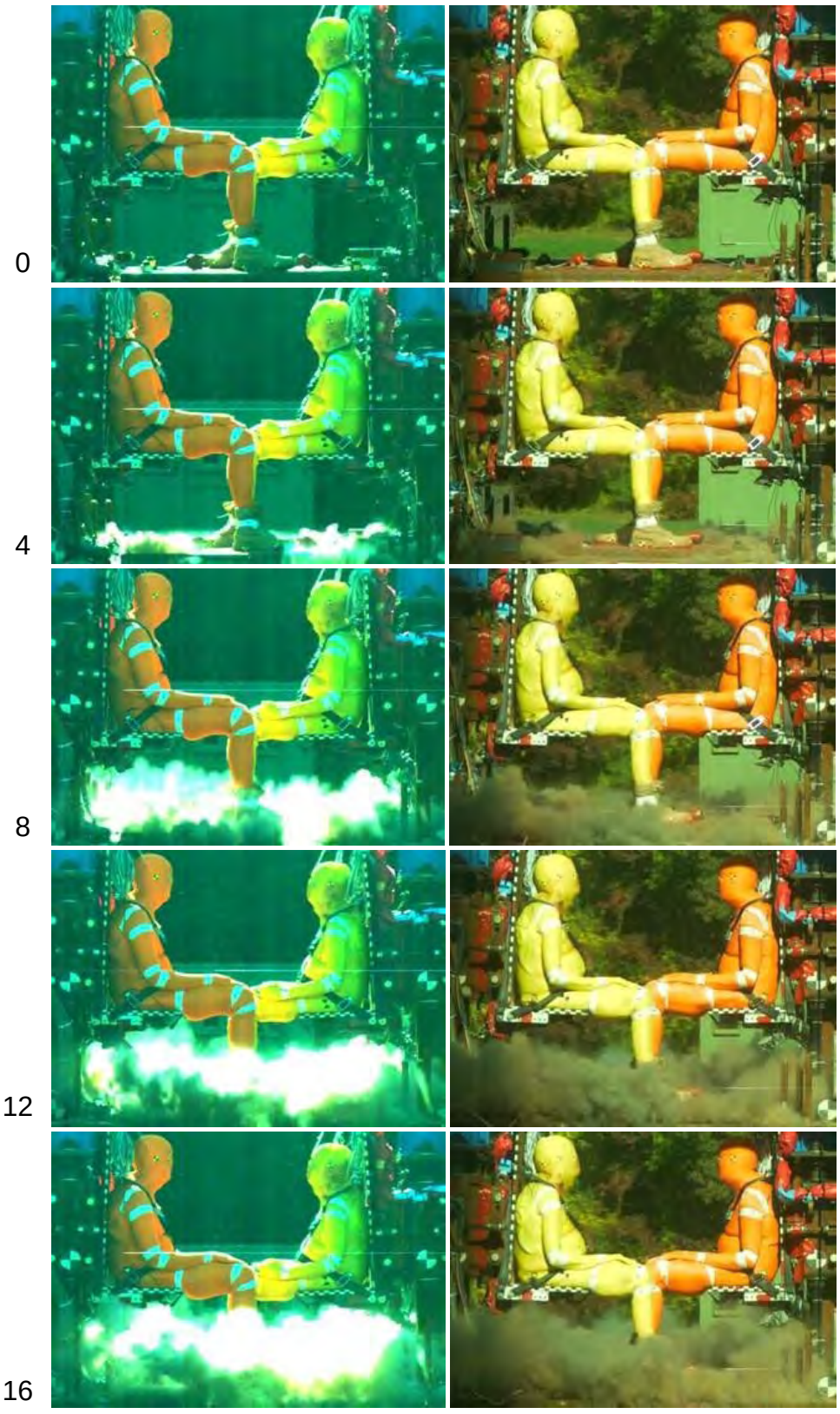

Figure 37. Male shot 1, lateral view (Crew 1: 50th percentile male, orange; Crew 2: 50th percentile male, yellow)

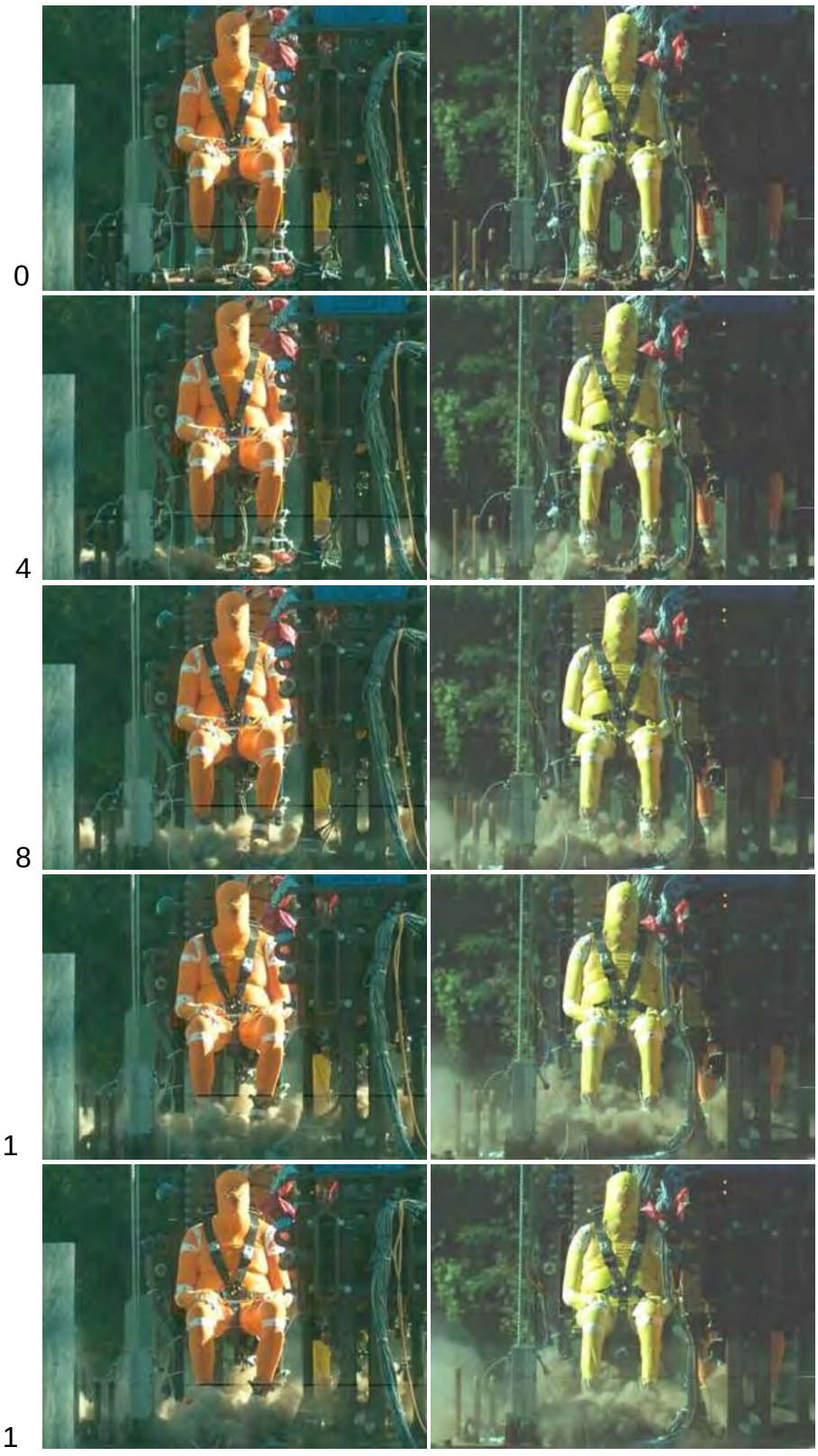

Figure 38. Male shot 1, frontal view (Crew 1: 50th percentile male, orange; Crew 2: 50th percentile male, yellow)

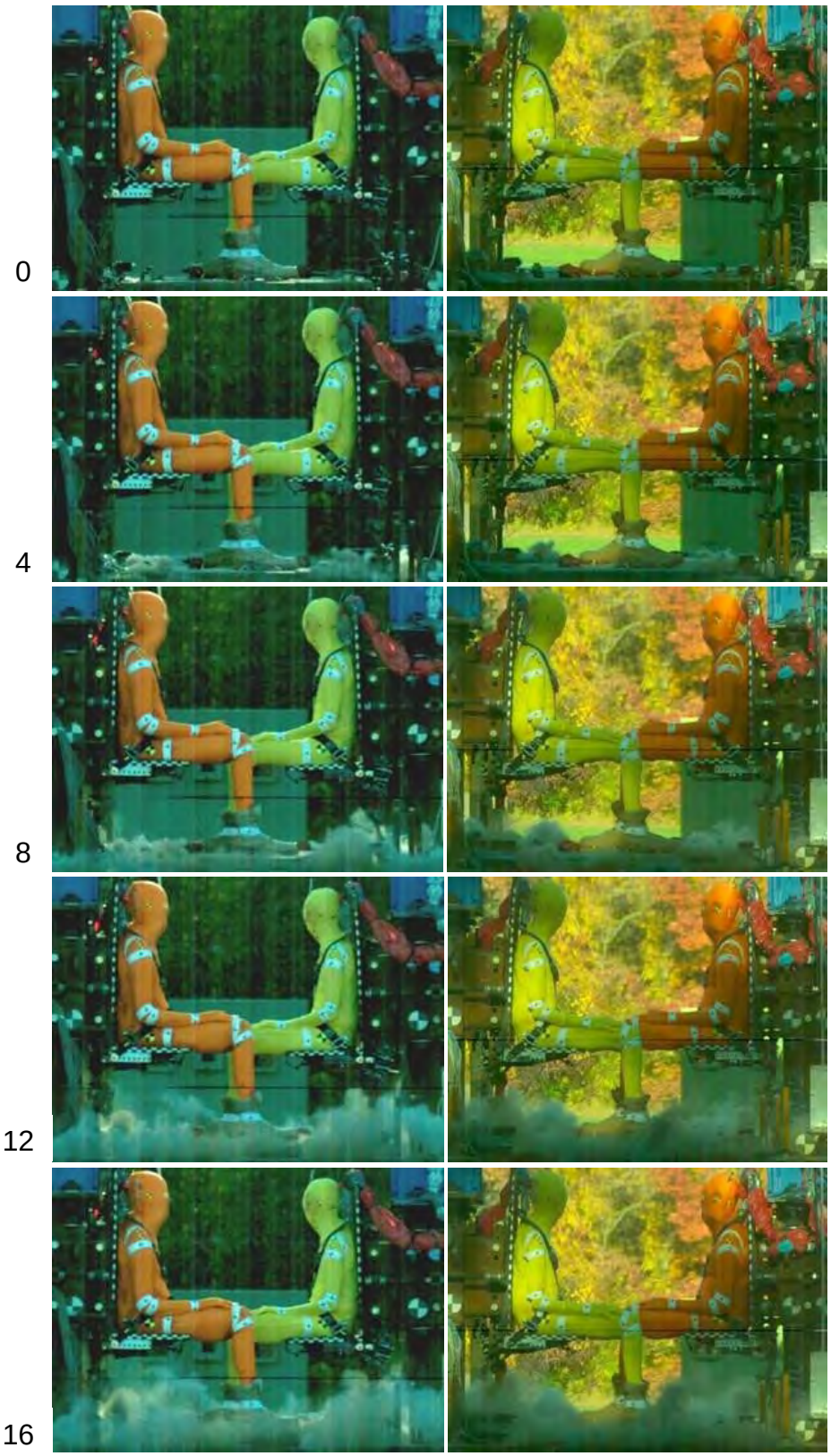

Figure 39. Male shot 2, lateral view (Crew 1: 50th percentile male, orange; Crew 2: 50th percentile male, yellow)

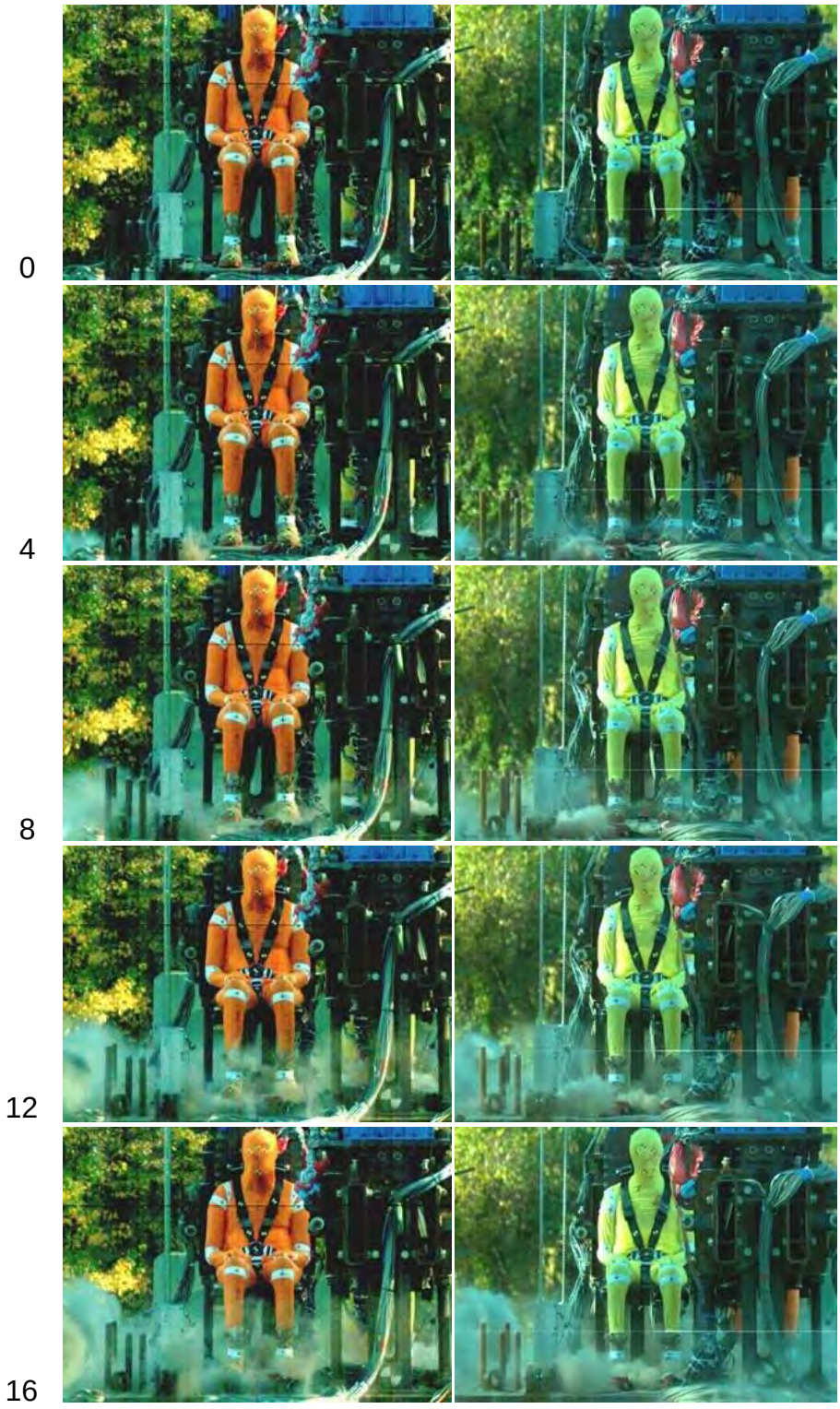

Figure 40. Male shot 1, frontal view (Crew 1: 50th percentile male, orange; Crew 2: 50th percentile male, yellow)

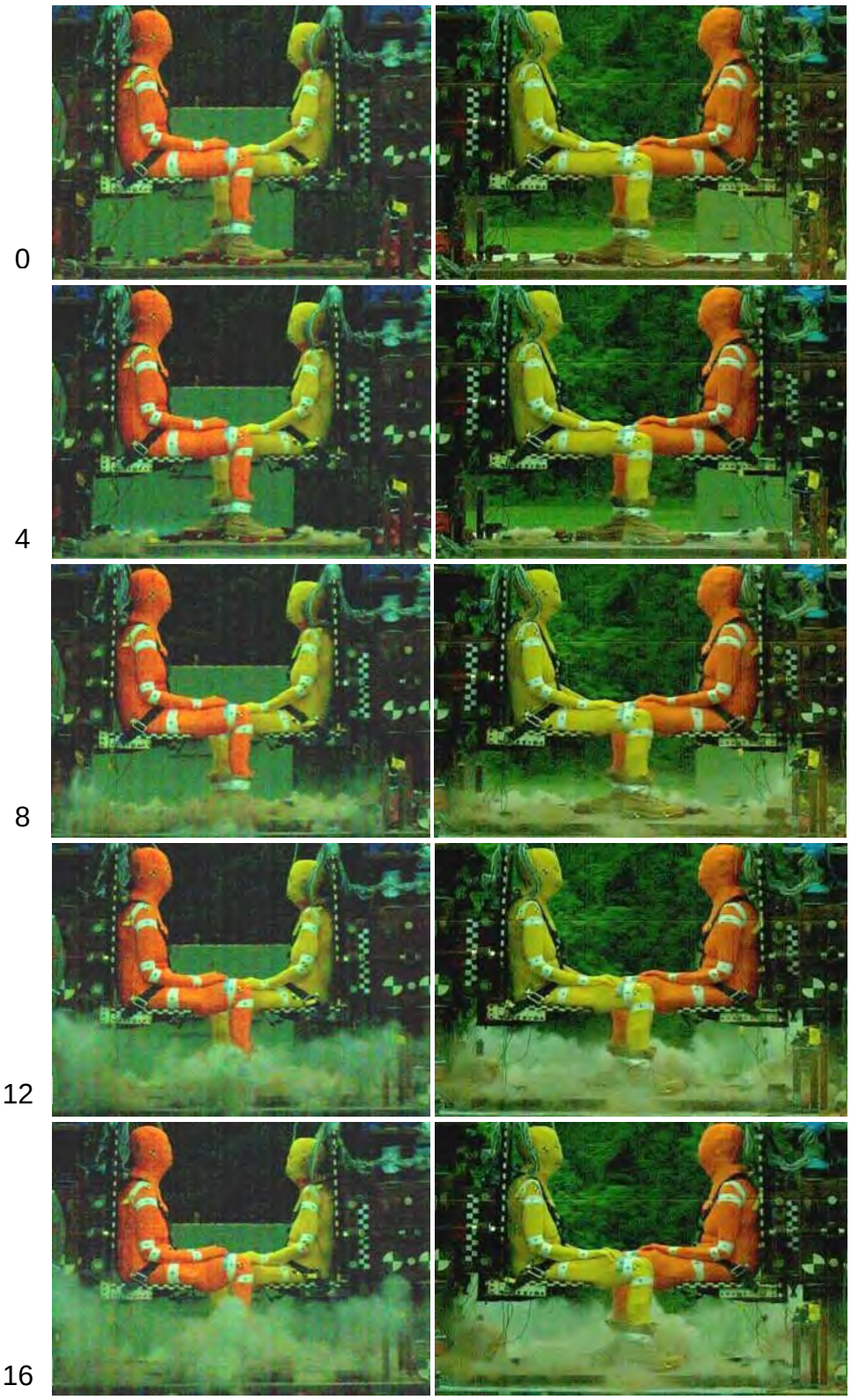

Figure 41. Female shot 1, lateral view (Crew 1: 75th percentile female, orange; Crew 2: 5th percentile female, yellow)

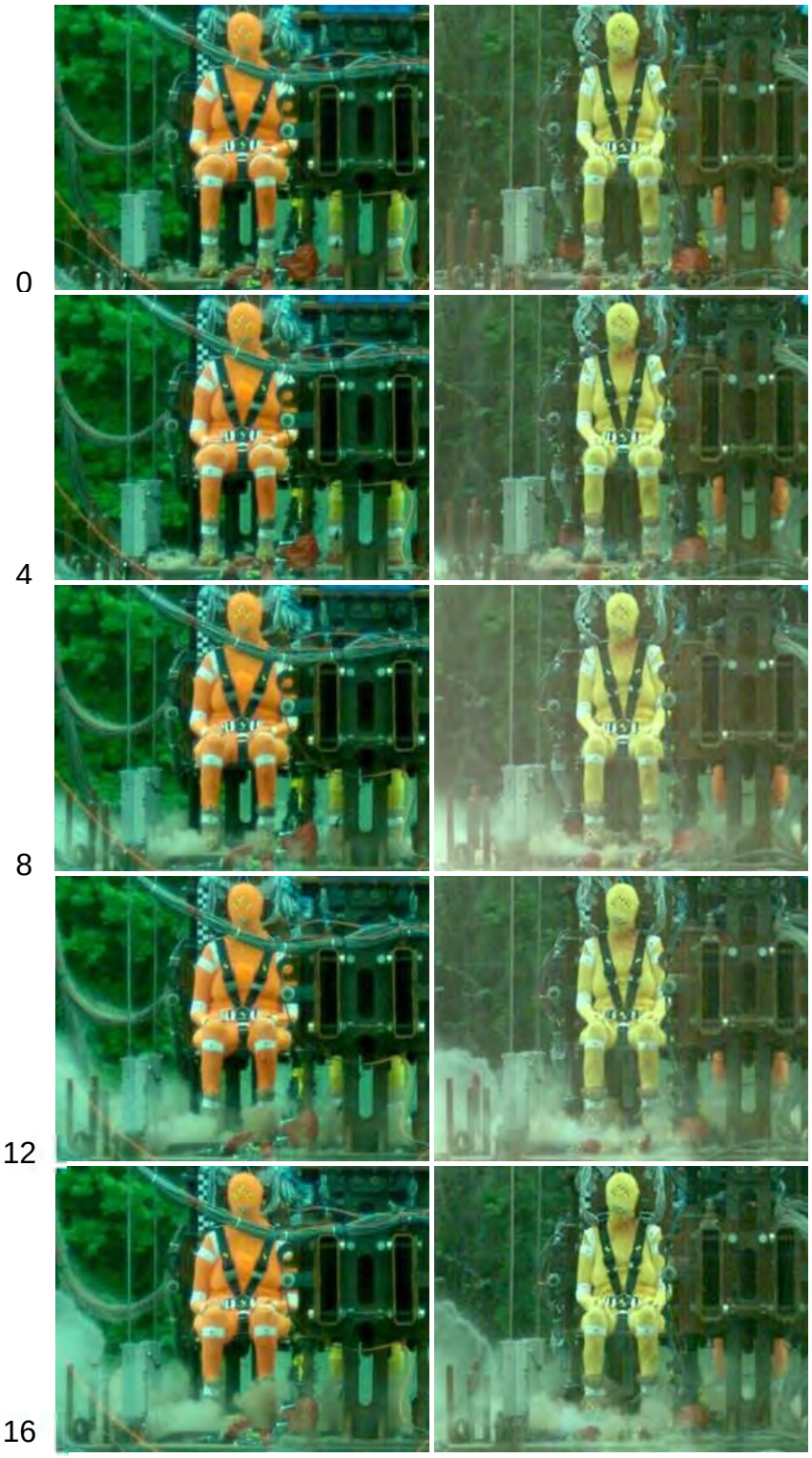

Figure 42. Female shot 1, frontal view (Crew 1: 75th percentile female, orange; Crew 2: 5th percentile female, yellow)

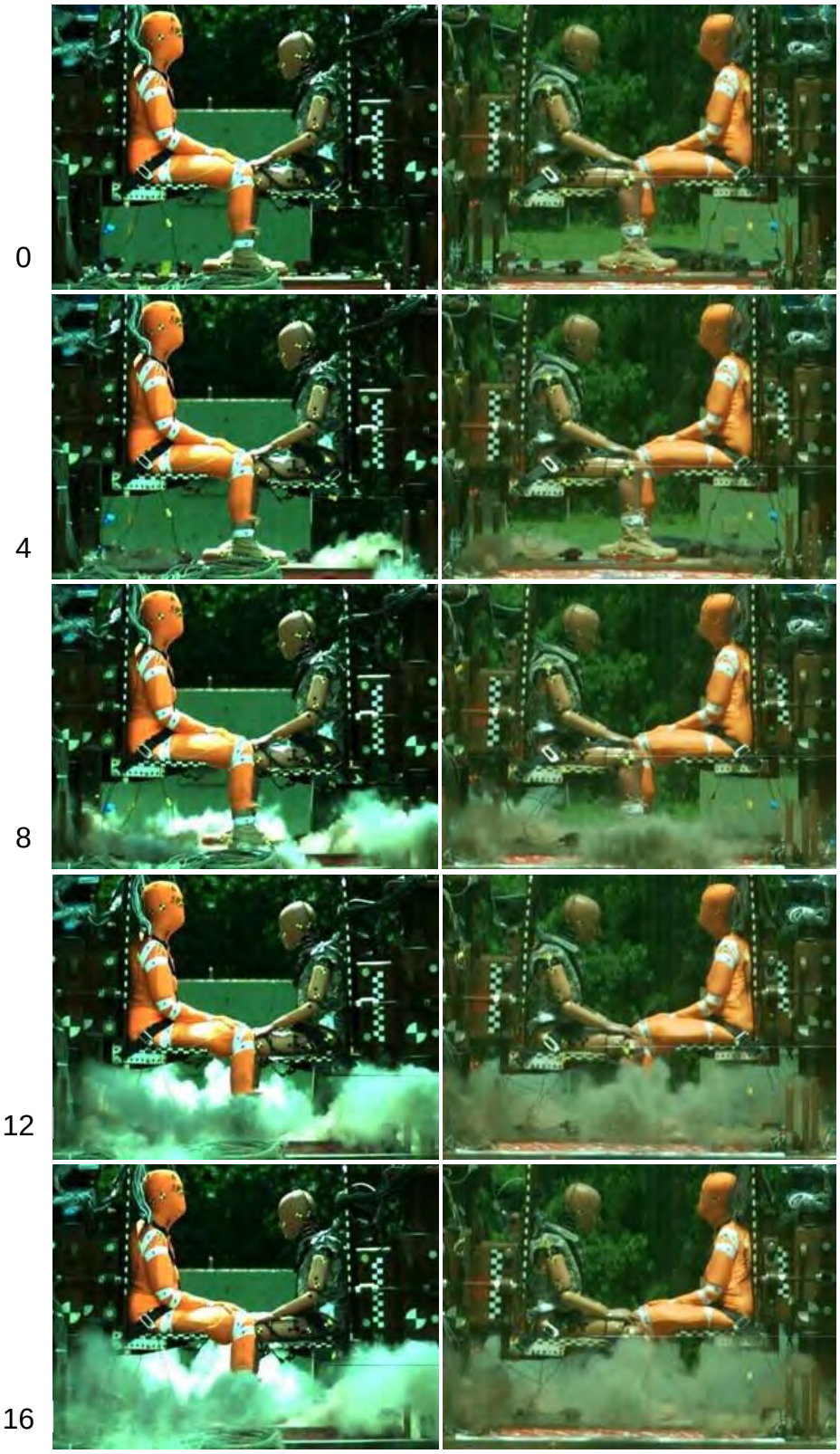

Figure 43. Female shot 2, lateral view (Crew 1: 75th percentile female, orange; Crew 2: Hybrid III 5th percentile female ATD)

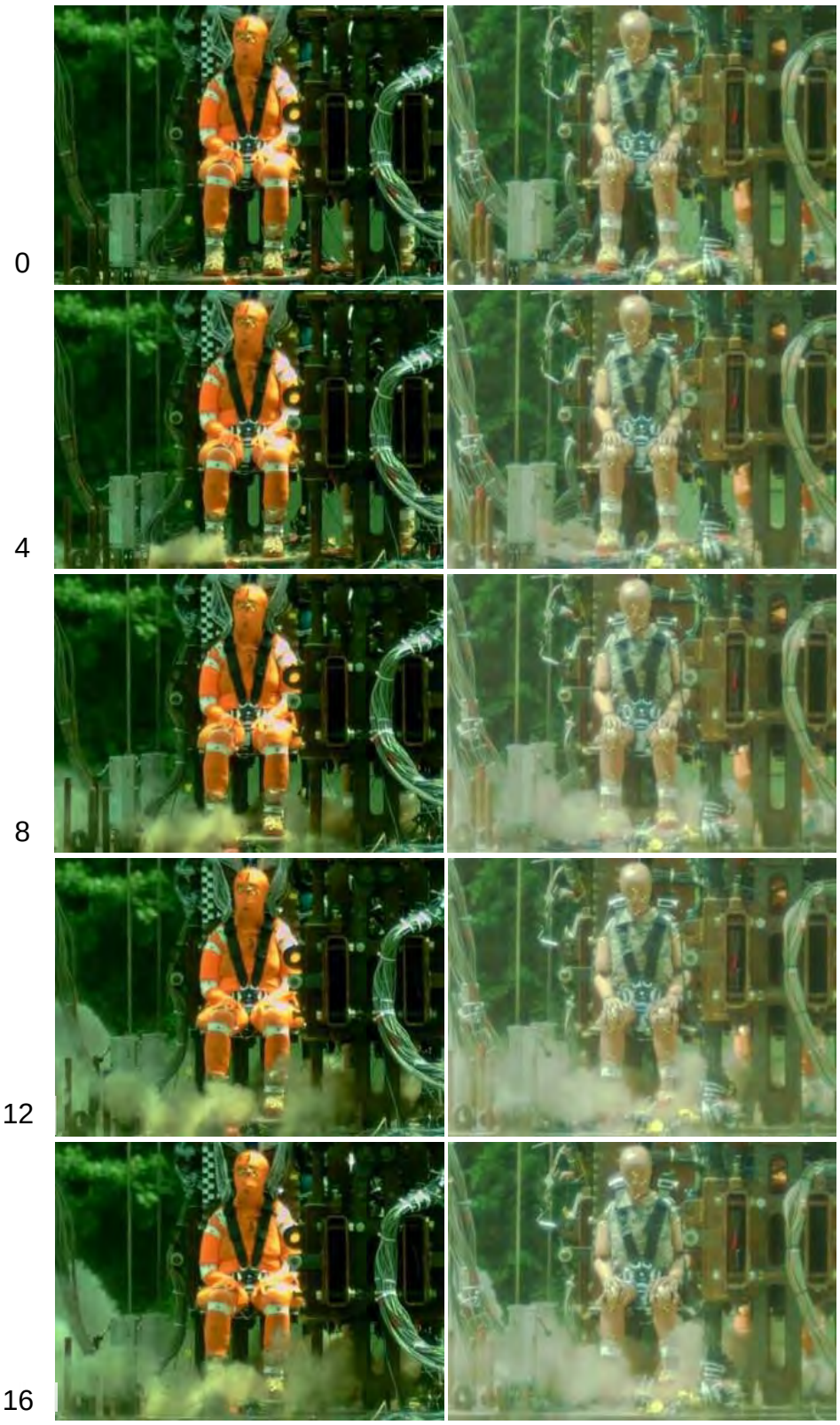

Figure 44. Female shot 2, frontal view (Crew 1: 75th percentile female, orange; Crew 2: Hybrid III 5th percentile female ATD)

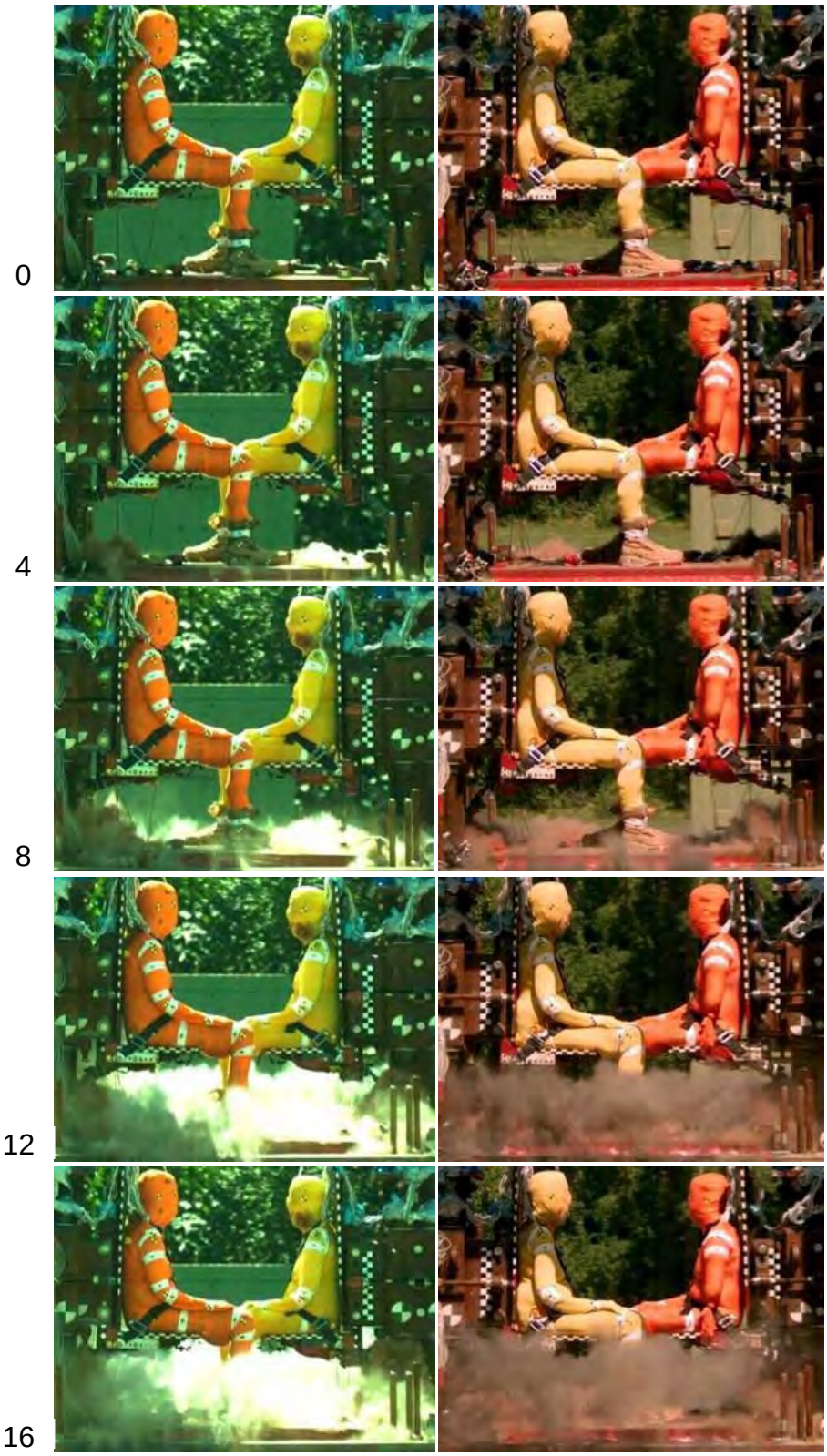

Figure 45. Female shot 3, lateral view (Crew 1: 75th percentile female, orange; Crew 2: 5th percentile female, yellow)

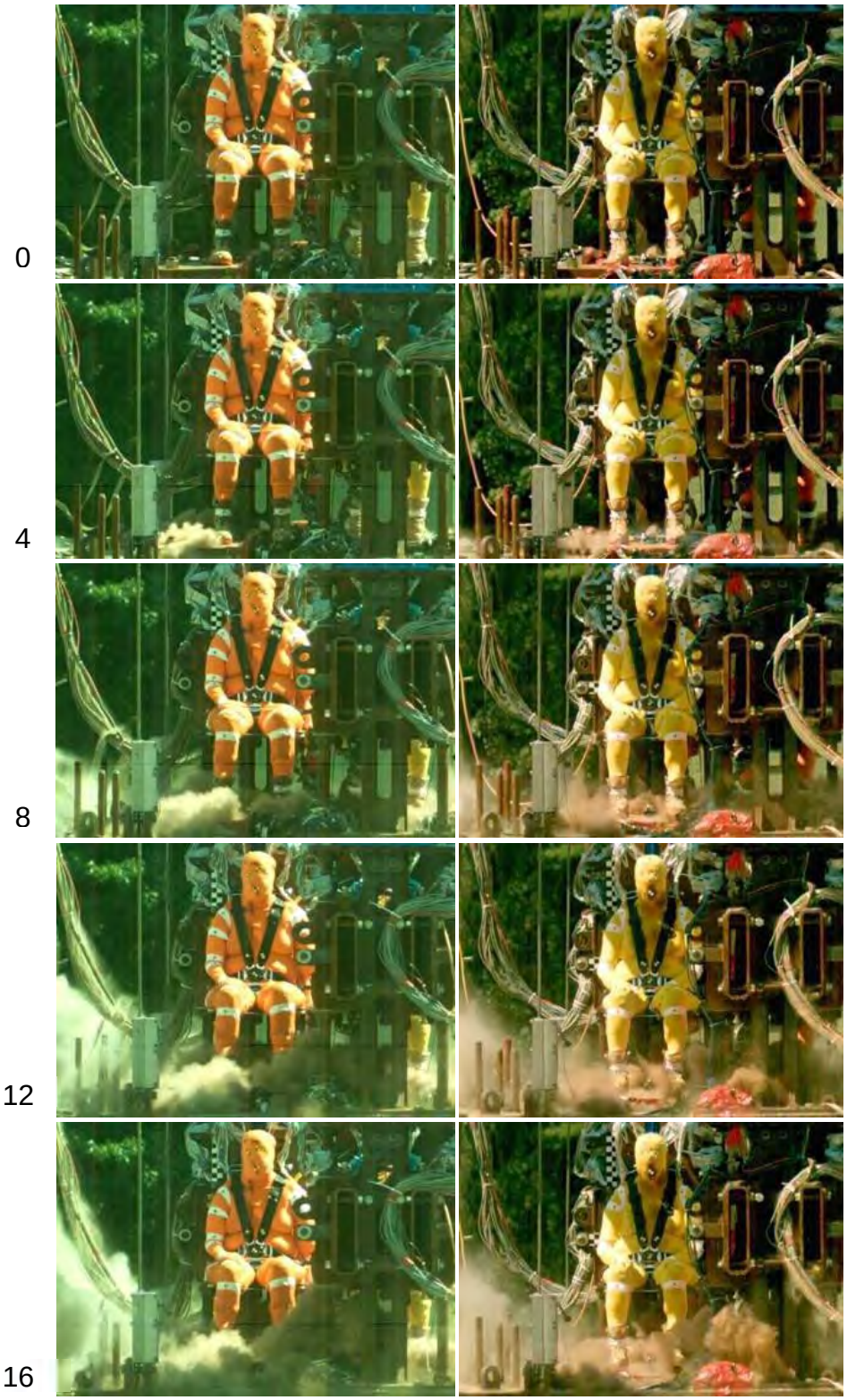

Figure 46. Female shot 3, frontal view (Crew 1: 75th percentile female, orange; Crew 2: 5th percentile female, yellow)

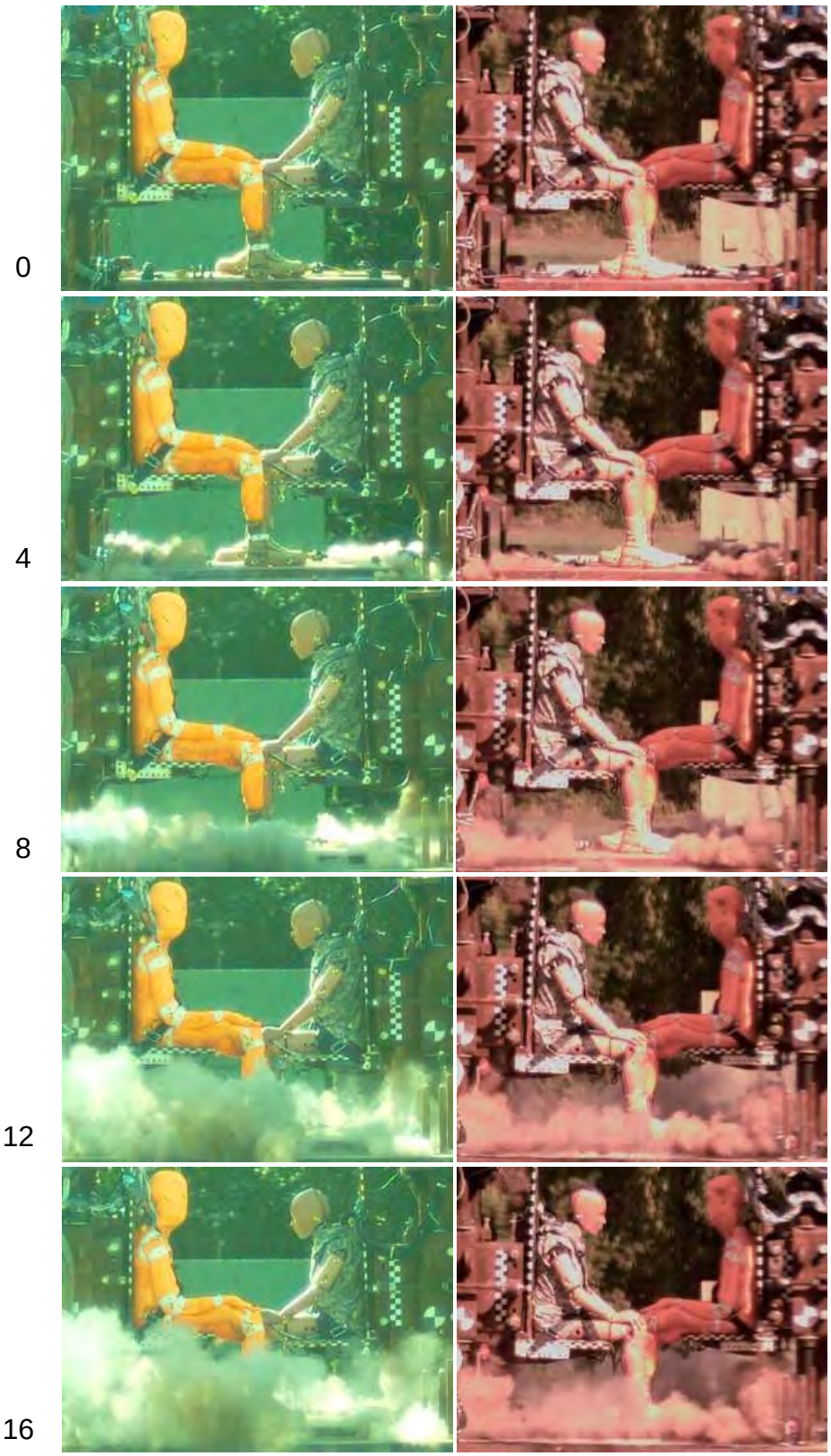

Figure 47. Female shot 4, lateral view (Crew 1: 5th percentile female, orange; Crew 2: Hybrid III 5th percentile female ATD

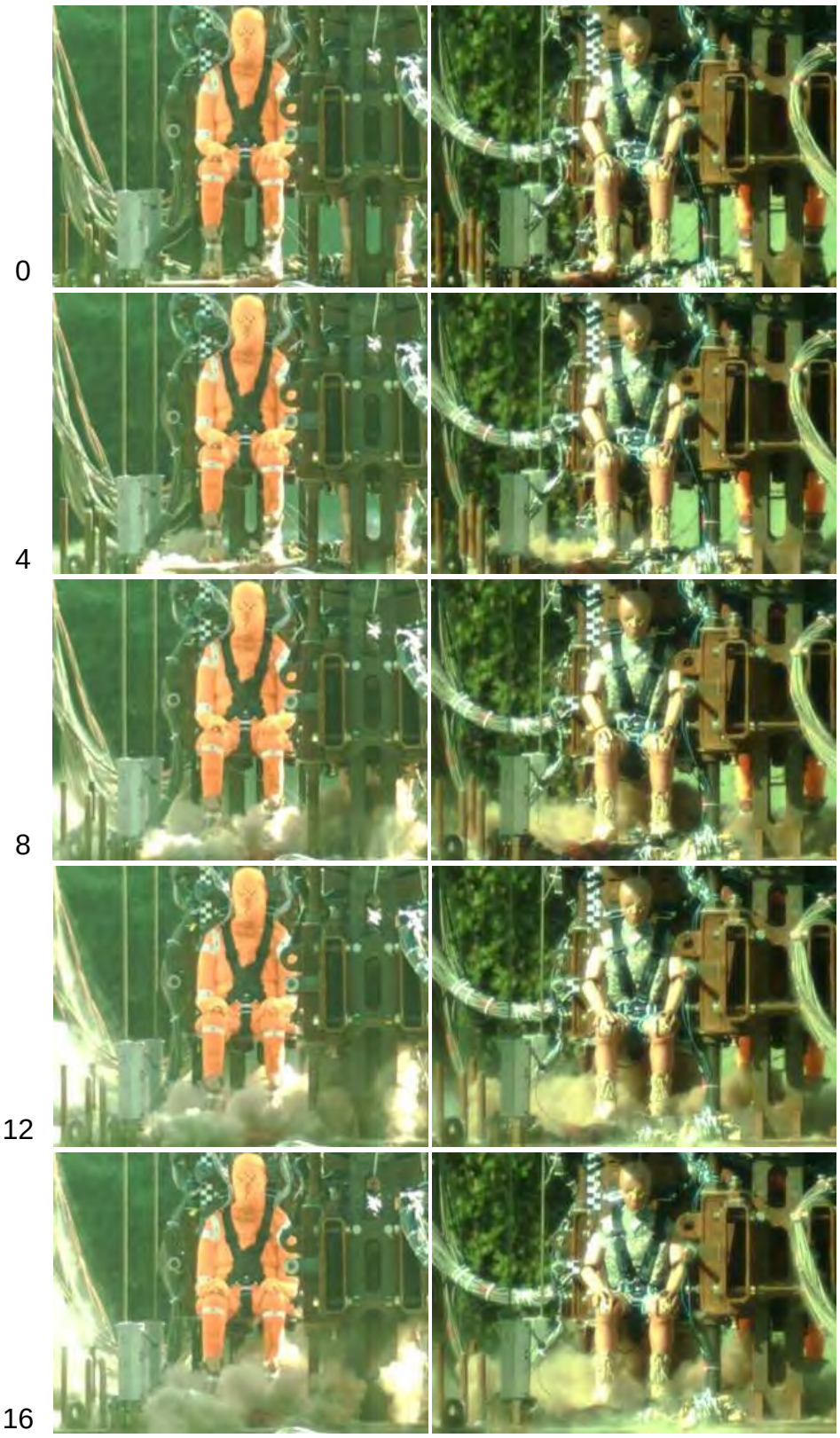

Figure 48. Female shot 4, frontal view (Crew 1: 5th percentile female, orange; Crew 2: Hybrid III 5th percentile female ATD)

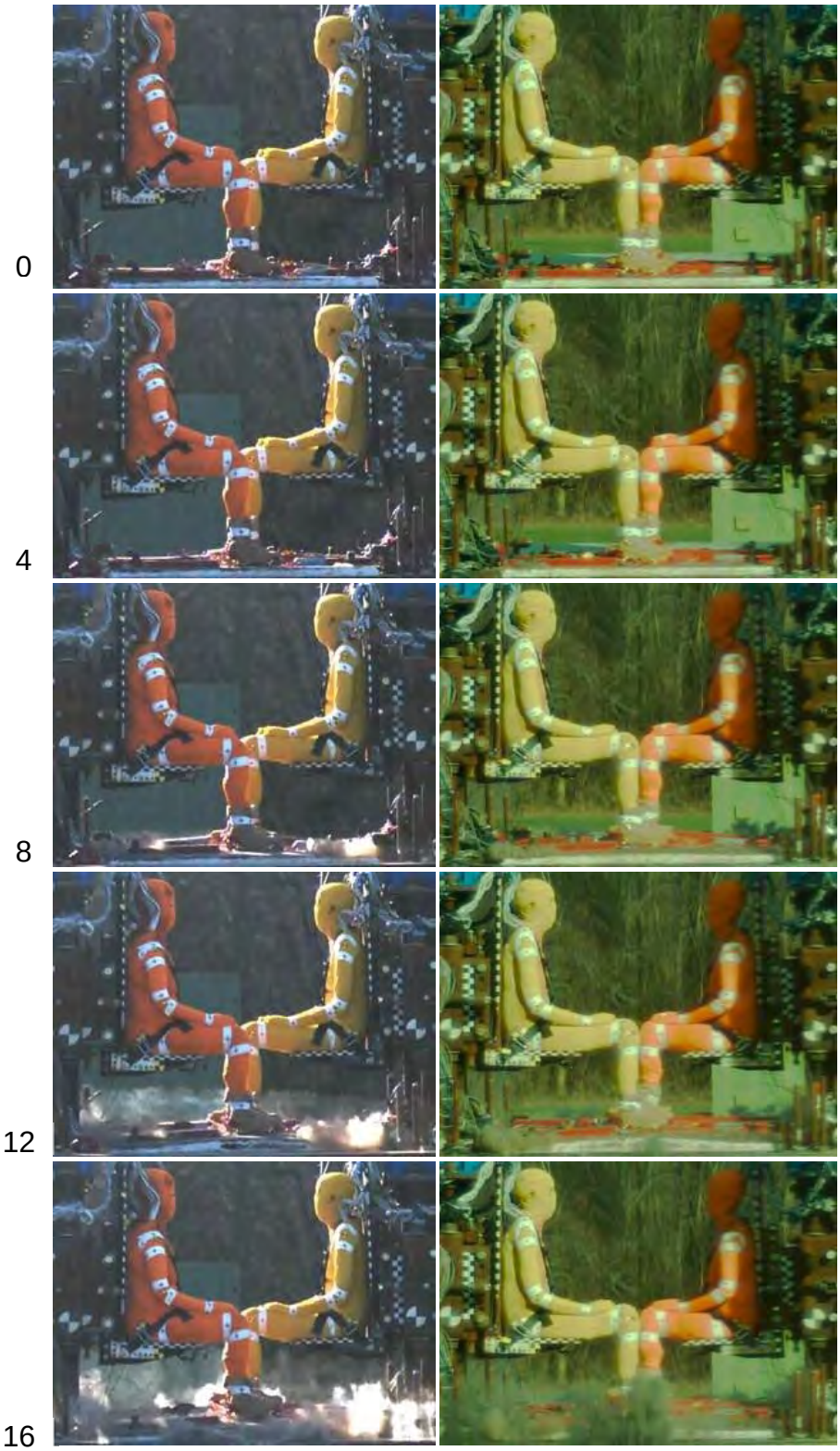

Figure 49. Female shot 5 (Crew 1: 75th percentile female, orange; Crew 2: 5th percentile female, yellow)

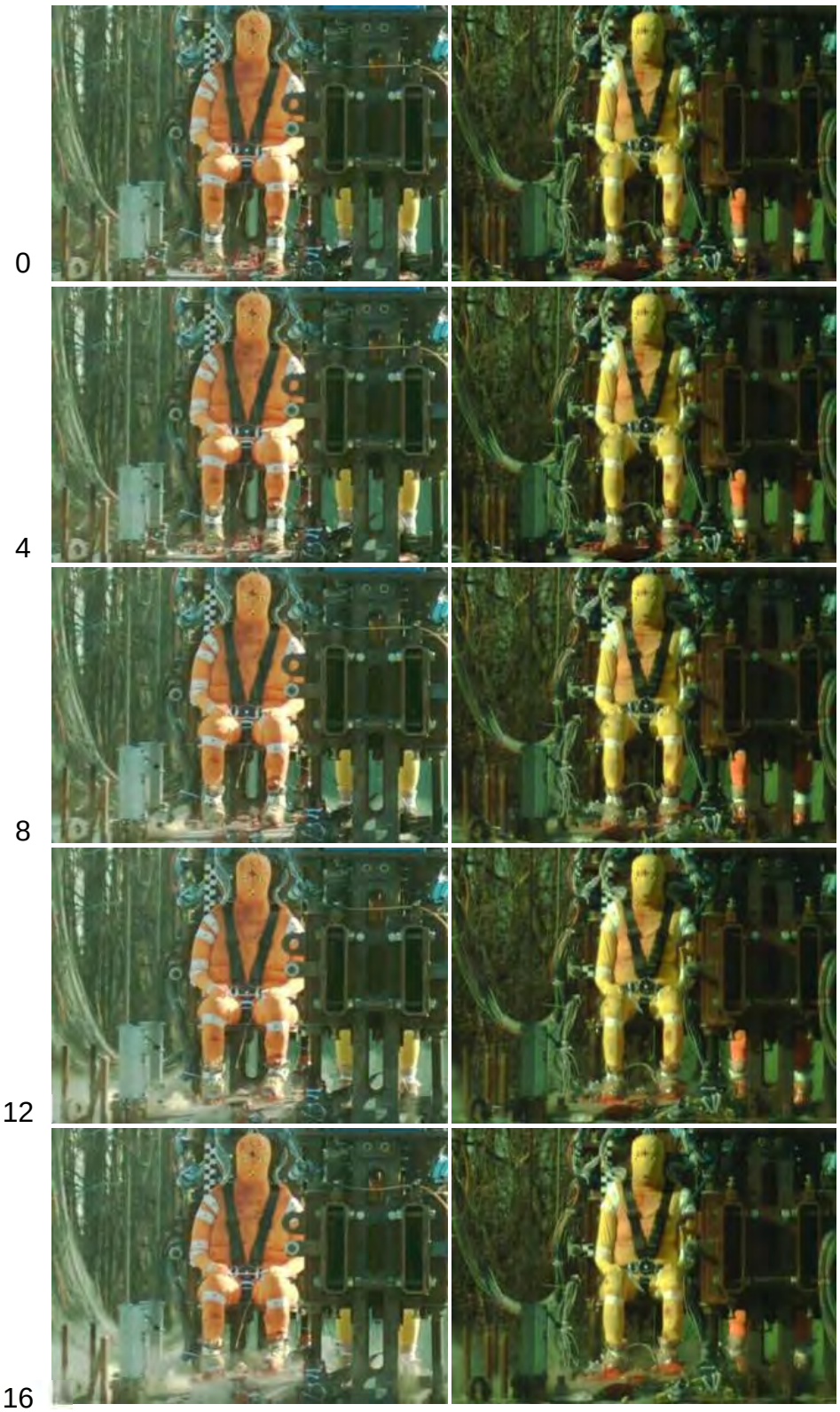

Figure 50. Female shot 5, frontal view (Crew 1: 75th percentile female, orange; Crew 2: 5th percentile female, yellow)

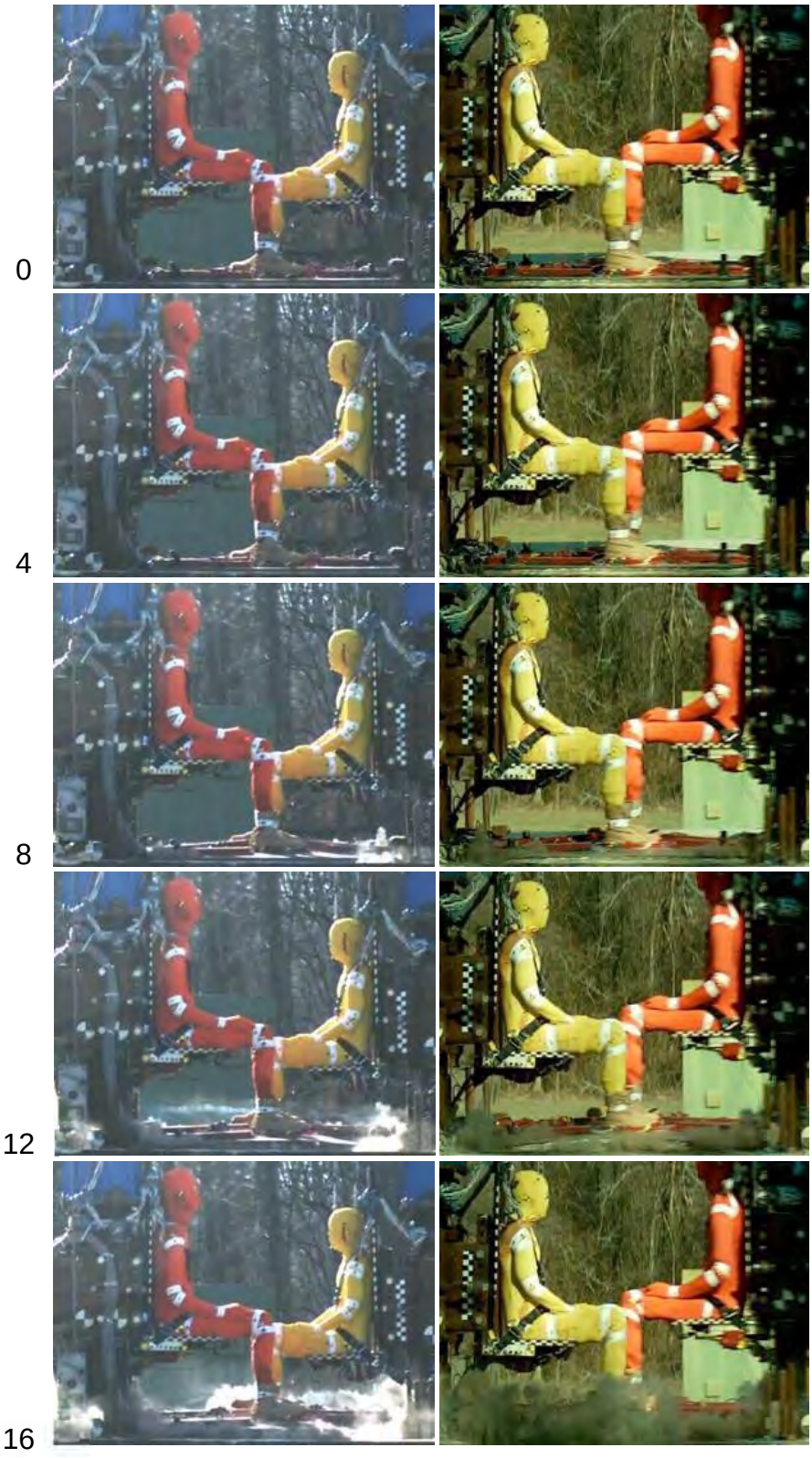

Figure 51. Female shot 6, lateral view (Crew 1: 50th percentile male, orange; Crew 2: 5th percentile female, yellow)

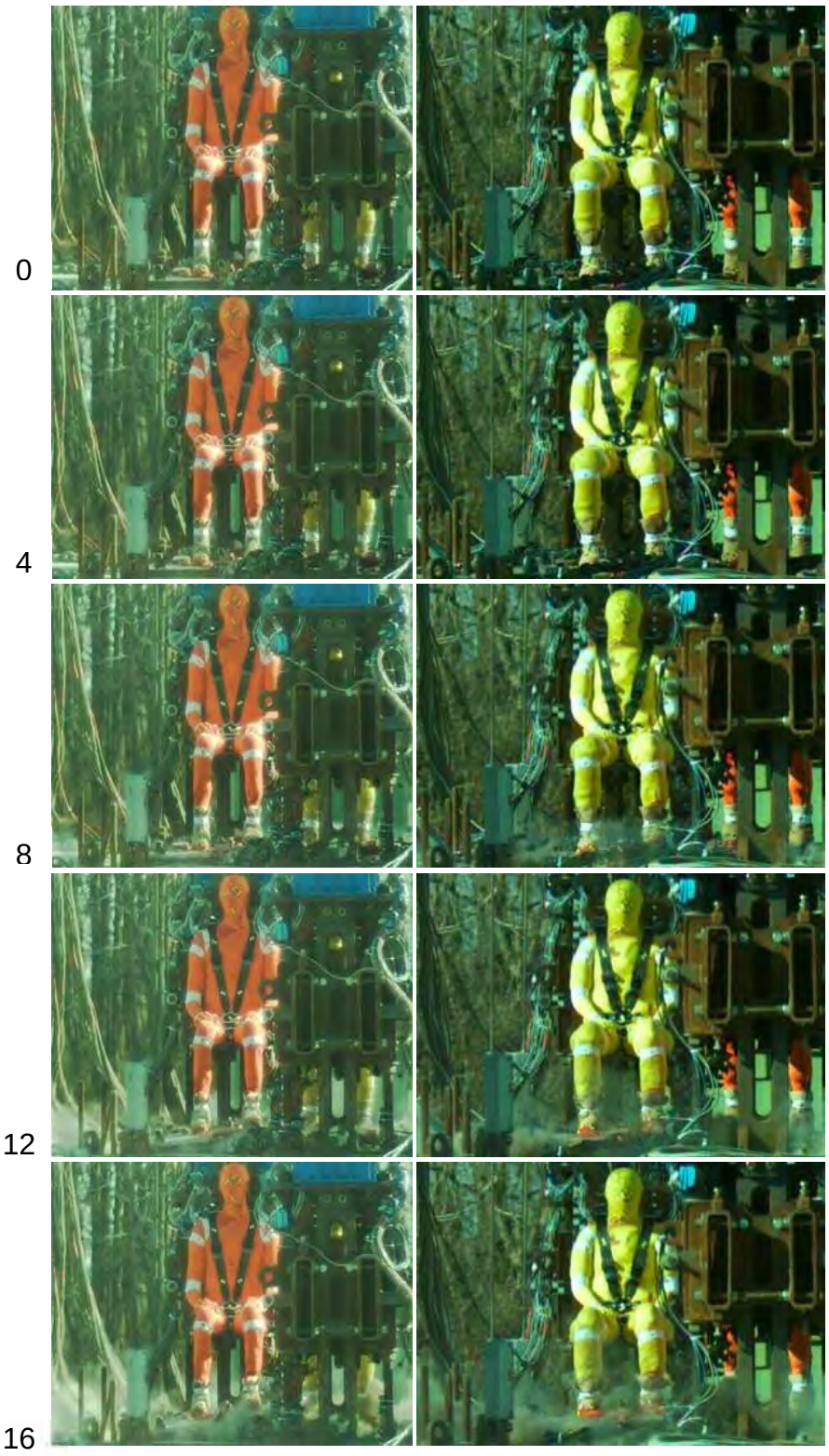

Figure 52. Female shot 6, frontal view (Crew 1: 50th percentile male, orange; Crew 2: 5th percentile female, yellow)

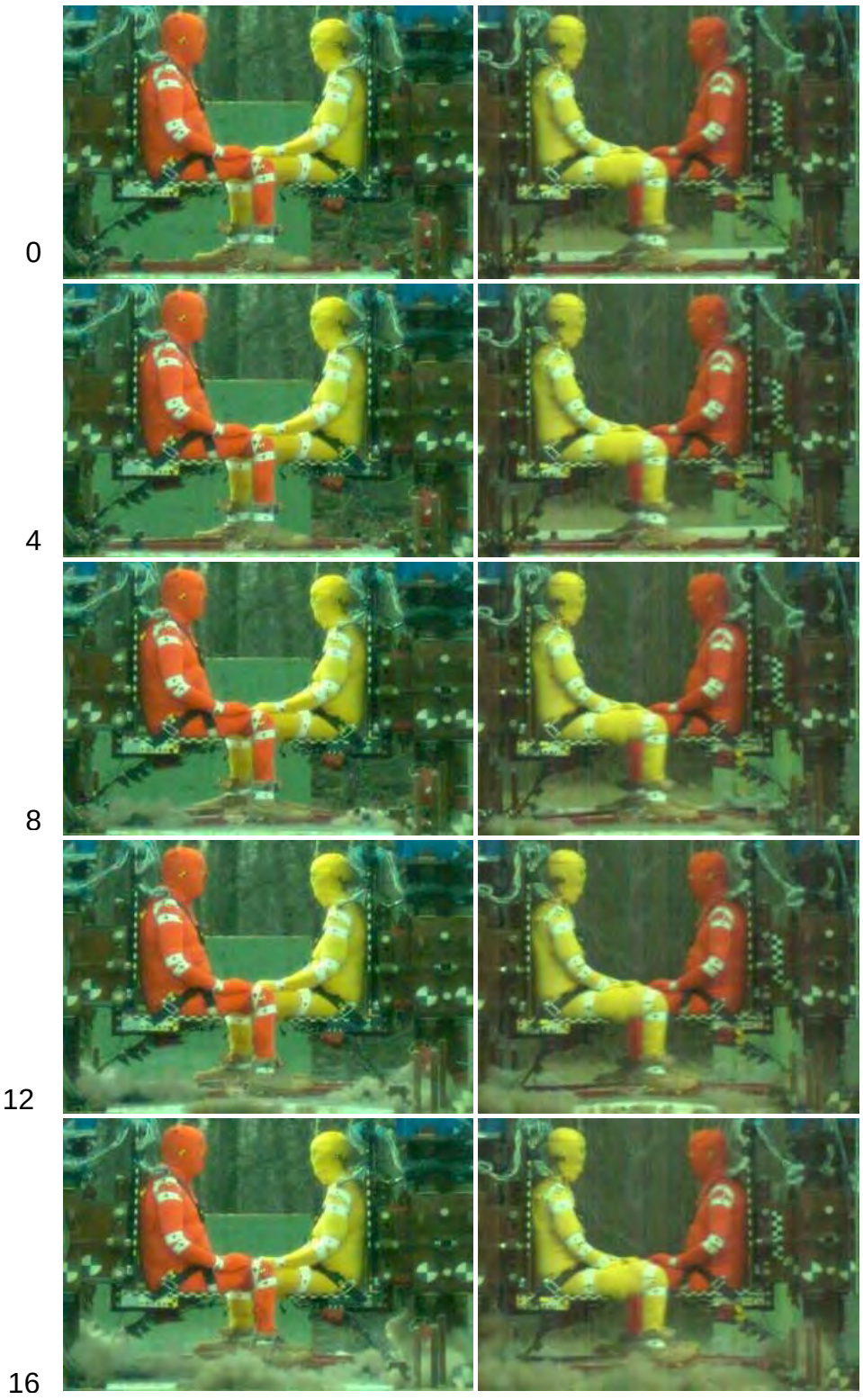

Figure 53. Female shot 7, lateral view (Crew 1: 50th percentile male, orange; Crew 2: 75th percentile male, yellow)

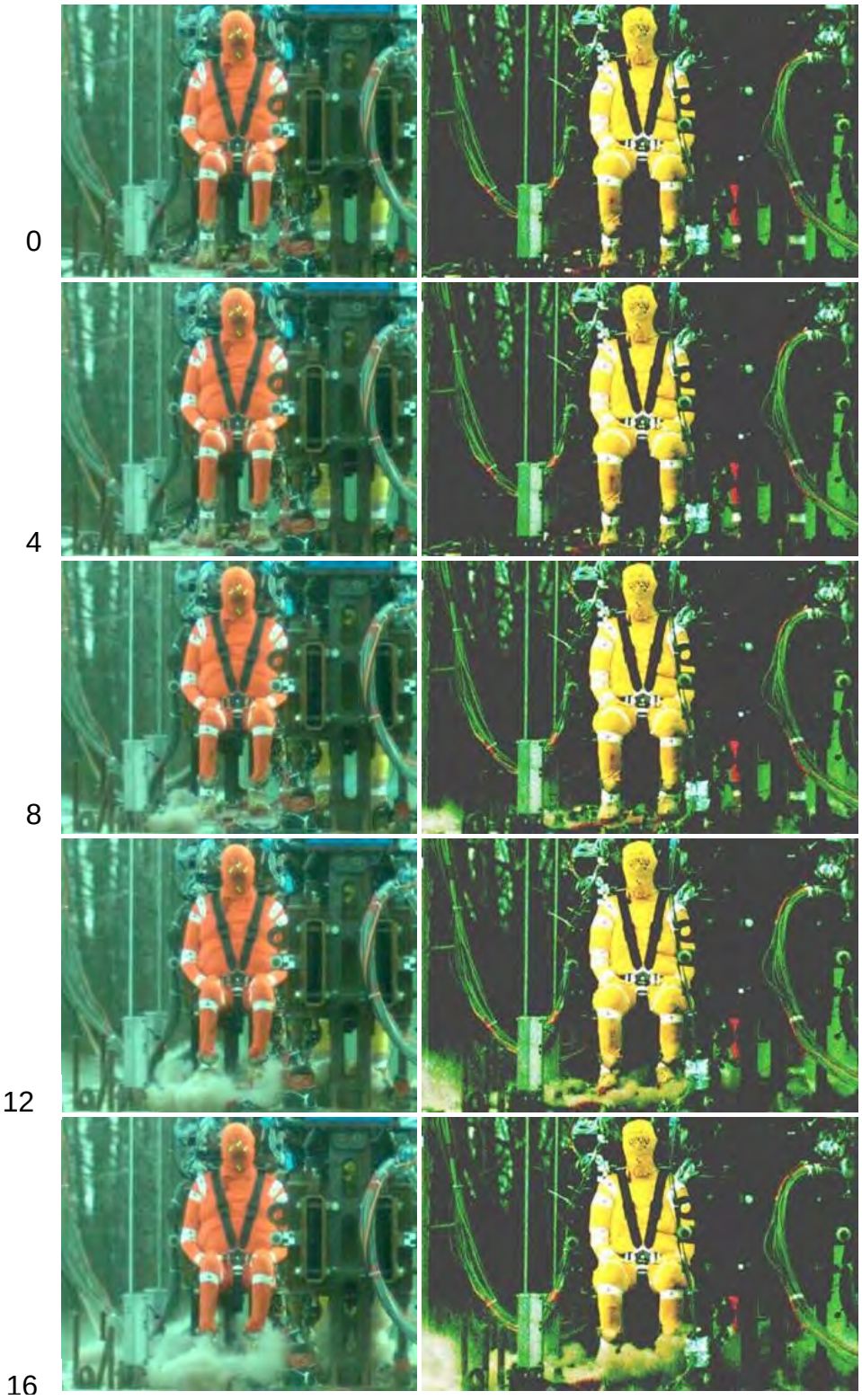

Figure 54. Female shot 7, frontal view (Crew 1: 50th percentile male, orange; Crew 2: 75th percentile male, yellow)

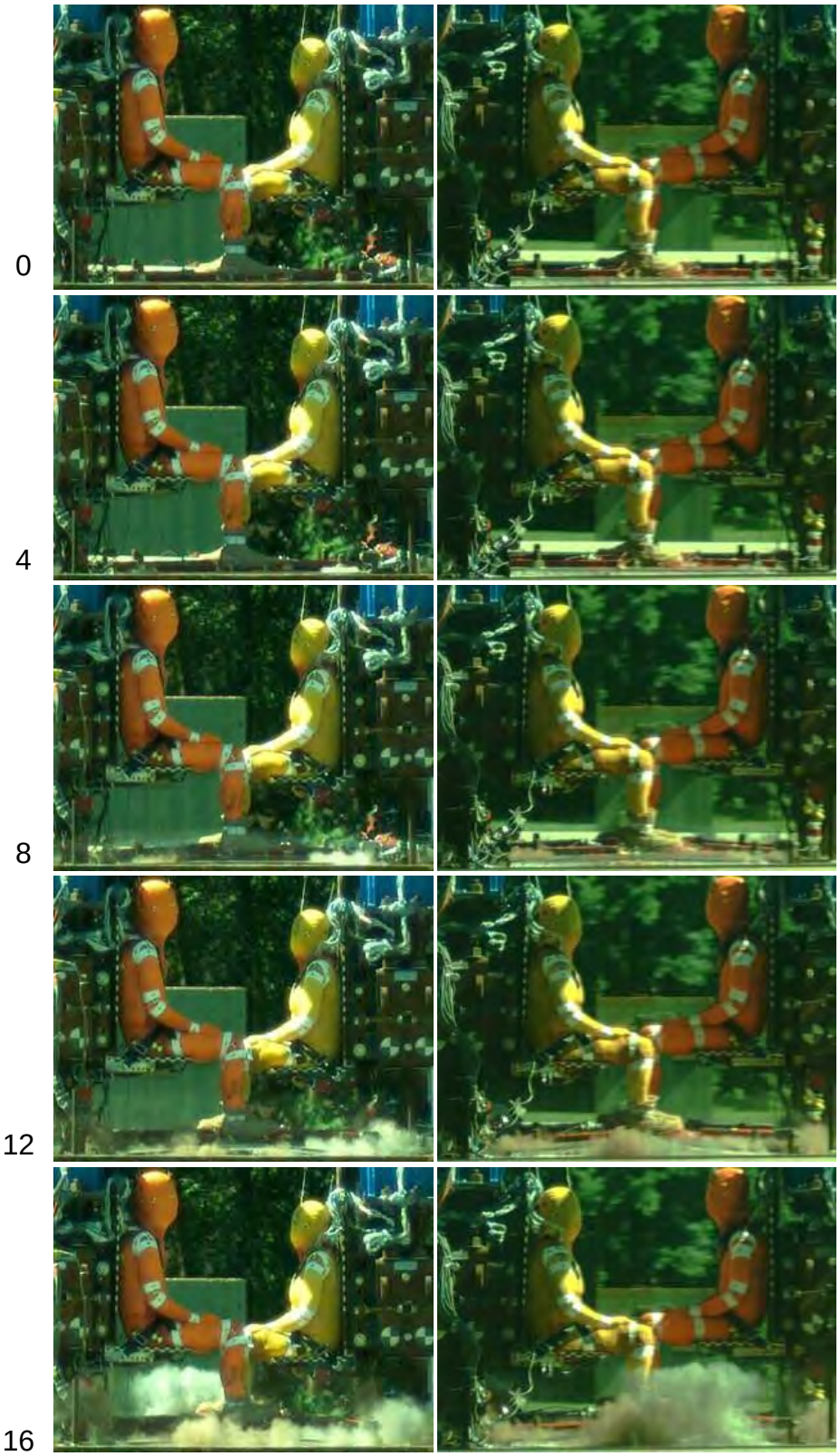

Figure 55. Female shot 8, lateral view (Crew 1: 50th percentile male, orange; Crew 2: 75th percentile female, yellow)

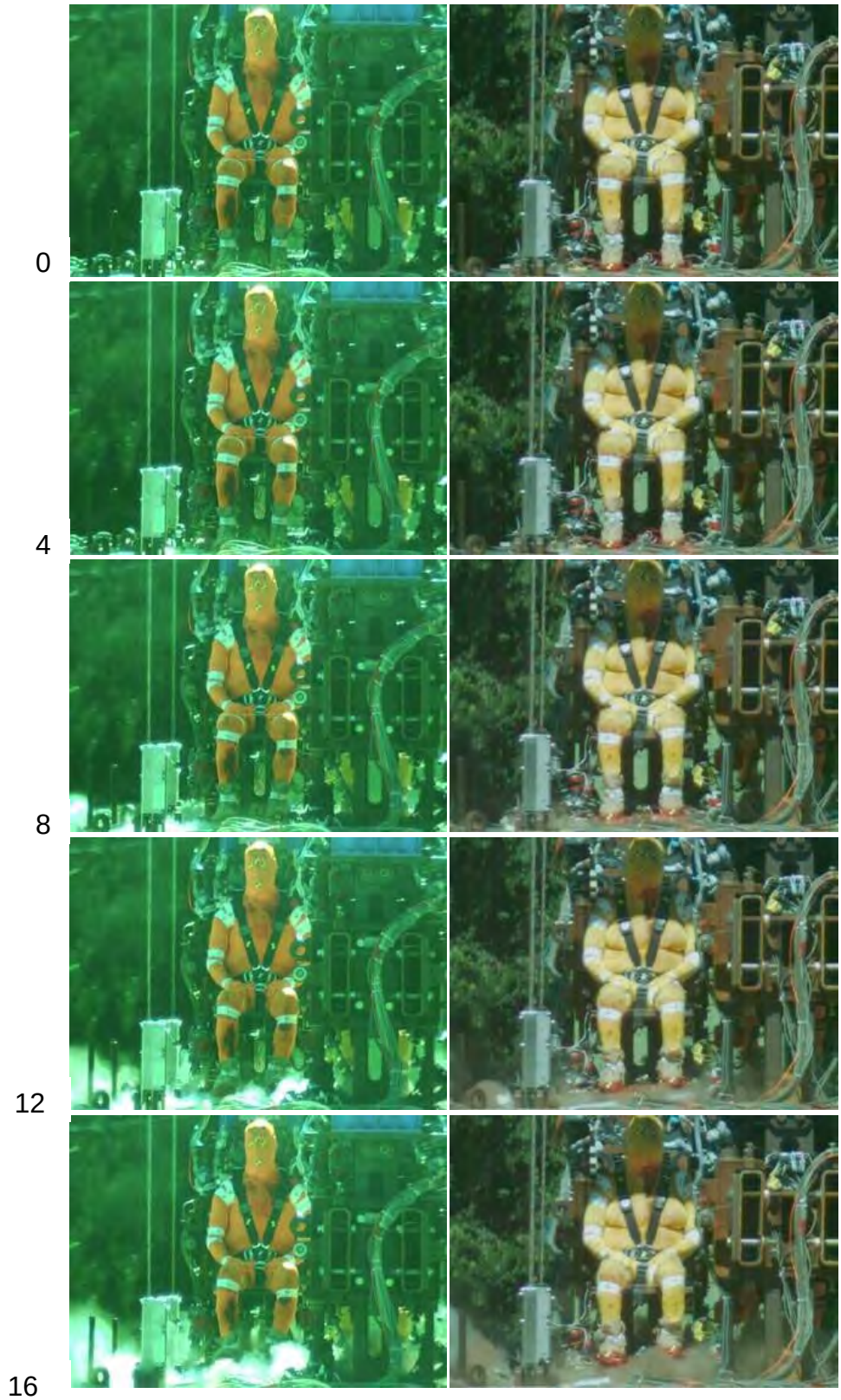

Figure 56. Female shot 8, frontal view (Crew 1: 50th percentile male, orange; Crew 2: 75th percentile female, yellow)

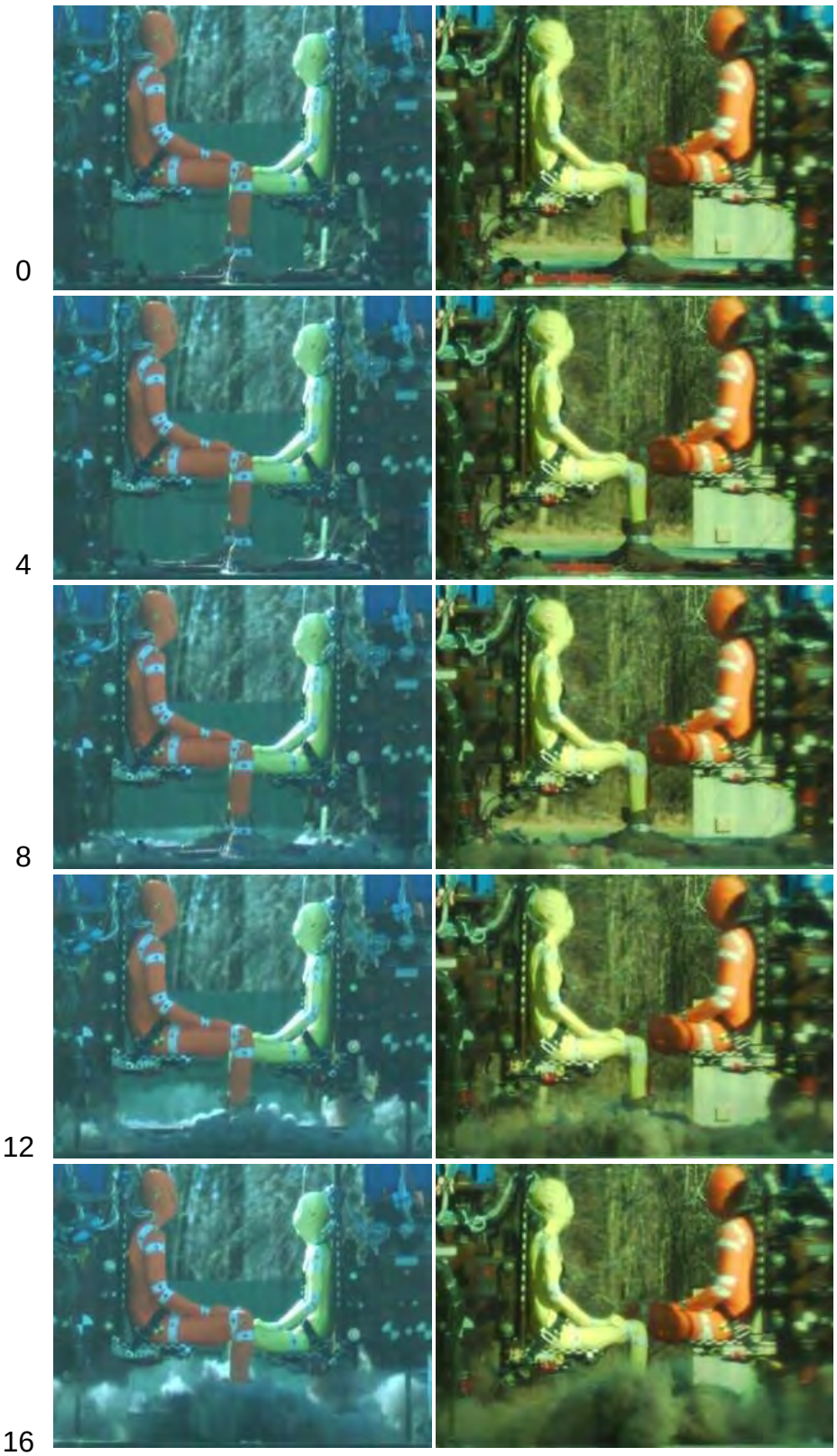

Figure 57. Female shot 9, lateral view (Crew 1: 50th percentile male, orange; Crew 2: 5th percentile female, yellow)

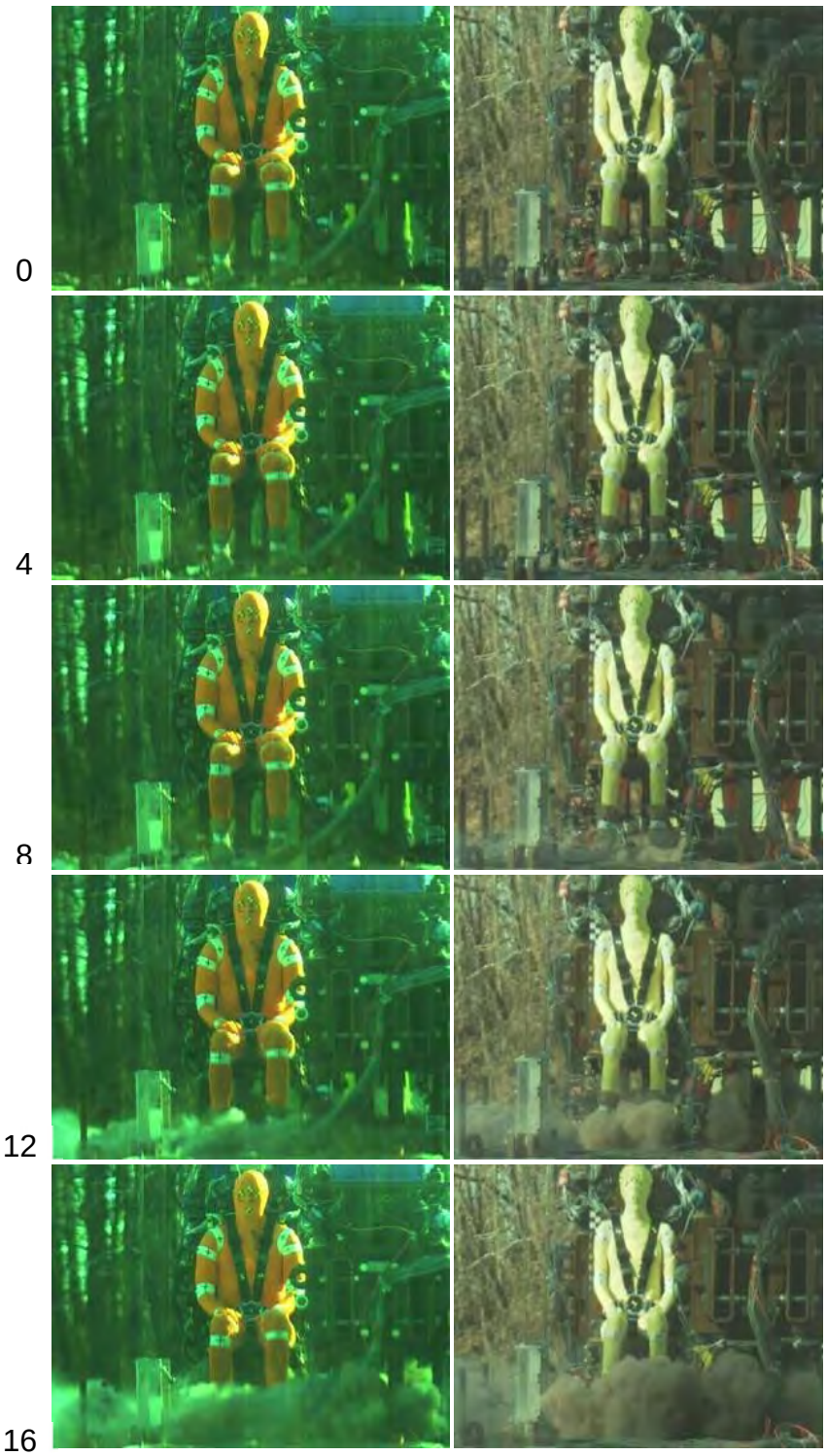

Figure 58. Female shot 9, frontal view (Crew 1: 50th percentile male, orange; Crew 2: 5th percentile female, yellow)

Table 5. Initial anatomical motions of the ankles and hips

Test	Side	Size	Ankle	Hip
M1C1	R	50th	Neutral	Neutral
	L		Eversion	Neutral
M1C2	R	50th	Neutral	Neutral
	L		Eversion	Neutral
M2C1	R	50th	Slight eversion	Neutral
	L		Slight eversion	Neutral
M2C2	R	50th	Slight eversion	Neutral
	L		Slight eversion	Neutral
S1C1	R	75th	Inversion	Neutral
	L		Neutral	Neutral
S1C2	R	5th	Dorsiflexion	External rotation
	L		Dorsiflexion	External rotation
S2C1	R	75th	Slight inversion	Neutral
	L		Slight inversion	Neutral
S3C1	R	75th	Neutral	Neutral
	L		Neutral	Neutral
S3C2	R	5th	Plantarflexion	Neutral
	L		Plantarflexion	Neutral
S4C1	R	5th	Slight inversion	Neutral
	L		Slight inversion	Neutral
S5C1	R	75th	Inversion	External rotation
	L		Inversion, dorsiflexion	External rotation
S5C2	R	5th	Dorsiflexion	Neutral
	L		Eversion, dorsiflexion	Neutral
S6C1	R	50th	Neutral	Neutral
	L		Slight eversion	Neutral
S6C2	R	5th	Inversion	Neutral
	L		Eversion, dorsiflexion	Neutral
S7C1	R	50th	Eversion	Neutral
	L		Eversion	Neutral
S7C2	R	75th	Inversion	Neutral
	L		Eversion	Neutral
S8C1	R	50th	Eversion, dorsiflexion	Neutral
	L		Eversion	Neutral
S8C2	R	75th	Eversion	Neutral
	L		Inversion, dorsiflexion	Neutral
S9C1	R	50th	Not visible	Neutral
	L		Not visible	Neutral
S9C2	R	5th	Eversion	Neutral
	L		Eversion	Neutral

3.2 Damage Response

3.2.1 Lower Extremity

The only instance of lower extremity damage under the lower energy floor condition of male CORALS and Series 1 was a partial neck fracture of the left talus of a 5th percentile female. The increased floor energy in Series 3 and 4 resulted in damage

throughout the lower extremities, which is summarized below. Table 6 shows a summary of the regions of the lower extremity that sustained damage. A capitalized and bolded “X” indicates that damage to this region was considered higher in severity. A detailed list of lower extremity damage with injury coding, injury descriptions, and photos is included in Appendix D.

3.2.1.1 Forefoot

There were four cases of forefoot damage. Damage to the 3rd, 4th, and 5th metatarsals was seen across all sexes and percentiles. Damage to the 5th phalange was seen in a 75th percentile female. All forefoot damage occurred on the left limb (the limb closest to the largest floor deformation at the center) and to the proximal portion of the bones.

3.2.1.2 Midfoot

There were five cases of damage to the navicular. All navicular damage was to the lateral and inferior aspect of the bone. The two observed cuboid fractures were associated with navicular fractures. All navicular and cuboid fractures were sustained by females.

3.2.1.3 Calcaneus

In Series 3 and 4, all PMHS sustained damage to either one or both calcanei, except for the 50th percentile male in shot 9. There were 15 calcaneus fractures, with 6 PMHS having bilateral calcaneus damage. Unilateral damage was observed in one 75th percentile female on the right side and two 50th percentile males on the left side. In four cases, the calcanei fractures were characterized by larger fragments. In all other cases, the calcanei were pulverized.

3.2.1.4 Talus

In Series 1, minor talus damage was sustained by one 5th percentile female. In Series 3 and 4, all females sustained talus damage and one male sustained talus damage. There were seven cases of minor damage to the talus and one case of severe damage to the talus, which was sustained by a 5th percentile female on the right side.

3.2.1.5 Distal Leg

In Series 3 and 4, four females and one male PMHS sustained damage to the distal tibia. There were three cases of major destruction of the distal tibia. These cases occurred on the left side of 75th percentile females and had ipsilateral fibula fractures. There were four cases of minor tibia damage that occurred across all sexes and percentiles.

3.2.1.6 Femur

There were three cases of severe femur fractures: two were sustained by 50th percentile males, whereas one was sustained by a 5th percentile female. All three cases occurred on the left side and at the mid-diaphysis.

Table 6. Damage to the lower extremities

Test	Size	Side	Femur	Tibia	Fibula	Talus	Calcaneus	Midfoot	Forefoot
M1C1	M 50th	R	...	...	...	...	...	...	...
		L	...	...	...	...	...	...	...
M1C2	M 50th	R	...	...	...	...	...	...	...
		L	...	...	...	...	...	...	...
M2C1	M 50th	R	...	...	...	...	...	...	...
		L	...	...	...	...	...	...	...
M2C2	M 50th	R	...	...	...	...	...	...	...
		L	...	...	...	...	...	...	...
S1C1	F 75th	R	...	...	...	...	...	...	...
		L	...	...	...	...	...	...	...
S1C2	F 5th	R	...	...	...	...	...	...	...
		L	...	...	...	...	...	...	...
S2C1	F 75th	R	...	...	...	...	...	...	...
		L	...	...	...	...	...	...	...
S3C1	F 75th	R	...	...	...	...	...	...	...
		L	...	...	...	...	...	...	...
S3C2	F 5th	R	...	...	...	...	...	...	...
		L	...	...	...	...	...	...	...
S4C1	F 5th	R	...	...	...	...	...	...	...
		L	...	...	...	x	...	...	...
S5C1	F 75th	R	...	x	...	x	**X**	x	...
		L	...	**X**	**X**	...	...	x	x
S5C2	F 5th	R	...	...	...	**X**	**X**	...	...
		L	**X**	x	...	...	**X**	x	x
S6C1	M 50th	R	...	...	...	...	**X**	...	...
		L	**X**	...	...	...	**X**	...	x
S6C2	F 5th	R	...	...	...	...	**X**	x	...
		L	...	...	...	x	**X**	...	...
S7C1	M 50th	R	...	...	...	...	...	...	...
		L	...	...	...	...	**X**	...	...
S7C2	F 75th	R	...	...	...	x	**X**	x	...
		L	...	**X**	**X**	x	**X**	...	...
S8C1	M 50th	R	...	x	...	x	...	...	...
		L	...	...	...	...	**X**	...	...
S8C2	F 75th	R	...	x	...	...	**X**	...	...
		L	...	**X**	**X**	x	**X**	...	x
S9C1	M 50th	R			...	...	...	...	...
		L		**X**	...	...	...	...	...
S9C2	F 5th	R		...	...	x	**X**	...	...
		L		...	...	...	**X**	...	...

3.2.2 Pelvis

Table 7 summarizes the regions of the pelvis that sustained damage. A detailed list of pelvis damage with injury coding, injury descriptions, and photos is included in Appendix D. Pelvis damage was observed at the ischial tuberosity, the sacroiliac joint, the ventral and dorsal alae, the sacrum, and the coccyx.

Table 7. Damage to the pelvis

Test	PMHS	Size	Bilateral isch. tub.	Bilateral SI joint	Right vent. ala	Left vent. ala	Right dors. ala	Left dors. ala	Sacrum	Coccyx
M1C1	SM117	50th	...	...	...	...	...	...	...	x
M1C2	SM118	50th	...	...	...	...	...	...	x	
M2C1	SM120	50th	...	...	...	...	...	...	...	x
M2C2	SM119	50th	...	...	...	...	...	...	...	x
S1C1	SF127	75th	...	...	...	...	...	...	...	x
S1C2	SF126	5th	...	...	S1, S2, S3	S1, S2, S3	S1, S2	S1	x	x
S2C1	SF128	75th	...	...	...	...	...	...	...	x
S3C1	SF131	75th	...	...	...	...	...	...	x	x
S3C2	SF132	5th	...	...	S2, S3, S4, S5	...	S2, S3, S4, S5	...	x	x
S4C1	SF133	5th	...	...	S1, S2, S3	S1, S2, S3	S1, S2, S3	S1, S2, S3	x	x
S5C1	SF138	75th	...		x	...	...	...	...	x
S5C2	SF134	5th		...		...	...	...	...	...
S6C1	SM140	50th		...		...	...	...	...	...
S6C2	SF135	5th		...		...	...	...	...	...
S7C1	SM141	50th		...		...	...	...	...	...
S7C2	SF142	75th		x			...	...	...	...
S8C1	SM145	50th		...		...	...	...	...	...
S8C2	SF148	75th		...		...	...	...	...	...
S9C1	SM150	50th		...		...	...	...	...	...
S9C2	SF151	5th		...		...	...	...	...	...

Note: ala, alae; dors, dorsal; isch. Tub., ischial tuberosity; SI, sacroiliac; vent, ventral.

3.2.3 Spine

Table 8 summarizes the regions of the spine that sustained damage to the vertebral bodies. Table 9 summarizes the regions of the spine that sustained damage to the transverse processes. A detailed list of spine damage with injury coding, injury descriptions, and photos is included in Appendix D. There was one fracture of a vertebral body in the thoracic spine of a 5th percentile female. There were eight fractures of vertebral bodies in the lumbar spine, all of which occurred in 50th percentile males and 75th percentile females. None of the fractures were catastrophic. All of the fractures were nondisplaced. There were four compression fractures, two burst fractures, one anterior wedge fracture, and one fracture involving a fragment of the vertebral body.

Table 8. Damage to the vertebral bodies of the spine

Test	PMHS	Size	T4	L1	L2	L3	L4	L5
M1C1	SM117	50th	...	...	...	x	...	...
M1C2	SM118	50th	...	...	...	...	...	...
M2C1	SM120	50th	...	...	...	...	x	...
M2C2	SM119	50th	...	...	...	...	x	...
S1C1	SF127	75th	...	...	...	...	...	...
S1C2	SF126	5th	...	...	...	...	...	...
S2C1	SF128	75th	...	...	...	...	...	...
S3C1	SF131	75th	...	...	...	...	...	...
S3C2	SF132	5th	...	...	...	...	...	...
S4C1	SF133	5th	...	...	...	...	...	...
S5C1	SF138	75th	...	...	...	x	...	...
S5C2	SF134	5th	x	...	...	...	...	...
S6C1	SM140	50th	...	...	...	...	...	...
S6C2	SF135	5th	...	...	...	...	...	...
S7C1	SM141	50th	...	...	...	...	x	
S7C2	SF142	75th	...	...	x	...	...	...
S8C1	SM145	50th	...	...	...	...	x	...
S8C2	SF148	75th	...	...	...	...	...	x
S9C1	SM150	50th	...	...	...	...	...	...
S9C2	SF151	5th	...	...	...	...	...	...

Table 9. Damage to the transverse processes of the spine

Test	Side	PMHS	Size	Side	L1	L2	L3	L4	L5
M1C1	R	SM117	50th	R	…	…	…	…	…
	L			L	…	…	…	…	…
M1C2	R	SM118	50th	R	…	…	…	…	…
	L			L	…	…	…	…	…
M2C1	R	SM120	50th	R	…	…	…	…	…
	L			L	…	…	…	…	…
M2C2	R	SM119	50th	R	…	…	…	…	…
	L			L	…	…	…	…	…
S1C1	R	SF127	75th	R	x	x	…	…	…
	L			L	…	x	…	…	…
S1C2	R	SF126	5th	R	…	…	…	…	…
	L			L	…	…	…	…	…
S2C1	R	SF128	75th	R	…	…	…	…	…
	L			L	…	…	…	…	…
S3C1	R	SF131	75th	R	…	…	…	…	…
	L			L	…	…	…	…	…
S3C2	R	SF132	5th	R	…	…	…	…	…
	L			L	…	…	…	…	…
S4C1	R	SF133	5th	R	…	x	x	…	…
	L			L	…	x	…	…	…
S5C1	R	SF138	75th	R	…	…	…	…	…
	L			L	…	…	…	…	…
S5C2	R	SF134	5th	R	…	…	…	x	…
	L			L	…	…	…	…	…
S6C1	R	SM140	50th	R	x	x	x	…	…
	L			L	x	x	x	…	…
S6C2	R	SF135	5th	R	x	…	…	…	…
	L			L	…	…	…	…	…
S7C1	R	SM141	50th	R	x	…	…	…	…
	L			L	…	…	…	…	…
S7C2	R	SF142	75th	R	x	…	…	…	…
	L			L	x	…	…	…	…
S8C1	R	SM145	50th	R	…	…	…	…	…
	L			L	…	…	…	…	…
S8C2	R	SF148	75th	R	x	x	x	x	…
	L			L	x	x	…	…	x
S9C1	R	SM150	50th	R	…	…	…	…	…
	L			L	…	…	…	…	…
S9C2	R	SF151	5th	R	…	…	…	…	…
	L			L	…	…	…	…	…

3.2.4 Ribs

Table 10 summarizes the ribs that sustained damage. A detailed list of rib damage with injury coding, injury descriptions, and photos is included in Appendix D. Damage was observed on ribs two through seven on both sides of the body. All PMHS types sustained damage to the ribs. Rib fractures are likely a result of interaction between the thorax and the five-point harness. Rib damage was more frequent in Series 3 and 4.

Table 10. Damage to the ribs

Test	Side	PMHS	Size	Side	Rib 2	Rib 3	Rib 4	Rib 5	Rib 6	Rib 7
M1C1	R	SM117	50th	R	…	…	…	…	…	…
	L			L	…	…	…	…	…	…
M1C2	R	SM118	50th	R	…	…	…	…	…	…
	L			L	…	…	…	…	…	…
M2C1	R	SM120	50th	R	x	x	x	x	x	…
	L			L	x	x	x	…	…	…
M2C2	R	SM119	50th	R	…	…	…	…	…	…
	L			L	…	…	…	…	…	…
S1C1	R	SF127	75th	R	…	…	…	…	…	…
	L			L	…	…	…	…	…	…
S1C2	R	SF126	5th	R	…	…	…	…	…	…
	L			L	…	…	…	…	…	…
S2C1	R	SF128	75th	R	…	…	…	…	…	…
	L			L	…	…	…	…	…	…
S3C1	R	SF131	75th	R	…	…	…	…	…	…
	L			L	…	…	…	…	…	…
S3C2	R	SF132	5th	R	…	…	…	…	…	…
	L			L	…	…	…	…	…	…
S4C1	R	SF133	5th	R	…	…	…	…	…	…
	L			L	…	…	…	…	…	…
S5C1	R	SF138	75th	R	…	…	…	…	x	…
	L			L	…	x	…	…	x	…
S5C2	R	SF134	5th	R	x	x	x	x	x	x
	L			L	x	x	x	x	x	x
S6C1	R	SM140	50th	R	…	x	x	x	x	…
	L			L	…	…	x	x	x	…
S6C2	R	SF135	5th	R	…	…	…	…	…	…
	L			L	…	…	…	x	…	…
S7C1	R	SM141	50th	R	…	…	…	…	…	…
	L			L	…	…	…	…	…	…
S7C2	R	SF142	75th	R	…	…	…	…	…	…
	L			L	…	…	…	…	…	…
S8C1	R	SM145	50th	R	…	…	…	…	…	…
	L			L	…	…	…	…	…	…
S8C2	R	SF148	75th	R	…	x	x	x	…	x
	L			L	x	x	x	x	x	…
S9C1	R	SM150	50th	R	…	…	…	…	…	…
	L			L	…	…	…	…	…	…
S9C2	R	SF151	5th	R	…	…	…	…	…	…
	L			L	…	…	…	…	…	…

3.3 Kinematics and Associated Damage Level

Several plots are generated to illustrate potential relationships between kinematics, sex, percentile, and damage level. The kinematics variables that are investigated include vertical speed and acceleration of the distal tibia and distal femur. Damage level is indicated by color, with green, yellow, and red indicating no damage, minor damage, and major damage, respectively. The shape of the markers is indicative of the sex and percentile, with circles, diamonds, and triangles representing 50th percentile males, 75th

percentile females, and 5th percentile females, respectively. Cases that have ipsilateral calcaneus and tibia damage are indicated by a black border on the marker.

The plots herein use a single value of speed or a single value of acceleration for each lower extremity throughout the entire event. They show damage level of the calcanei or tibiae on the y-axis and peak values of speed or acceleration of the tibiae or femura on the x-axis. Every plot contains a total of forty points, with individual points representing each lower extremity of each crew in every shot.

In addition to the plots that use peak kinematic values on the x-axis, additional plots are generated using the value of speed or acceleration at the approximated time of fracture for the lower extremities that sustained damage to the calcaneus or tibia. These plots are labeled “less-censored” (L-C), and they contain a combination of the peak kinematic values for nondamage cases and the L-C kinematic values for damage cases. The methods for fracture-timing estimation are described in Section 3.5.1. Each lower extremity that sustained damage to the calcaneus and/or tibia has two estimations of the time of fracture, with the first estimation representing the initiation of the fracture and the second estimation representing a more conservative estimate at a time when the fracture is very likely to be occurring. The L-C values used in the current analysis are the speeds and accelerations associated with the second estimation of fracture timing.

3.3.1 Calcaneus Damage Level

Calcaneus and tibia fractures are associated with Series 3 and 4, which implemented a higher-energy floor.

3.3.1.1 Distal Tibia Vertical Acceleration

The plots showing calcaneus damage as a function of peak vertical acceleration of the distal tibia (Figure 59) show some separation between damage and nondamage cases, with damage to the calcaneus being associated with tibiae that reach higher peak accelerations during the event. There is some overlap in the acceleration values between the damage and nondamage cases, meaning some nondamage cases are associated with higher accelerations than damage cases. The nondamage cases with higher accelerations are associated with high-fracture tolerance or lower mass of the lower extremities. In addition, cases in which the calcaneus did not sustain damage and the tibia did sustain damage are always associated with higher accelerations. In the L-C plot (Figure 60), there is a smaller range of acceleration values seen. The L-C damage cases shift to the left, indicating that the damage occurs at values lower than the peak acceleration. It is interesting to note that the nondamage cases that are associated with

higher accelerations that overlap with the damage cases are all 50th percentile males, with the exception of one 75th percentile female, which incurred damage to the tibia.

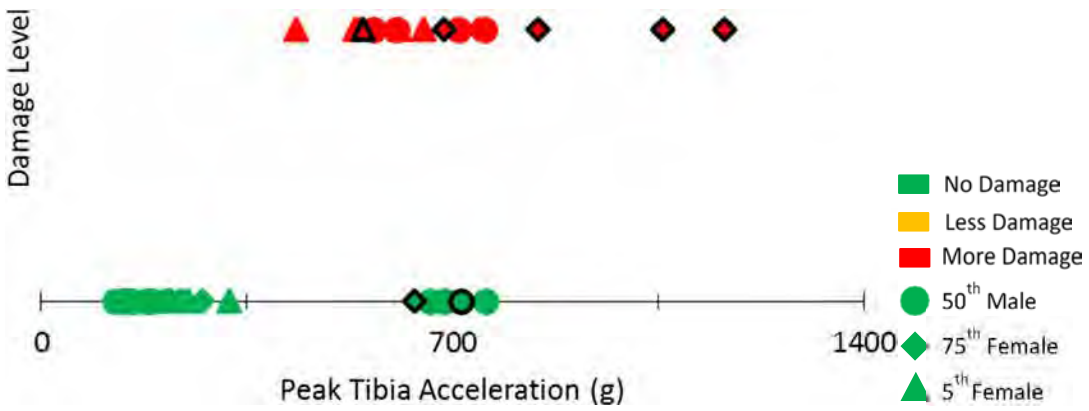

Figure 59. Calcaneus damage vs. peak tibia vertical acceleration. Cases that have ipsilateral tibia damage are indicated by a black border.

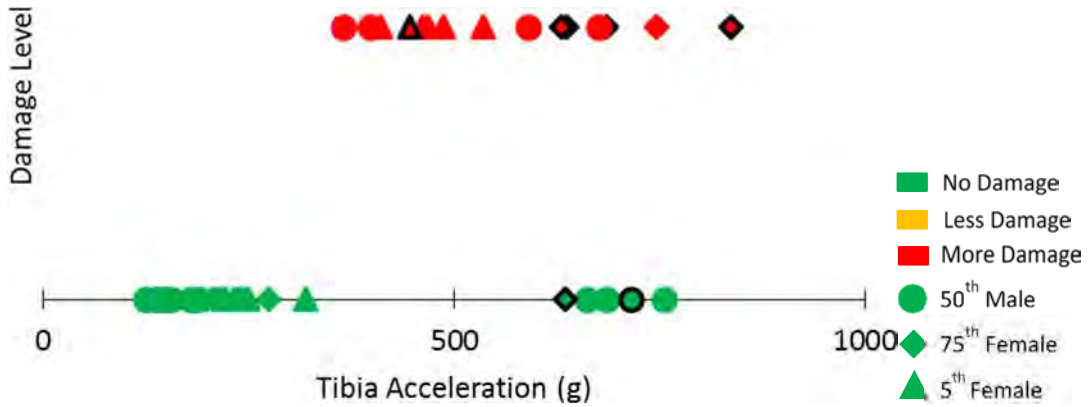

Figure 60. Calcaneus damage vs. L-C tibia vertical acceleration. Cases that have ipsilateral tibia damage are indicated by a black border.

3.3.1.2 Distal Tibia Vertical Speed

The plot showing calcaneus damage as a function of peak vertical speed of the distal tibia (Figure 61) shows some separation between damage and nondamage cases, with damage to the calcaneus being associated with tibiae that reach higher peak speeds during the event. This pattern is not present in the L-C plot (Figure 62), which shows that damage to the calcaneus is occurring at much lower distal tibia speeds. The calcaneus is the first hard tissue structure that is impacted by the rapidly deforming floor plate. Similar to the crumple zone in a vehicle, the calcaneus absorbs the energy of the axial loading. Once the calcaneus is crushed, the fragments can then continue to transfer the load of the floor up through the leg. At the time of fracture of the calcaneus, the distal tibia is being accelerated, but it has not picked up much speed.

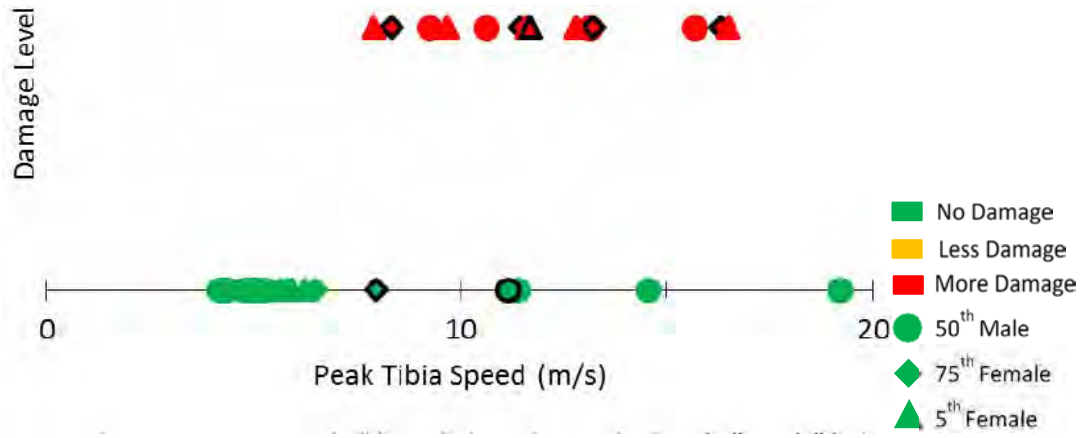

Figure 61. Calcaneus damage vs. peak tibia vertical speed. Cases that have ipsilateral tibia damage are indicated by a black border.

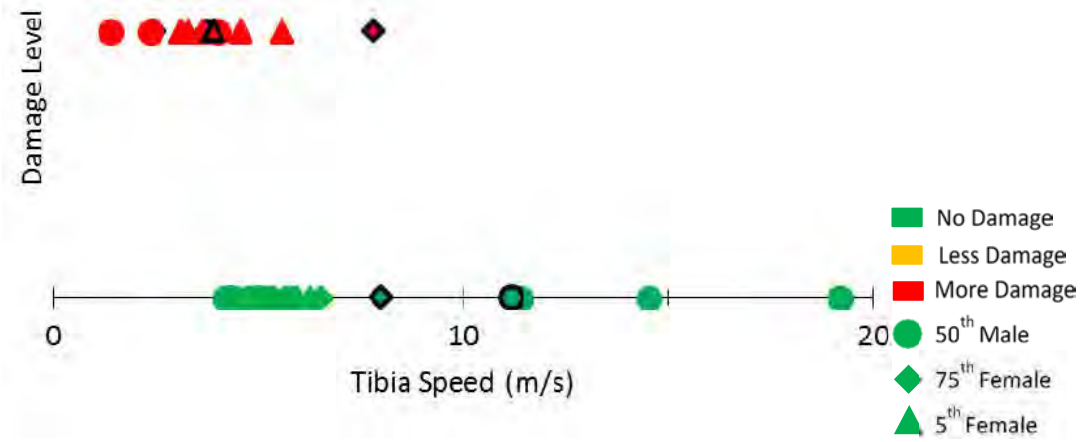

Figure 62. Calcaneus damage vs. L-C tibia vertical speed. Cases that have ipsilateral tibia damage are indicated by a black border.

3.3.1.3 Distal Femur Vertical Acceleration

The plot showing damage to the calcaneus as a function of peak distal femur vertical acceleration (Figure 63) shows that damage to the calcaneus is generally associated with femura that reach higher peak accelerations; however, the plot showing calcaneus damage as a function of L-C femur acceleration (Figure 64) indicates that this trend actually reversed. The fracture time of the calcaneus is occurring at a much lower femur acceleration than the peak acceleration. The femur is somewhat decoupled from the shank, with much of the damage to the calcaneus occurring at a time when the femur is undergoing low accelerations.

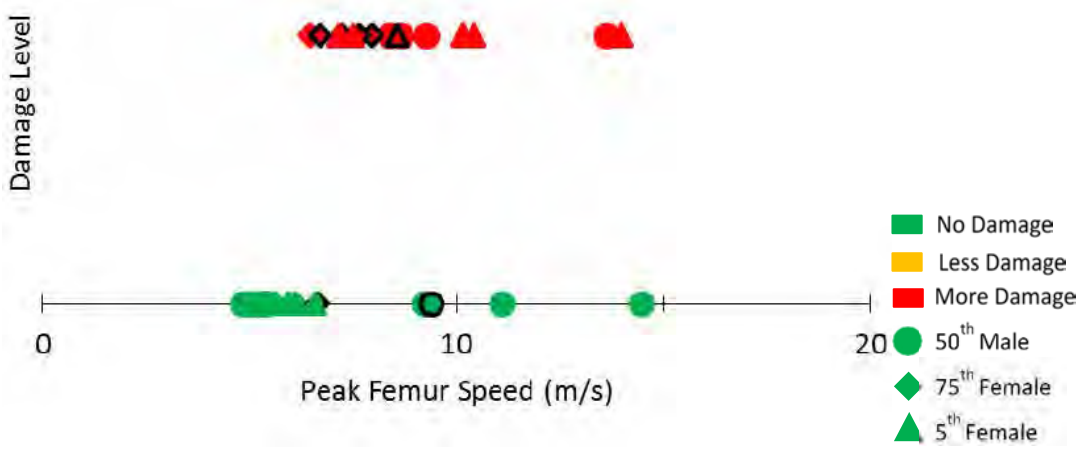

Figure 63. Calcaneus damage vs. peak femur vertical acceleration. Cases that have ipsilateral tibia damage are indicated by a black border.

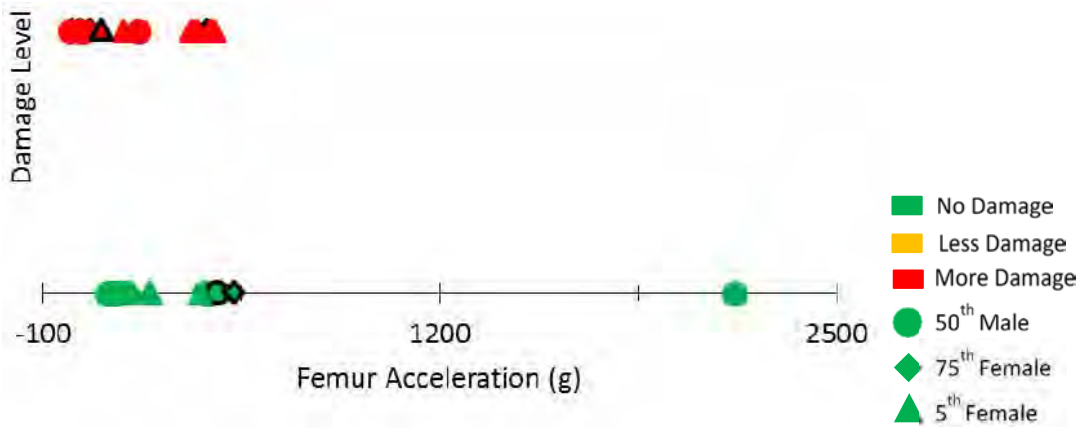

Figure 64. Calcaneus damage vs. L-C femur vertical acceleration. Cases that have ipsilateral tibia damage are indicated by a black border.

3.3.1.4 Distal Femur Vertical Speed

The plot showing calcaneus damage as a function of peak femur vertical speed (Figure 65) indicates that damage to the calcaneus is generally associated with femura that reach higher peak speeds during the event. The plot using L-C femur speed shows that damage to the calcaneus occurs at very low femur speeds (Figure 66).

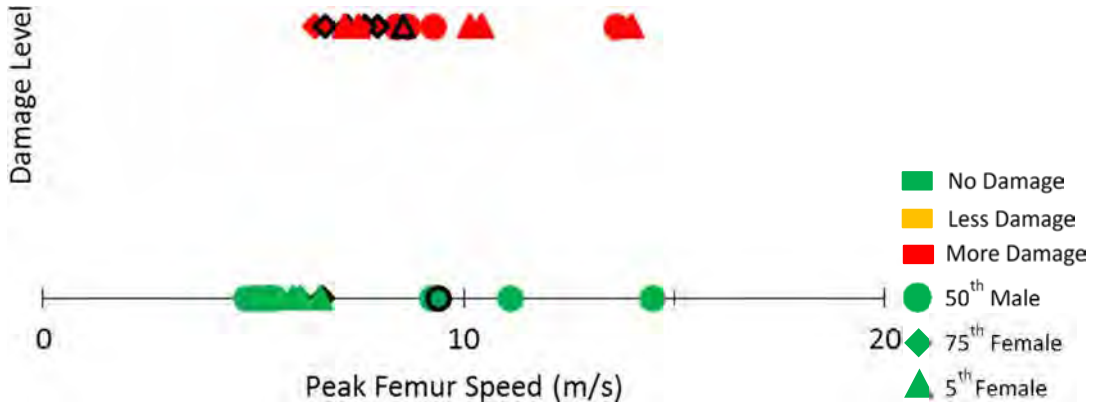

Figure 65. Calcaneus damage vs. peak femur vertical speed. Cases that have ipsilateral tibia damage are indicated by a black border.

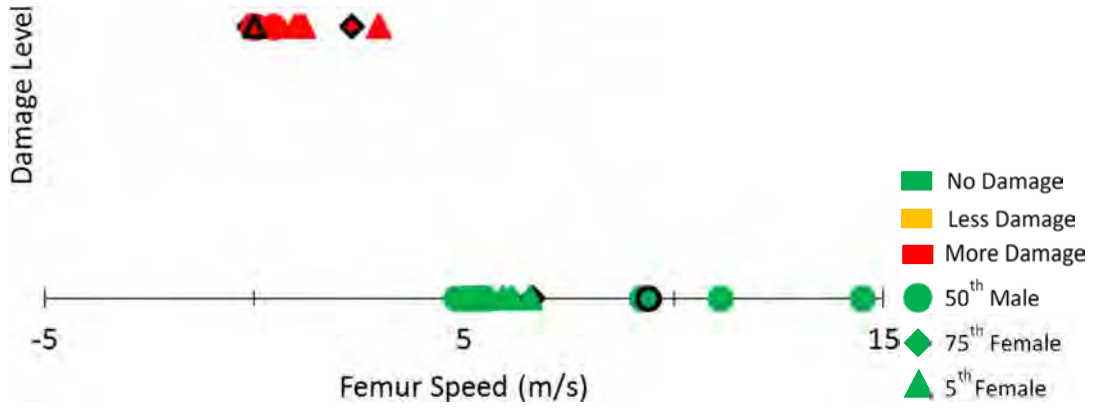

Figure 66. Calcaneus damage vs. L-C femur vertical speed. Cases that have ipsilateral tibia damage are indicated by a black border.

3.3.2 Tibia Damage Level

In general, damage to the tibia was isolated to females, with the exception of a 50th percentile male, which sustained minor damage to the tibia.

3.3.2.1 Distal Tibia Vertical Acceleration

The damage level to the tibia associated with peak tibia acceleration (Figure 67) indicates that in general, greater damage to the tibiae is associated with tibiae that reach higher accelerations during the event. This trend is not seen in the L-C plot (Figure 68).

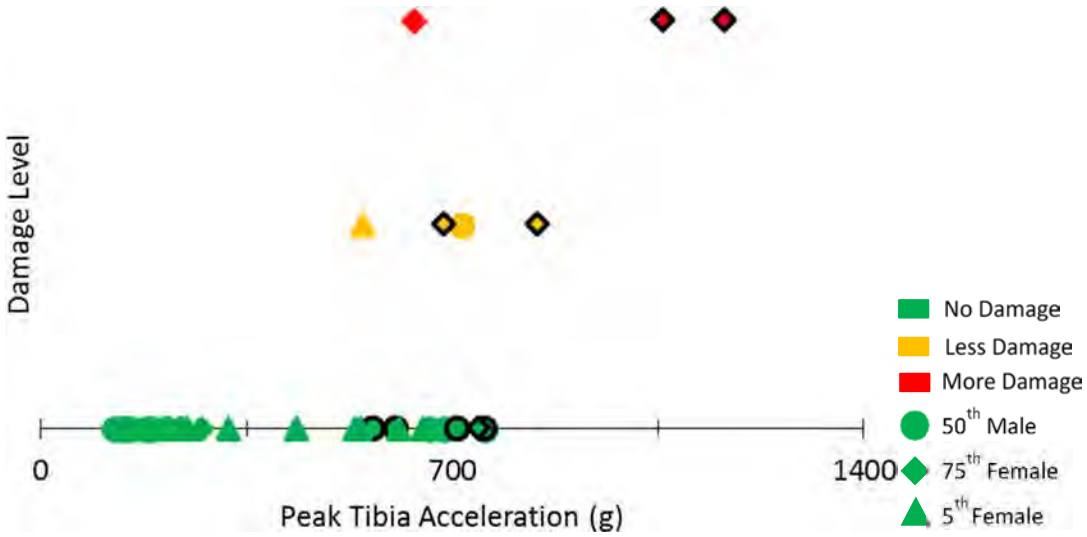

Figure 67. Tibia damage vs. peak tibia vertical acceleration. Cases that have ipsilateral tibia damage are indicated by a black border.

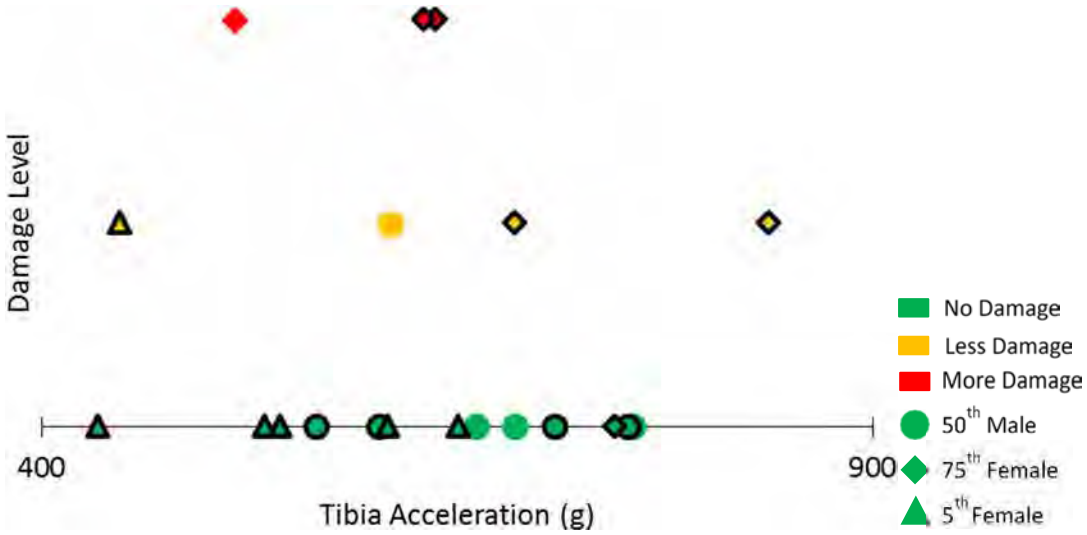

Figure 68. Tibia damage vs. L-C tibia vertical acceleration. Cases that have ipsilateral tibia damage are indicated by a black border.

3.3.2.2 Distal Tibia Vertical Speed

The plot showing tibia damage as a function of peak distal tibia speed (Figure 69) shows cases with damage tend to have a higher speed, but the limited number of data points makes it harder to see the trend. The L-C plot (Figure 70) shows that damage to the tibia is associated with lower tibia speeds. This makes sense, because the tibia fractures occur early on, before the tibia picks up much speed.

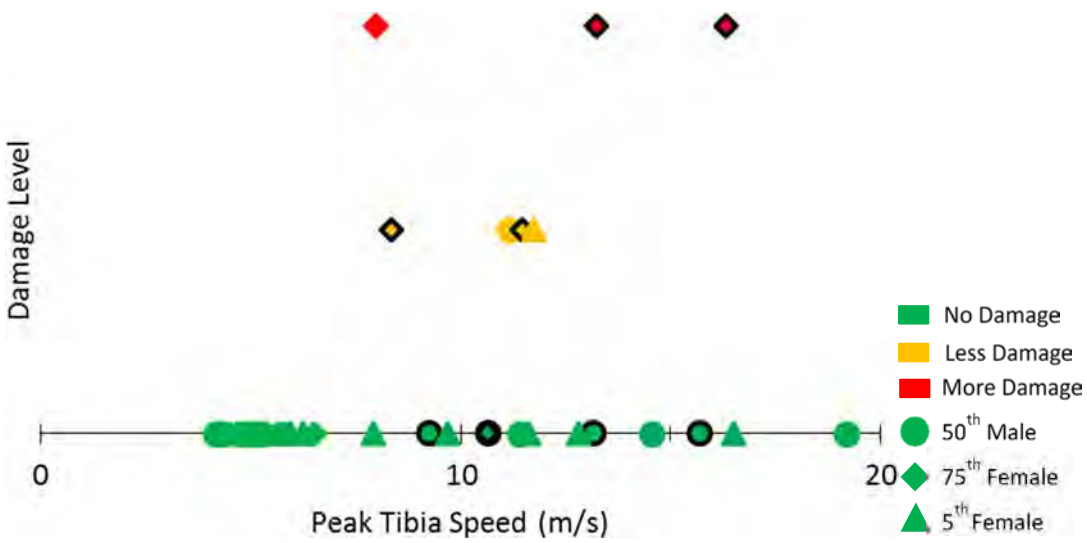

Figure 69. Tibia damage vs. peak tibia vertical speed. Cases that have ipsilateral tibia damage are indicated by a black border.

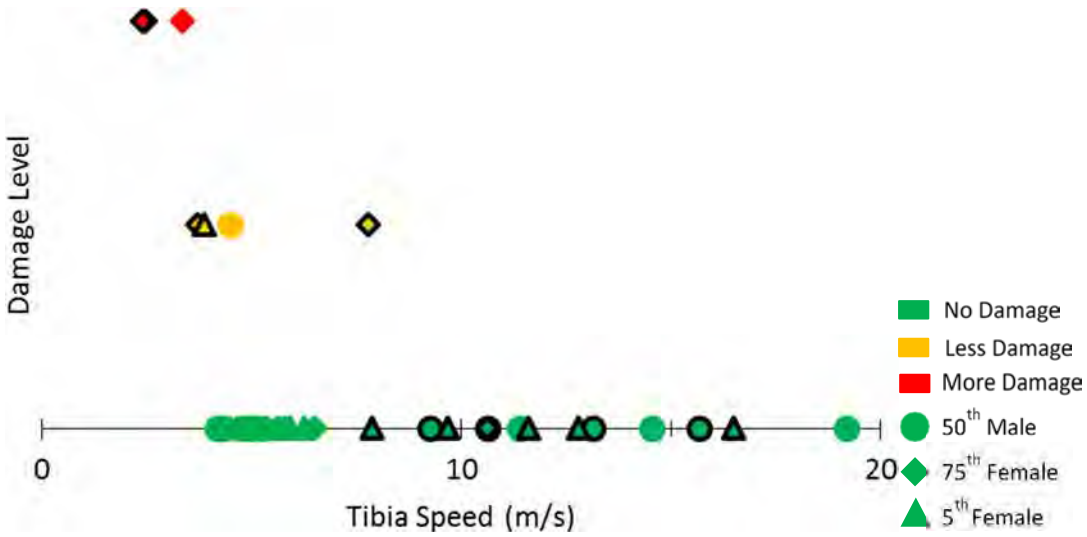

Figure 70. Tibia damage vs. L-C tibia vertical speed. Cases that have ipsilateral tibia damage are indicated by a black border.

3.3.2.3 Distal Femur Vertical Acceleration

The plot showing tibia damage as a function of peak femur acceleration (Figure 71) shows that damage to the tibia is generally associated with femura that reach higher peak accelerations during the event. The nondamage cases that occur at the higher end of acceleration tend to have associated calcaneus damage. The L-C plot (Figure 72) suggests that greater damage to the tibia occurs at lower femur accelerations. This

could be related to energy from the floor going into fracturing the tibia rather than moving the leg.

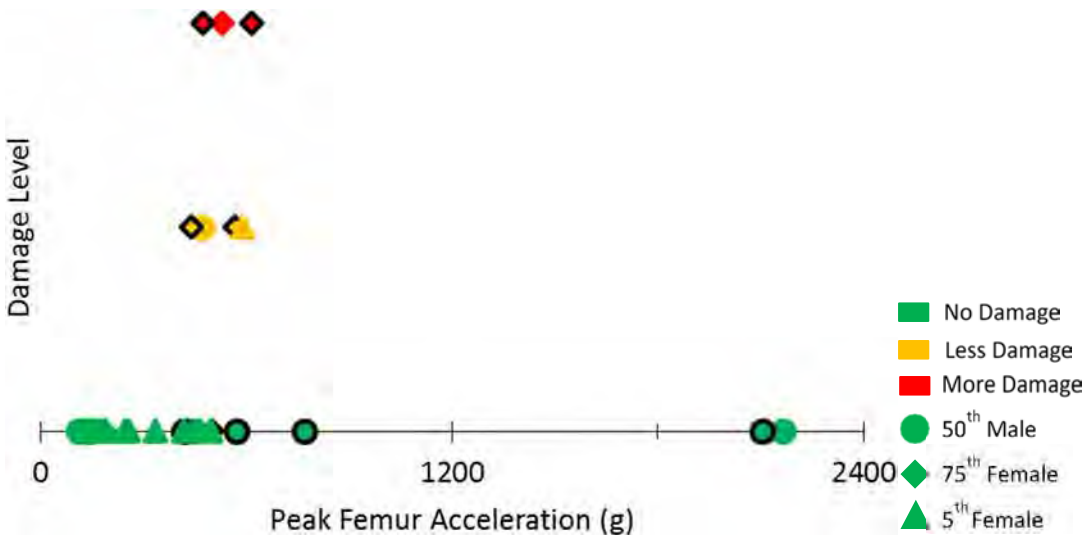

Figure 71. Tibia damage vs. peak femur vertical acceleration. Cases that have ipsilateral tibia damage are indicated by a black border.

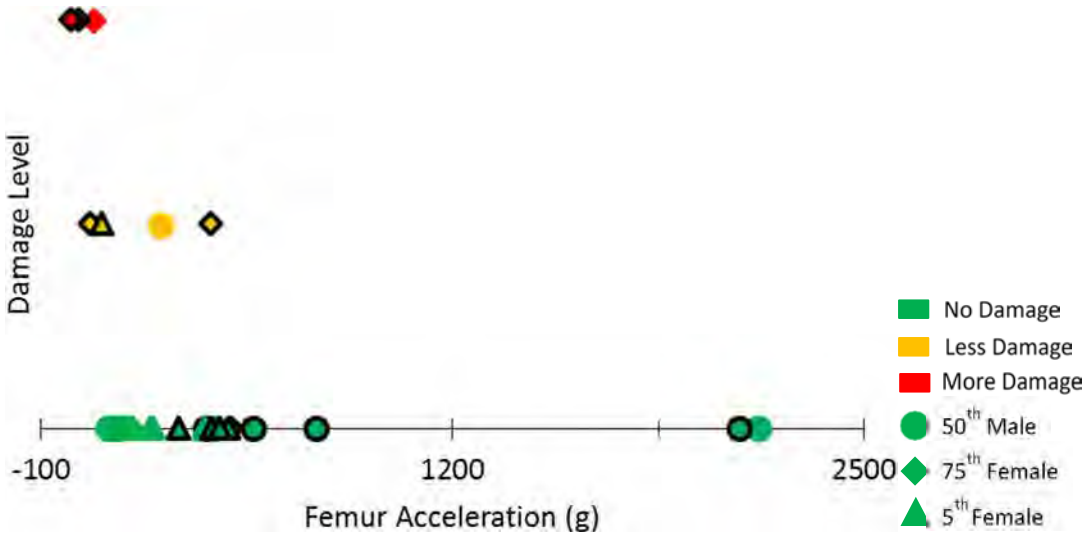

Figure 72. Tibia damage vs. L-C femur vertical acceleration. Cases that have ipsilateral tibia damage are indicated by a black border.

3.3.2.4 Distal Femur Vertical Speed

The plot showing tibia damage level as a function of peak vertical speed of the femur (Figure 73) does not reveal a distinct trend. When the L-C values are used (Figure 74), it is revealed that tibia damage is associated with lower femur speed.

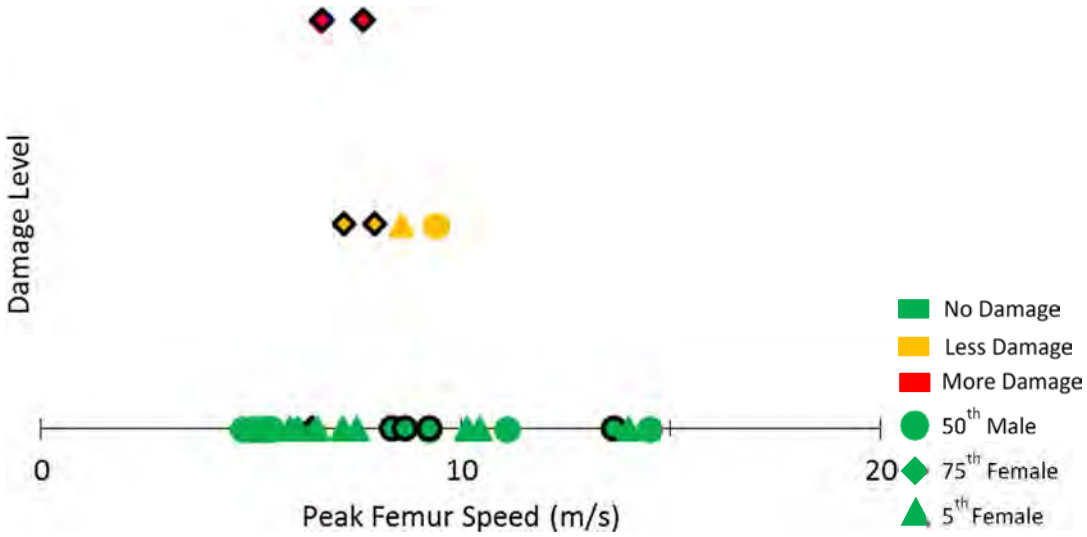

Figure 73. Tibia damage vs. peak femur vertical speed. Cases that have ipsilateral tibia damage are indicated by a black border.

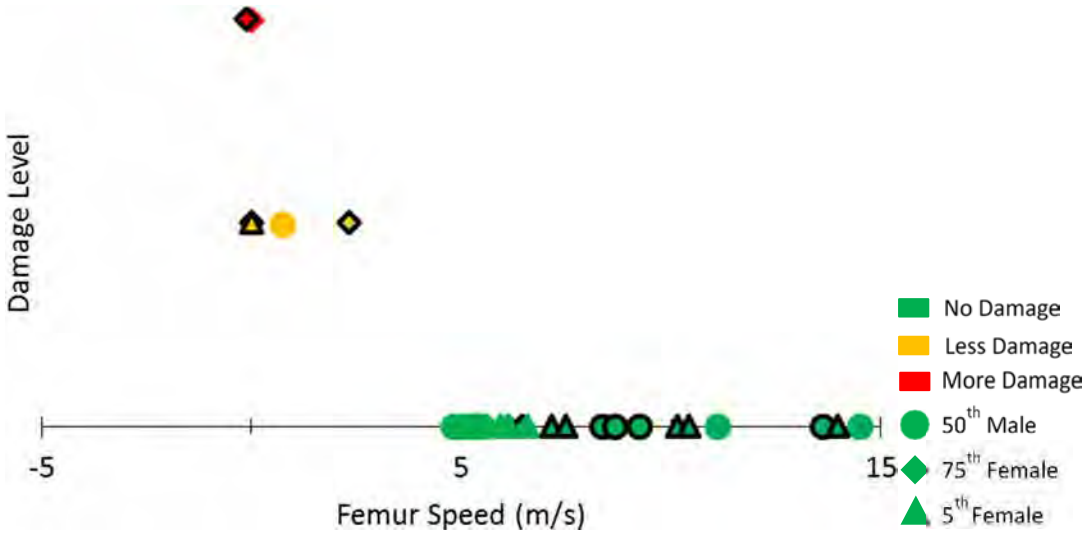

Figure 74. Tibia damage vs. L-C femur vertical speed. Cases that have ipsilateral tibia damage are indicated by a black border

3.4 Mass Analysis

3.4.1 Mass Estimation

Damage location and severity may be influenced by the mass of the lower extremities. Heavier, lower extremities require more inertia to move, so it is postulated that this could lead to increased contact time between the floor and the boot and/or a longer period over which the mass takes to set into motion. This could foster greater energy

transfer to the load-bearing structures of the lower extremity, potentially changing the characteristics of damage.

The mass of the lower extremities is summarized in Table 11. The CT segmentation is used to estimate the mass of the thigh, shank, and foot, bilaterally, for each specimen. The lower extremity mass is also measured during some autopsies to compare to the CT estimates. To accomplish this, the lower extremities are removed at the hip joint with the soft tissue being cut along the groin and gluteal furrow. The CT estimations are used for the mass analyses in the following Section, 3.4.2 Influence of Mass on Kinematics and Damage.

Table 11. Lower extremity mass estimation

Test ID	PMHS	Size	Sex	Total body mass (kg)	Laboratory measurement (kg)		CT estimation (kg)	
					Right	Left	Right	Left
MS1C1	SM117	50th	Male	95.10	…	…	22.248	22.548
MS1C2	SM118	50th	Male	82.50	…	…	16.414	17.053
MS2C1	SM120	50th	Male	81.80	…	…	19.851	19.481
MS2C2	SM119	50th	Male	65.00	…	…	12.824	13.562
FS1C1	SF127	75th	Female	69.25	…	…	16.627	16.314
FS1C2	SF126	5th	Female	47.10	…	…	10.623	10.996
FS2C1	SF128	75th	Female	66.06	…	…	12.388	12.709
FS2C2	ATD	5th	…	48.90	…	…	…	…
FS3C1	SF131	75th	Female	68.49	…	…	11.701	11.619
FS3C2	SF132	5th	Female	66.36	…	…	15.940	15.359
FS4C1	SF133	5th	Female	57.42	…	…	14.682	13.760
FS4C2	ATD	5th	…-	48.90	…	…	…	…
FS5C1	SF138	75th	Female	74.74	9.19[a]	9.19[a]	14.955	14.867
FS5C2	SF134	5th	Female	60.57	8.55[a]	8.55[a]	13.989	13.345
FS6C1	SM140	50th	Male	68.72	8.53[a]	8.53[a]	13.447	13.886
FS6C2	SF135	5th	Female	56.88	9.50[a]	9.50[a]	16.693	17.199
FS7C1	SM141	50th	Male	93.85	6.60[a]	6.60[a]	13.794	14.034
FS7C2	SF142	75th	Female	88.13	9.64[a]	09.64[a]	19.710	18.824
FS8C1	SM145	50th	Male	75.30	10.07	10.34	15.813	17.102
FS8C2	SF148	75th	Female	69.35	8.26	7.08	9.139	7.957
FS9C1	SM150	50th	Male	78.02	11.34	11.34	18.743	18.719
FS9C2	SF151	5th	Female	36.51	4.99	4.76	7.792	7.750

[a] Average

3.4.2 Influence of Mass on Kinematics and Damage

It is likely that the mass distribution of the lower extremity is an influential factor for injury mechanism, because mass recruitment throughout the event may affect the duration and level of loading of the lower extremity. To explore this factor, the peak vertical acceleration and speed of the distal tibia and femur are plotted as a function of mass of the lower extremity below the knee. Mass below the knee is considered the most pertinent to mass effects on the lower extremity because the fractures to the leg

occur before the mass of the thigh has moved much. Additional plots are generated using total body mass. The plots use color to indicate damage level, with green, yellow, and red indicating no damage, minor damage, and major damage, respectively. The shape of the markers is indicative of the sex and percentile, with circles, diamonds, and triangles representing 50th percentile males, 75th percentile females, and 5th percentile females, respectively. Cases that have ipsilateral calcaneus and tibia damage are indicated by markers with a black border.

3.4.2.1 Mass below the Knee

The plots herein use a single-peak value of speed or a single-peak value of acceleration for each lower extremity throughout the entire event. They show these peak kinematic values on the y-axis and estimated mass of the lower extremity below the knee (from CT segmentation) on the x-axis. Damage level of the calcaneus is indicated by the color of the marker. Every plot contains a total of 40 points, with individual points representing each lower extremity of each crew in every shot.

In general, the legs with the highest masses did not sustain calcaneus damage; however, not all of the legs with lower mass sustained damage (Figures 75 through 78). In general, legs with the highest masses did not sustain tibia fractures, but not all lower-mass legs fractured (Figures 79 through 82). However, many of these relational analyses to not contain many fracture data points.

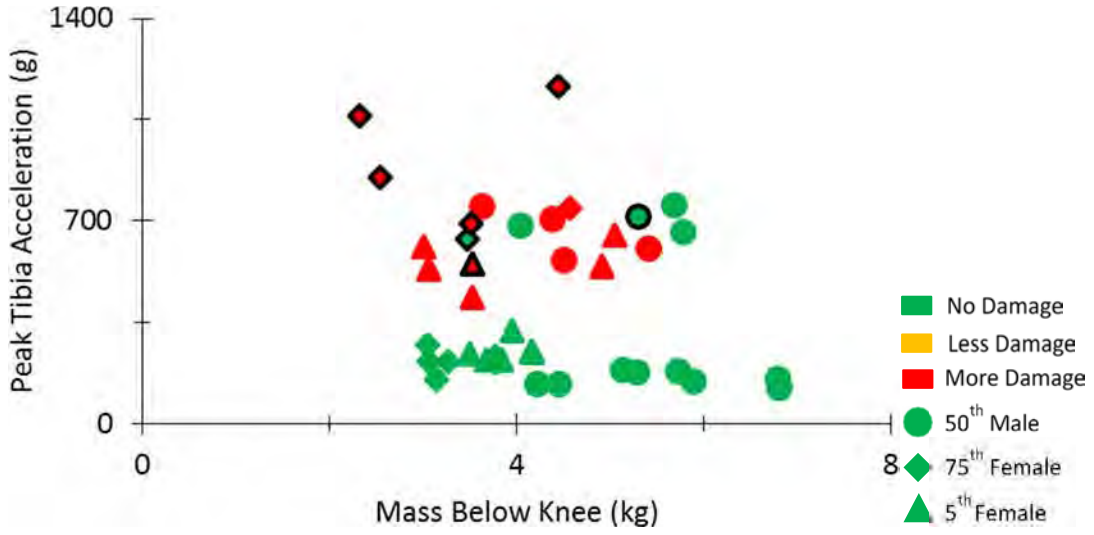

Figure 75. Peak tibia vertical acceleration vs. mass below knee (calcaneus damage). Cases that have ipsilateral tibia damage are indicated by a black border.

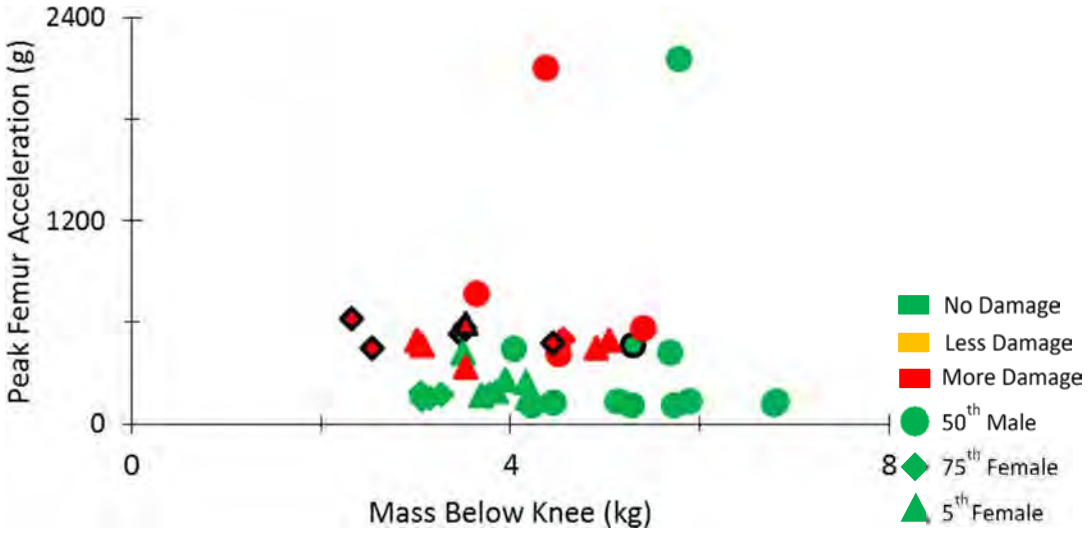

Figure 76. Peak femur vertical acceleration vs. mass below knee (calcaneus damage). Cases that have ipsilateral tibia damage are indicated by a black border.

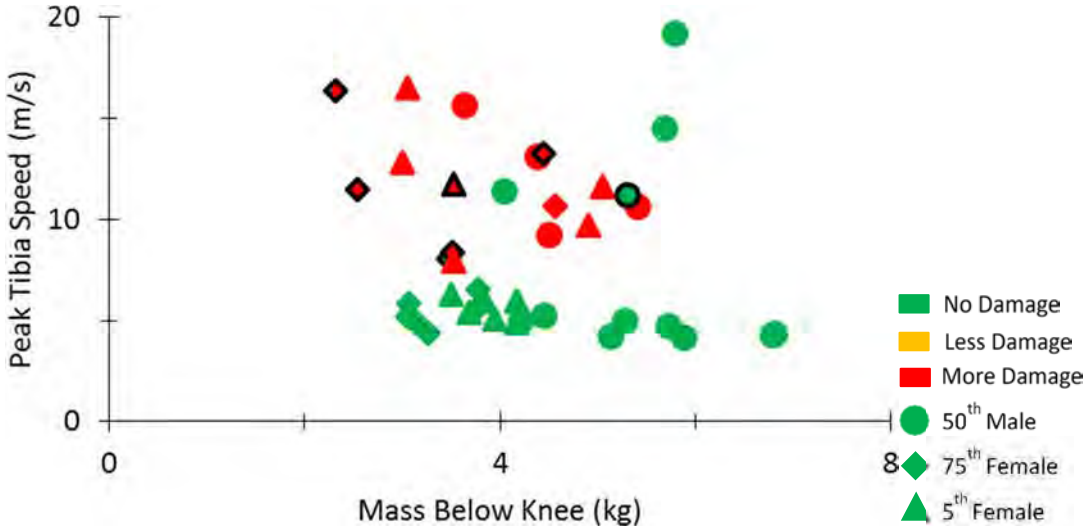

Figure 77. Peak vertical tibia speed vs. mass below knee (calcaneus damage). Cases that have ipsilateral tibia damage are indicated by a black border.

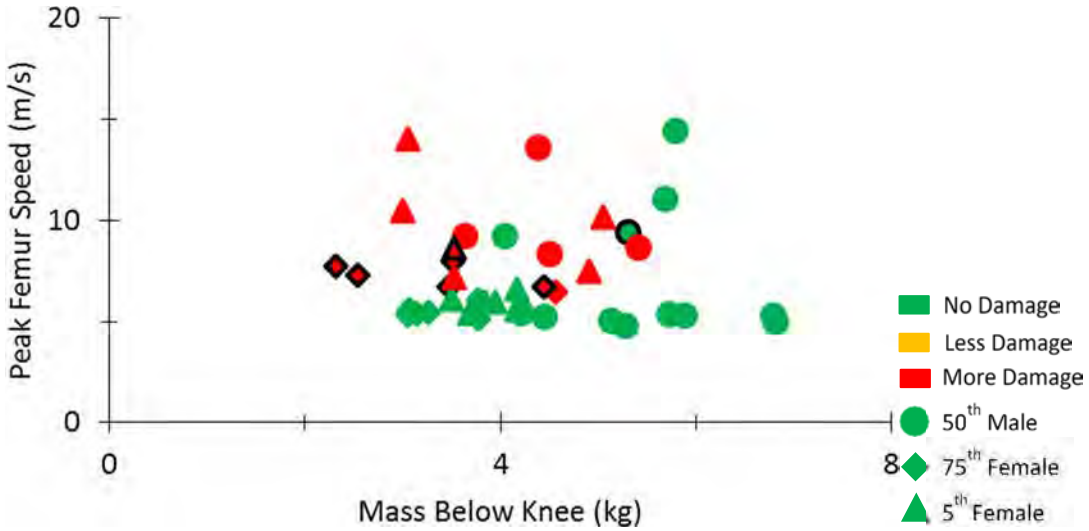

Figure 78. Peak vertical femur speed vs. mass below knee (calcaneus damage). Cases that have ipsilateral tibia damage are indicated by a black border.

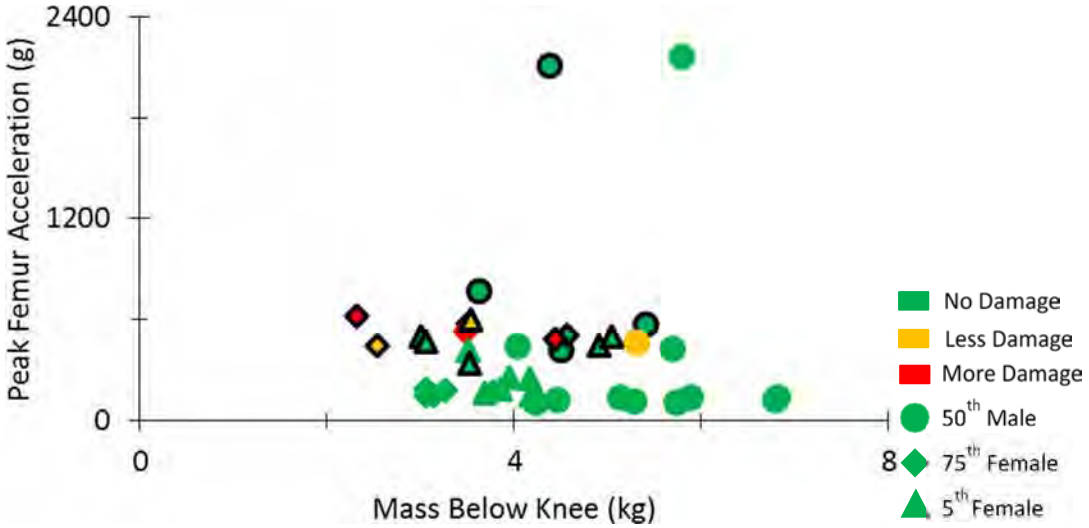

Figure 79. Peak vertical femur acceleration vs. mass below knee (tibia damage). Cases that have ipsilateral calcaneus damage are indicated by a black border.

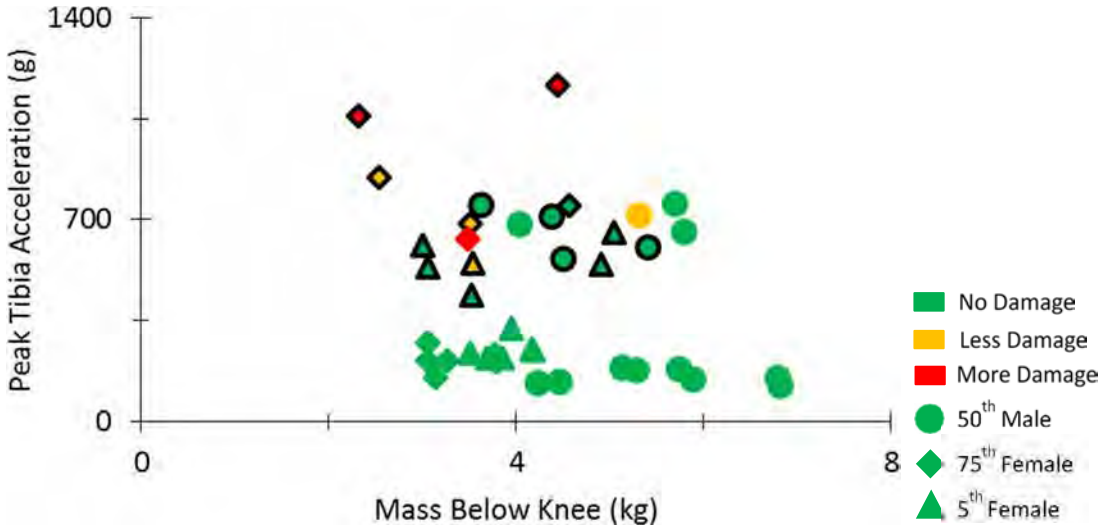

Figure 80. Peak vertical tibia acceleration vs. mass below knee (tibia damage). Cases that have ipsilateral calcaneus damage are indicated by a black outline border.

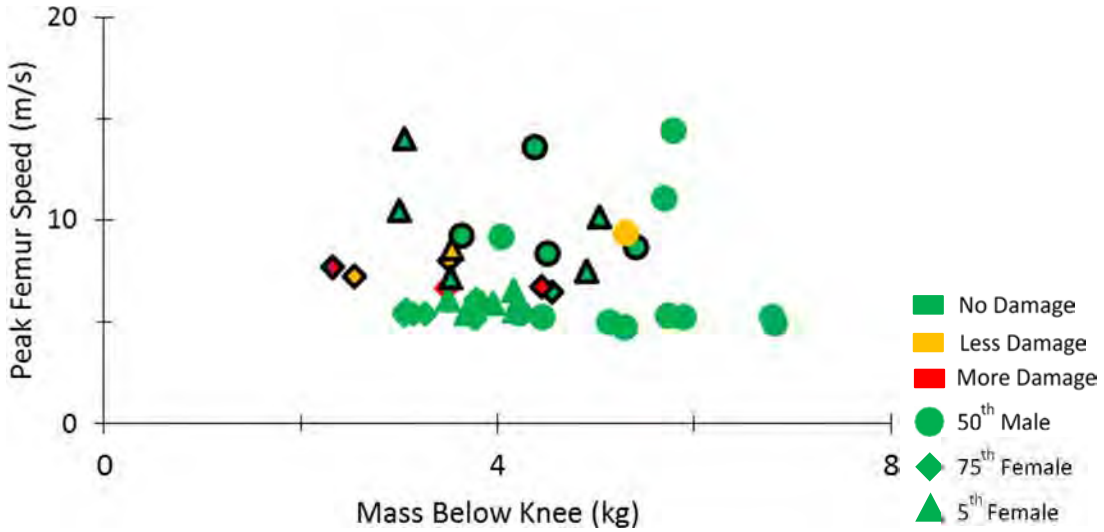

Figure 81. Peak vertical femur speed vs. mass below knee (tibia damage). Cases that have ipsilateral calcaneus damage are indicated by a black border.

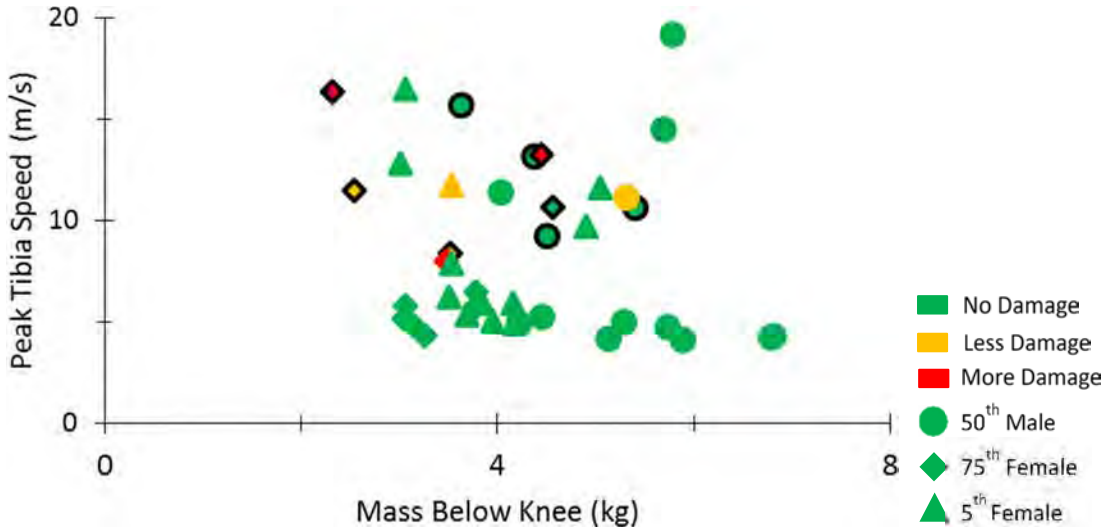

Figure 82. Peak vertical tibia speed vs. mass below knee (tibia damage). Cases that have ipsilateral calcaneus damage are indicated by a black border.

3.4.2.2 Total Body Mass

The plots herein use a single-peak value of speed or a single-peak value of acceleration for each lower extremity throughout the entire event. They show these peak kinematic values on the y-axis and estimated total body mass on the x-axis. Damage level of the calcaneus is indicated by the color of the marker. Every plot contains a total of 40 points, with individual points representing each lower extremity of each crew in every shot. Calcaneus damage might be associated with lower body mass and higher peak vertical acceleration of the tibia (Figures 83 through 86). Damage to the tibia might be associated with higher body mass and greater peak vertical acceleration of the tibia and femur (Figures 87 through 90). Regardless of mass, fracture is characterized by greater acceleration and speed. However, many of these relational analyses to not contain many fracture data points.

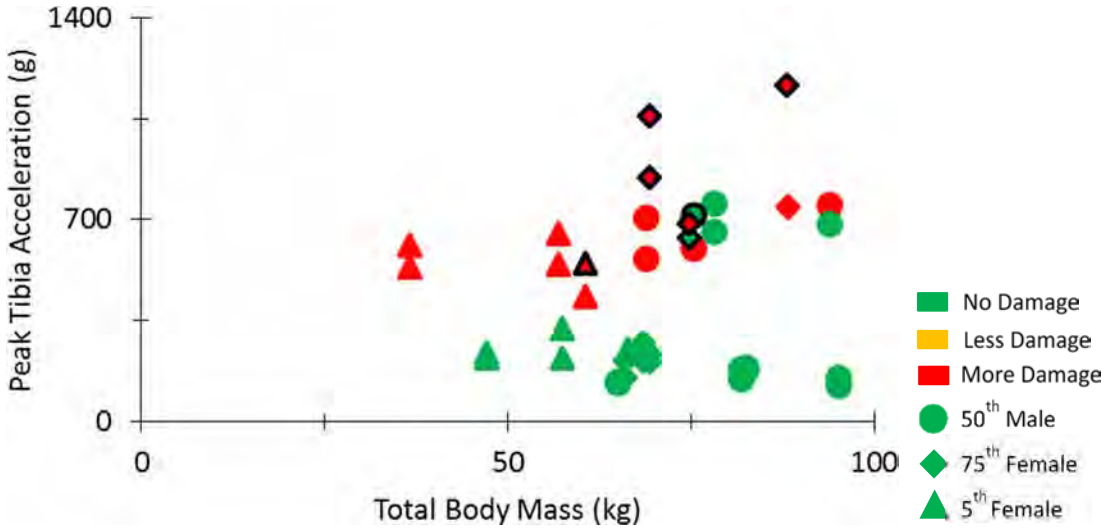

Figure 83. Peak tibia vertical acceleration vs. total body mass (calcaneus damage). Cases that have ipsilateral tibia damage are indicated by a black border.

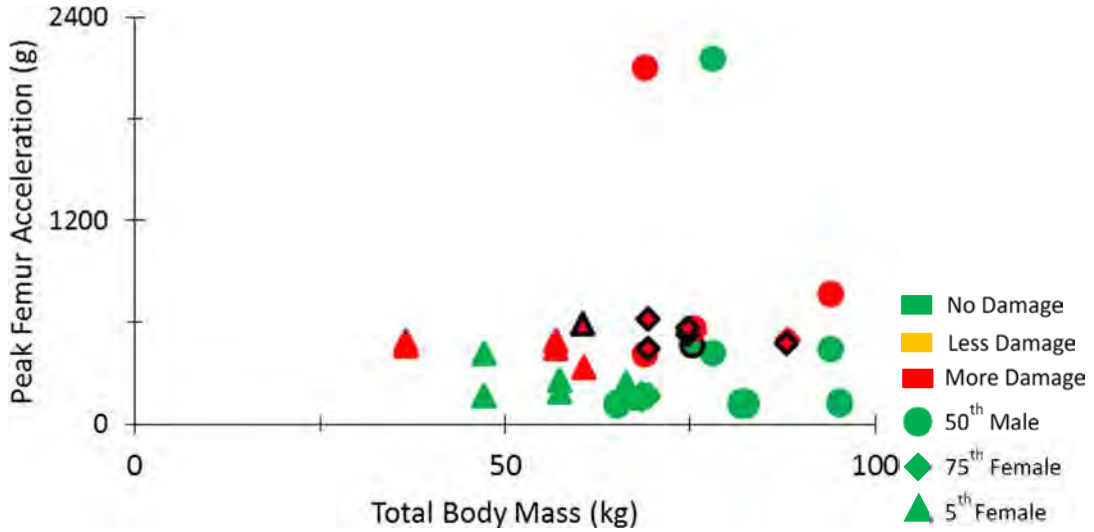

Figure 84. Peak femur vertical acceleration vs. total body mass (calcaneus damage). Cases that have ipsilateral tibia damage are indicated by a black border.

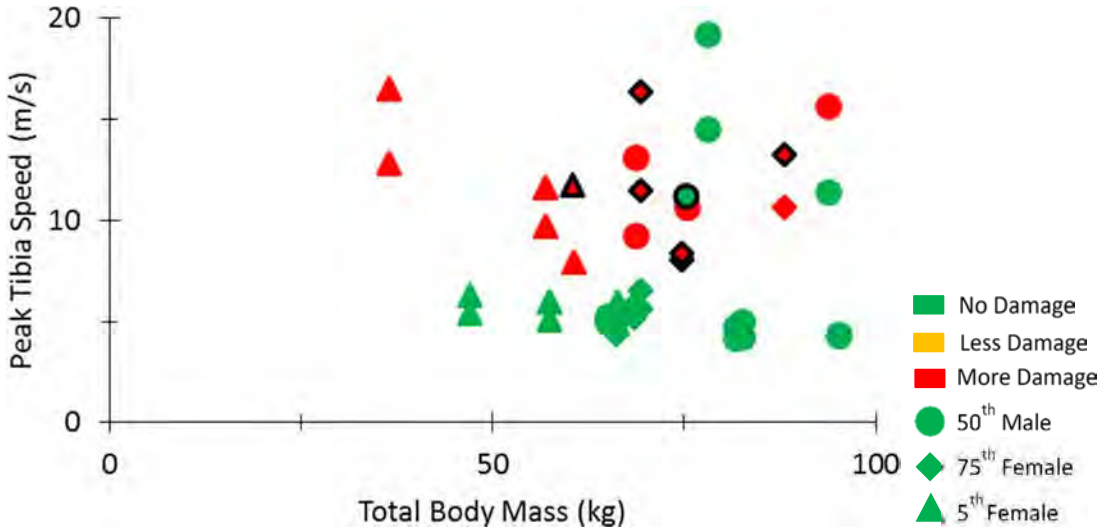

Figure 85. Peak vertical tibia speed vs. total body mass (calcaneus damage). Cases that have ipsilateral tibia damage are indicated by a black border.

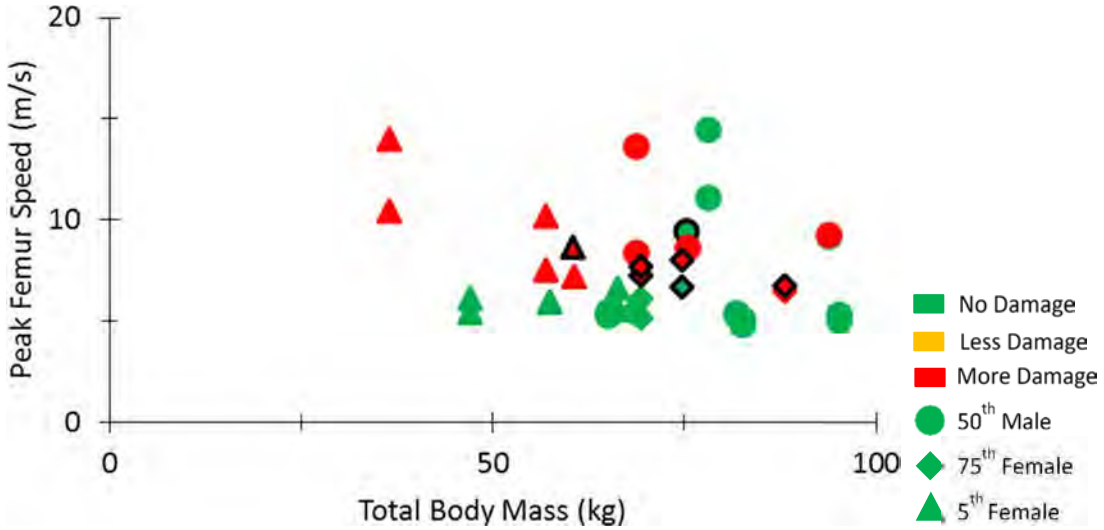

Figure 86. Peak vertical femur speed vs. total body mass (calcaneus damage). Cases that have ipsilateral tibia damage are indicated by a black border.

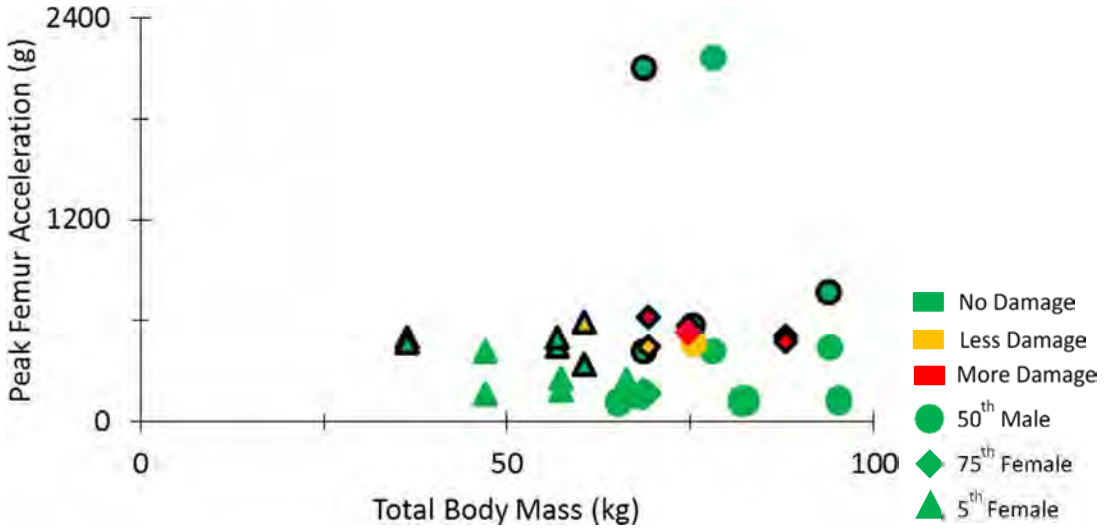

Figure 87. Peak vertical femur acceleration vs. total body mass (tibia damage). Cases that have ipsilateral calcaneus damage are indicated by a black border.

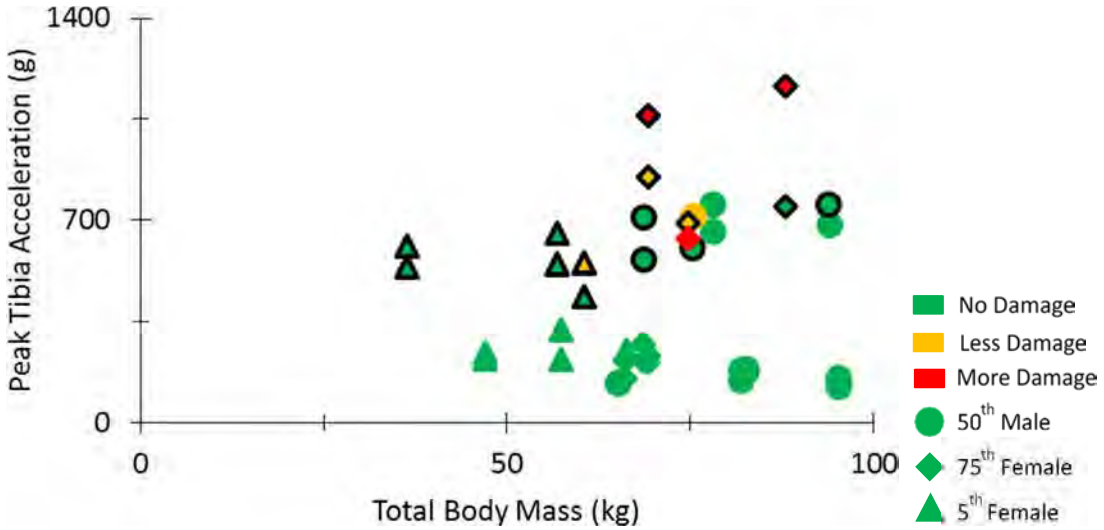

Figure 88. Peak vertical tibia acceleration vs. total body mass (tibia damage). Cases that have ipsilateral calcaneus damage are indicated by a black border.

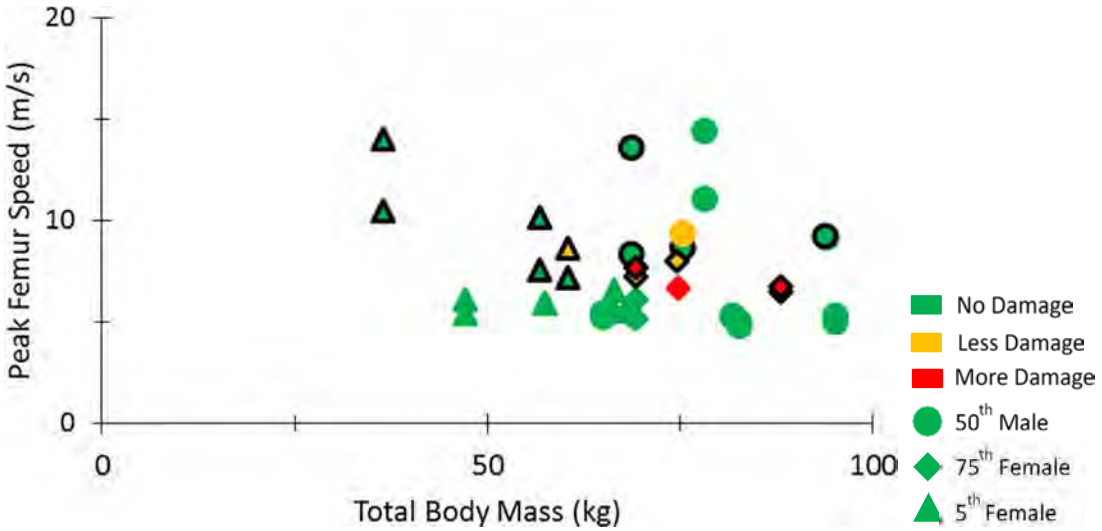

Figure 89. Peak vertical femur speed vs. total body mass (tibia damage). Cases that have ipsilateral calcaneus damage are indicated by a black border.

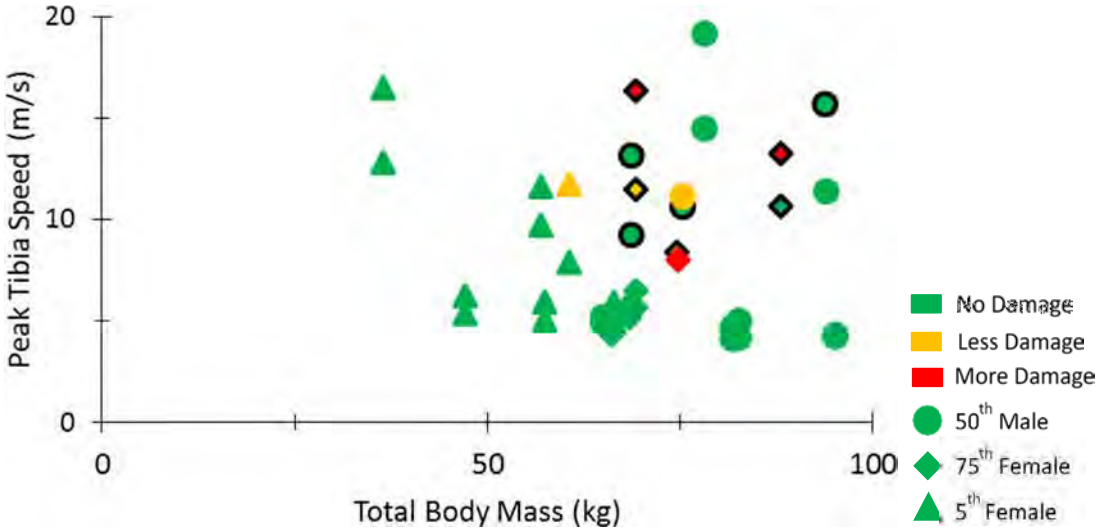

Figure 90. Peak vertical tibia speed vs. total body mass (tibia damage). Cases that have ipsilateral calcaneus damage are indicated by a black border.

3.5 Damage Timing Analysis

3.5.1 Damage Timing Estimation

Approximate times of fracture initiation for the calcaneus, distal tibia, and proximal femur are summarized for Series 3 and 4 in Table 12. The time of fracture is determined with respect to time zero. Fractures of the calcaneus and tibia occur at approximately the same time, with the femur fractures occurring afterwards. For each limb that sustained damage to the calcaneus, tibia, or both, two probable times of fracture are suggested.

Cases with femur fractures provide a third estimation of the time of fracture. All fractures occur within 10 ms of time zero.

Table 12. Estimated fracture time for Series 3 and 4 (high-energy floor condition) from time zero

PMHS	Side	Time of fracture (ms)		Femur
		Calcaneus or tibia 1	Calcaneus or tibia 2	
	R	3.1	3.25	-
S5C1				
	L	1.98	2.22	-
	R	2.97	3.47	-
S5C2				
	L	2.13	2.36	9.6
	R	3.56	4.09	-
S6C1				
	L	1.93	2.42	8.64
	R	3.4	3.98	-
S6C2				
	L	2.19	2.8	-
	R	-	-	-
S7C1				
	L	2.16	2.44	-
	R	3.66	3.84	-
S7C2				
	L	2.18	2.46	-
	R	4.45	3.85	-
S8C1				
	L	2.55	2.77	-
	R	2.82	4.59	-
S8C2				
	L	2.39	2.82	-
	R	-	-	-
S9C1				
	L	-	-	7.91
	R	2.98	3.76	-
S9C2				
	L	3.05	3.84	-

Time of fracture is estimated by examining (1) a plot overlaying the calcaneus and distal tibia strain on one y-axis and (2) the calcaneus acceleration, the distal tibia vertical speed and acceleration, and the femur vertical speed on a second y-axis. Strain signals are filtered with a cut-off frequency of 4,950 Hz. The calcaneus and distal tibia acceleration traces are scaled. The values of speed and acceleration are irrelevant for this analysis; the shape of the traces provide the pertinent information about fracture timing (i.e., zeroes and local minimums and maximums).

Fracture timing is characterized by a set of associated kinematics. In general, the first initiation of fracture is indicated by an inflection point in the distal tibia vertical speed (local minimum in acceleration), whereas a second fracture initiation manifests as a noticeable drop in speed, because a considerable amount of energy contributes to the

fracture rather than to moving the limb. To illustrate these concepts, an exemplar plot is shown in Figure 91.

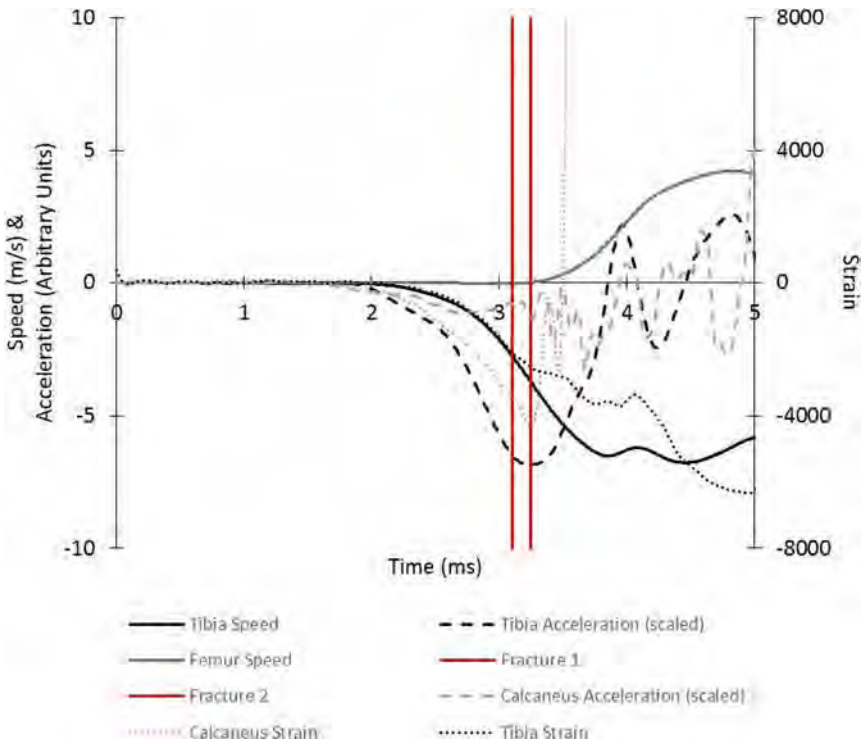

Figure 91. Plot used to determine fracture timing for S5C1 right extremity

Negative strain indicates compression. Vertical motion of the tibia motion block occurs in the z-axis, which is oriented from superior to inferior, so negative tibia speed/acceleration indicates that the motion block is traveling/accelerating upward and away from the floor. Vertical motion of the femur motion block occurs in the x-axis, which is oriented posterior to anterior. When seated, the x-axis of the thigh points upwards, so positive femur speed indicates that the femur is accelerating upward and away from the floor. Initially, calcaneus loading increases with increasing distal tibia speed.

Peak compression of the calcaneus results in a fracture that is accompanied by an inflection point in distal tibia speed. In other words, the distal tibia speed continues to increase after the fracture occurs; however, it is increasing at a slower rate. This is illustrated by the coinciding local minimum in distal tibia acceleration. The second fracture occurs near a local maximum in distal tibia speed. After the fracture occurs, speed decreases. This is shown by the acceleration trace, which is zero around the time of fracture. After the tibia fracture occurs, acceleration becomes negative. The femur speed trace indicates that the femur begins to move after fracture of the leg has begun.

Therefore, a substantial portion of the lower extremity mass is recruited before the tibia fracture occurs.

3.5.2 Influence of Time-to-Peak on Damage

Damage level may be influenced by the duration of loading. In this report, plots show the peak kinematics values for each limb as a function of the time taken to reach those peak values (time to peak [TTP]). The kinematics variables that are investigated include vertical speed and acceleration of the distal tibia and distal femur. Damage level is indicated by color, with green, yellow, and red indicating no damage, minor damage, and major damage, respectively. The shape of the markers is indicative of the sex and percentile, with circles, diamonds, and triangles representing 50th percentile males, 75th percentile females, and 5th percentile females, respectively. Cases that have ipsilateral calcaneus and tibia damage are indicated by a black border on the marker. The plots use a single value of speed or a single value of acceleration for each lower extremity throughout the entire event. Every plot contains a total of 40 points, with individual points representing each lower extremity of each crew in every shot.

3.5.2.1 Calcaneus Damage

Calcaneus damage cases are characterized by higher peak vertical acceleration and shorter TTP for both the tibia and femur response (Figures 92 and 93). Calcaneus damage is generally associated with higher peak tibia speed for a given time to peak, although two nonfracture points do not follow this trend (Figure 94). Calcaneus damage is also associated with higher peak vertical speed and shorter TTP of the tiba and femur (Figure 95).

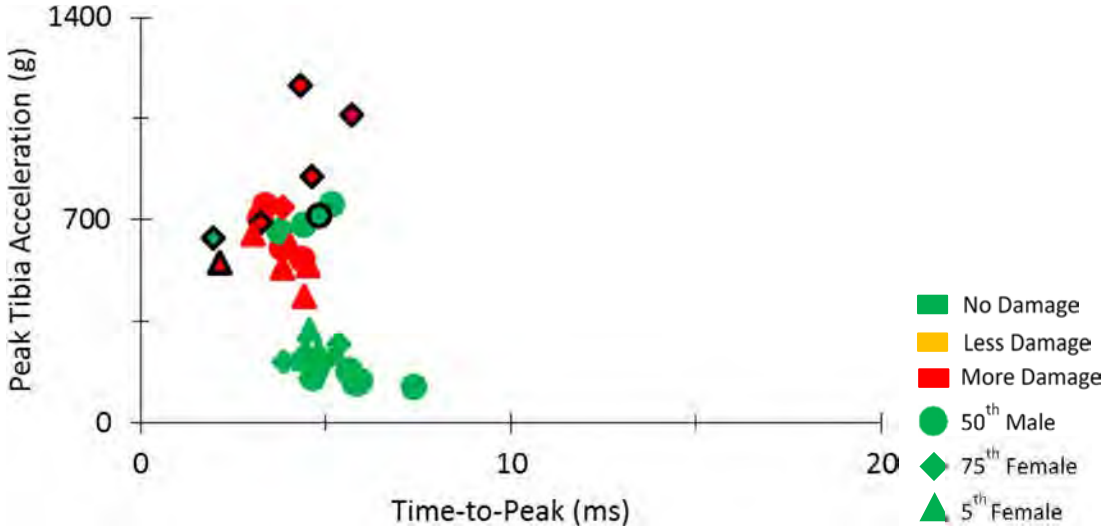

Figure 92. Peak tibia vertical acceleration vs. TTP (calcaneus damage). Cases that have ipsilateral tibia damage are indicated by a black border.

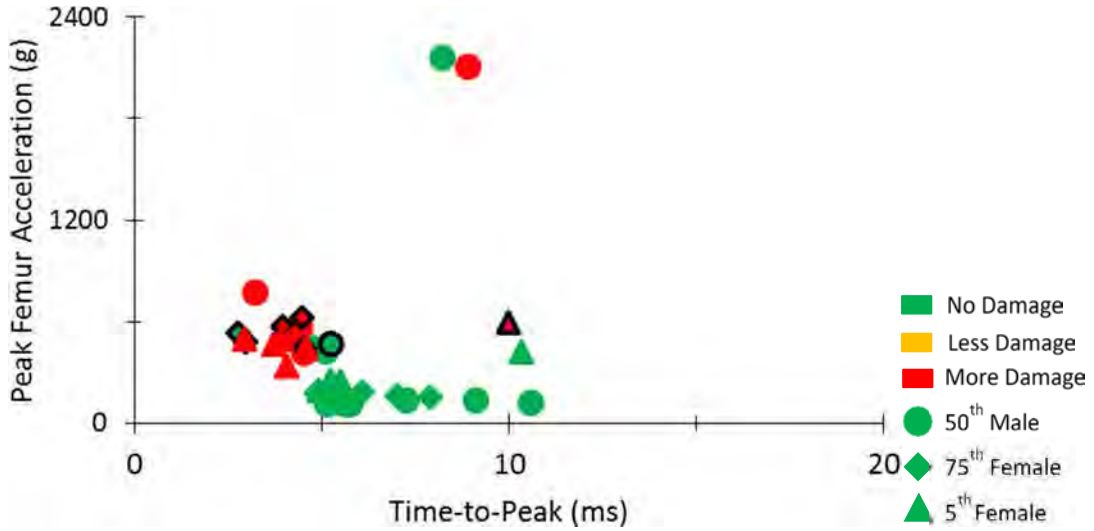

Figure 93. Peak femur vertical acceleration vs. TTP (calcaneus damage). Cases that have ipsilateral tibia damage are indicated by a black border.

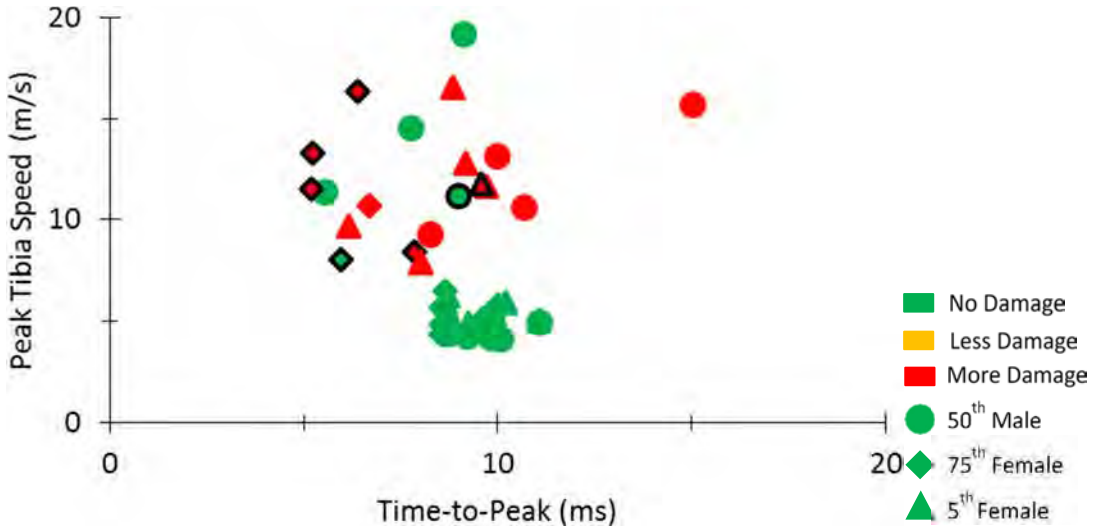

Figure 94. Peak vertical tibia speed vs. TTP (calcaneus damage). Cases that have ipsilateral tibia damage are indicated by a black border.

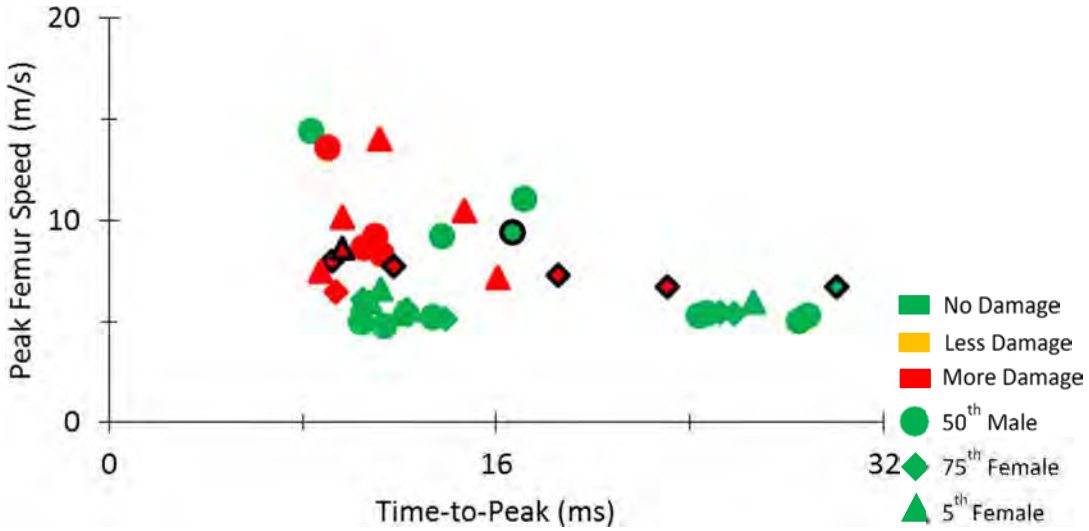

Figure 95. Peak vertical femur speed vs. TTP (calcaneus damage). Cases that have ipsilateral tibia damage are indicated by a black border.

3.5.2.2 Tibia Damage

Tibia damage cases are characterized by greater peak vertical acceleration and shorter TTP of both the tibia and femur (Figures 96 and 97). Tibia damage is also associated with greater peak vertical speed and shorter TTP of the tibia (Figure 98). More severe damage of the tibia might be associated with short TTP for tibia speed and longer TTP for femur speed (Figure 99).

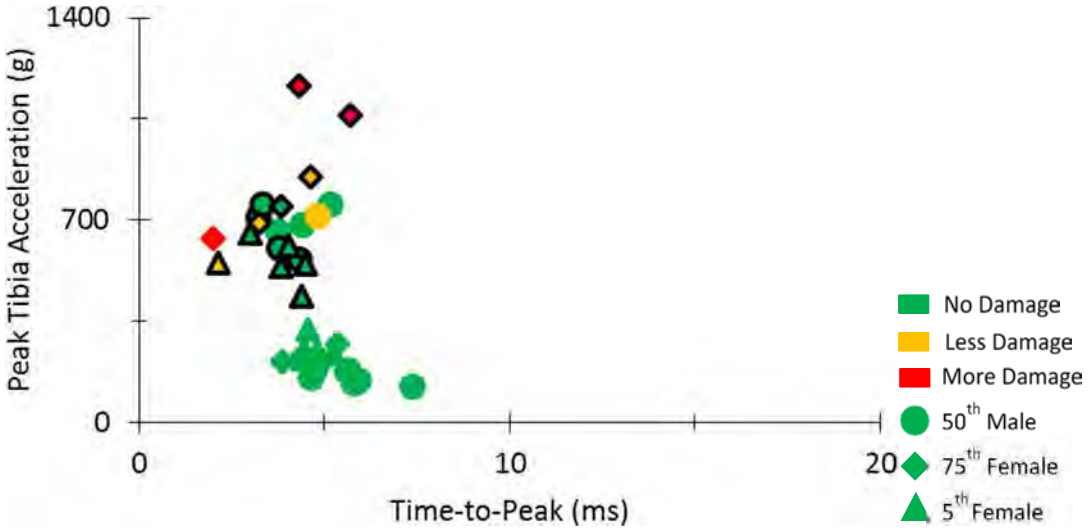

Figure 96. Peak vertical tibia acceleration vs. TTP (tibia damage). Cases that have ipsilateral calcaneus damage are indicated by a black border.

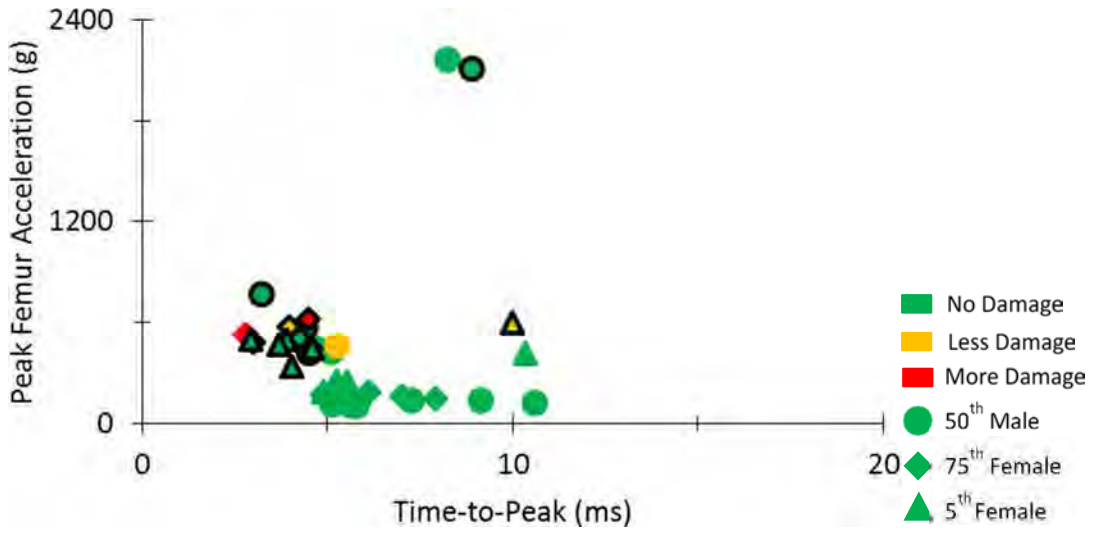

Figure 97. Peak vertical femur acceleration vs. TTP (tibia damage). Cases that have ipsilateral calcaneus damage are indicated by a black border.

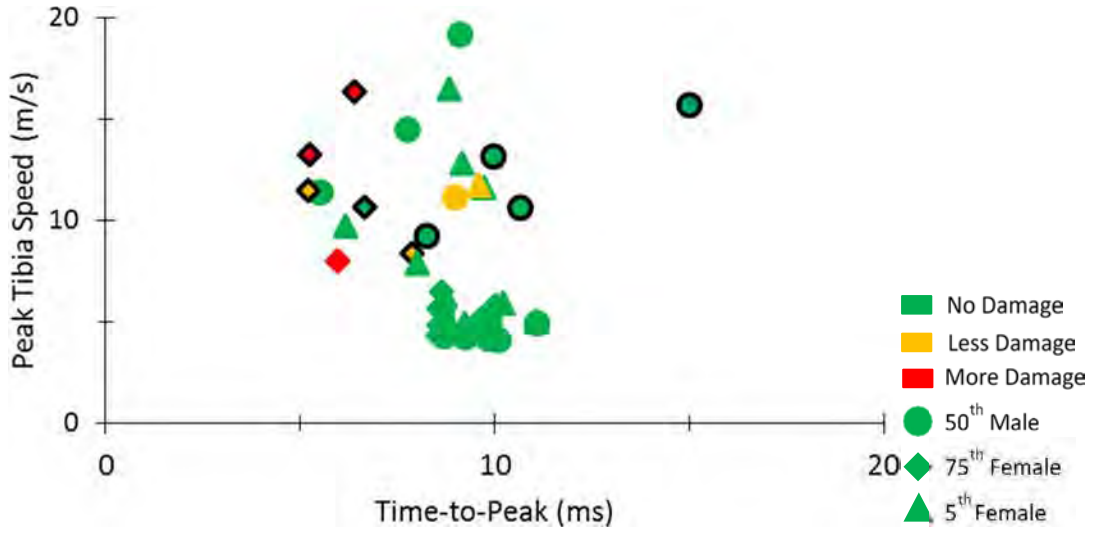

Figure 98. Peak vertical tibia speed vs. TTP (tibia damage). Cases that have ipsilateral calcaneus damage are indicated by a black border.

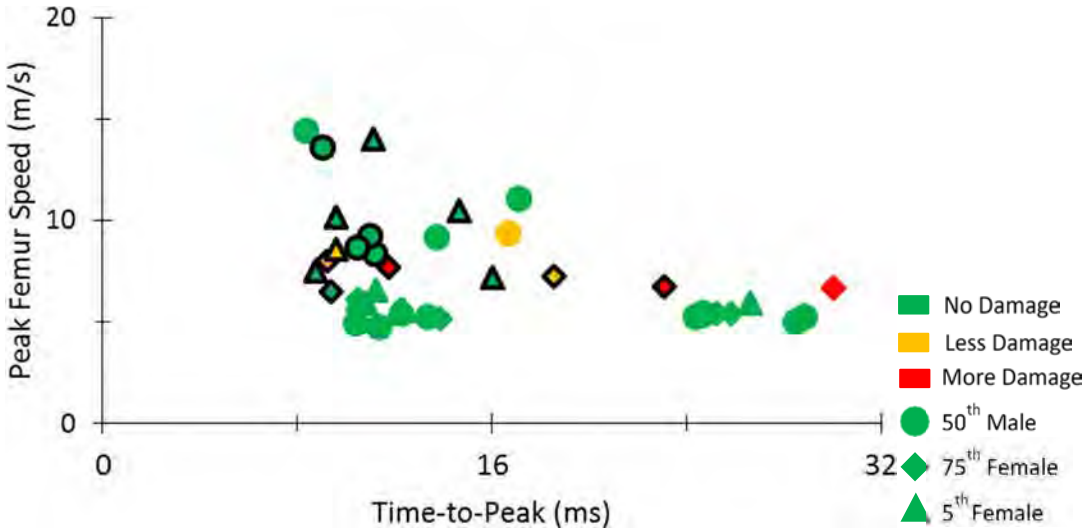

Figure 99. Peak vertical femur speed vs. TTP (tibia damage). Cases that have ipsilateral calcaneus damage are indicated by a black border.

4. DISCUSSION

4.1 Kinematics Response

4.1.1 Lower Extremity

Initial interpretation of the results suggests that the kinematics response of the lower extremities of female PMHS is different from the male PMHS, as exhibited by the transducer data. The primary measured difference is that the tibiae and femura of the female PMHS attain higher speeds at earlier times in the event. The femur acceleration responses of both the females and males in male CORALS and Series 1 exhibit an oscillatory square unimodal response. In Series 3 and 4, the heavier lower extremities of the female PMHS exhibit a second-order effect in the vertical speed response of the femur. The associated female vertical acceleration responses are triangular and bimodal in nature, in contrast to those observed during male CORALS and Series 1. The mass of the lower extremities is an important driver of the kinematics. Lighter extremities likely reach higher acceleration and speed earlier. The differences observed in the response of the tibiae are not considered to be a result of the differences in anatomy of the lower extremity. Additional structural-level testing is required to fully explore these phenomena.

4.1.2 Pelvis

There are miniscule differences seen in the kinematics response of the pelvis between the damage and nondamage cases. The pelvis does not rotate prior to lumbar spine fracture occurrence and moves very little at the time of fracture. The right and left halves of the pelvis move in unison. In Series 3 and 4, the pelves of the 75th percentile female PMHS maintain greater speed and attain greater acceleration peaks throughout the event than those of the other surrogates. Additional structural-level testing with pelvis components will examine possible differences in fracture pattern due to differences in anatomy.

4.1.3 Lumbar Spine

The fractures occur at the onset of lumbar motion, when the lumbar spine begins to engage the torso mass. Lumbar spine fracture influences the kinematics at the third lumbar vertebra. The kinematics of the lumbar spine change in cases with lumbar spine fractures. The vertical speed response shows that the third lumbar vertebrae experiences higher peak speeds earlier in the event for the PMHS that sustained damage to the lumbar spine. In addition, the rotation of the third lumbar vertebra is minimized early in the event in cases that did not result in lumbar spine fracture. When

the lumbar spine fractures, the coupling between the lumbar spine and the thoracic spine is disrupted. The resulting vertical accelerations of the 12th thoracic vertebrae (T12) are greater, with earlier peaks, in cases without lumbar spine fracture. Less energy is transferred to T12, and it is transferred more gradually, in cases with lumbar spine fractures. Similarly, a minimal moment is transferred to the thorax in the case of lumbar spine fracture, which results in almost no rotation at T12.

The 50th percentile males and 75th percentile females PMHS attain greater peak vertical accelerations and reach higher angular speeds throughout the event during male CORALS and Series 1, which had the higher target peak speed and shorter target TTP for the seats. Damage to the lumbar spine was limited to these two surrogate types.

4.2 Damage Response

4.2.1 Lower Extremity

4.2.1.1 Hindfoot and Ankle

The calcaneus, which is the first hard tissue structure responsible for bearing axial load applied to the lower extremity, sustains a characteristic comminution due to the severe overmatch conditions of UBB. Major injuries to the calcaneus are a concern in the context of UBB, because destruction of this bone makes ambulation immediately after injury very difficult. In the current study, the most frequent type of severe damage was a crushed calcaneus (15 cases). There were seven cases with damage to the distal tibia. Three of those cases involved severe damage to the distal tibia. All three of the severe cases had associated damage to the fibula. When the distal leg was severely damage, associated damage to the calcaneus was less severe (i.e., in two cases the calcaneus was fractured into larger sections rather than crushed, and in one case the calcaneus was intact). Thus, in the absence of severe damage to the calcaneus, the distal bones of the leg are catastrophically damaged. Accordingly, when the calcaneus was crushed, the damage proximal to the calcaneus was less severe.

There were eight cases with talus damage. The only instance of severe talus damage was associated with a crushed calcaneus and no damage to the distal leg. Two cases of talus damage had no associated calcaneus damage. Furthermore, talus fractures occurred in the absence of damage to the distal tibia in five cases, suggesting that sustained loading of the talus without fracture of the distal tibia is possible. Within these tests, damage to the distal tibia occurred when there was no damage to the talus bone in three cases.

Six female PMHS incurred both major and minor damage to the tibia, whereas just one male sustained minor damage to the tibia. Only 75th percentile females sustained major damage of the distal tibia. Only 75th percentile females sustained damage to the fibula. During Series 3 and 4, all females sustained some form of damage to one or both tali, whereas only one male sustained damage to the talus.

4.2.1.2 Midfoot

Damage to the midfoot occurred to the navicular and cuboid. Damage consistently occurred to the lateral and inferior corner (beak) of the navicular (five cases). The mechanism for this fracture might involve a flattening of the foot with the head of the talus being driven into the navicular. Two cuboid fractures were observed throughout testing. In both cases, the damage was located at the lateral portion of the cuboid and there was associated damage to the navicular. It is interesting to note that damage to the midfoot was isolated to the female PMHS. Fractures of the navicular and cuboid are of concern; these bones play an essential role in maintaining the structural integrity of the arches of the foot. In addition, treatment of fractures to the midfoot are especially difficult due to the limited vasculature in this region.

4.2.1.3 Forefoot

Females and males sustained damage to the forefoot. Damage to the forefoot consistently occurred to the proximal ends of the lateral three metatarsals (four cases) and, in one case, to the proximal end of the 5th phalange. Injuries to the lateral forefoot are a likely result of the ankle undergoing inversion or supination. Fractures of the base of the 5th metatarsal in particular are a likely result of a twisting force through the foot.

4.2.1.4 Femur

The left femur sustained severe damage in three cases. These were not associated with a particular damage pattern to the distal portion of the lower extremities. All of these fractures occurred to the diaphysis and resulted in three pieces with multiple small fragments. Two 50th percentile male PMHS and one 5th percentile female PMHS sustained femur fractures. One male sustained a spiral wedge fracture of the left femur due to a combination of bending and torsion. The torsional component potentiated this damage, which resulted from inertia of the thigh. The second male sustained a fragmented wedge fracture of the femur with a similar mechanism to the first male. The 5th percentile female sustained a segmented bending fracture of the left femur that resulted from bending, with torsion being a possible contributor. It is possible that the combined higher acceleration and lower bone strength could have made an inertial fracture more likely for the female, even in the absence of appreciable torsion. The

female had relatively lower mass lower extremities and relatively higher peak vertical femur acceleration. This suggests that reduced tolerance could be a factor.

It appears that the bowing of the floor pushes the left foot towards the right foot. In the two femur fracture cases where the ankle is visible (S5C2 and S6C1), the ankle everts and the plantar surface of the boot maintains contact with the floor.

4.2.2 Pelvis

As expected, damage to the coccyx was the most frequent, with a total of 19 cases. Excluding the coccyx, the vast majority of damage to the pelvis occurred during male CORALS and Series 1. This is likely due to the target peak seat speed of 5 m/s for male CORALS and Series 1 compared to Series 3 and 4, which was 4 m/s. Male CORALS and Series 1 also have shorter target TTP for the seats (4 ms) than Series 3 and 4 (7 ms). With the exception of the coccyx fractures and one sacrum fracture of a 50th percentile male during male CORALS, all damage to the pelvis was incurred by females. All damage to the sacral alae was sustained by 5th percentile females.

4.2.3 Lumbar Spine

Damage to the lumbar spine is representative of injuries seen in theater. Most of the fractures occurred in lower levels of the spine. The primary mechanism of damage is compression of the vertebral body. In the one case of a wedge fracture, flexion of the spine was also a contributing factor. This resulted in a slight collapsing of the anterior aspect of the vertebral body. Burst fractures are more severe than compression fractures and involve multiple fractures of the vertebral body. All of the damage to the vertebral bodies of the lumbar spine was sustained by 50th percentile males and 75th percentile females.

4.2.4 Summary of Damage Response

Initial interpretation of damage results suggests that the damage response of the female PMHS is different from the male PMHS. Damage differences are considered to be a result of sex-related tolerance, anatomy, and/or size (mass) phenomena. Differences in weight distribution between females and males may be an important consideration. The results are confounded by phenomena associated with instantaneous effective mass and mass recruitment, which is the degree of coupling of soft tissues to the bone. Additional data are needed to determine specific damage tolerances and mechanisms. These factors will be quantified through future component tests.

5. CONCLUSIONS

The results presented herein suggest that both the kinematics and damage response of female PMHS are different from male PMHS. The primary measured difference is that the female PMHS attain a higher velocity at an earlier time for the lower extremities. Damage differences due to sex-related tolerance and anatomy need to be investigated further through component testing to determine whether there are differences in fracture morphology or tolerance between females and males. At this time, the development of a female ATD may be needed for UBB if occupant kinematics are required to develop injury countermeasures. However, additional testing would be required to confirm this conclusion. If kinematics are not considered critical, an extensive investigation into female response for a range of percentiles could be conducted to develop validated mapping schemes between the existing WIAMan ATD and the female Warfighter.

6. REFERENCES

1. Gordon, C. C., Blackwell, C. L., Bradtmiller, B., Parham, J. L., Barrientos, P., Paquette, S. P., Corner, B. D., Carson, J. M., Venezia, J. C., & Rockwell, B. M. et al. (2014). *2012 Anthropometric survey of U.S. Army personnel: methods and summary statistics*. D.a.E.C. U.S. Army Natick Soldier Research (Ed).

2. National Highway Traffic Safety Administration. (2010). *Report to Congress NHTSA's Crash Data Collection Programs*. https://crashstats.nhtsa.dot.gov/Api/Public/ViewPublication/811337

3. WIAMan Signal Conversion Tiger Team [ScoTT]. (2013). *Recommendations for anatomical reference, rev. 0.6* (WIAMan Program Office Internal Document). [unpublished].

4. SAE International. (2007). *Surface vehicle recommended practice* (SAE J211).

5. Rupp, J. R. & Reed, M. P. (2015) *Draft PMHS positioning procedures 9/Dec/2015. Version 0.7.*

Appendix A – Finite Element Modeling Results

A finite element model of the Warrior Injury Assessment Manikin (WIAMan)-LX was developed (Figure A-1) in LS-DYNA software (LSTC, Livermore, CA) based on CAD drawings of the physical anthropomorphic test device (ATD). All parts, hardware, and instrumentation for the ATD were explicitly modeled to fully encompass the kinetics and kinematics involved in the impact. The rotational joints were modeled using surface contacts with a smoothing option added. Bolted connections were modeled using tied contacts. Load cells were represented using a defined cross section with responses output in a locally defined coordinate system. Six-degrees-of-freedom accelerometers and angular rate sensors were output at a single node defined at the center of mass of each sensor array using the *CONSTRAINED_INTERPOLATION card. The final lower limb model has 212,001 nodes, 164,755 hexahedral elements, and 22,027 tetrahedral elements, and it was obtained after successive mesh smoothing and mesh convergence studies. Use of tetrahedral elements was confined to the leg flesh, a nonstructural component surrounding the tibia shaft.

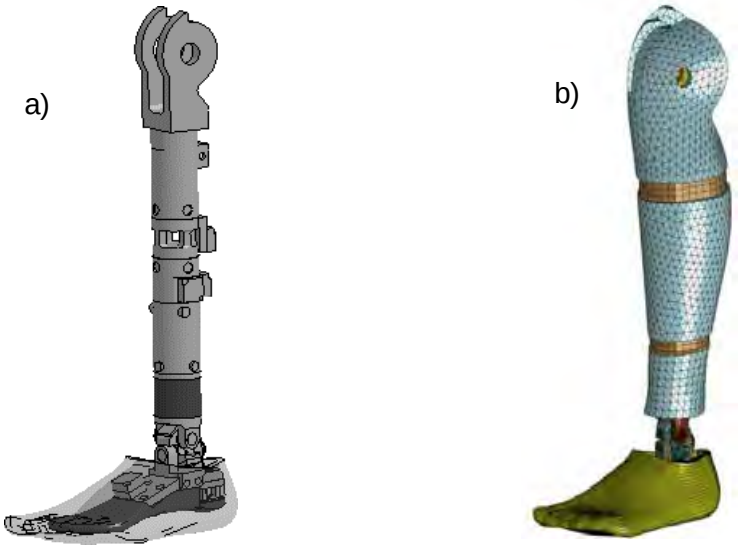

Figure A-1. a) The WIAMan-LX soft components of the lower limb and the instrumentation used to assess risk of injury; b) WIAMan-LX FE model

Five polymeric components of the ATD (leg flesh, foot flesh, calcaneus cap, foot plate, and tibia compliant element) were selected so ATD responses match postmortem human surrogates (PMHS) response corridors at various loading conditions. A simplified rubber material[1] (MAT 181, LS-DYNA) was developed for each of the five compliant parts of the ATD. To develop the simplified rubber material, stress-strain curves from the uniaxial tension and compression tests were tabulated at discrete strain rates. To verify the simplified rubber material for each of the five components, a single element

[1] Livermore Software Technology Corporation. (2003, April*). LS-DYNA keyword user's manual* (Version 970).

(1 mm^3) in LS-DYNA was assigned one of the five materials. Simulations were then performed where the element was deformed at constant speeds corresponding to experimental strain rates.

The lower limb model was validated based on the test data recorded in a series of impact experiments conducted on two test rigs, which vertically loaded the physical WIAMan-LX to simulate an under-body blast. Experiments conducted on the Vertical Accelerator[2] (VertAc; Medical College of Wisconsin) provided one loading condition (2 m/s preimpact velocity). Experiments using the Vertically Accelerated Load Transfer System[3] ([VALTS] Johns Hopkins Applied Physics Laboratory) at three load severities (2, 4, and 6 m/s preimpact velocities) provided a second set of model validation responses. These impact severities were chosen to provide a range of severities available for validation while preventing physical damage to the ATD.

Validation of the leg finite element model was performed against the time histories of forces and accelerations along the longitudinal (z) axis as well as bending moments about the y-axis recorded in testing. The strength of correlation between the experimental and simulation results was evaluated using the objective rating systems correlation and analysis (CORA) and the recently conceived International Organization for Standardization (ISO) metric.

The WIAMan-LX FE model showed good correlation to the averaged data of 3 tests recorded on the VertAc at an impact velocity of 2 m/s (Figure A-2). Correlation scores calculated using both the CORA and ISO methods are provided for each response. The scores are a weighted value between 0 (the worst) and 1 (the best) to assess the correlation between the numerical results and corresponding ATD test data. WIAMan and H-III ATD responses were compared with PMHS VertAc experiments to examine their biofidelity. A comparison of the axial force at the knee shows that the WIAMan is able to closely mimic the human response and replicate the load transfer through the lower limb.

A comparison between LS-DYNA simulations and VALTS experiments (Figure A-3) shows the model accurately predicted the distribution of forces entering the leg through the heel and toe, respectively. In addition, the WIAMan-LX model was able to accurately replicate the force and acceleration responses of the ATD for preimpact speeds of 2.4,

[2] Pintar, F. A., Schlick, M. B., Yoganandan, N., Voo, L., Merkle, A. C., & Kleinberger, M. (2016) Biomechanical response of military booted and unbooted foot-ankle-tibia from vertical loading. *Stapp Car Crash Journal*, 60, 247–285. doi: 10.4271/2016-22-0010

[3] Ott, K., Drewry, D., Luongo, M., Andrist, J., Armiger, R., Titus, J., & Demetropoulos, C. (2020) Comparison of human surrogate responses in underbody blast loading conditions. *Journal of Biomechanical Engineering*, 142(9), 091010. doi: 10.1115/1.4046638

3.9, and 5.8 m/s, respectively (Figure A-4). The correlation between the experiment and the simulation results was quantified by CORA and ISO scores for each signal as well.

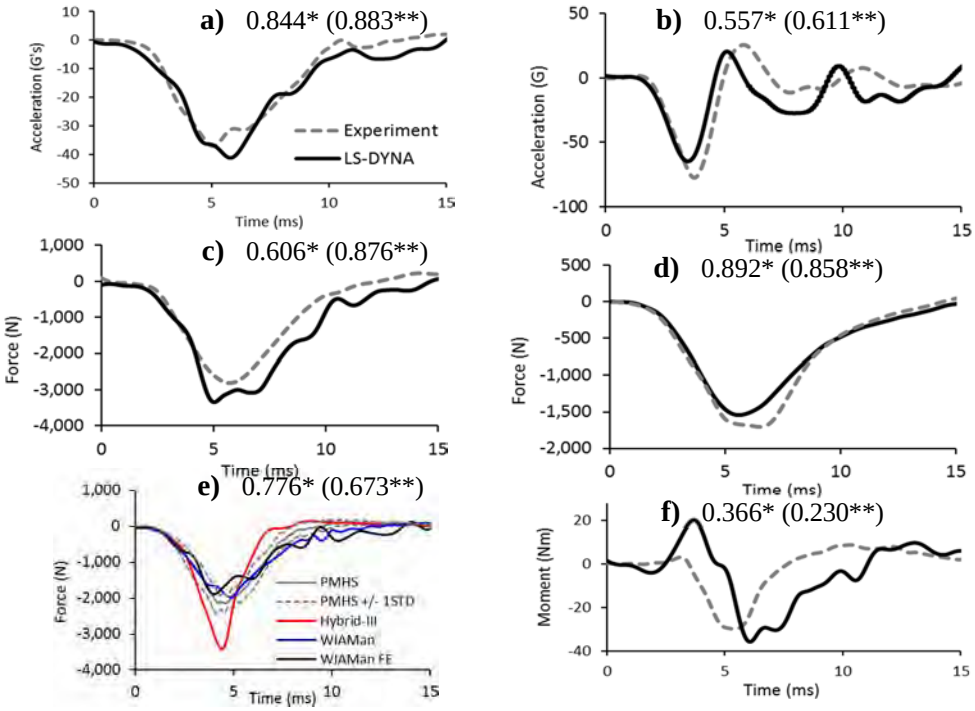

Figure A-2 Comparison between WIAMAN-LX results and VertAc test data: a) tibia acceleration (z-axis); b) foot acceleration (z-axis); c) knee force (z-axis); d) calcaneus force (z-axis); e) tibia force (z-axis); and f) tibia moment (y-axis). Both *ISO score and **CORA scores are provided.

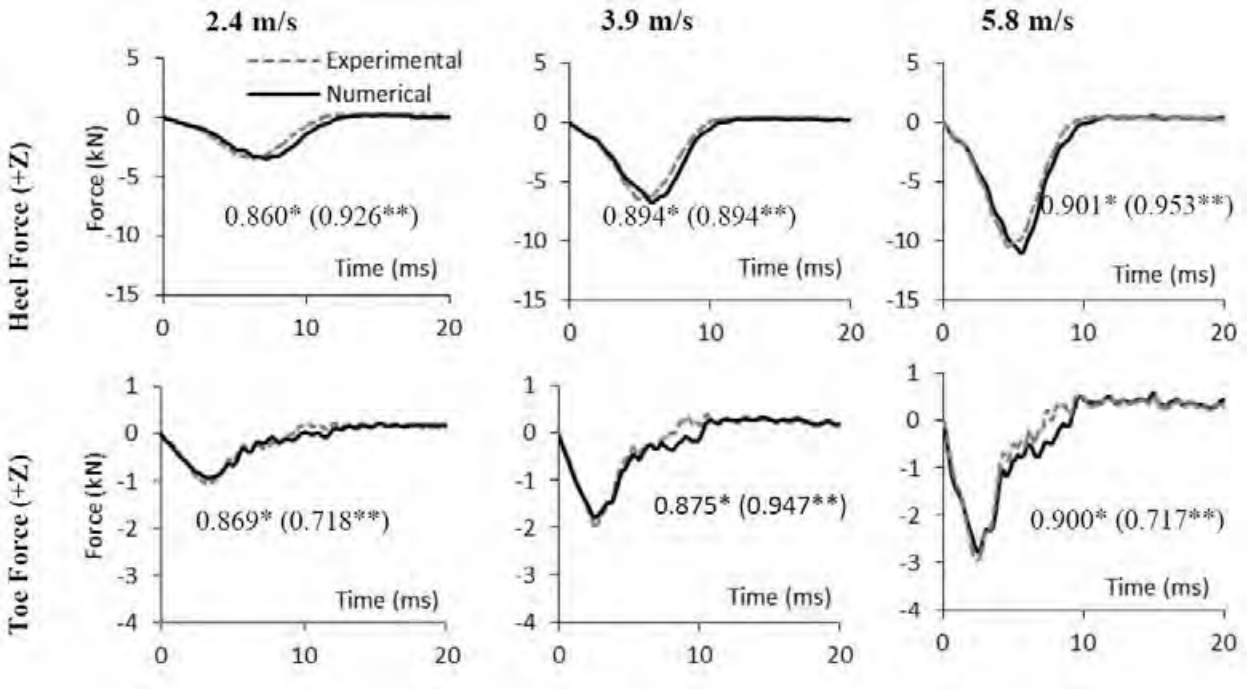

Figure A-3. Comparison of simulations to VALTS experiments at the heel and toe load cells fixed to the foot platen. For each signal, both *ISO and **CORA scores are provided.

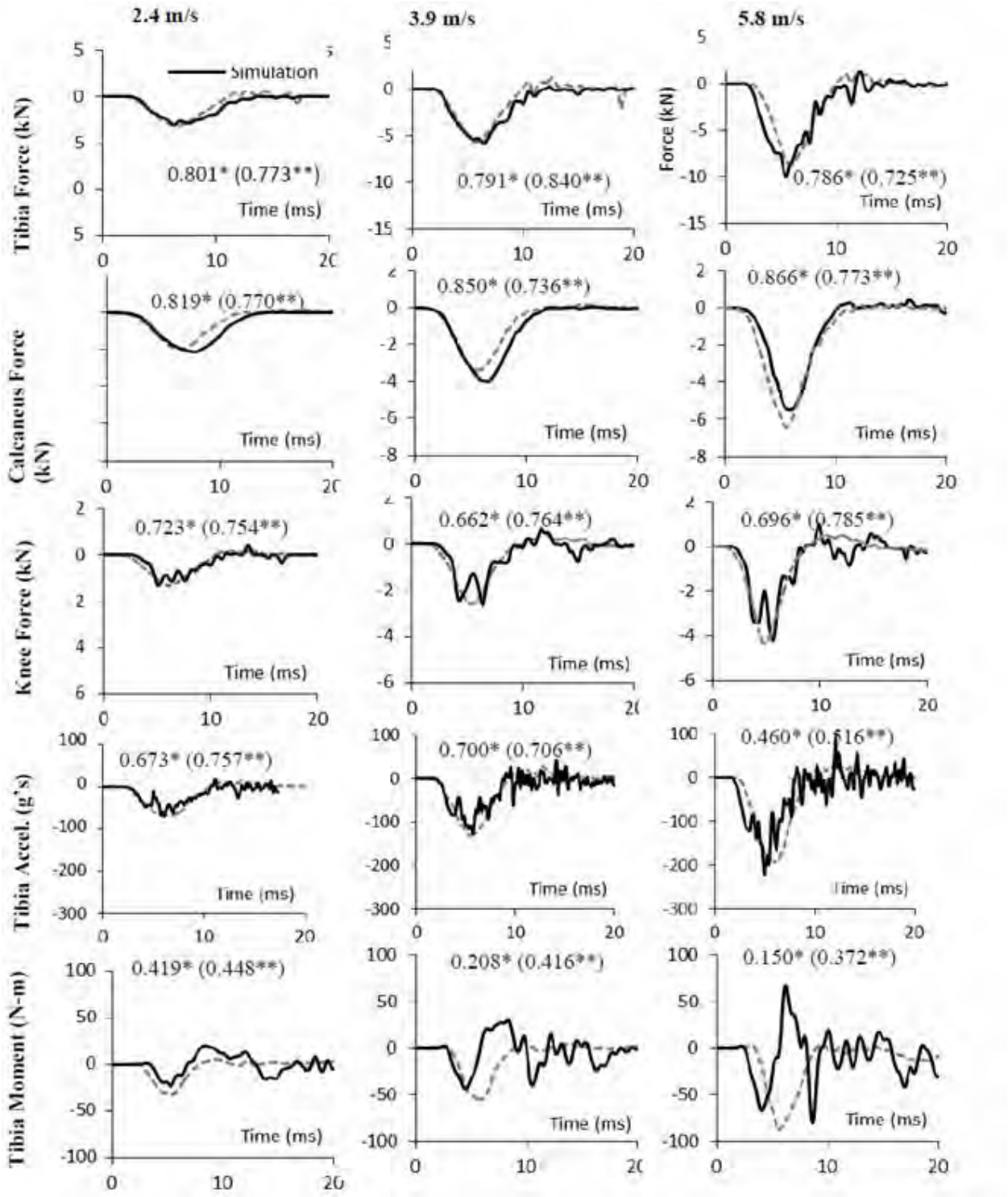

Figure A-4. Comparing simulations to VALTS experiments at impact conditions of 2.4, 3.9, and 5.8 m/s. For each signal, both *ISO and **CORA scores are provided.

Appendix B – Kinematics Envelopes

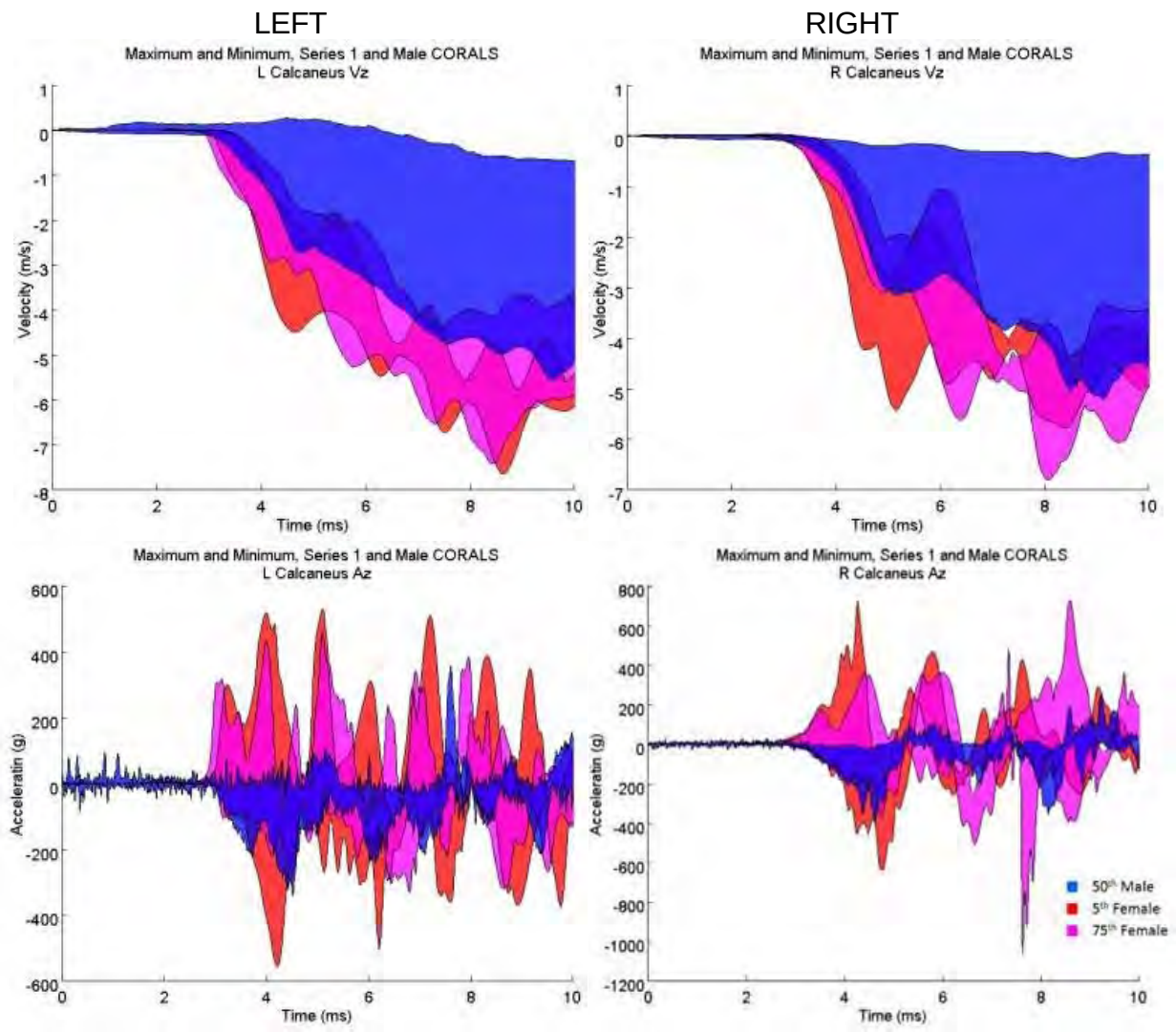

Figure B-1. Male CORALS and Series 1 calcaneus vertical speed and acceleration

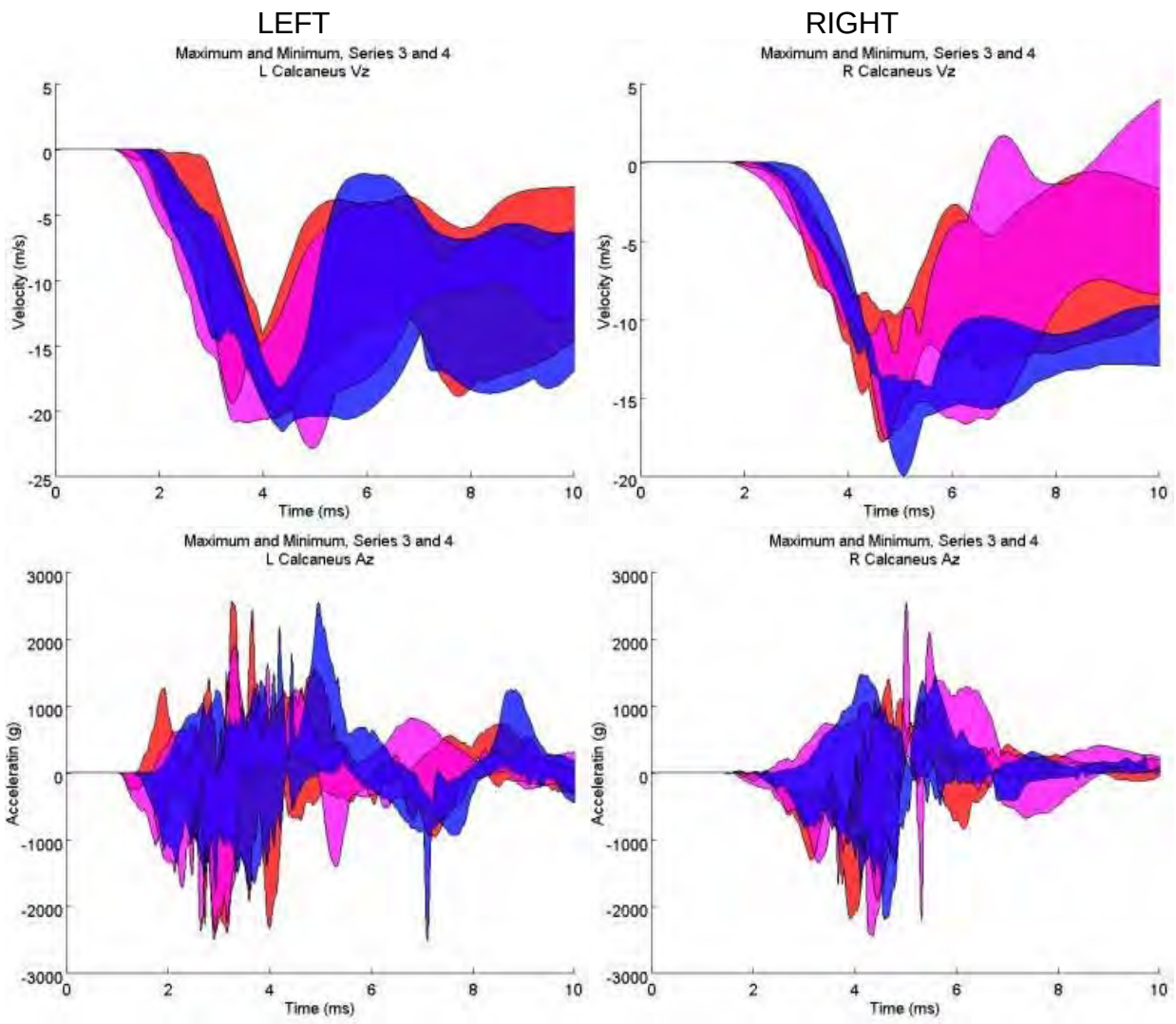

Figure B-2. Series 3 and 4 calcaneus vertical speed and acceleration

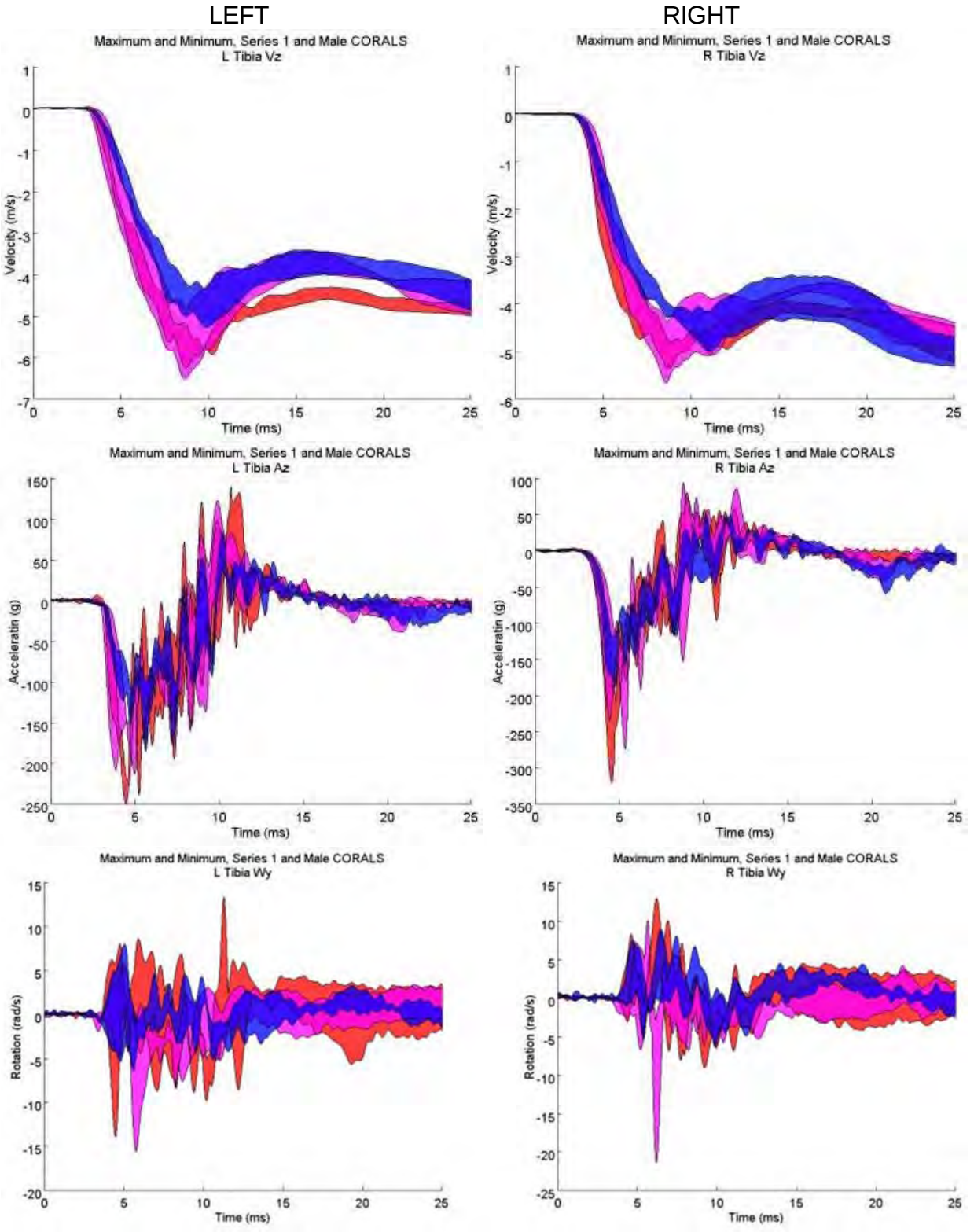

Figure B-3. Male CORALS and Series 1 tibia vertical speed, acceleration, and angular speed in the sagittal plane

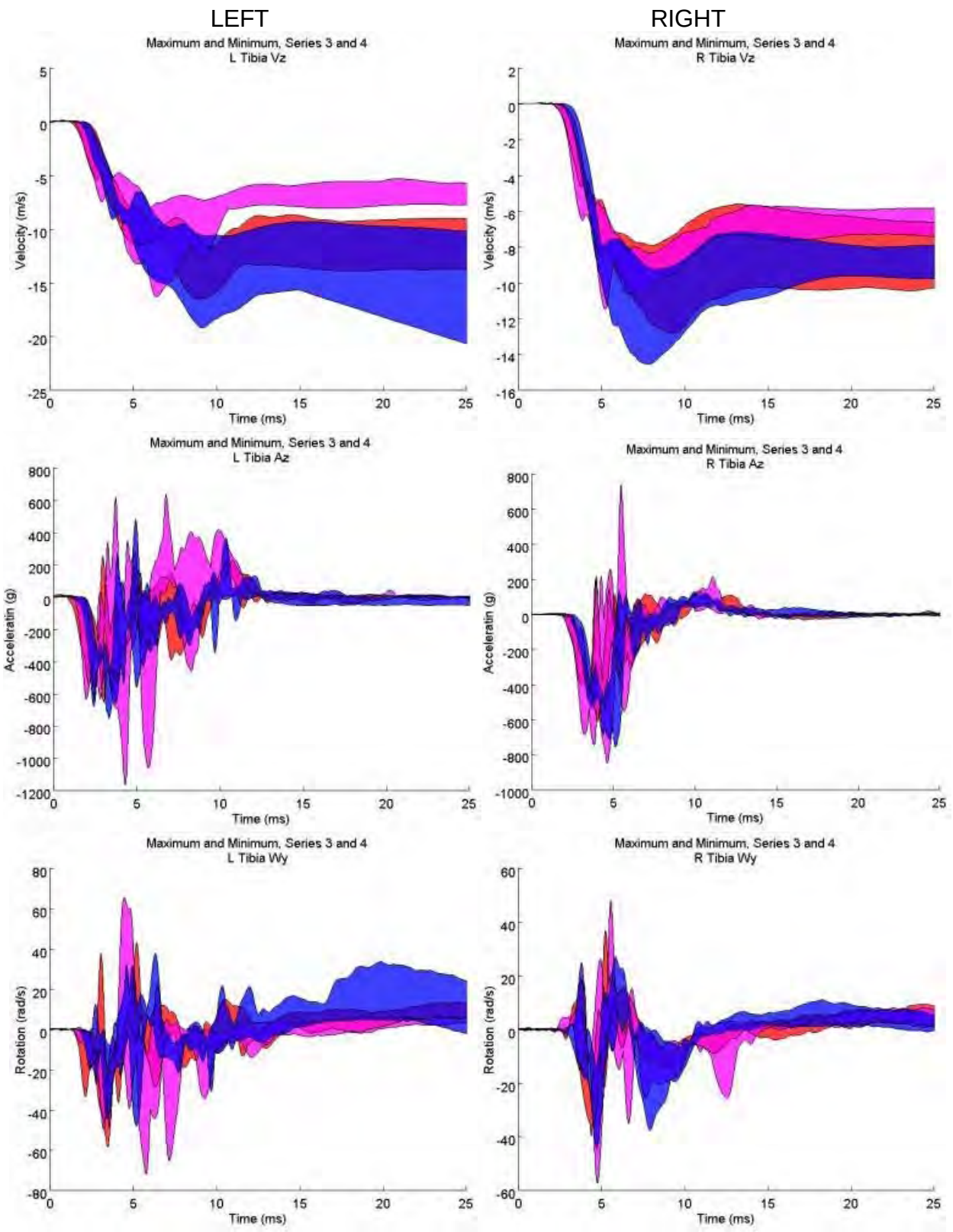

Figure B-4. Series 3 and 4 tibia vertical speed, acceleration, and angular speed in the sagittal plane

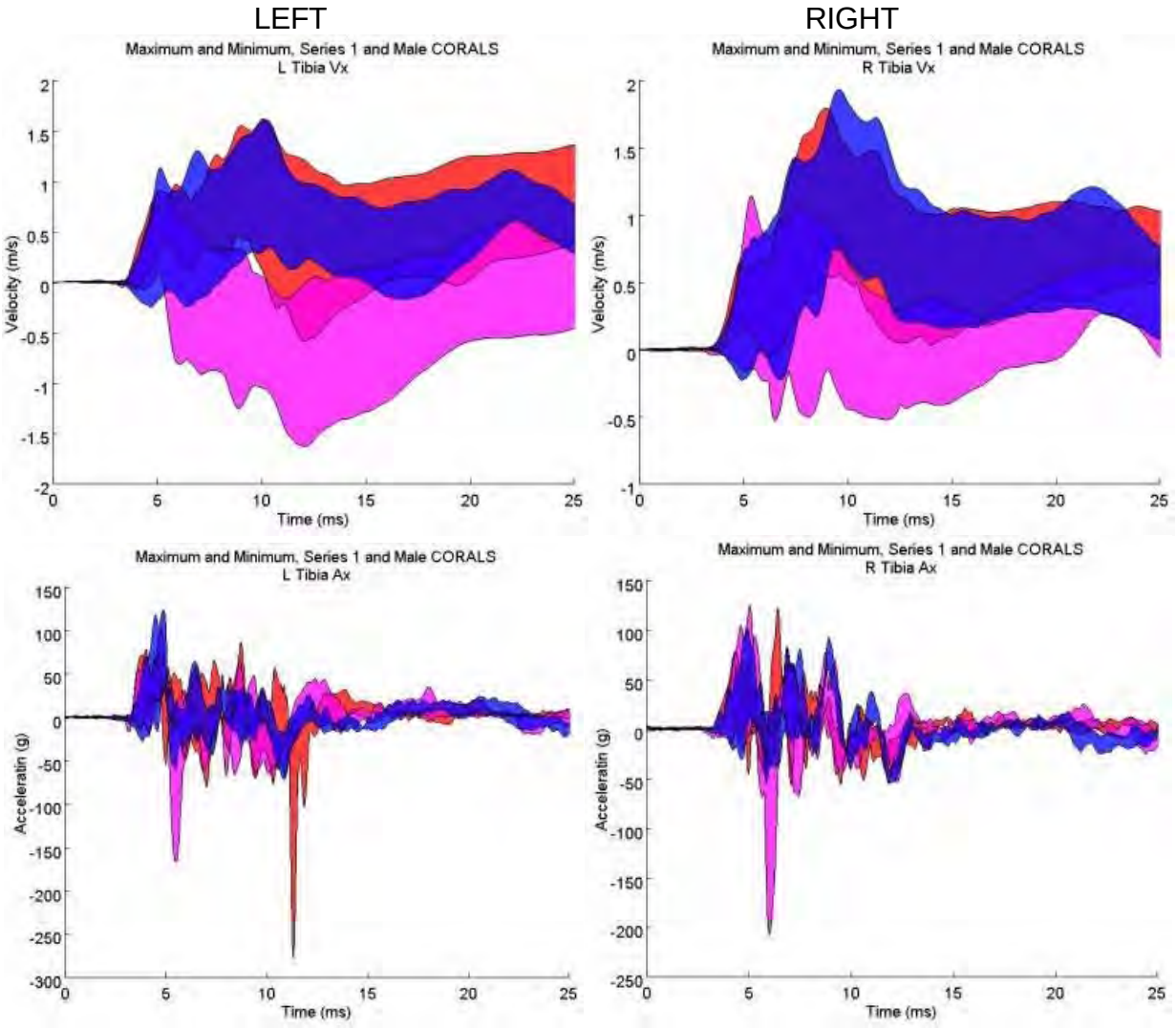

Figure B-5. Male CORALS and Series 1 tibia fore-aft speed and acceleration

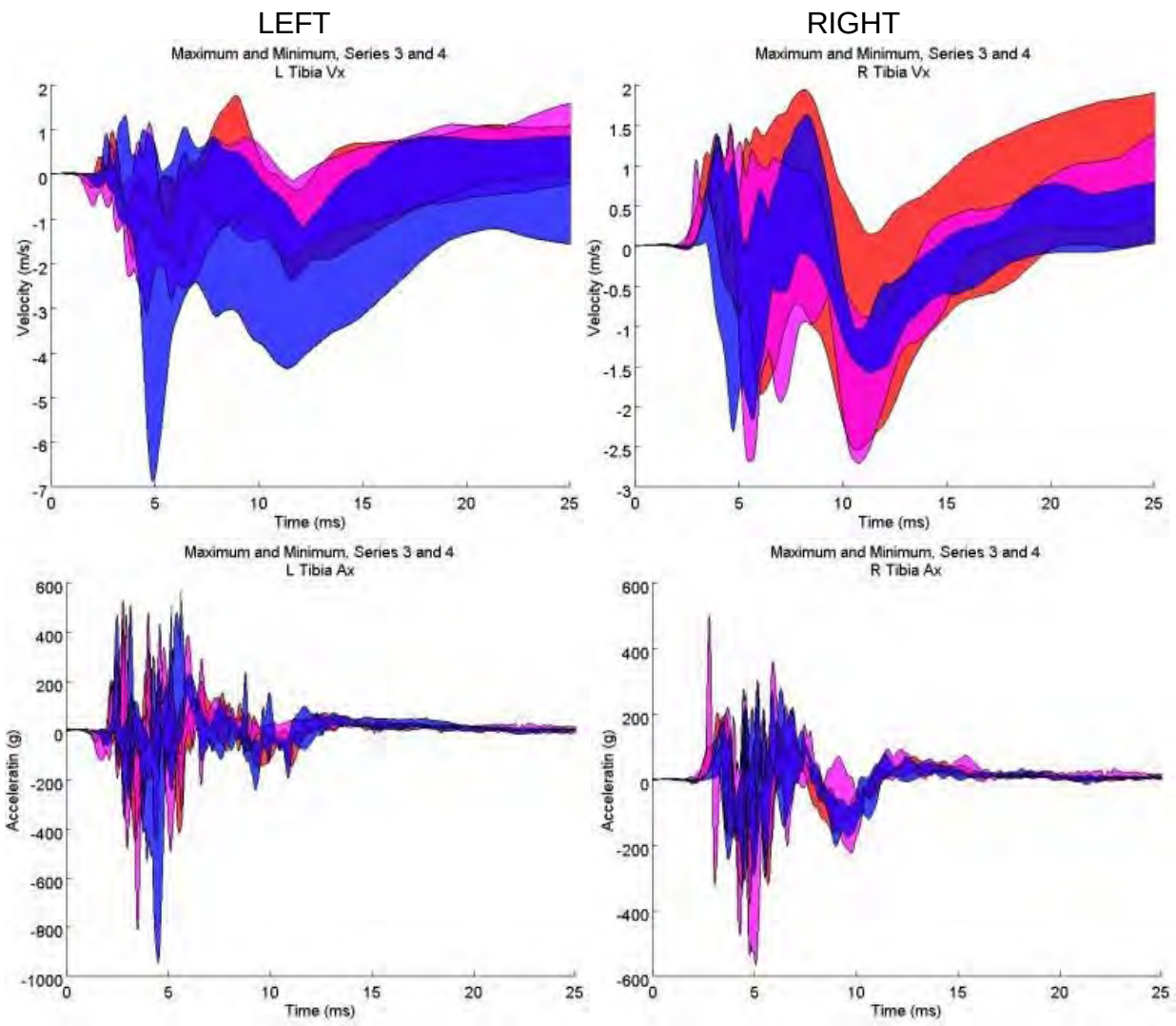

Figure B-6. Series 3 and 4 tibia fore-aft speed and acceleration

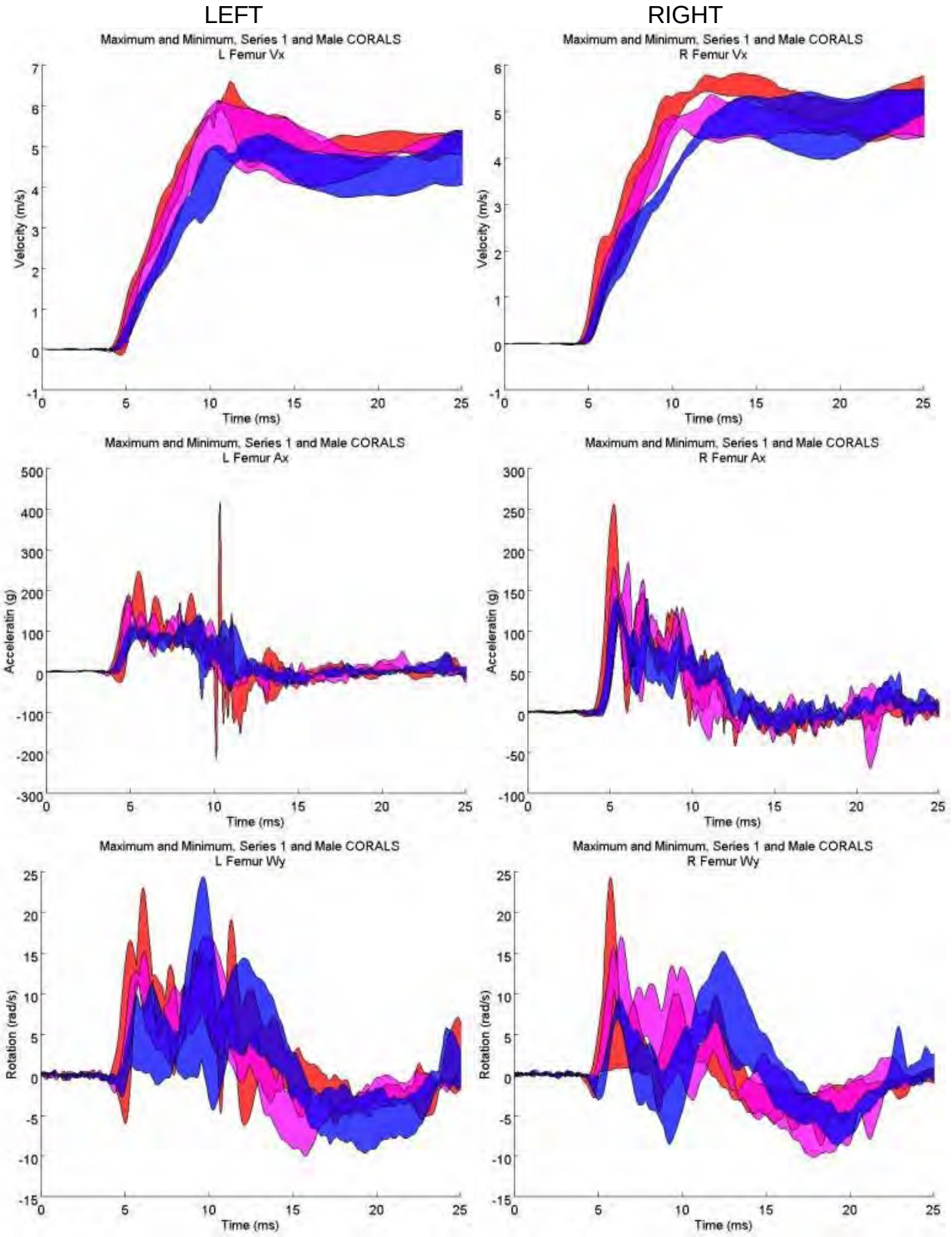

Figure B-7. Male CORALS and Series 1 femur vertical speed, acceleration, and angular speed in the sagittal plane

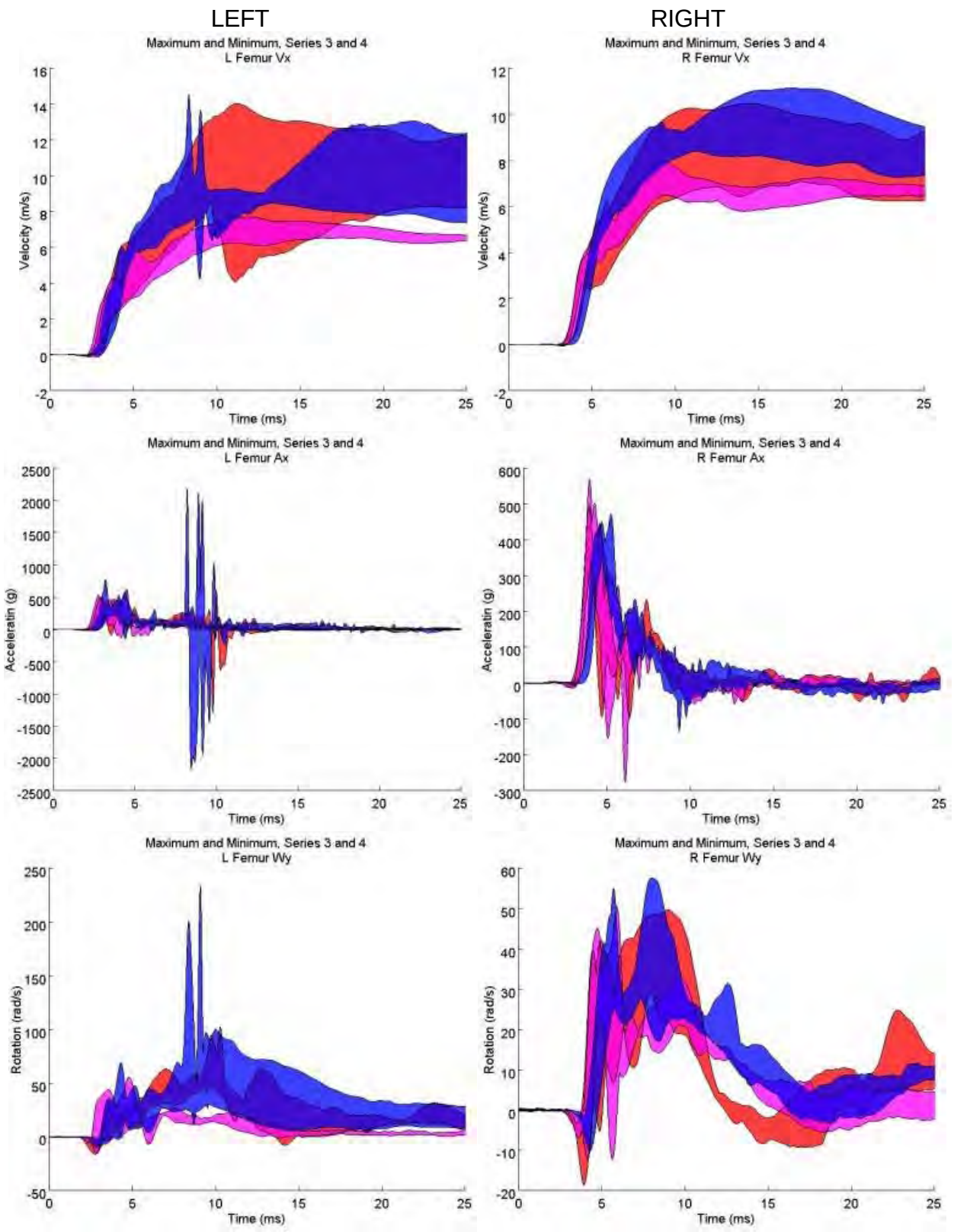

Figure B-8. Series 3 and 4 femur vertical speed, acceleration, and angular speed in the sagittal plane

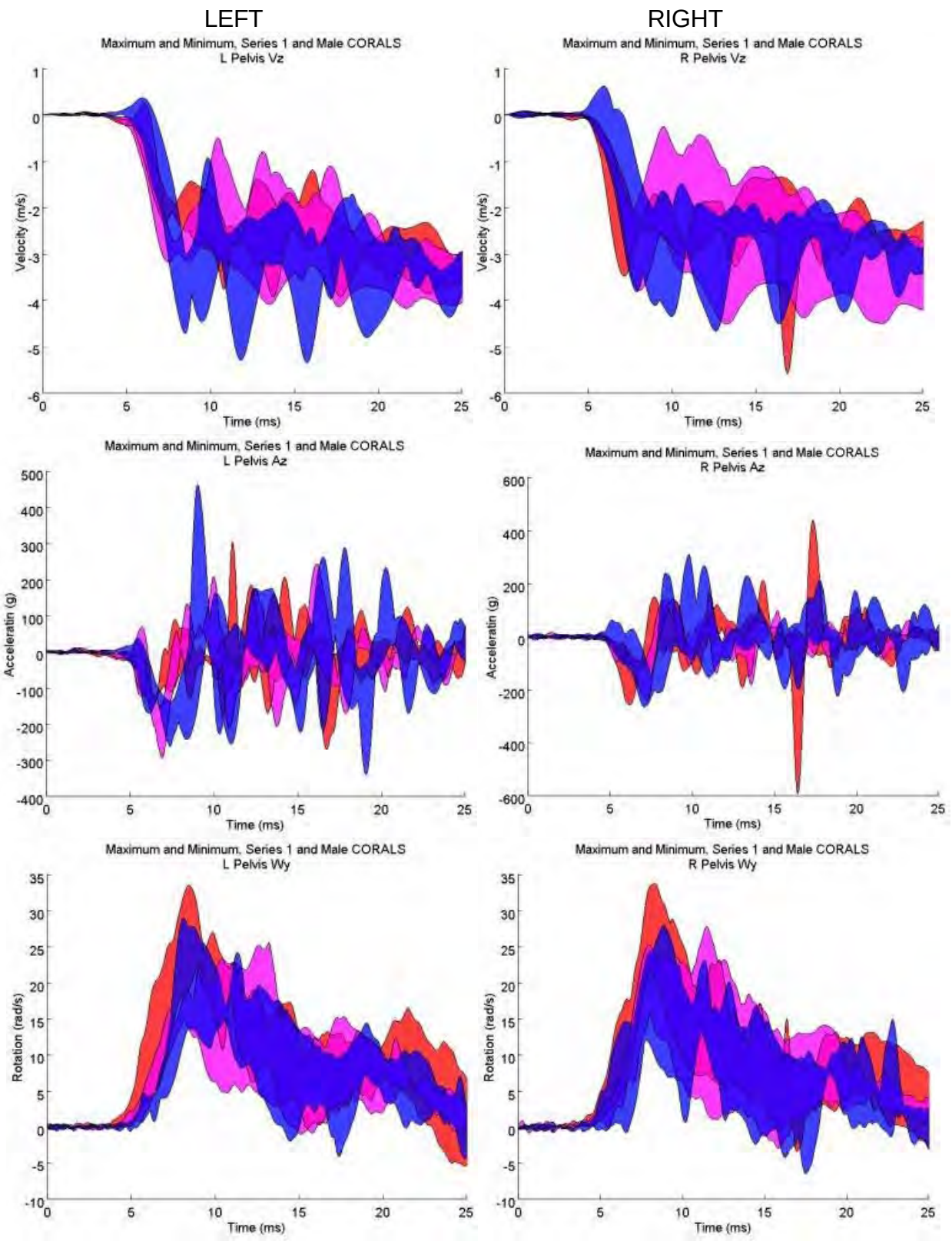

Figure B-9. Male CORALS and Series 1 pelvis vertical speed, acceleration, and angular speed in the sagittal plane

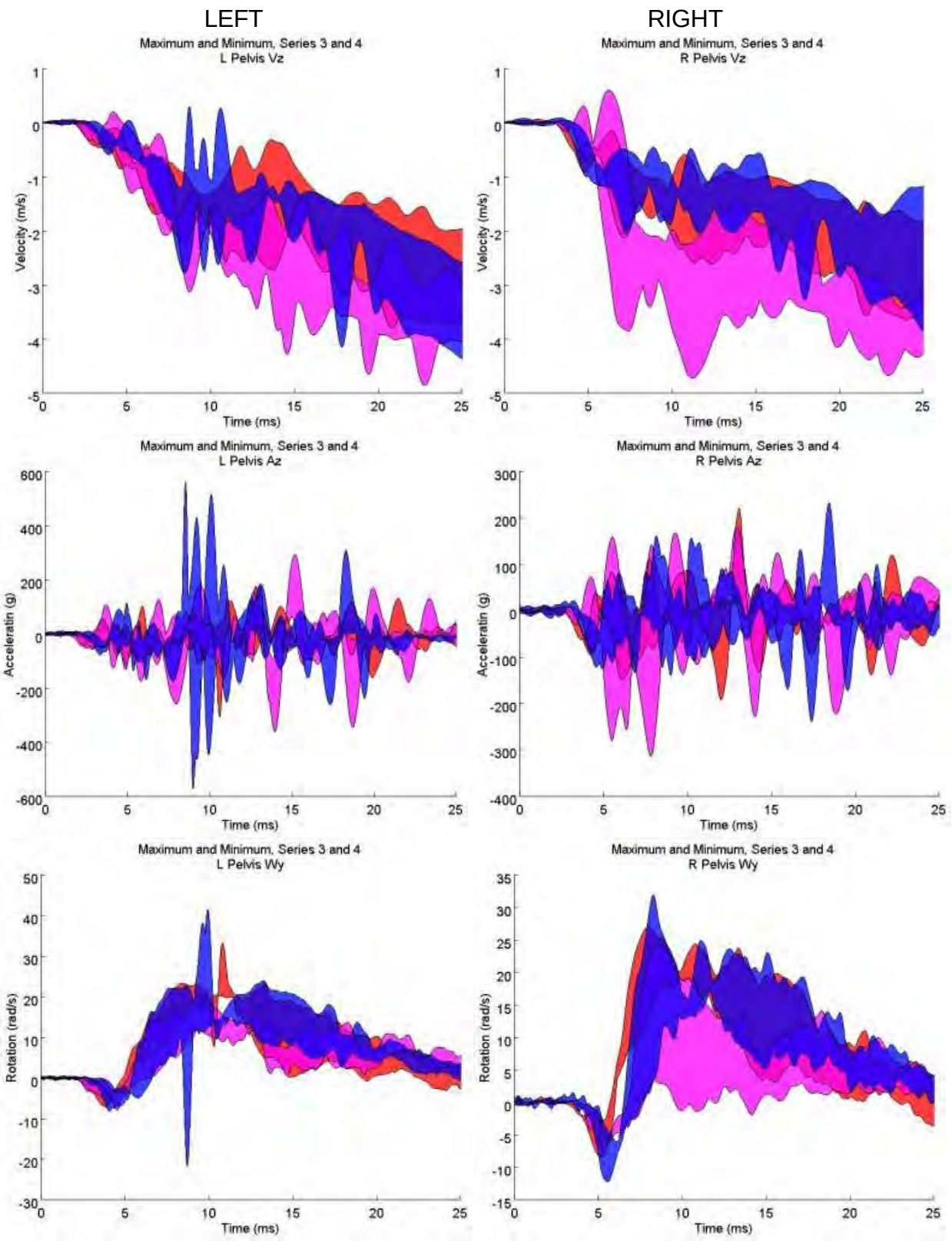

Figure B-10. Series 3 and 4 pelvis vertical speed, acceleration, and angular speed in the sagittal plane

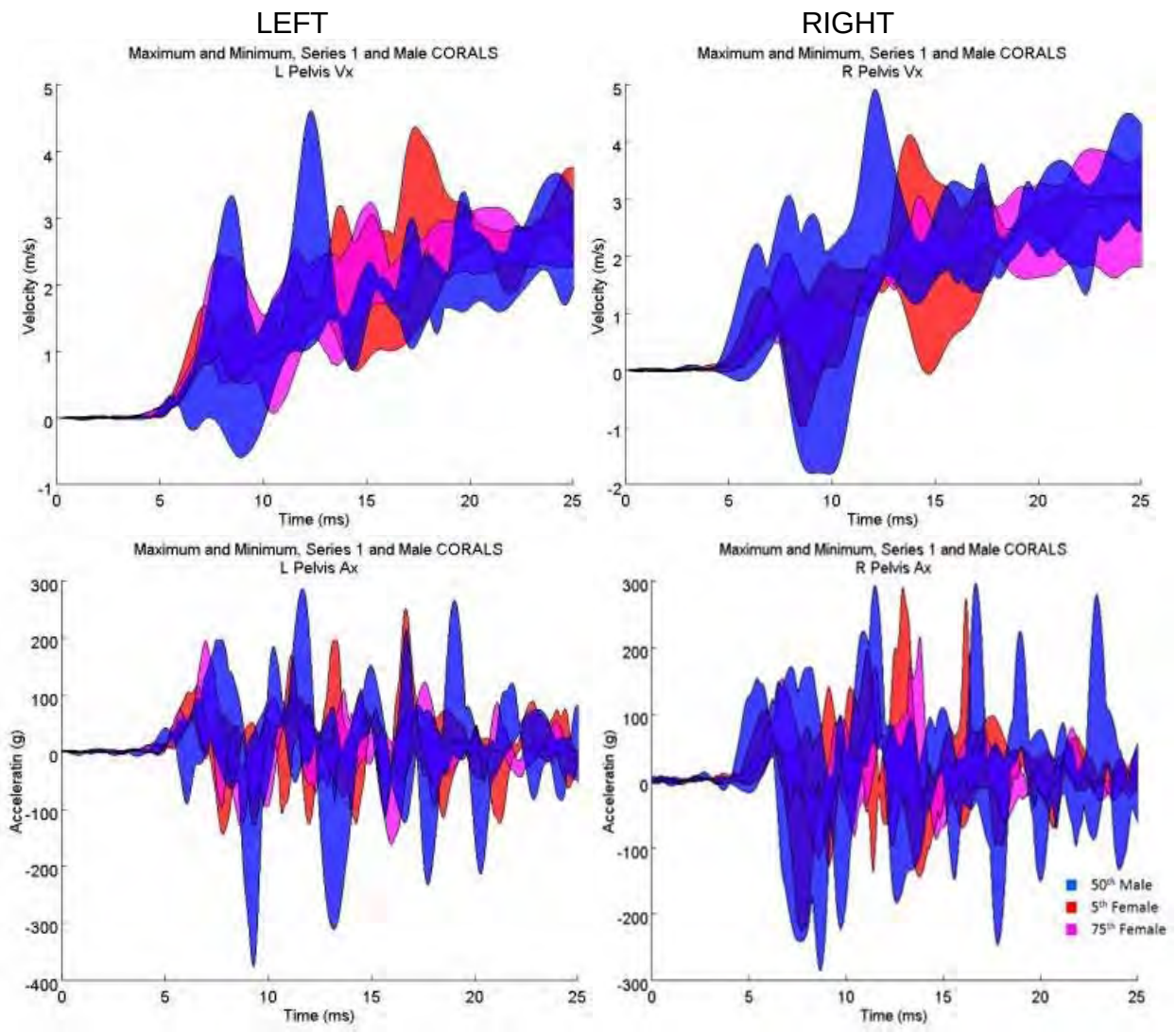

Figure B-11. Male CORALS and Series 1 pelvis fore-aft speed and acceleration

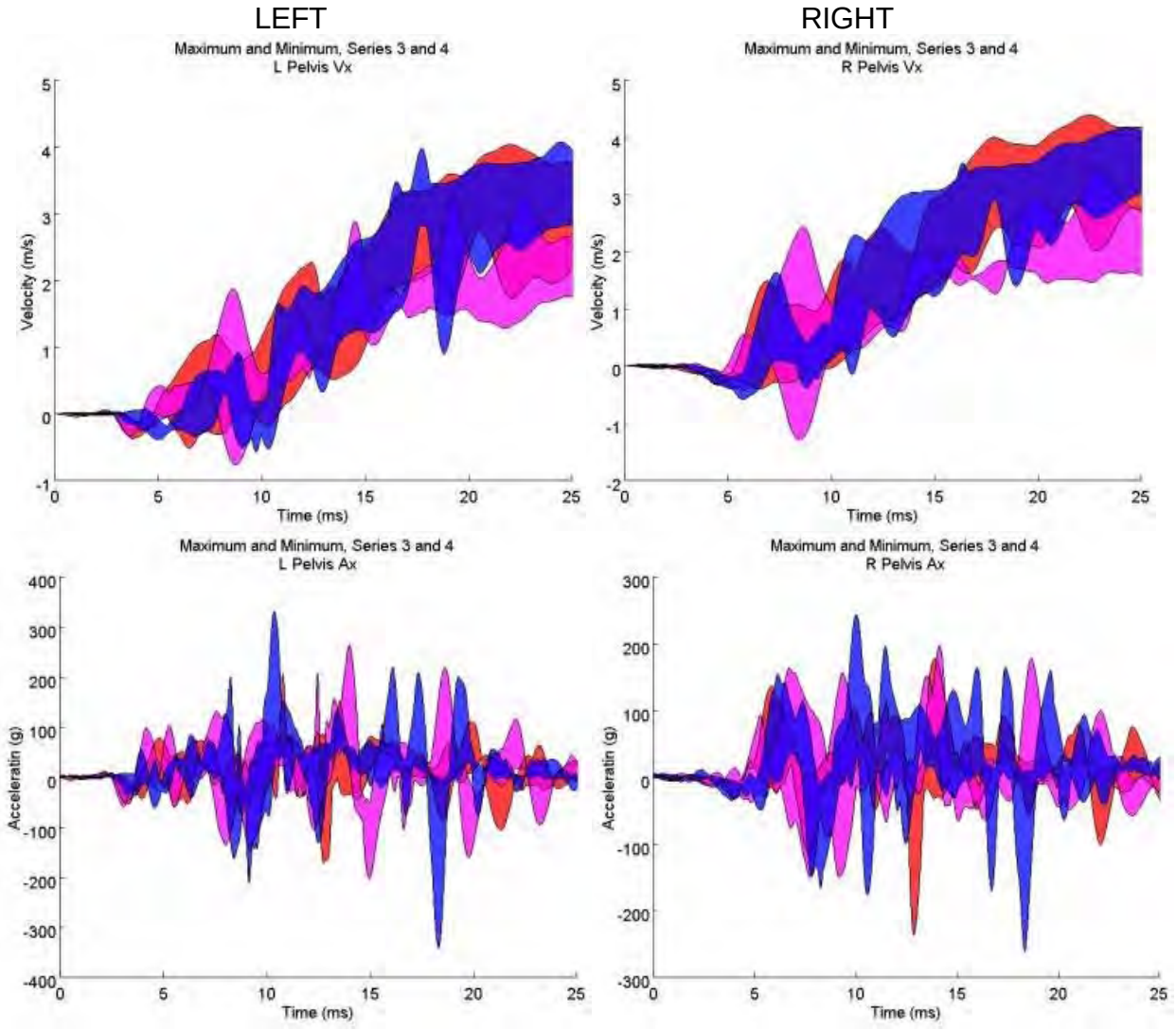

Figure B-12. Series 3 and 4 pelvis fore-aft speed and acceleration

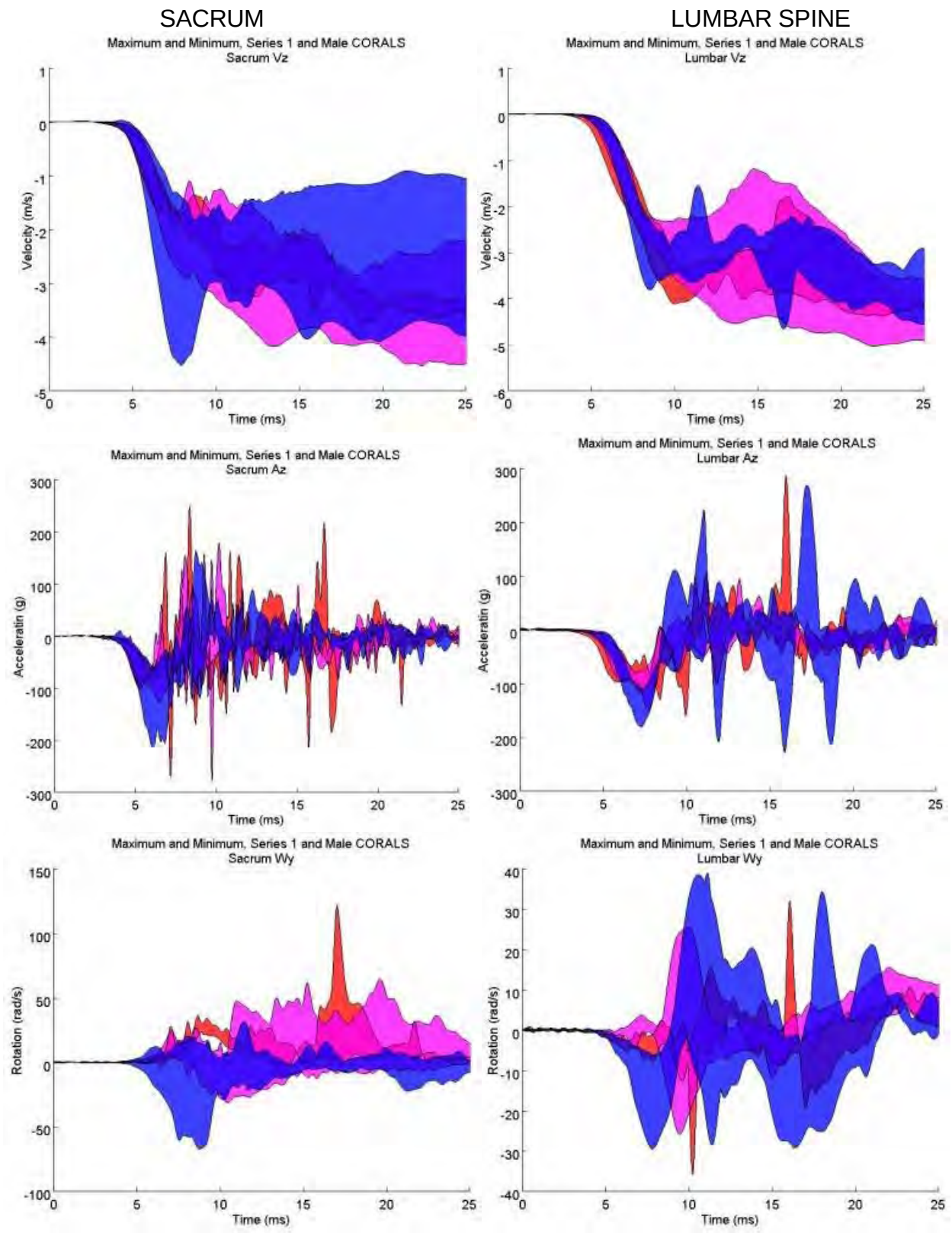

Figure B-13. Male CORALS and Series 1 sacrum and lumbar spine vertical speed, acceleration, and angular speed in the sagittal plane

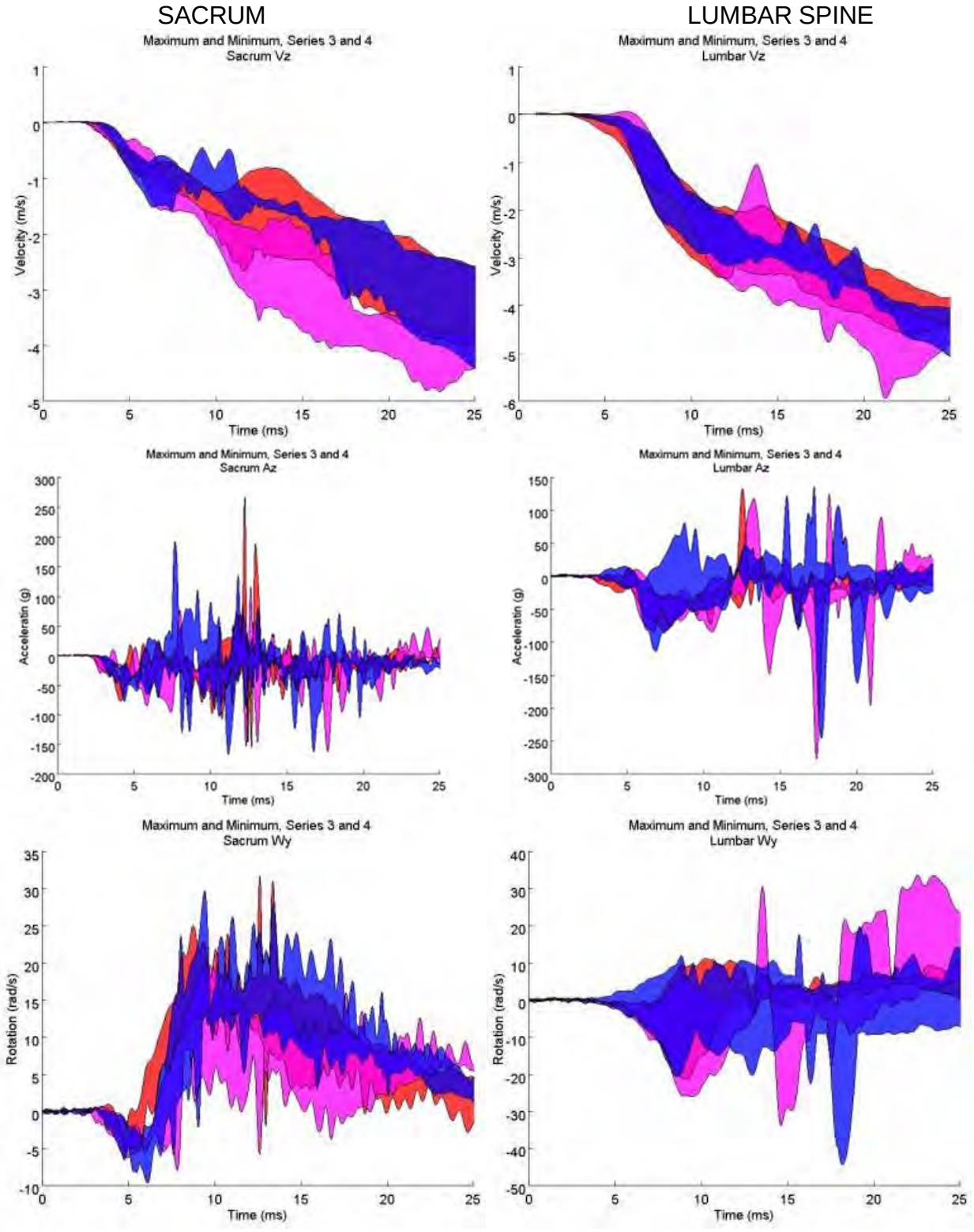

Figure B-14. Series 3 and 4 sacrum and lumbar spine vertical speed, acceleration, and angular speed in the sagittal plane

Appendix C – Kinematics Traces

C.1 TIBIA: vertical acceleration and speed

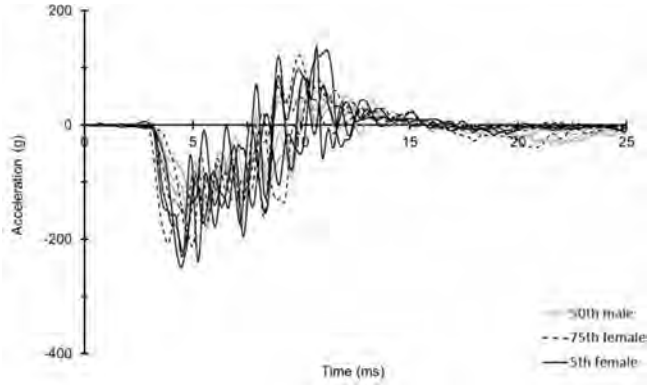

Figure C-1. Male CORALS and Series 1 left distal tibia vertical acceleration (z-direction)

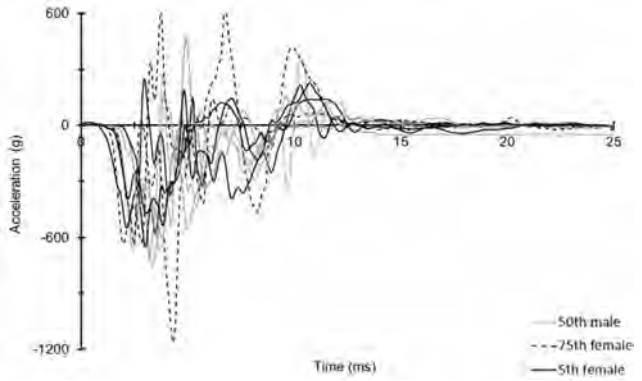

Figure C-2. Series 3 and 4 left distal tibia vertical acceleration (z-direction)

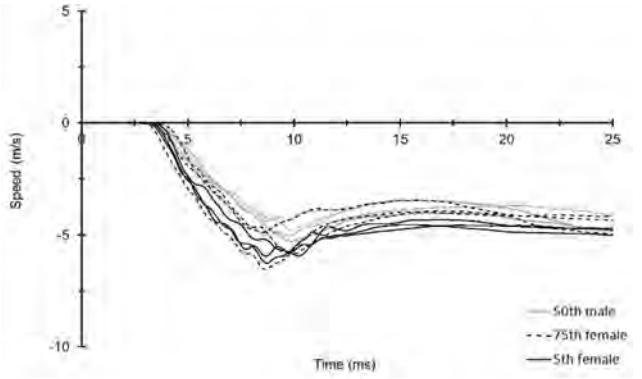

Figure C-3. Male CORALS and Series 1 left distal tibia vertical speed (z-direction)

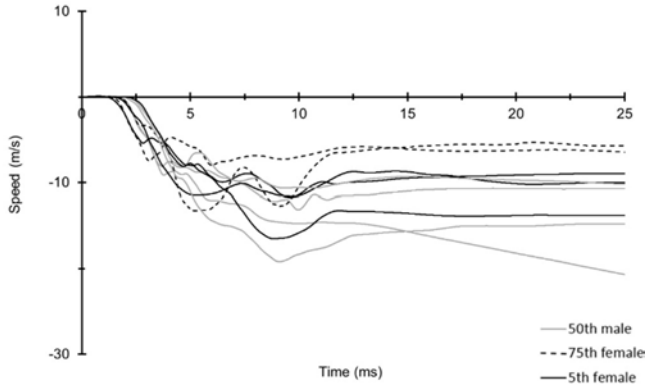

Figure C-4. Series 3 and 4 left distal tibia vertical speed (z-direction)

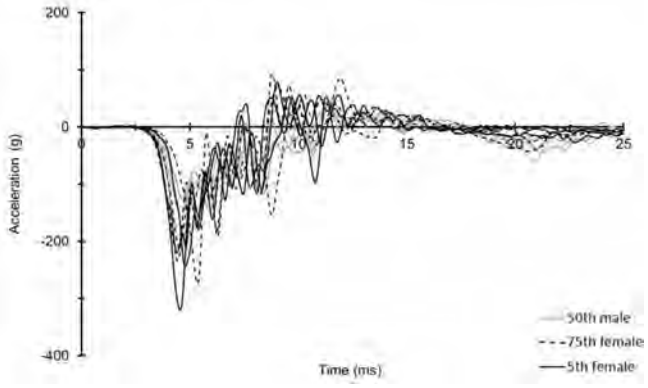

Figure C-5. Male CORALS and Series 1 right distal tibia vertical acceleration (z-direction)

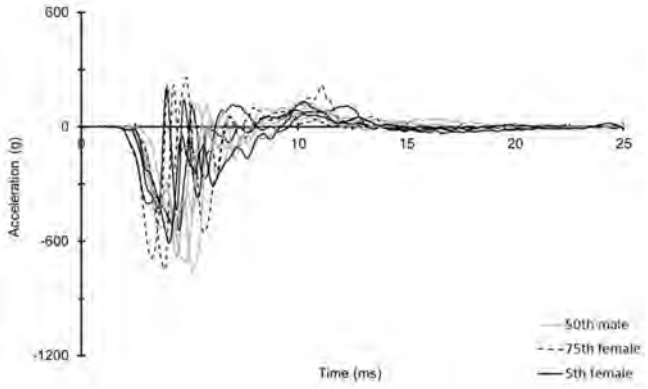

Figure C-6. Series 3 and 4 right distal tibia vertical acceleration (z-direction)

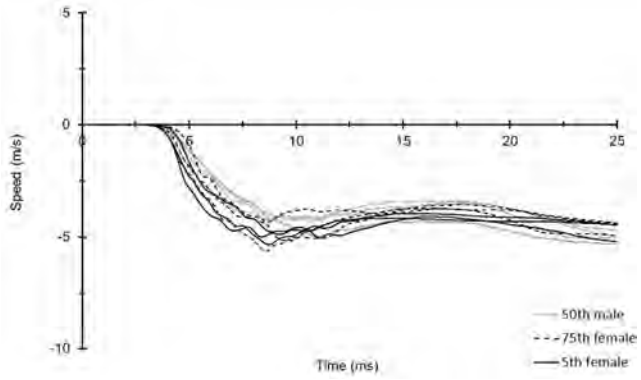

Figure C-7. Male CORALS and Series 1 right distal tibia vertical speed (z-direction)

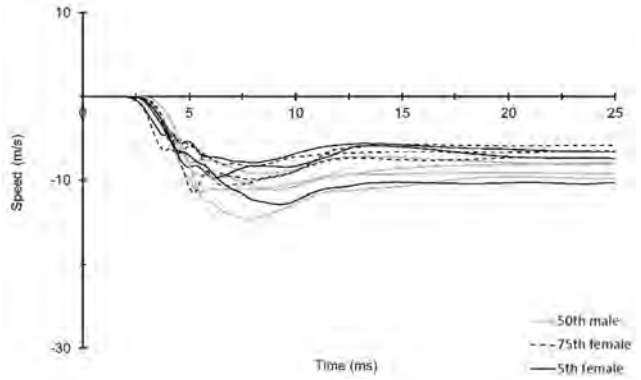

Figure C-8. Series 3 and 4 right distal tibia vertical speed (z-direction)

C.2 TIBIA: fore-aft acceleration and speed

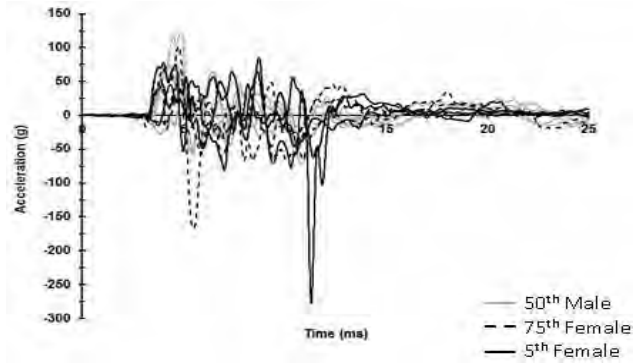

Figure C-9. Male CORALS and Series 1 left distal tibia fore-aft acceleration (x-direction)

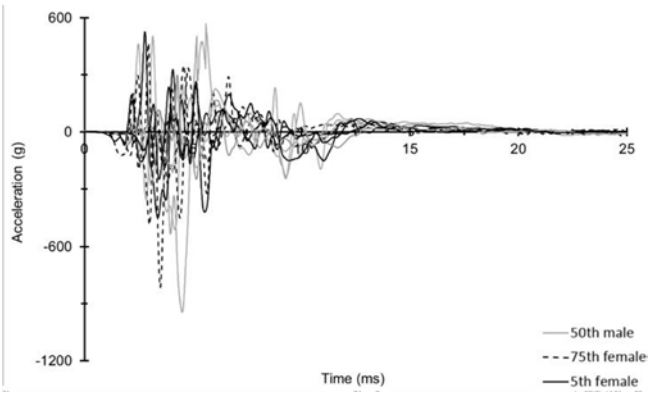

Figure C-10. Series 3 and 4 left distal tibia fore-aft acceleration (x-direction)

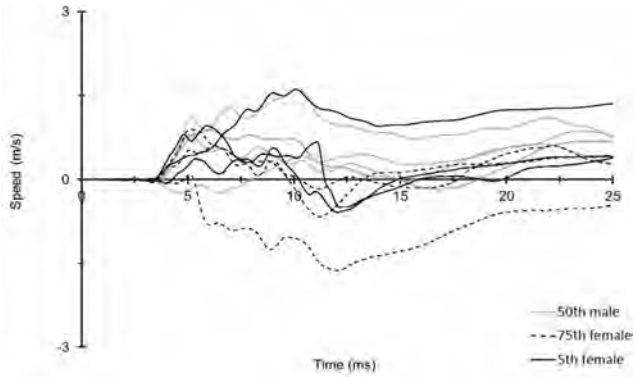

Figure C-11. Male CORALS and Series 1 left distal tibia fore-aft speed (x-direction)

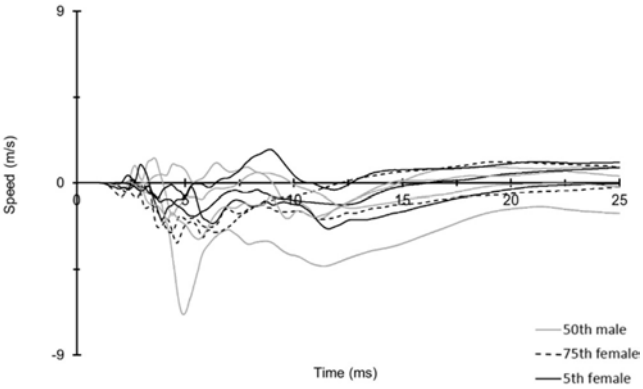

Figure C-12. Series 3 and 4 left distal tibia fore-aft speed (x-direction)

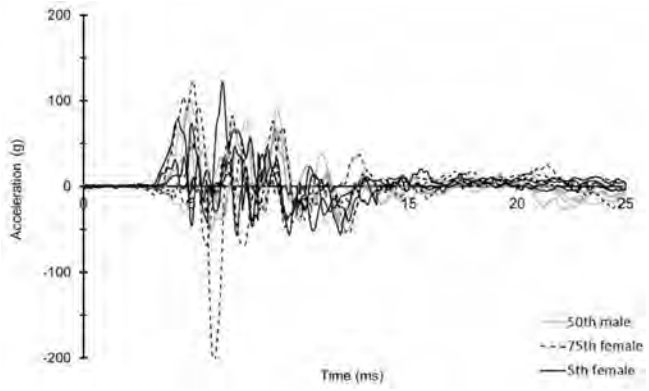

Figure C-13. Male CORALS and Series 1 right distal tibia fore-aft acceleration (x-direction)

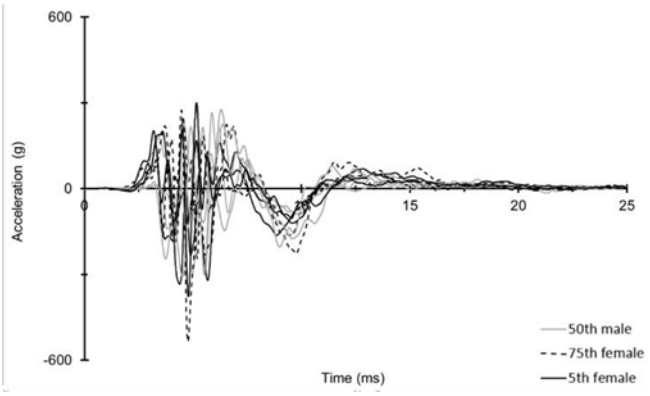

Figure C-14. Series 3 and 4 right distal tibia fore-aft acceleration (x-direction)

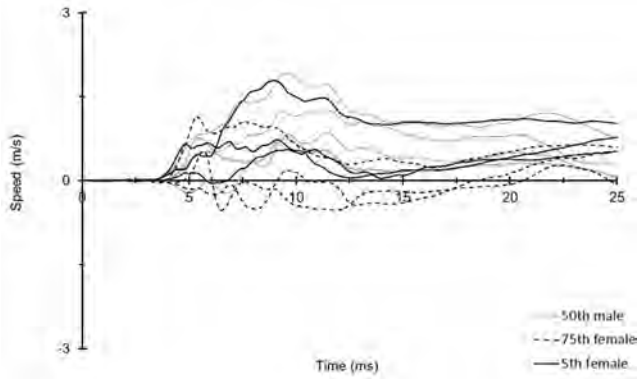

Figure C-15. Male CORALS and Series 1 right distal tibia fore-aft speed (x-direction)

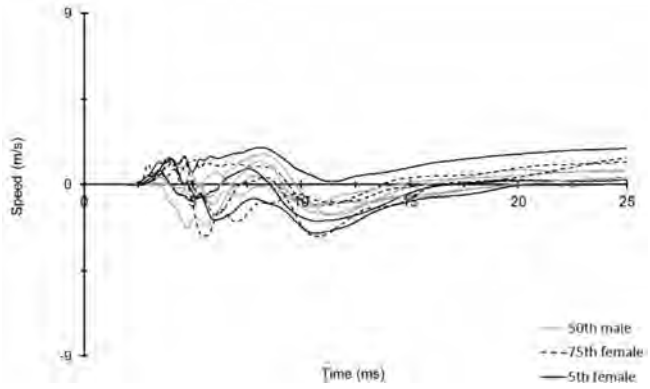

Figure C-16. Series 3 and 4 right distal tibia fore-aft speed (x-direction)

C.3 TIBIA: angular speed in the sagittal plane

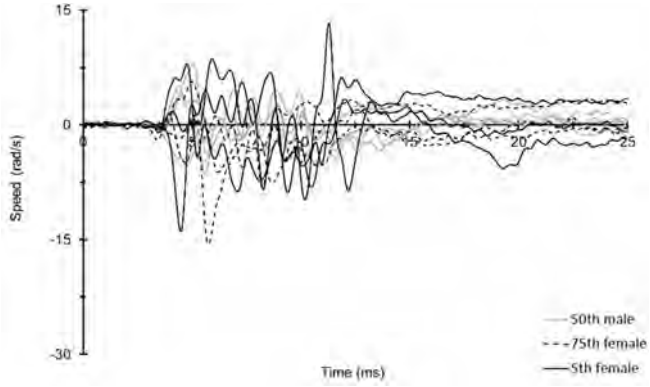

Figure C-17. Male CORALS and Series 1 left distal tibia angular speed in the sagittal plane (along the y-axis)

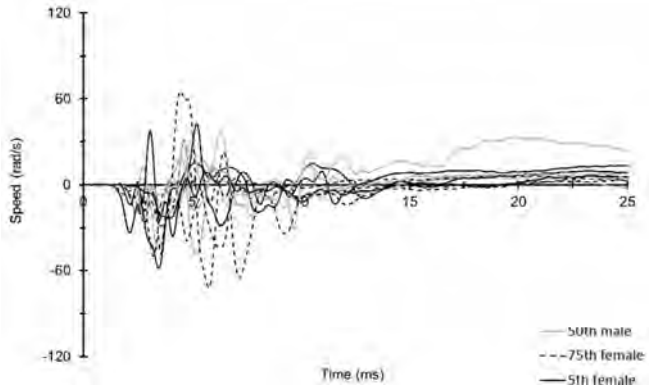

Figure C-18. Series 3 and 4 left distal tibia angular speed in the sagittal plane (along the y-axis)

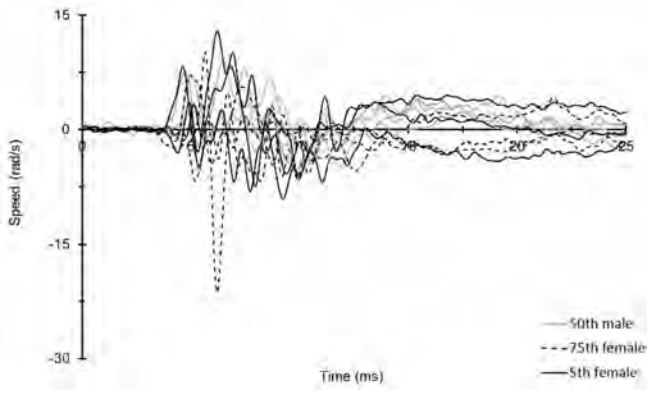

Figure C-19. Male CORALS and Series 1 right distal tibia angular speed in the sagittal plane (along the y-axis)

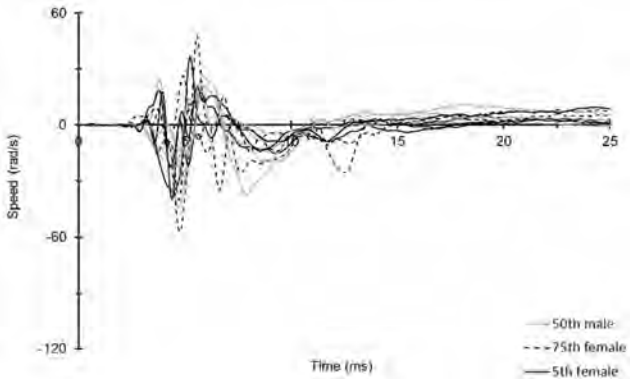

Figure C-20. Series 3 and 4 right distal tibia angular speed in the sagittal plane (along the y-axis)

C.4 FEMUR: vertical acceleration and speed

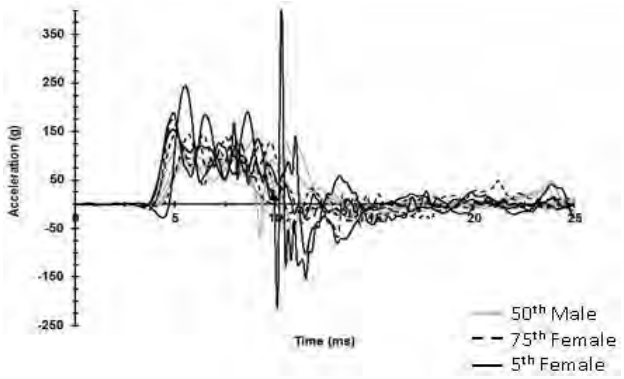

Figure C-21. Male CORALS and Series 1 left distal femur vertical acceleration (x-direction)

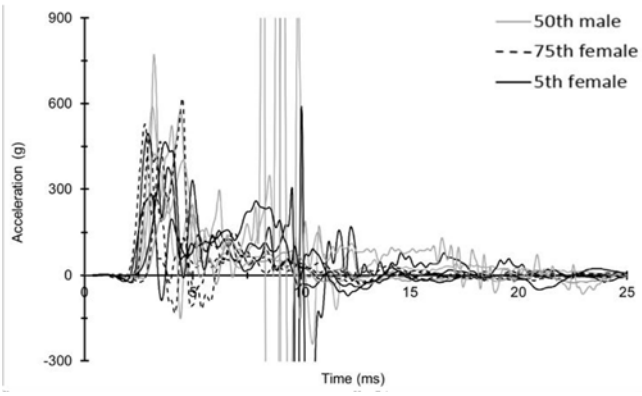

Figure C-22. Series 3 and 4 left distal femur vertical acceleration (x-direction)

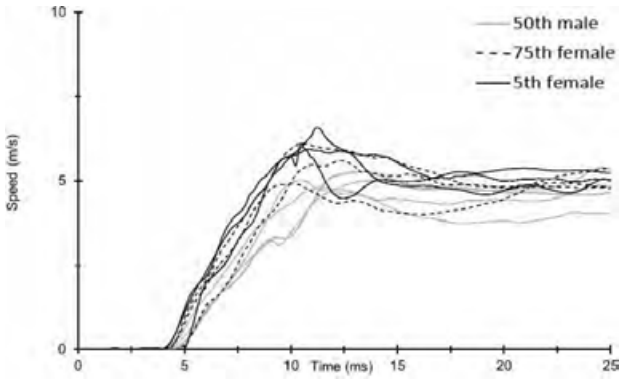

Figure C-23. Male CORALS and Series 1 left distal femur vertical speed (x-direction)

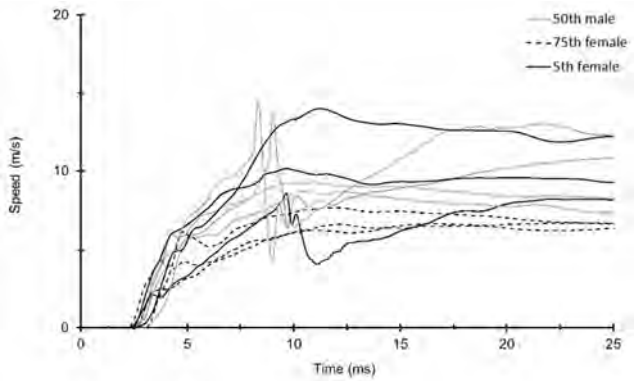

Figure C-24. Series 3 and 4 left distal femur vertical acceleration (x-direction). The three traces with noticeable drops in speed are the three cases with femur fractures.

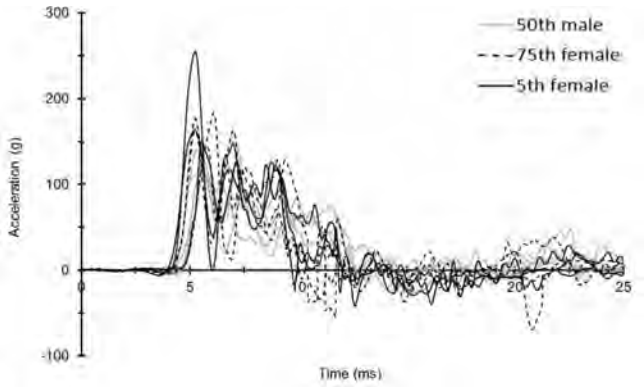

Figure C-25. Male CORALS and Series 1 right distal femur vertical acceleration (x-direction)

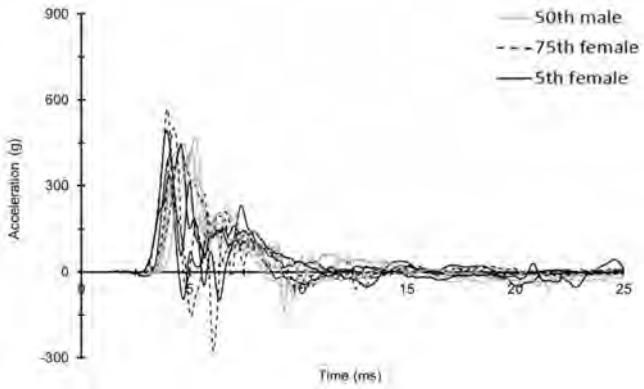

Figure C-26. Series 3 and 4 right distal femur vertical acceleration (x-direction)

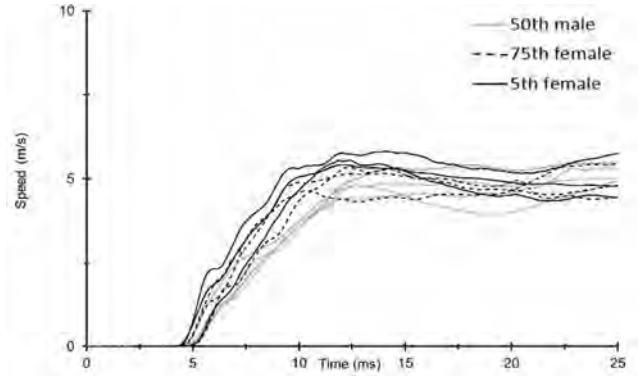

Figure C-27. Male CORALS and Series 1 right distal femur vertical speed (x-direction)

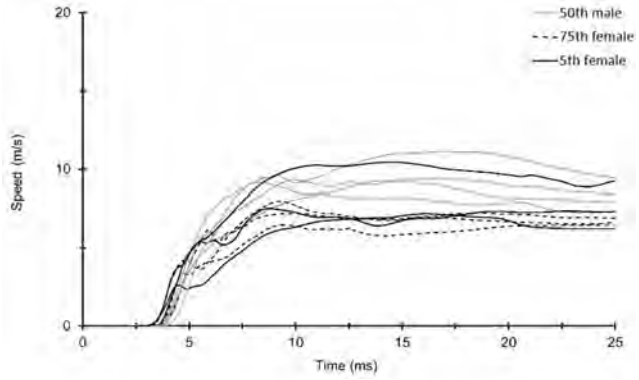

Figure C-28. Series 3 and 4 right distal femur vertical speed (x-direction)

C.5 FEMUR: angular speed in the sagittal plane

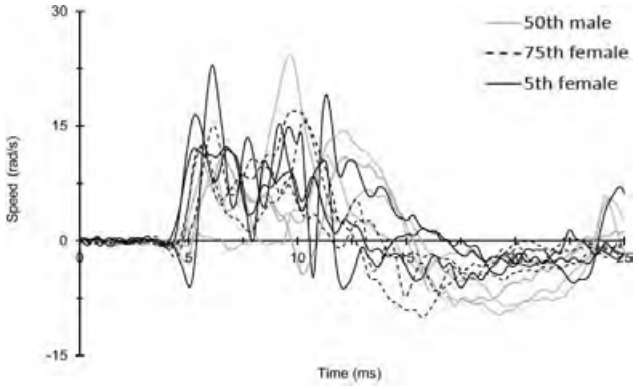

Figure C-29. Male CORALS and Series 1 left distal femur rotational speed in the sagittal plane (along the y-axis)

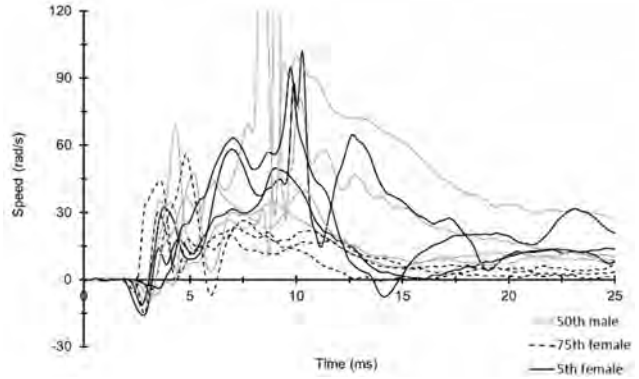

Figure C-30. Series 3 and 4 left distal femur rotational speed in the sagittal plane (along the y-axis)

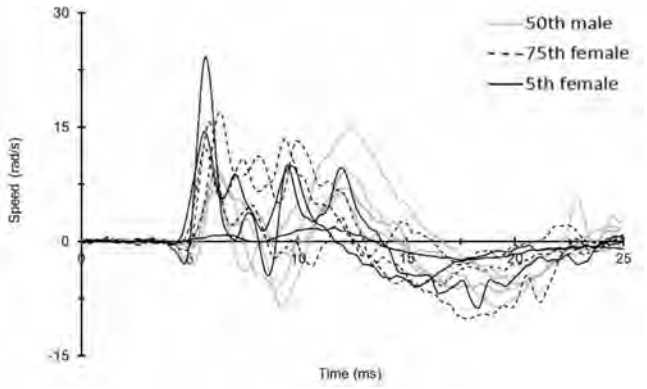

Figure C-31. Male CORALS and Series 1 right distal femur rotational speed in the sagittal plane (along the y-axis)

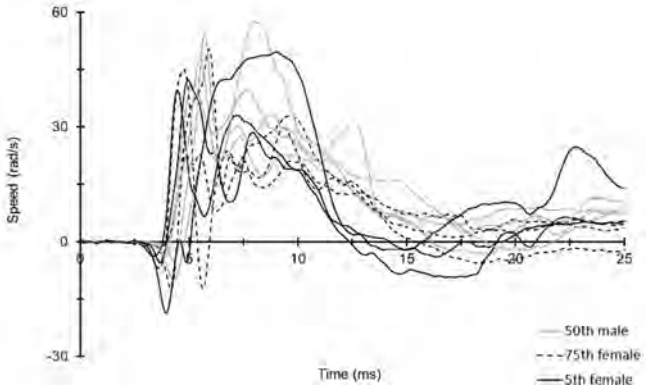

Figure C-32. Series 3 and 4 right distal femur rotational speed in the sagittal plane (along the y-axis)

C.6 PELVIS: vertical acceleration and speed

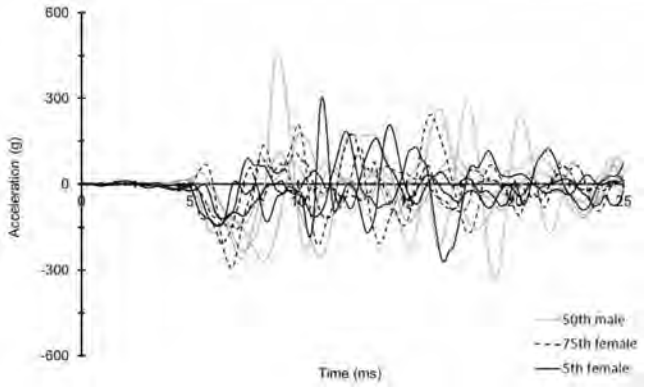

Figure C-33. Male CORALS and Series 1 left side pelvis vertical acceleration (z-direction)

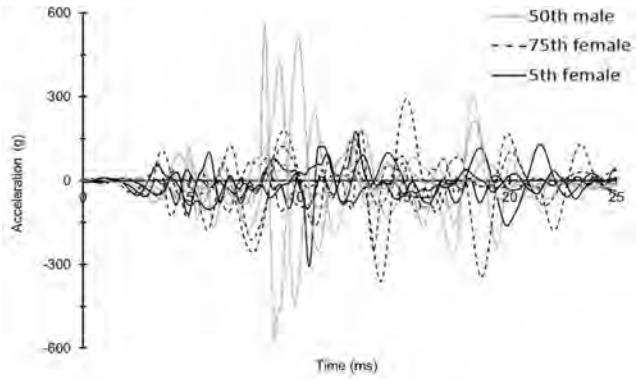

Figure C-34. Series 3 and 4 left side pelvis vertical acceleration (z-direction)

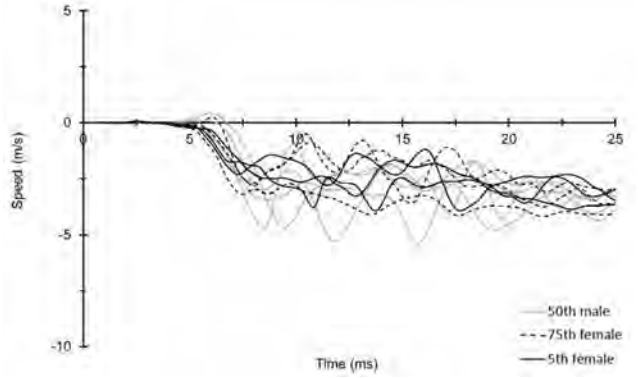

Figure C-35. Male CORALS and Series 1 left side vertical speed (z-direction)

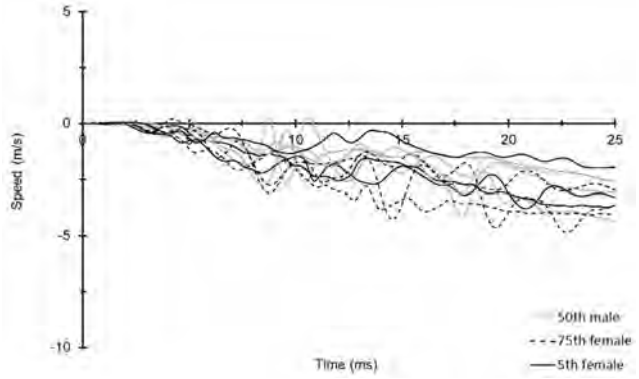

Figure C-36. Series 3 and 4 left side pelvis vertical speed (z-direction)

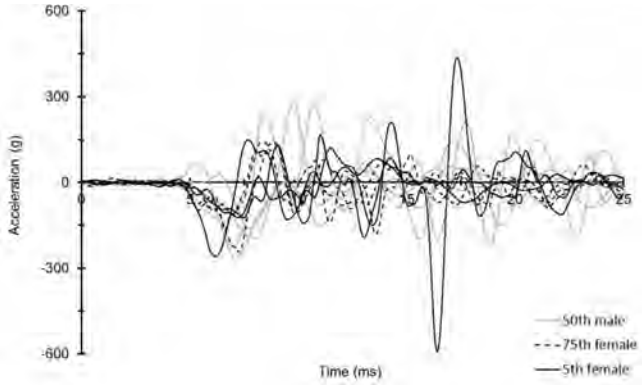

Figure C-37. Male CORALS and Series 1 right side pelvis vertical acceleration (z-direction)

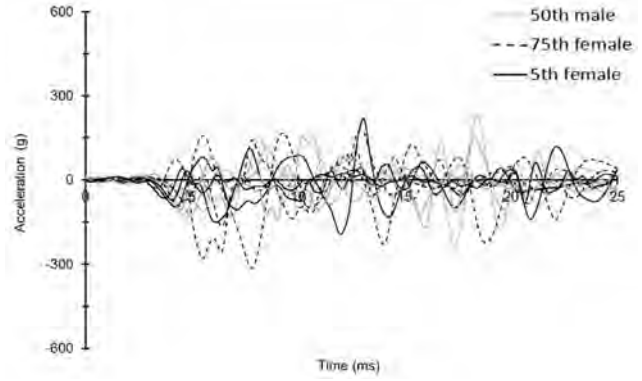

Figure C-38. Series 3 and 4 right side pelvis vertical acceleration (z-direction)

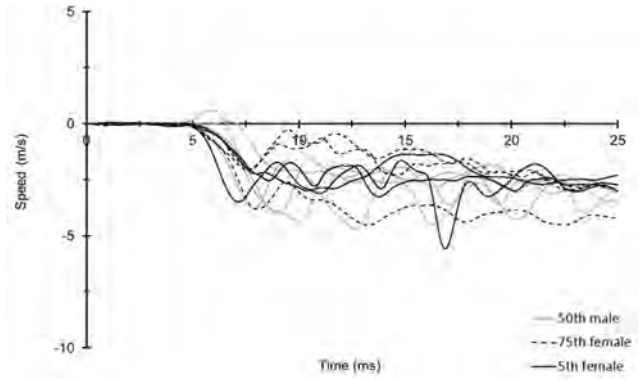

Figure C-39. Male CORALS and Series 1 right side pelvis vertical speed (z-direction)

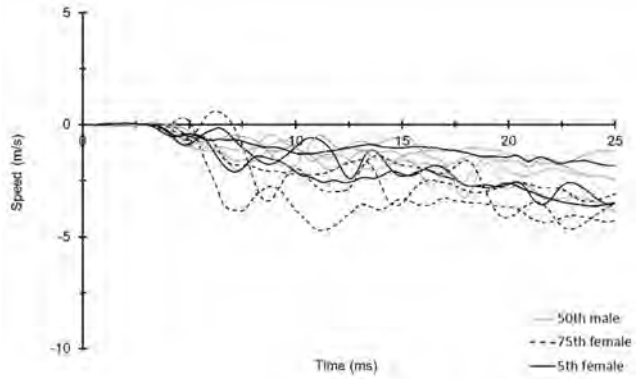

Figure C-40. Series 3 and 4 right side pelvis vertical speed (z-direction)

C.7 PELVIS: fore-aft acceleration and speed

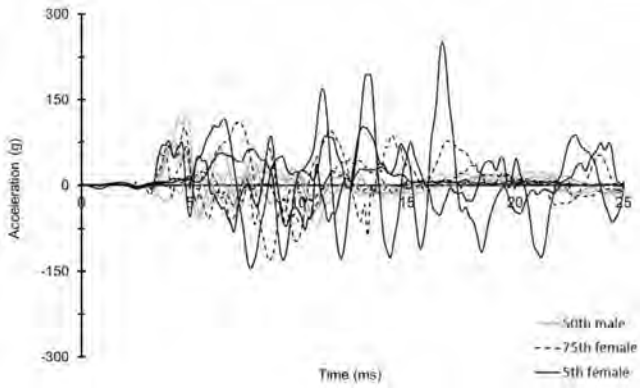

Figure C-41. Male CORALS and Series 1 left side pelvis fore-aft acceleration (x-direction)

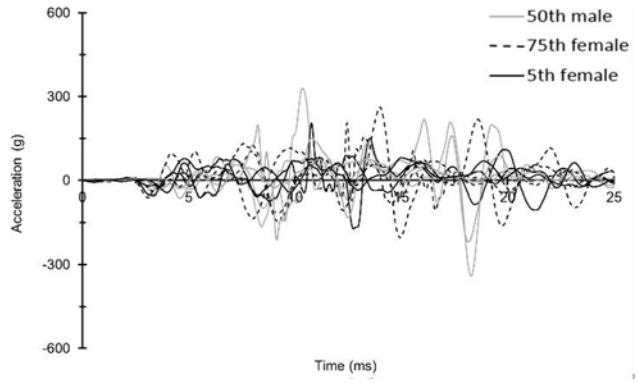

Figure C-42. Series 3 and 4 left side pelvis fore-aft acceleration (x-direction)

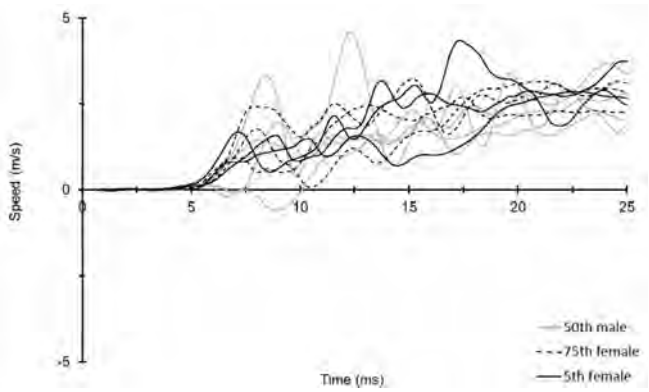

Figure C-43. Male CORALS and Series 1 left side pelvis fore-aft speed (x-direction)

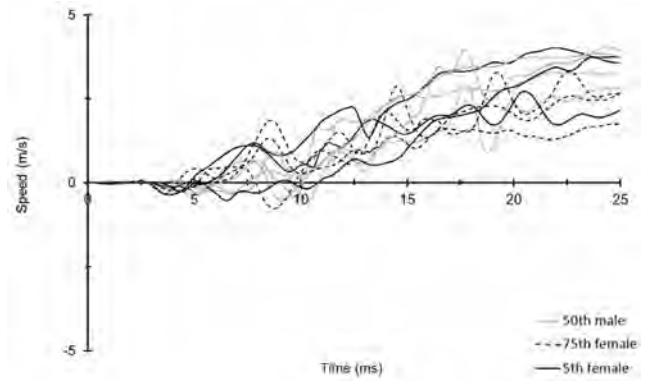

Figure C-43. Series 3 and 4 left side pelvis fore-aft speed (x-direction)

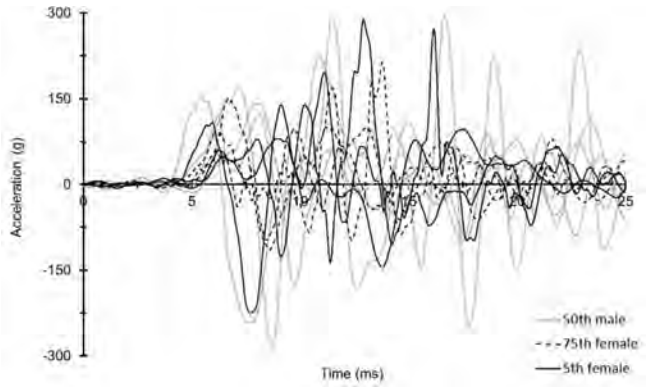

Figure C-44. Male CORALS and Series 1 right side pelvis fore-aft acceleration (x-direction)

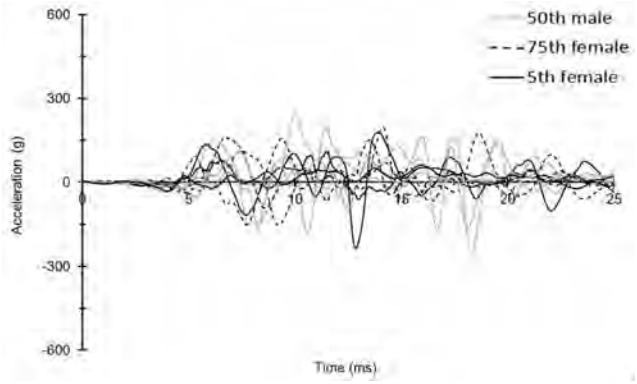

Figure C-45. Series 3 and 4 right side pelvis fore-aft acceleration (x-direction)

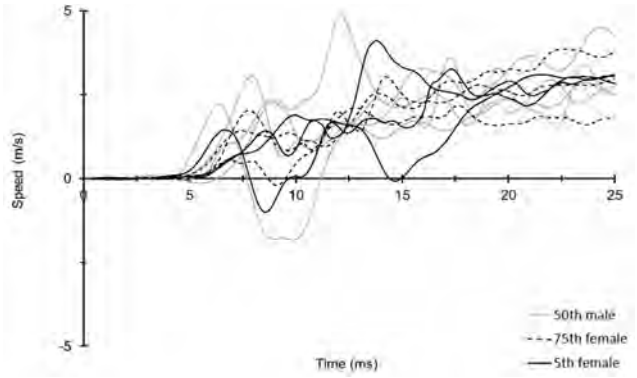

Figure C-46. Male CORALS and Series 1 right side pelvis fore-aft speed (x-direction)

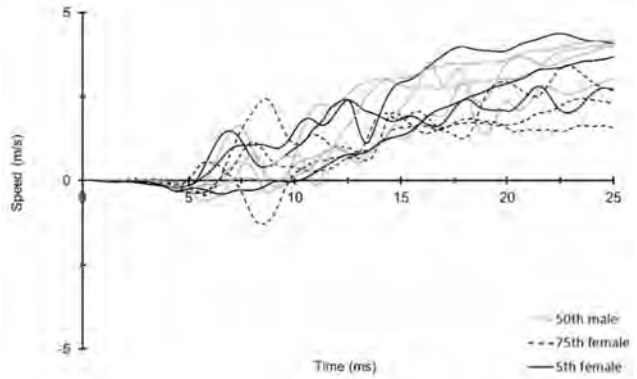

Figure C-47. Series 3 and 4 right side pelvis fore-aft speed (x-direction)

C.8 PELVIS: angular speed in the sagittal plane

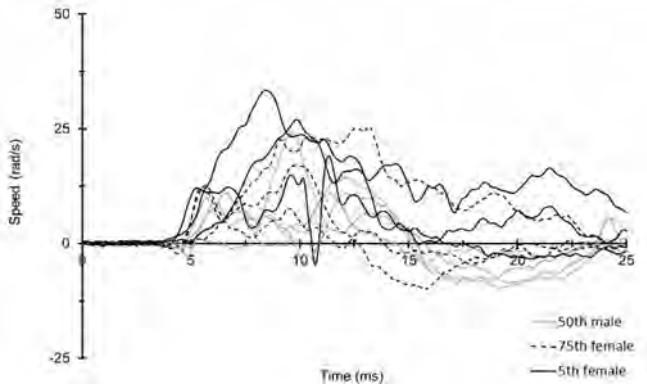

Figure C-48. Male CORALS and Series 1 left side pelvis angular speed in the sagittal plane (about the y-axis)

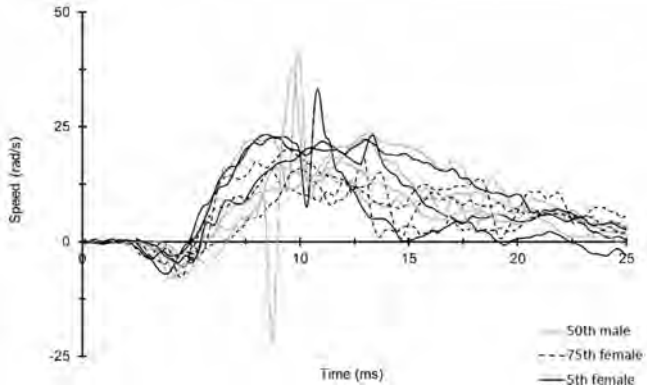

Figure C-49. Series 3 and 4 left side pelvis rotational speed in the sagittal plane (about the y-axis)

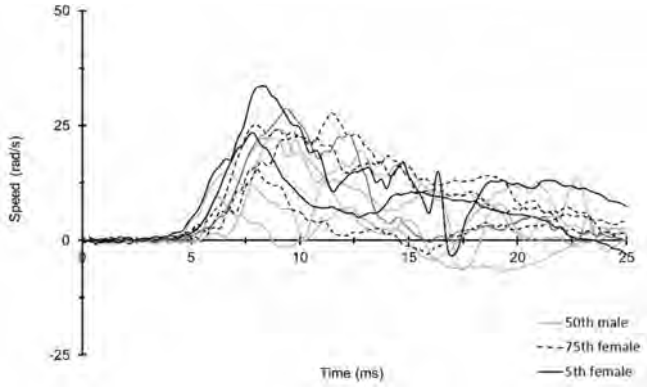

Figure C-50. Male CORALS and Series 1 right side pelvis angular speed in the sagittal plane (about the y-axis)

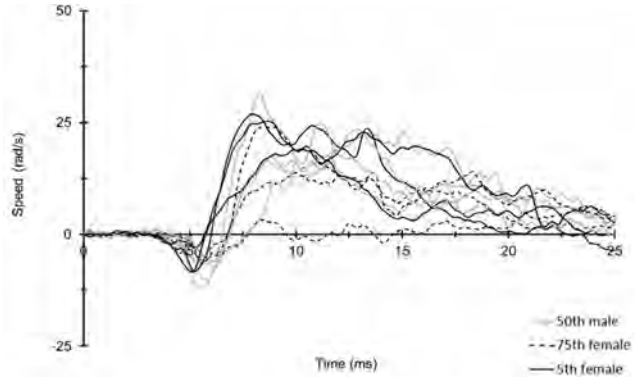

Figure C-51. Series 3 and 4 right side pelvis rotational speed in the sagittal plane (about the y-axis)

C.9 LUMBAR SPINE: vertical acceleration, vertical speed, and angular speed in the sagittal plane

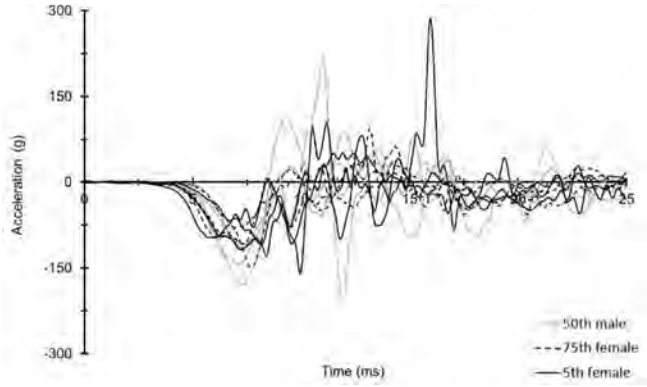

Figure C-52. Male CORALS and Series 1 lumbar spine vertical acceleration (z-direction)

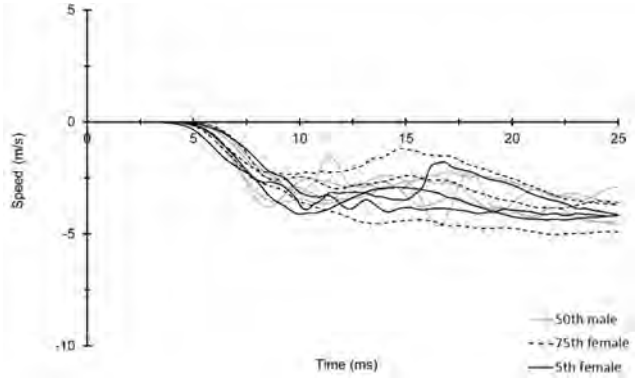

Figure C-53. Male CORALS and Series 1 lumbar spine vertical speed (z-direction)

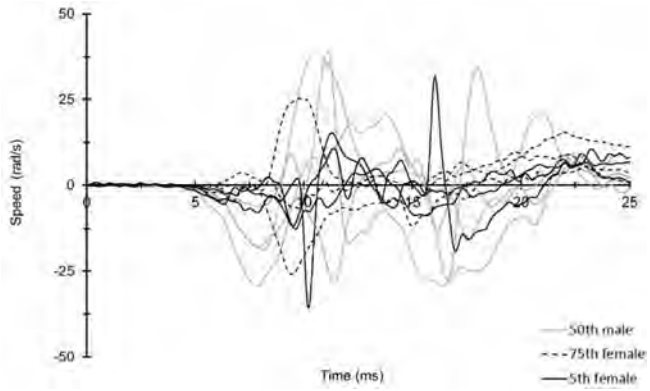

Figure C-54. Male CORALS and Series 1 lumbar spine rotational speed in the sagittal plane (about the y-axis)

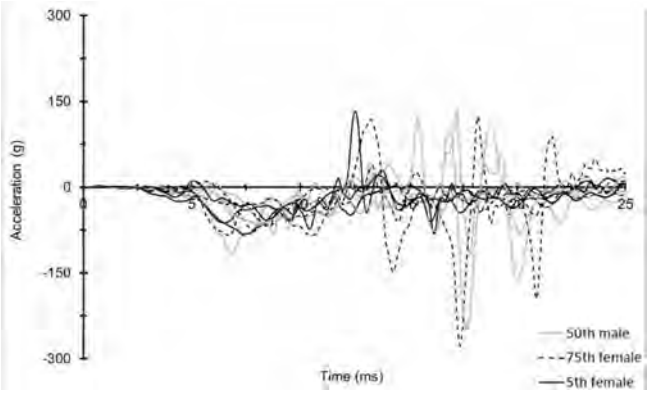

Figure C-55. Series 3 and 4 lumbar spine vertical acceleration (z-direction)

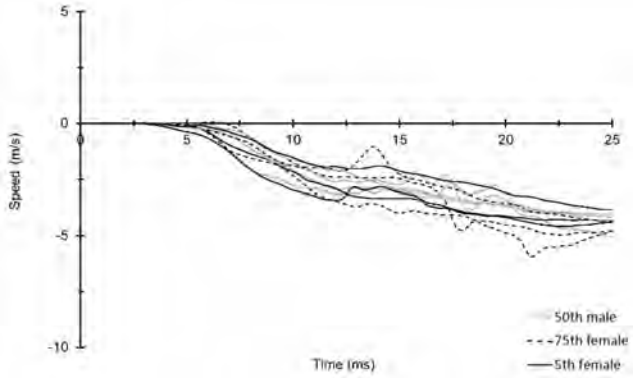

Figure C-56. Series 3 and 4 lumbar spine vertical speed (z-direction)

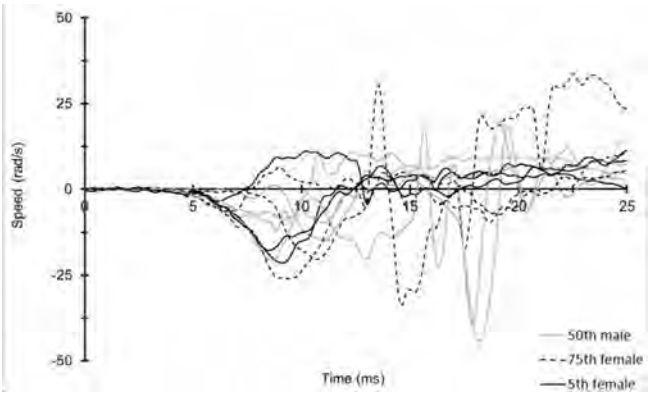

Figure C-57. Series 3 and 4 lumbar spine rotational speed in the sagittal plane (about the y-axis)

Appendix D – Extended Video Results

Figure D-1. Male (CORALS) shot 1 – Crew 1: 50th percentile male, orange; Crew 2: 50th percentile male, yellow

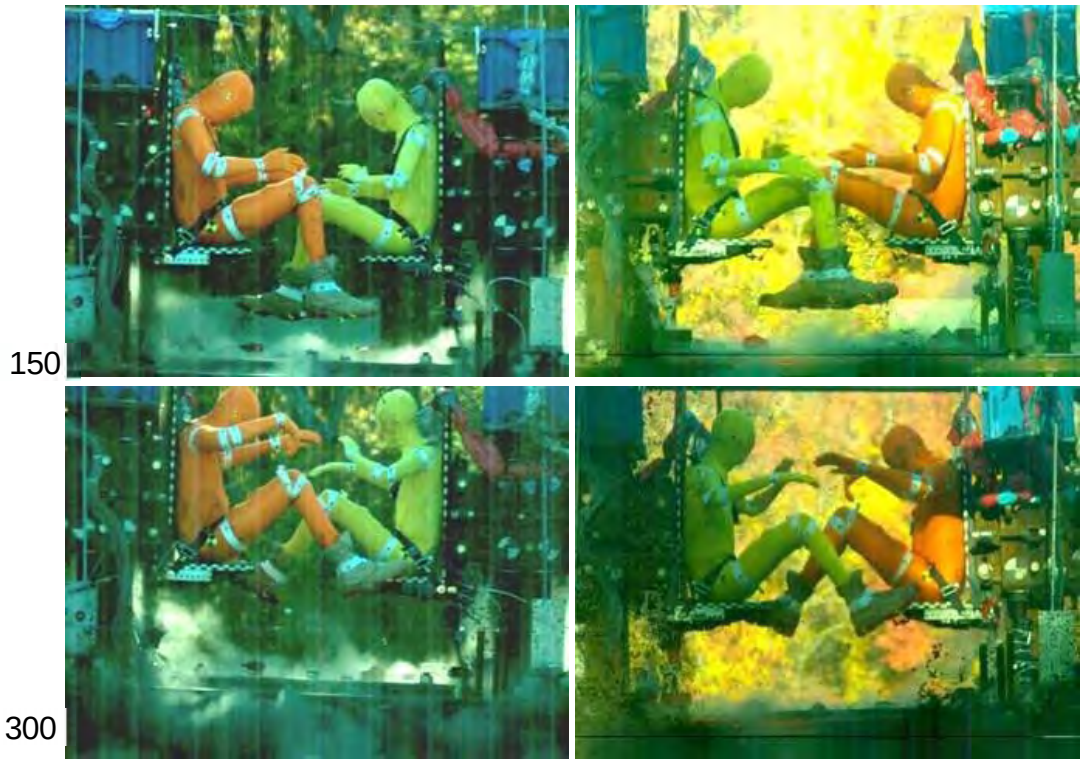

Figure D-2. Male (CORALS) shot 2 – Crew 1: 50th percentile male, orange; Crew 2: 50th percentile male, yellow

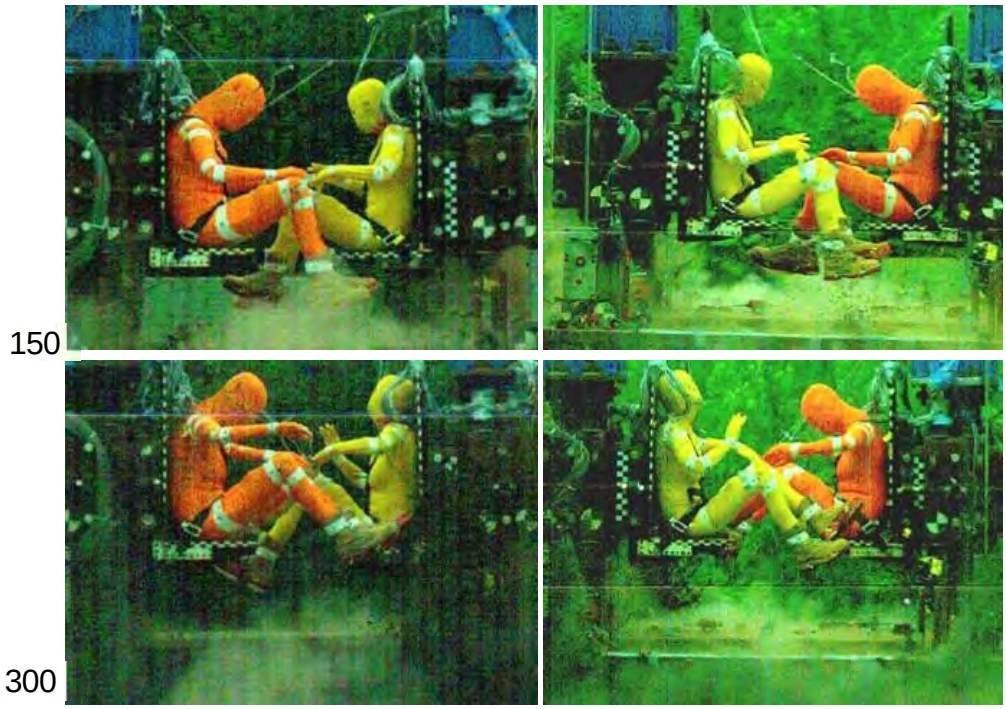

Figure D-3. Female shot 1 – Crew 1: 75th percentile female, orange; Crew 2: 5th percentile female, yellow

Figure D-4. Female shot 2 – Crew 1: 75th percentile female, orange; Crew 2: Hybrid III 5th percentile female anthropomorphic test device (ATD)

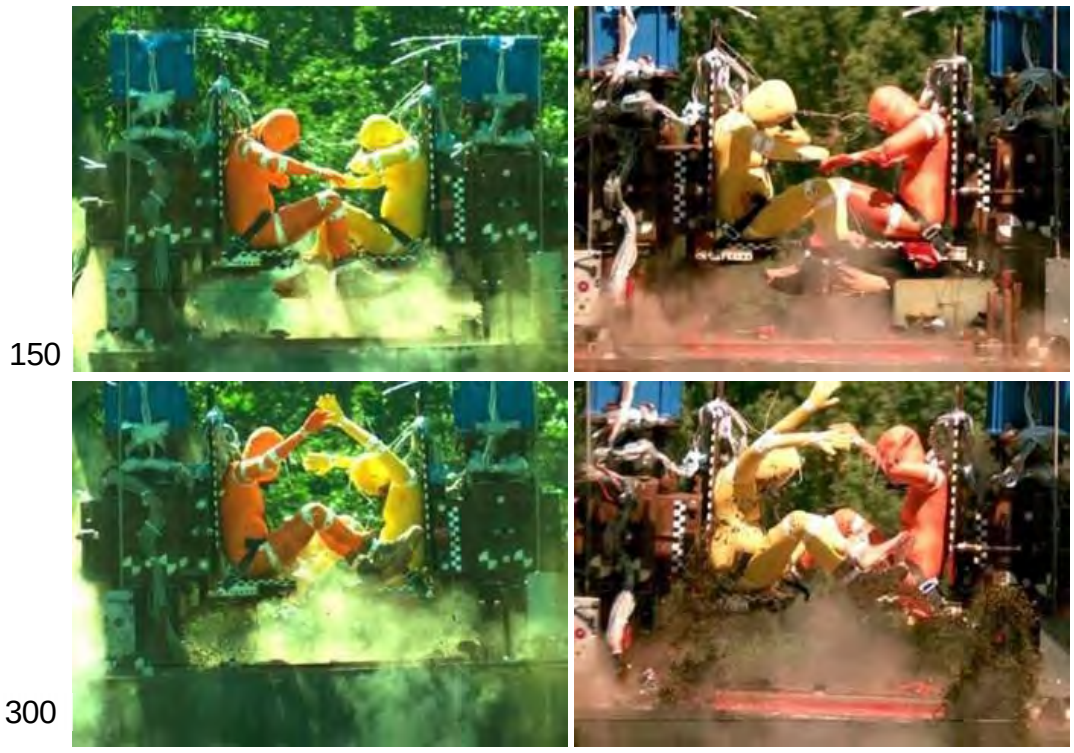

Figure D-5. Female shot 3 – Crew 1: 75th percentile female, orange; Crew 2: 5th percentile female, yellow

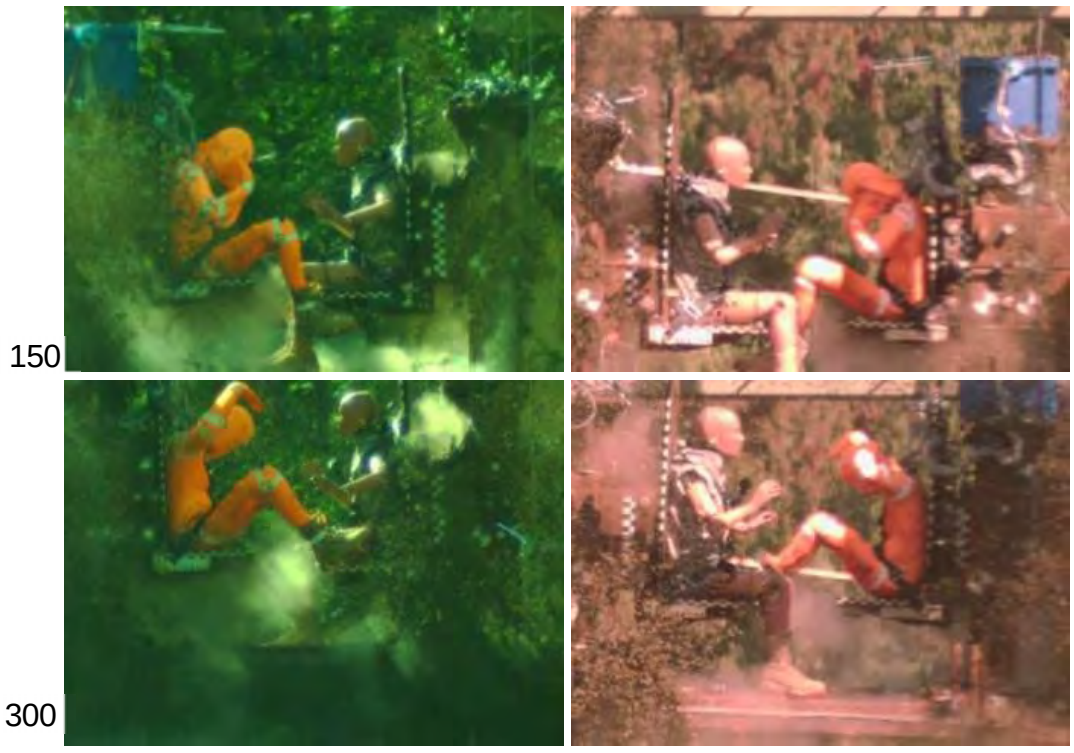

Figure D-6. Female shot 4 – Crew 1: 5th percentile female, orange; Crew 2: Hybrid III 5th percentile female ATD

Figure D-7. Female Shot 5 – Crew 1: 75th percentile female, orange; Crew 2: 5th percentile female, yellow

Figure D-8. Female shot 6 – Crew 1: 50th percentile male, orange; Crew 2: 5th percentile female, yellow

Figure D-9. Female shot 7 – Crew 1: 50th percentile male, orange; Crew 2: 75th percentile male, yellow

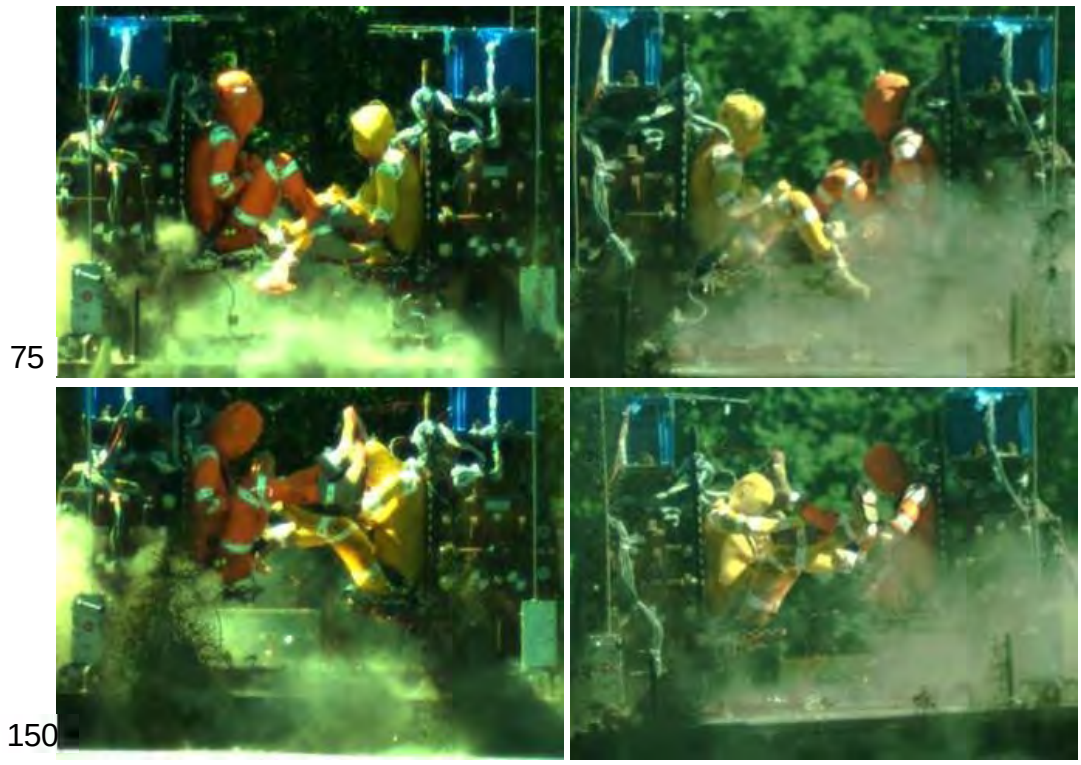

Figure D-10. Female shot 8 – Crew 1: 50th percentile male, orange; Crew 2: 75th percentile female, yellow

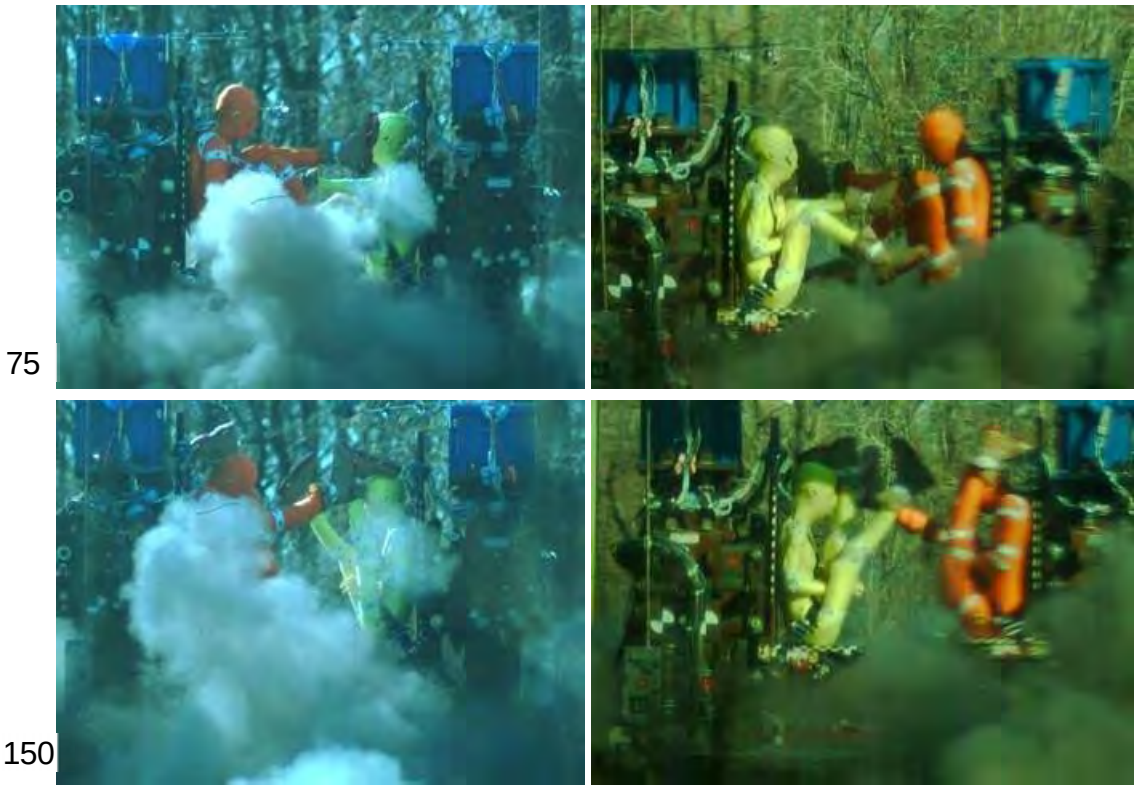

Figure D-11. Female shot 9 – Crew 1: 50th percentile male, orange; Crew 2: 5th percentile female, yellow

Appendix E – Damage Results

E.1 Male Shot 1 Crew 1: 50th percentile male

Thorax

- None

Spine

- L3 non-displaced compression Fx

Pelvis

- Coccyx Fx/dislocation @ 2 distal-most articulations/joints

Lower Extremity

- None

Detailed damage description and photos

MS1C1 sustained a nondisplaced compression fracture of the body of the third lumbar vertebra (Figures E-1 and E-2), as well as a coccyx fracture/dislocation at the two distal-most articulations/joints (not pictured).

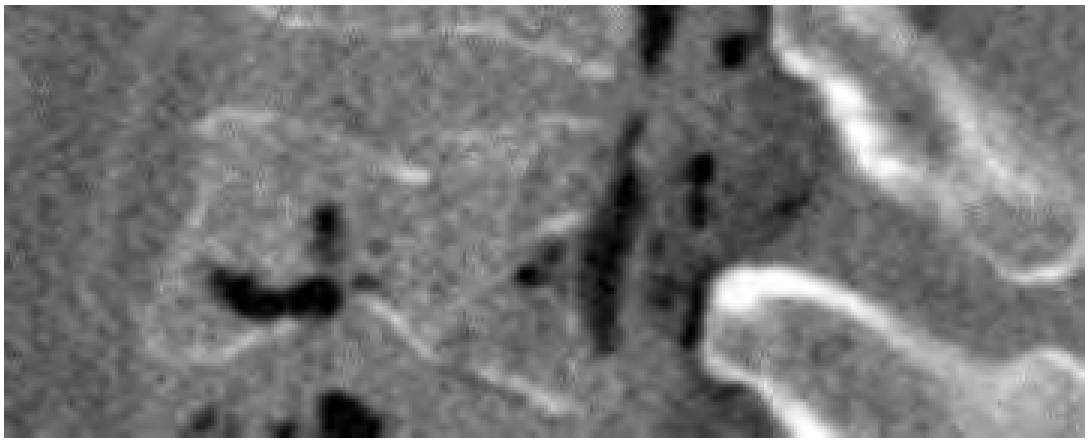

Figure E-1. CT image of compression fracture of L3 of MS1C1 (left lateral view)

Figure E-2. CT segmentation of compression fracture of L3 of MS1C1 (left lateral view)

E.2 Male Shot 1 Crew 2: 50th percentile male

Thorax

- None

Spine

- None

Pelvis

- S2/S3 Fx/dislocation @ mount screws

Lower Extremity

- None

Detailed damage description and photos

MS1C2 sustained a fracture/dislocation at the articulation of S2 and S3 that resulted from placement of the screws used to attach sacrum instrumentation (not pictured).

E.3 Male Shot 2 Crew 1: 50th percentile male

Thorax

- Ribs
- Right R2, 2 anterolateral
- Right R3, 2 anterolateral
- Right R4, 2 anterolateral
- Right R5, 1 anterior
- Right R6, 1 anterior
- Left R2, 2 anterolateral
- Left R3, 2 anterolateral
- Left R4, 1 anterior

Spine

- L4 nondisplaced compression Fx

Pelvis

- Coccyx Fx/dislocation @ 2nd joint from tip

Lower Extremity

- None

Detailed damage description and photos
MS2C1 sustained several rib fractures (not pictured), a nondisplaced compression fracture of the fourth lumbar vertebra (Figures E-3 and E-4), and a fracture/dislocation of the coccyx at the second joint from caudal (Figure E-5).

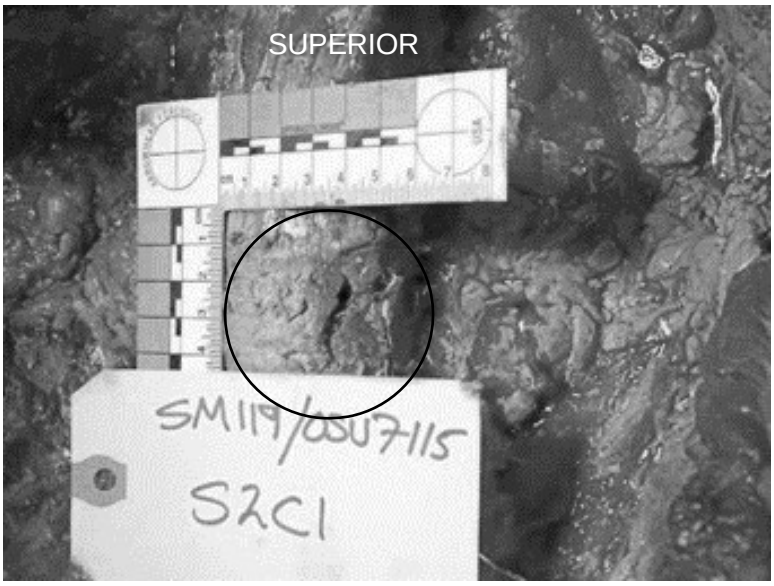

Figure E-3. Compression fracture of the body of L4 of MS2C1 (anterior view in situ)

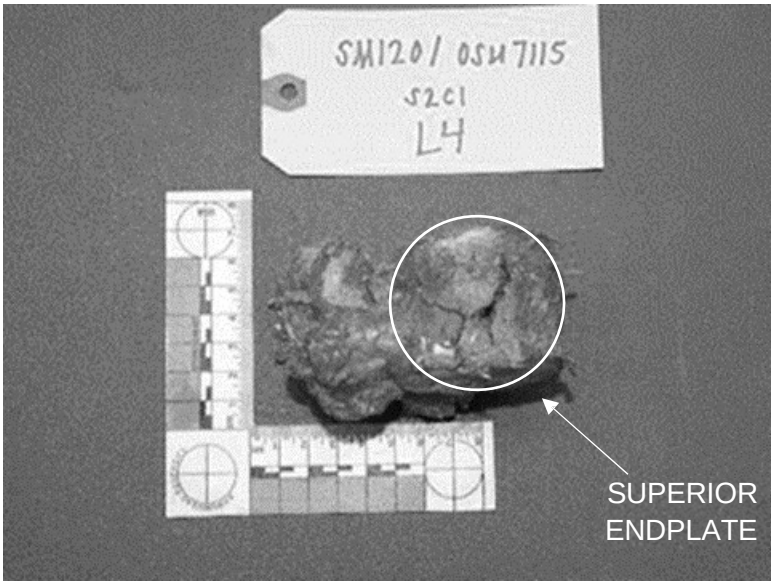

Figure E-4. Compression fracture of the body of L4 of MS2C1 (right lateral view)

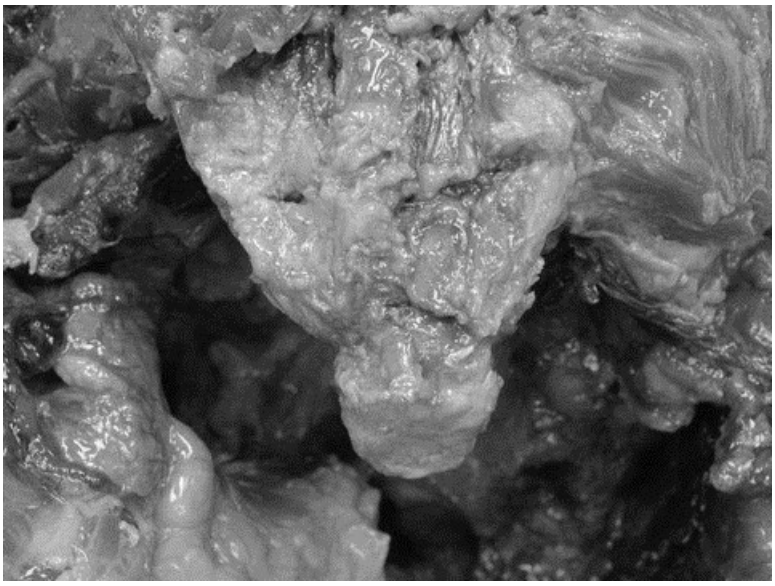

Figure E-5. Fracture of the coccyx of MS2C1 (posterior view)

E.4 Male Shot 2 Crew 2: 50th percentile male

Thorax

- None

Spine

- L4 nondisplaced compression Fx

Pelvis

- Coccyx Fx/dislocation @ 3rd joint from tip (sacrum junction)

Lower Extremity

- None

Detailed damage description and photos

MS2C2 sustained a nondisplaced compression fracture of the body of the fourth lumbar vertebra (Figure E-6) and a fracture/dislocation at the third joint from caudal of the coccyx (not pictured).

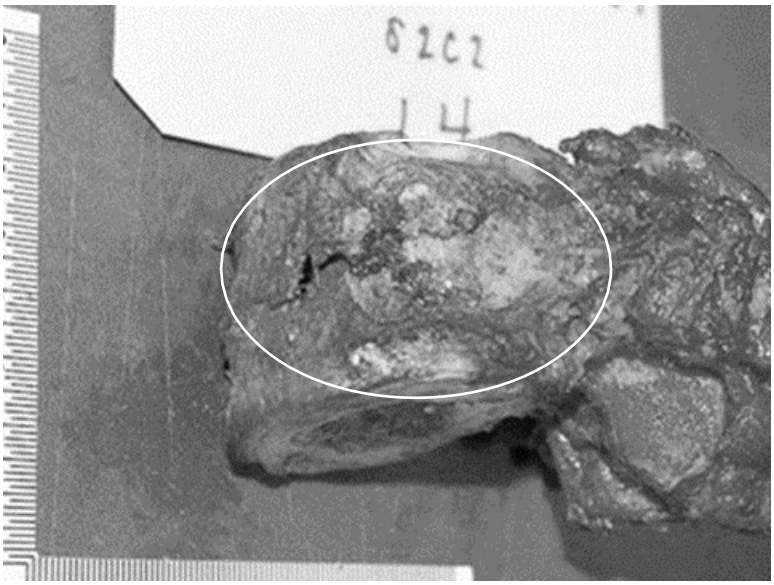

Figure E-6. Nondisplaced compression fracture of L4 of MS2C2 (left lateral view)

E.5 Female Shot 1 Crew 1: 75th percentile female

Thorax

- None

Spine

- L1 transverse process tip Fx, right
- AIS: 650620.2 Lumbar spine transverse process fracture
- BioPT bin 2: Posterior vertebra (simple fx; no canal compromise)
- L2 transverse process tip Fx, bilateral
- AIS: 650620.2 Lumbar spine transverse process fracture
- BioPT bin 2: Posterior vertebra (simple fx; no canal compromise)

Pelvis

- Coccyx Fx/dislocation @ 2nd and 3rd joints from caudal
- AIS 856151.2 Pelvic ring fracture, posterior arch intact; isolated fracture not destroying the integrity of the pelvic ring
- BioPT bin 61-A3.1 (row 23)
- OTA pelvis 61-A3.1

Lower Extremity

- None

Detailed damage description and photos

S1C1 sustained a fracture of the tip of the right transverse process of the first lumbar vertebra (Figure E-7), a fracture of the tip of both transverse processes of the second lumbar vertebra (Figures E-8 and E-9), and a fracture/dislocation of the coccyx at the second and third joints from caudal (Figure E-10).

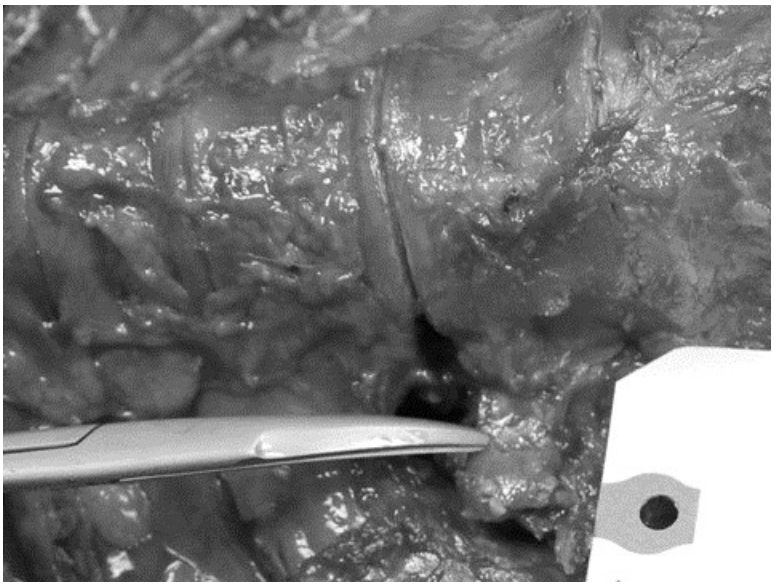

Figure E-7. Fracture of the right transverse process of the first lumbar vertebra of S1C1 (anterior view)

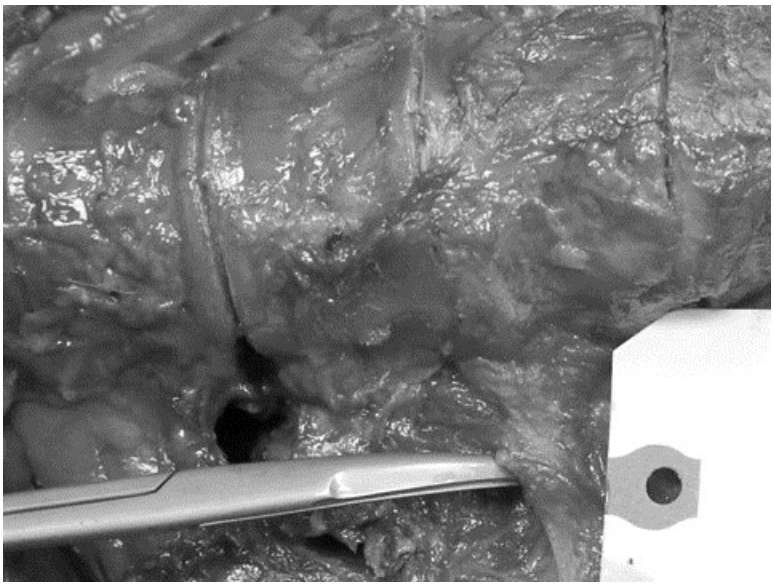

Figure E-8. Fracture of the right transverse process of the second lumbar vertebra of S1C1 (anterior view)

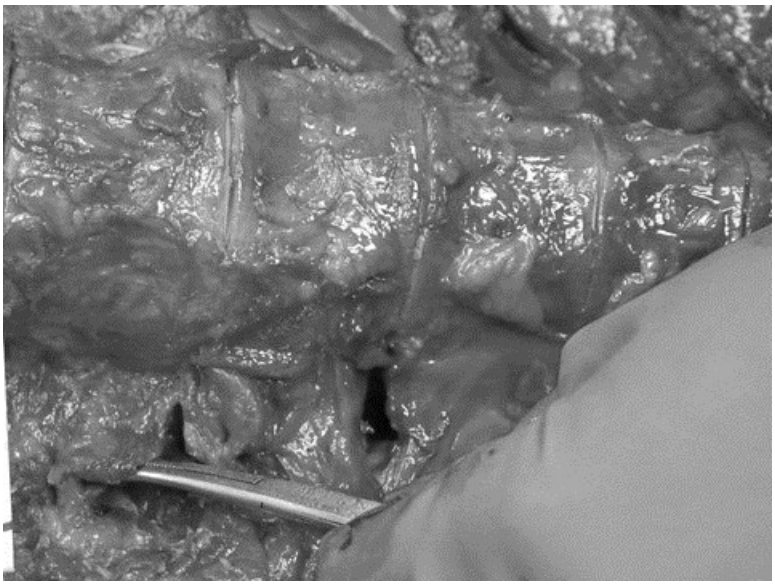

Figure E-9. Fracture of the left transverse process of the second lumbar vertebra of S1C1 (anterior view)

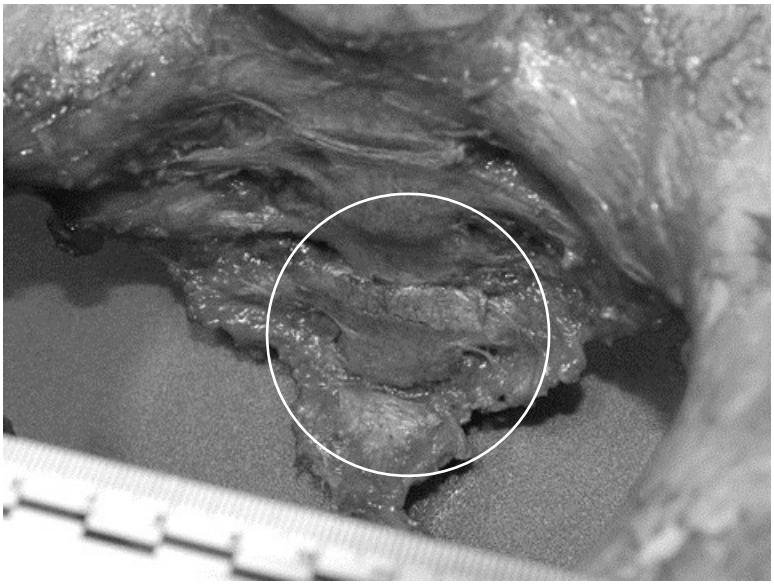

Figure E-10. Fracture of the coccyx of S1C1 (anterior view)

E.6 Female Shot 1 Crew 2: 5th percentile female

The following damage was not included in the damage analysis because cancer spread to the bone, which changed the material properties.

Upper Extremity

- Glenoid/neck Fx, right
- Radius Fx, right, proximal

Pelvis

- S1 ventral Ala bilateral fragment Fx and dorsal separation from Ilium - Not displaced based on CT images
- AIS 856151.2 Pelvic ring fracture, posterior arch intact; isolated fracture not destroying the integrity of the pelvic ring
- Not coded separately
- Does not really fit in the BioPT bins because it is not transverse and not unstable
- S2 ventral Ala bilateral separation, dorsal Ala separation from Ilium, right - Not displaced based on CT images
- AIS 856151.2 Pelvic ring fracture, posterior arch intact; isolated fracture not destroying the integrity of the pelvic ring
- Not coded separately
- Does not really fit in the BioPT bins because it is not transverse and not unstable
- S3 ventral Ala bilateral separation from ilium - Not displaced based on CT images
- AIS 856151.2 Pelvic ring fracture, posterior arch intact; isolated fracture not destroying the integrity of the pelvic ring
- Not coded separately
- Does not really fit in the BioPT bins because it is not transverse and not unstable
- S3/S4 Fx/dislocation, transverse, complete: instrumentation - Not displaced based on CT images
- AIS 856151.2 Pelvic ring fracture, posterior arch intact; isolated fracture not destroying the integrity of the pelvic ring
- Not coded separately
- Does not really fit in the BioPT bins because it is not transverse and not unstable
- Coccyx Fx/dislocation from S5, transverse, complete
- Same AIS as above, not coded separately

- Coccyx Fx/dislocation @ 1st joint from tip
- AIS 856151.2 Pelvic ring fracture, posterior arch intact; isolated fracture not destroying the integrity of the pelvic ring (but this would not be coded separately from below)
- BioPT bin 61-A3.1 (row 23)
- OTA pelvis 61-A3.1

Lower Extremity

- Femur Fx, left, proximal

Detailed damage description and photos

S1C2 sustained fragment fractures of both ventral alae at S1 that were nondisplaced and resulted in dorsal separation from the ilia (Figure E-11); separation of both ventral alae (Figure E-12) and separation of the right dorsal ala from the ilium at S2 (Figure E-13) that were nondisplaced; separation of both ventral alae from the ilia at S3 that were nondisplaced (Figure E-12); transverse and complete fracture/dislocation at S3/S4 that was nondisplaced and a result of instrumentation (Figure E-13); a transverse and complete fracture/dislocation of the coccyx from S5 (Figure E-14); and a fracture/dislocation of the coccyx at the first joint from caudal (Figure E-14).

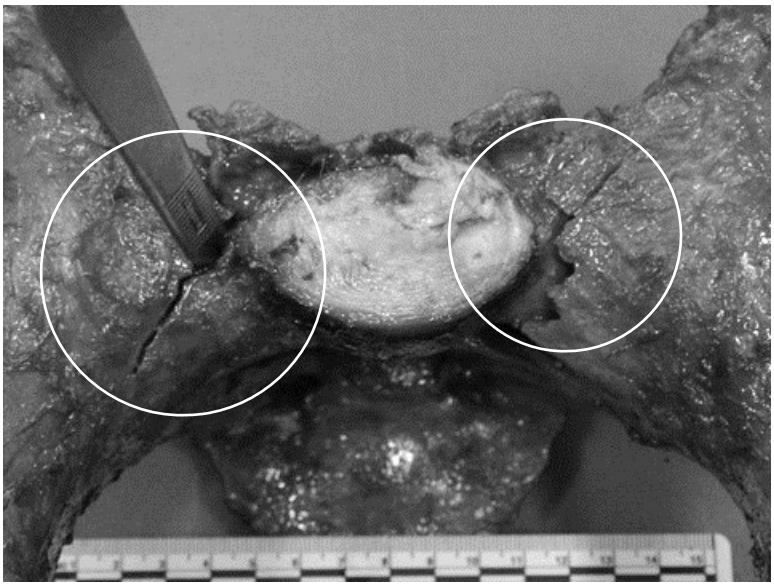

Figure E-11. Fracture of both ventral alae at S1 of S1C2 (superior view, lumbar spine removed)

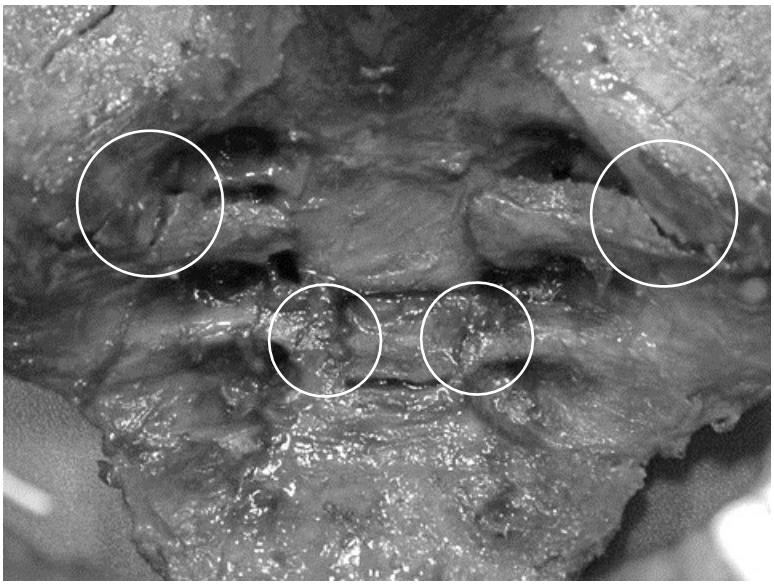

Figure E-12. Separation of both ventral alae from the ilium at S2 of S1C2 (anterior view)

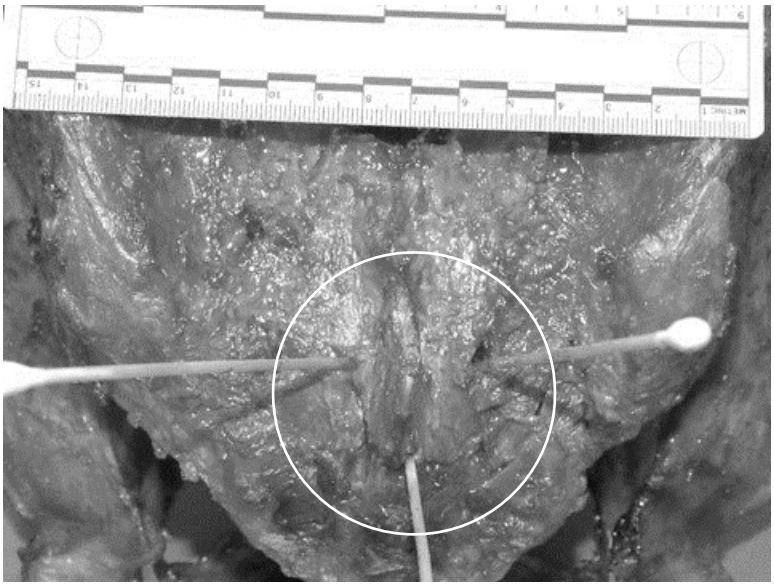

Figure E-13. Separation of the right dorsal ala from the ilium at S2 of S1C2 (posterior view)

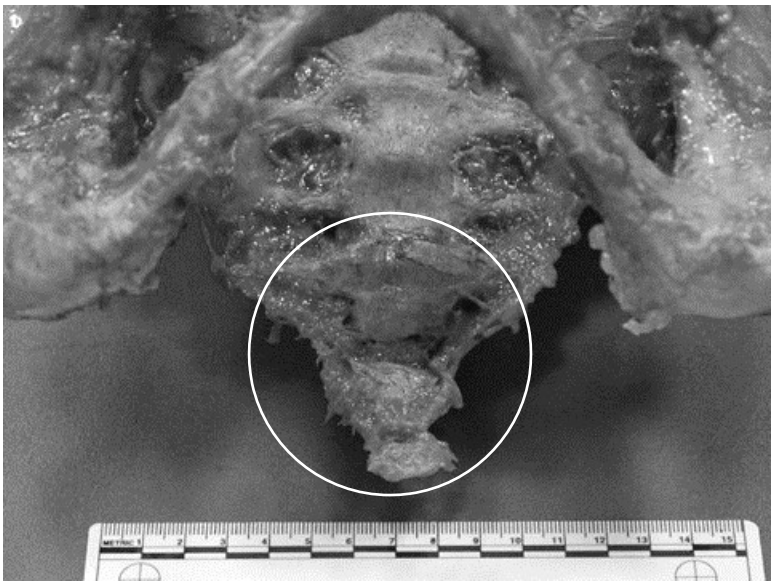

Figure E-14. Fractures of the coccyx of S1C2 (anterior view)

E.7 Female Shot 2 Crew 1: 75th percentile female

Thorax

- None

Spine

- None

Pelvis

- Coccyx Fx/dislocation @ 2nd joint from caudal
- AIS 856151.2 Pelvic ring fracture, posterior arch intact; isolated fracture not destroying the integrity of the pelvic ring
- BioPT bin 61-A3.1 (row 23)
- OTA pelvis 61-A3.1

Lower Extremity

- None

Detailed damage description and photos

S2C1 sustained a fracture/dislocation of the coccyx at the second joint from caudal (Figures E-15 and E-16).

Figure E-15. Fractured coccyx of S2C1 (posterior view)

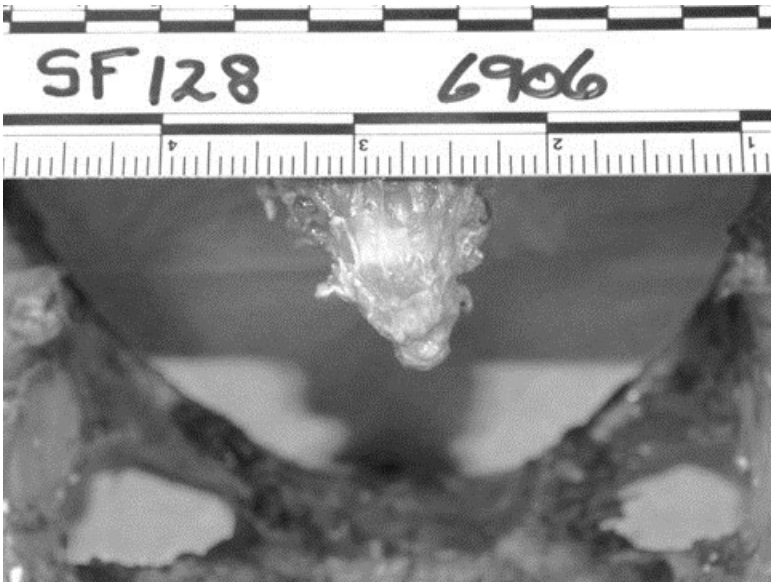

Figure E-16. Fractured coccyx of S2C1 (posterior view, detail)

E.8 Female Shot 3 Crew 1: 75th percentile female

Thorax

- None

Spine

- None

Pelvis

- S5 vertical Fx, lateral aspect, left
- AIS 856151.2 Pelvic ring fracture, posterior arch intact; isolated fracture not destroying the integrity of the pelvic ring
- Does not really fit in the BioPT bins because it is not transverse and not unstable
- Coccyx Fx/dislocation from sacrum - same as above, not coded separately
- AIS 856151.2 Pelvic ring fracture, posterior arch intact; isolated fracture not destroying the integrity of the pelvic ring
- Not coded separately
- Coccyx Fx/dislocation @ 2rd joint from caudal
- AIS 856151.2 Pelvic ring fracture, posterior arch intact; isolated fracture not destroying the integrity of the pelvic ring (but this would not be coded separately from below)
- BioPT bin 61-A3.1 (row 23)
- OTA pelvis 61-A3.1

Lower Extremity

- None

Detailed damage description and photos

S3C1 sustained a vertical fracture on the left and lateral aspect of S5 (Figure E-17); a fracture/dislocation of the coccyx from the sacrum (Figure E-18), and a fracture/dislocation of the coccyx at the second joint from caudal (Figure E-18).

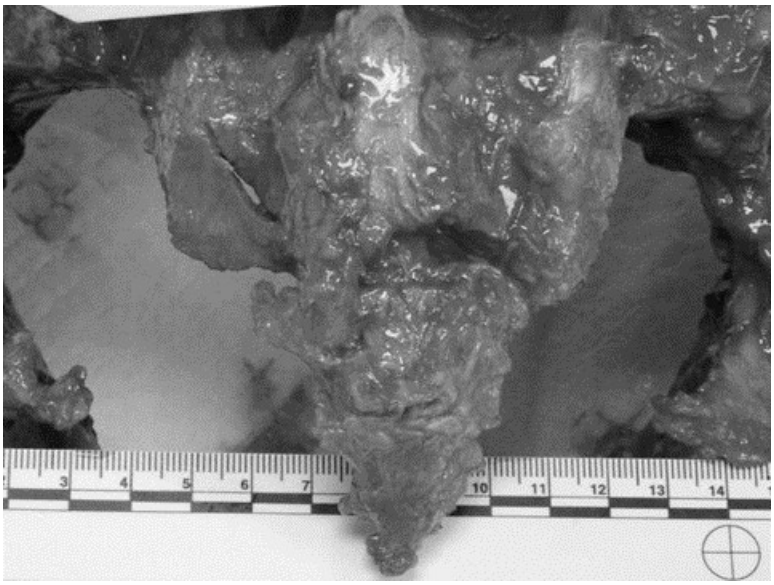

Figure E-17. Fracture of left aspect of S5 of S3C1 (posterior view)

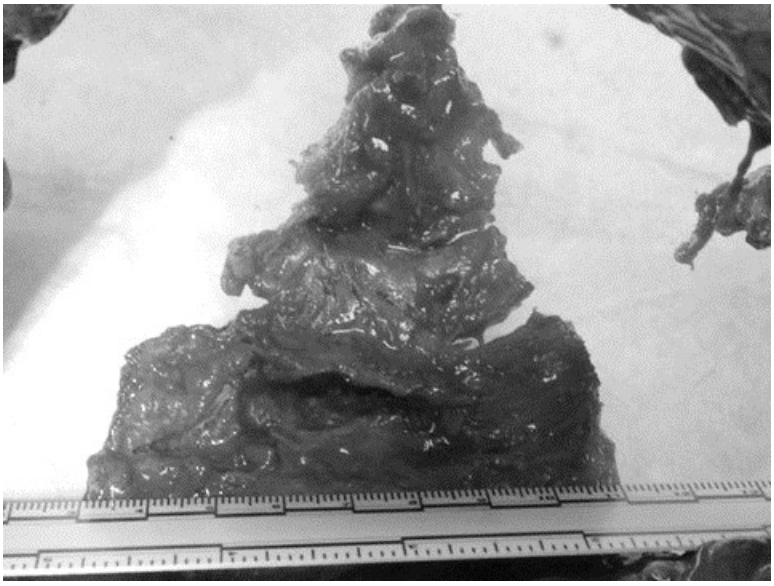

Figure E-18. Fracture/dislocation of the coccyx at the sacrum and the second joint from caudal of S3C1 (anterior view)

E.9 Female Shot 3 Crew 2: 5th percentile female

Thorax

- None

Spine

- None

Pelvis

- S2-S5 multiple Ala Fx, right
- AIS 856151.2 Pelvic ring fracture, posterior arch intact; isolated fracture not destroying the integrity of the pelvic ring
- Not coded separately
- Does not really fit in the BioPT bins because it is not transverse and not unstable
- Not a Denis fracture zone because it was not through the whole sacrum and was not unstable
- Coccyx Fx/dislocation from sacrum - same as above, not coded separately
- AIS 856151.2 Pelvic ring fracture, posterior arch intact; isolated fracture not destroying the integrity of the pelvic ring
- Not coded separately
- Coccyx Fx/dislocation @ 3rd joint from caudal
- AIS 856151.2 Pelvic ring fracture, posterior arch intact; isolated fracture not destroying the integrity of the pelvic ring (but this would not be coded separately from below)
- BioPT bin 61-A3.1 (row 23)
- OTA pelvis 61-A3.1

Lower Extremity

- None

Detailed damage description and photos

S3C2 sustained multiple fractures to the alae on the right side of S2–S5 (Figure E-19); a fracture/dislocation of the coccyx at the sacrum (Figure E-20); and a fracture/dislocation of the coccyx at the third joint from caudal (Figure E-20).

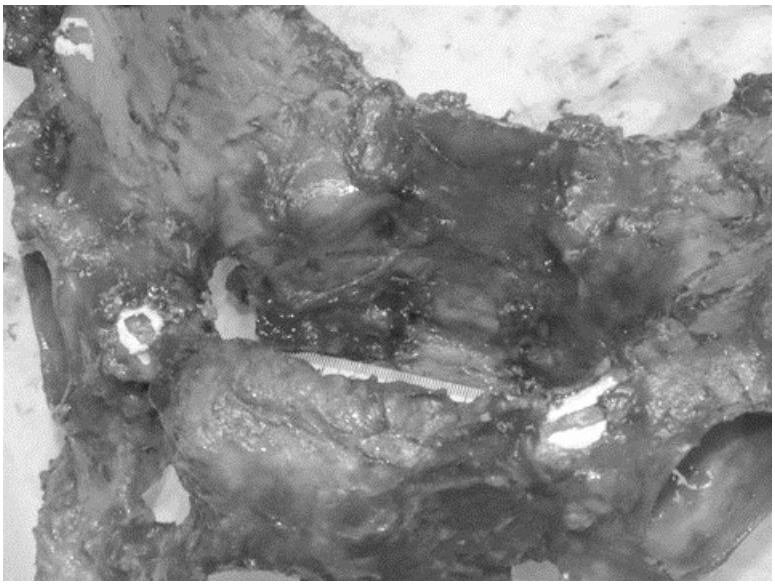

Figure E-19. Fractures to the alae on the right side of S2–S5 of S3C2 (anterior view)

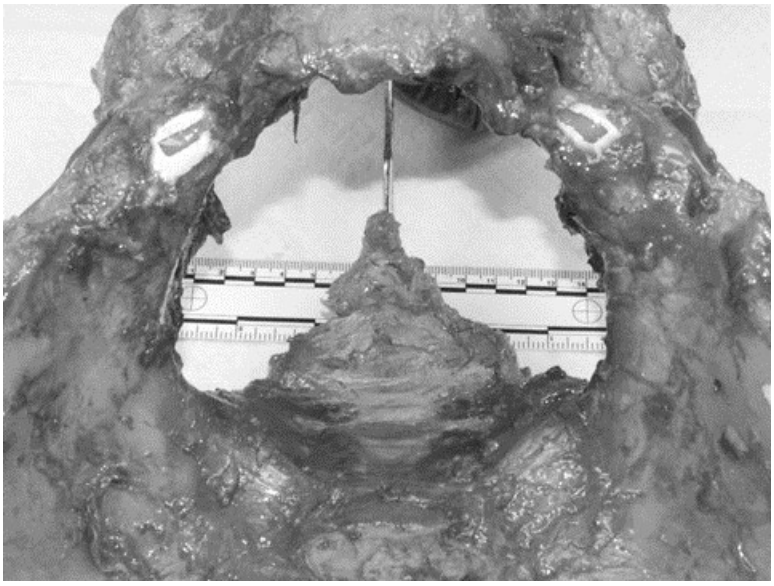

Figure E-20. Fracture/dislocation of the coccyx at the sacrum and the third joint from caudal (anterior view)

E.10 Female Shot 4 Crew 1: 5th percentile female

Thorax

- None

Spine

- L2 bilateral Fx, lateral process tip
- AIS: 650620.2 Lumbar spine transverse process fracture
- BioPT bin 2: Posterior vertebra (simple fx; no canal compromise)
- L3 Fx, lateral process tip, right
- AIS: 650620.2 Lumbar spine transverse process fracture
- BioPT bin 2: Posterior vertebra (simple fx; no canal compromise)

Pelvis

- S2-3 and S1 Ala Fx/separation
- AIS 856151.2 Pelvic ring fracture, posterior arch intact; isolated fracture not destroying the integrity of the pelvic ring
- Not coded separately
- Does not really fit in the BioPT bins because it is not transverse and not unstable
- Not a Denis fracture zone because it was not through the whole sacrum and was not unstable
- S4/5 and S1/2 Fx/dislocation
- AIS 856151.2 Pelvic ring fracture, posterior arch intact; isolated fracture not destroying the integrity of the pelvic ring
- Not coded separately
- Does not really fit in the BioPT bins because it is not transverse and not unstable
- Not a Denis fracture zone because it was not through the whole sacrum and was not unstable
- Coccyx Fx/dislocation @ 2nd joint from caudal
- AIS 856151.2 Pelvic ring fracture, posterior arch intact; isolated fracture not destroying the integrity of the pelvic ring (but this would not be coded separately from below)
- BioPT bin 61-A3.1 (row 23)
- OTA pelvis 61-A3.1

Lower Extremity

- Talus, left - partial neck fx medial/dorsal aspect
- AIS: 857261.2 fracture line into one joint surface; talus body
- BioPT Bin 2: Talus fracture (fx nondisplaced or simple displacement; Hawkins Type I and II)
- No Hawkins classification because the fracture line does not extend through the neck

Detailed damage description and photos

S4C1 sustained a fracture of the right transverse process of the third lumbar vertebra (Figure E-21); fractures of the tips of both transverse processes of the second lumbar vertebra (Figures E-21 and E-22); fracture/separation of the alae of S2–3 and S1 (Figure E-23); fracture/dislocation at S1/2 and S4/5 (Figures E-23 and E-24); a fracture/dislocation of the coccyx at the second joint from caudal (Figure E-24), and minor damage to the head of the left talus (Figure E-25).

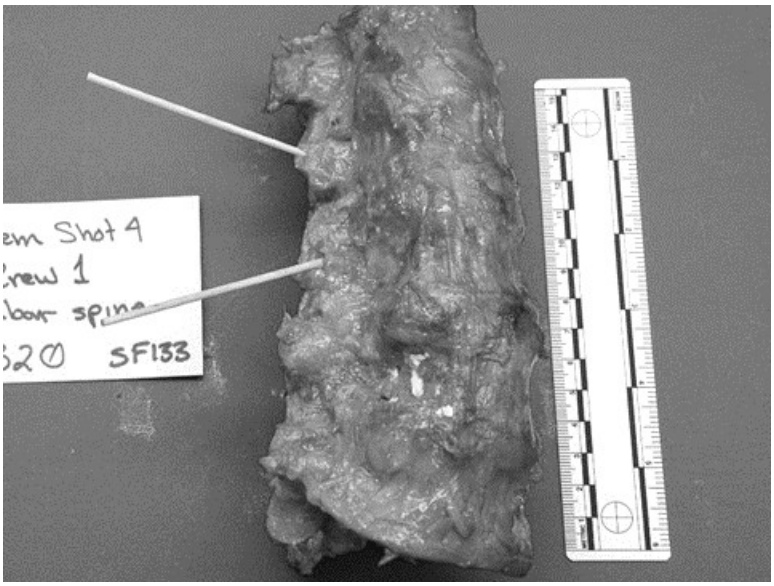

Figure E-21. Fractures of the right transverse processes of the second and third lumbar vertebrae of S4C1 (right lateral view)

Figure E-22. Fracture of the left transverse process of the second lumbar vertebra of S4C2 (left lateral view)

Figure E-23. Fracture/separation of the alae of S2–3 and S1; fracture/dislocation at S1/2 and S4/5 of S4C1 (anterior view)

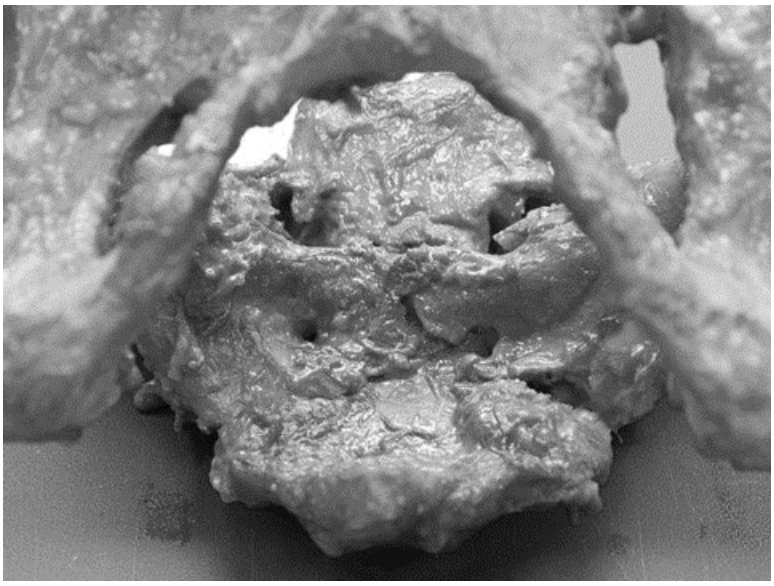

Figure E-24. Fracture/dislocation at S1/2 and S4/5; fracture/dislocation of the coccyx at the second joint from caudal of S4C1 (inferior view)

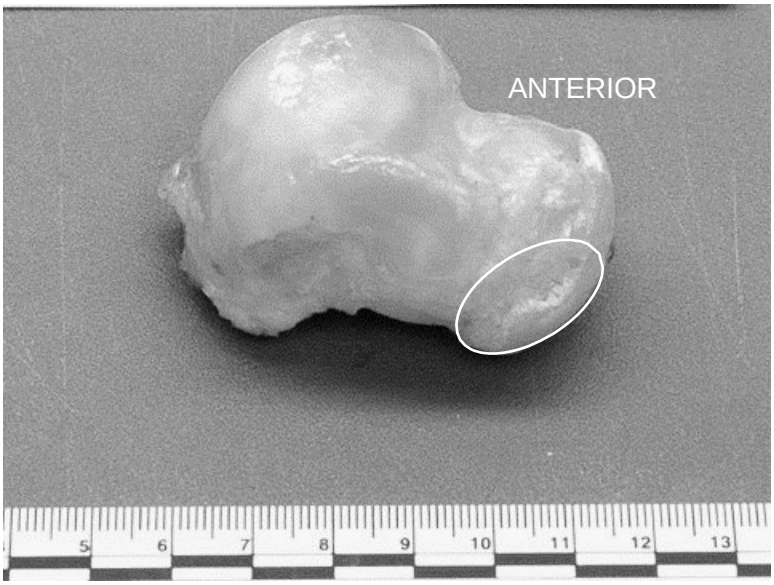

Figure E-25. Partial fracture of the articular surface—facies articularis navicularis of the left talus of S4C1 (superomedial view)

E.11 Female Shot 5 Crew 1: 75th percentile female

Thorax

- Rib fractures
- AIS 450203.3 fracture(s) without flail, any location unilateral or bilateral not further specified (NFS) ≥3 ribs
- Left rib 3, fx (6.0 cm)* // see above, group rib fx together
- Right rib 6, fx (8.0 cm)* // see above, group rib fx together
- Left rib 6, fx (5.5 cm)* // see above, group rib fx together
- * Measured from sternum midline; left rib 5 fx occurred during rib harvesting

Spine

- L3 body, chip on right side
- AIS: 650632.2 minor compression (≤20% loss of anterior height)
- BioPT Bin 1: VB (simple fx; no canal compromise)

Pelvis

- Pelvis – bilateral sacroiliac joint fx
    - *AIS: 856161.3 Pelvic ring fracture, incomplete disruption of posterior arch NFS- this might be over coding, but I bumped it up to this because of the SI joint fracture; there is no anterior component involvement so it is not unstable*
- Pelvis – coccyx, fx
    - *AIS 856151.2 Pelvic ring fracture, posterior arch intact; isolated fracture not destroying the integrity of the pelvic ring (but this would not be coded separately from below)*
    - *BioPT bin 61-A3.1 (row 23)*
    - *OTA Pelvis 61-A3.1*

Lower Extremity

- Distal tibia, right - pilon fx
    - *AIS: 854361.2 distal tibia partial articular*
    - *OTA 43-B1 pure split*
    - *BioPT Bin 6: Distal tibia fracture (partial articular; simple pilon; OTA Type 43-B)*
- Talus, right - chip on posterior facet and head
    - *AIS: 857261.2 fracture line into one joint surface; talus body*

    - *BioPT Bin 2: Talus fracture (fx nondisplaced or simple displacement; Hawkins Type I and II)*
    - *No Hawkins classification, not a neck fracture*
- Calcaneus, right - crushed
    - *AIS: 857371.2 fracture line into ≥2 joint surfaces*
    - *BioPT Bin 5: Calcaneus fracture (comminuted crush, comminuted, Sanders Type III and Type IV)*
    - *Sanders Type IV, 3 or more fracture lines*
- Navicular, right - fx
    - *AIS: 857461.2 fracture line into one joint surface*
    - *BioPT Bin 1: Tarsal bone fracture (navicular, cuboid, and cuneiforms)*
- Cuboid, right - fx
    - *AIS: 857661.2 fracture line into one joint surface*
    - *BioPT Bin 1: Tarsal bone fracture (navicular, cuboid, and cuneiforms)*
- Distal tibia, left - compression fx
    - *AIS: 854371.2 distal tibia complete articular*
    - *OTA type 43-C3 articular multifragmentary*
    - *BioPT Bin 7: Distal tibia fracture (complete articular; comminuted pilon; OTA Type 43-C)*
- Distal fibula, left - oblique fx
    - *AIS: 854471.2 above joint (suprasyndesmotic); isolated shaft, head or neck; Weber C*
    - *BioPT Bin 10: Distal fibula fracture (simple, complex bimalleolar)*
    - *Weber classification: C*
- Navicular, left - fx
    - *AIS: 857461.2 fracture line into one joint surface*
    - *BioPT Bin 1: Tarsal bone fracture (navicular, cuboid, and cuneiforms)*
- Cuboid, left - chip
    - *AIS: 857661.2 fracture line into one joint surface*
    - *BioPT Bin 1: Tarsal bone fracture (navicular, cuboid, and cuneiforms)*
- 4th proximal metatarsal, left - chip
    - *AIS: 858163.2 partial articular*
- 5th proximal metatarsal, left - crushed
    - *AIS: 858173.2 complete articular*
- 5th proximal phalanx, left - fx
    - *AIS: 858163.2 partial articular*

Detailed damage description and photos

S5C1 sustained three rib fractures (Figures E-26, E-27, and E-28); a chip on the right side of the body of the third lumbar vertebra (Figure E-29); bilateral fractures at the sacroiliac joint (Figure E-30); and a fracture of the coccyx (Figure E-31). The right lower extremity sustained a fracture through the inferior and lateral corner of the navicular (Figures E-32, E-33, and E-34), a fracture of the lateral aspect of the articular surface for the calcaneus on the cuboid (Figures E-32 and E-35), a chip fracture on both the posterior facet and head of the talus (Figure E-36), a crushed calcaneus (Figures E-37 and E-38), and a pilon fracture of the distal tibia (Figure E-39). The left lower extremity sustained a vertical fracture of the proximal end of the 5th proximal phalange (Figure E-40), a chip fracture of the proximal end of the 4th metatarsal (Figure E-41), a compression fracture of the proximal end of the 5th metatarsal (Figure E-42), a fracture through the inferior and lateral corner of the navicular (Figure E-43), a fracture of the cuboid at the cuneocuboid joint (Figure E-44), a compression fracture of the distal tibia (Figures E-45 and E-46), and an oblique fracture of the distal fibula (Figures E-45 and E-47).

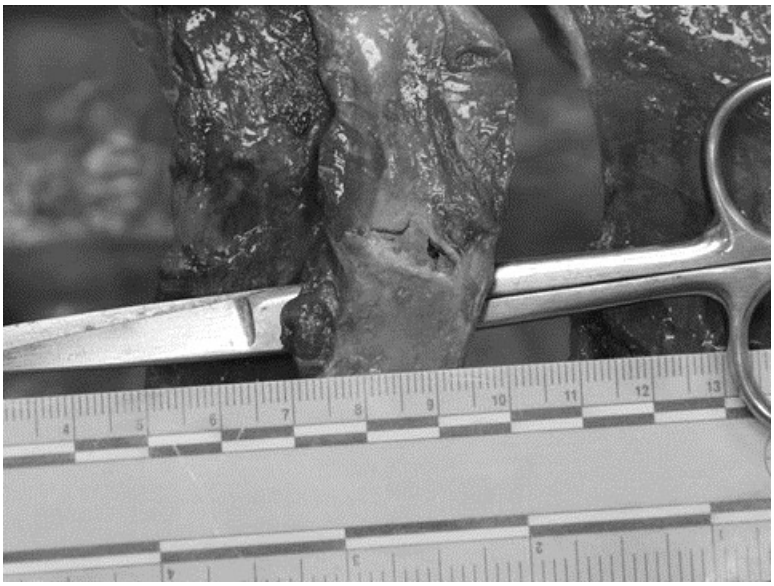

Figure E-26. Fracture of the right sixth rib of S5C1 (8 cm from the sternum midline)

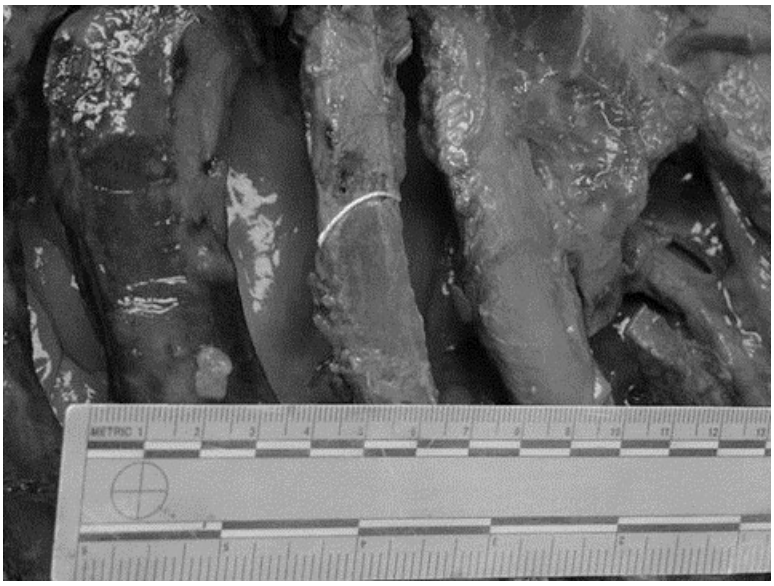

Figure E-27. Fracture of the left third rib of S5C1 (6 cm from sternum midline)

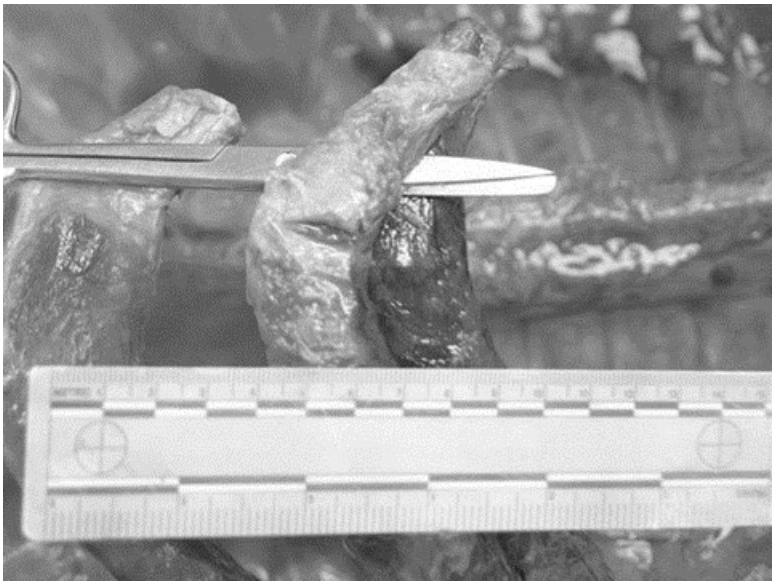

Figure E-28. Fracture of the left sixth rib of S5C1 (5.5 cm from sternum midline)

Figure E-29. Chip fracture to the right side of L3 of S5C1 (right lateral view)

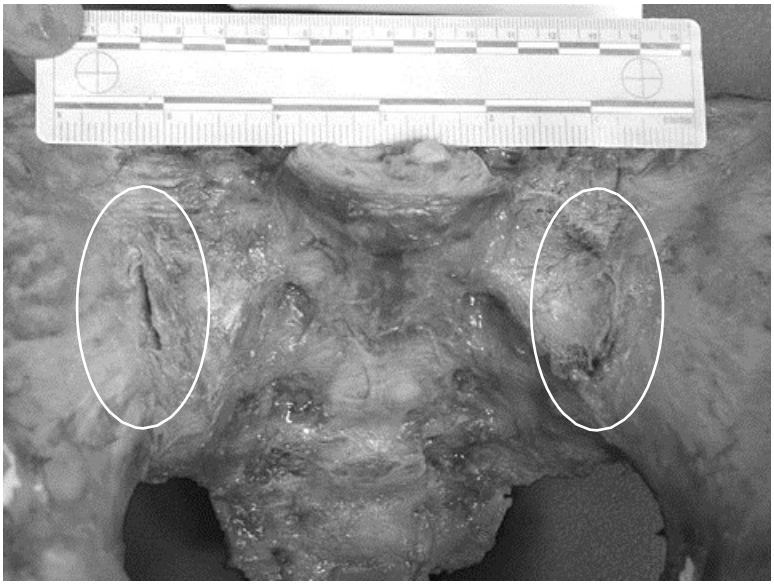

Figure E-30. Bilateral sacroiliac joint fractures of S5C1

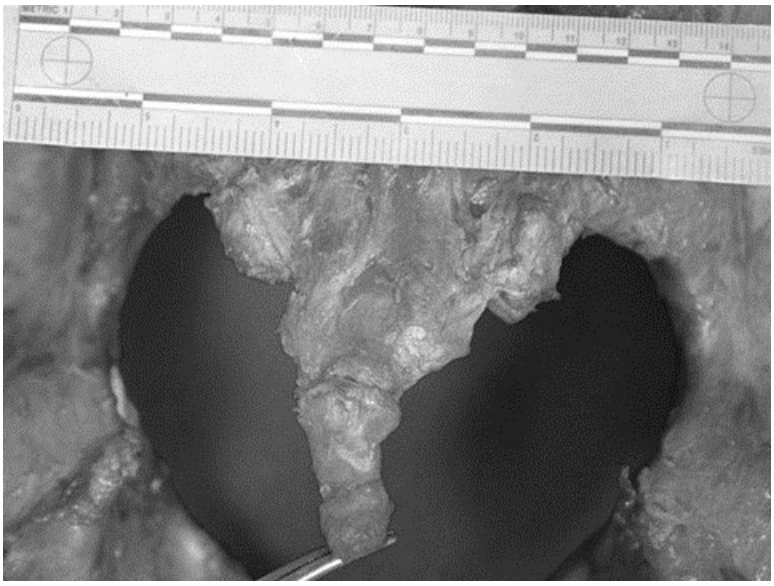

Figure E-31. Fracture of the coccyx of S5C1

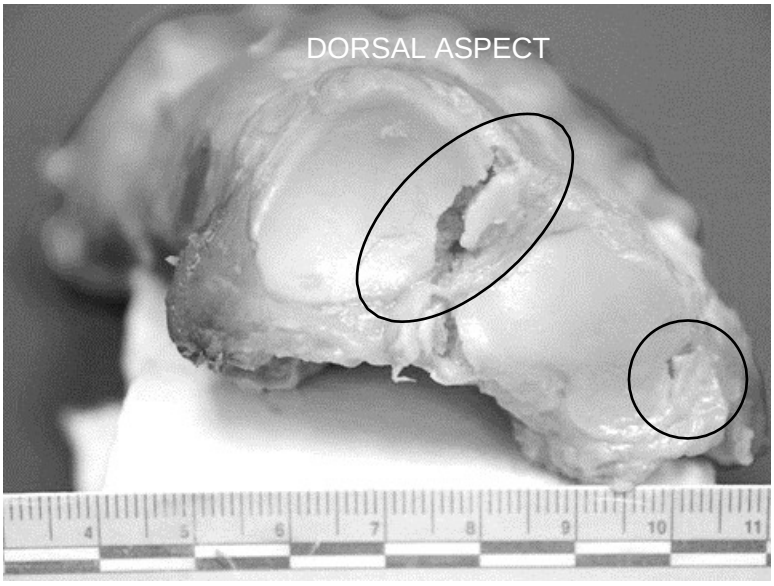

Figure E-32. Fracture of the beak of the right navicular and the lateral portion of the posterior surface of the right cuboid of S5C1 (posterior view, talus and calcaneus removed)

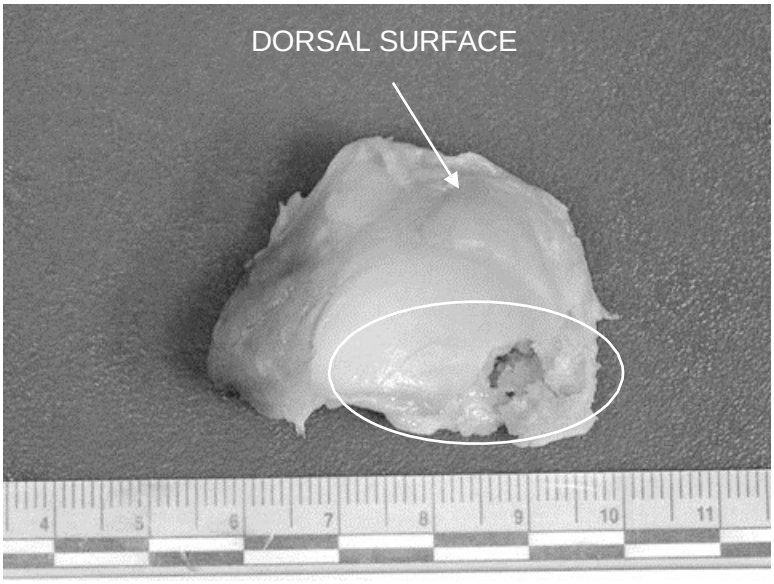

Figure E-33. Fracture to the beak of the right navicular of S5C1 (posterior view showing talar articular surface)

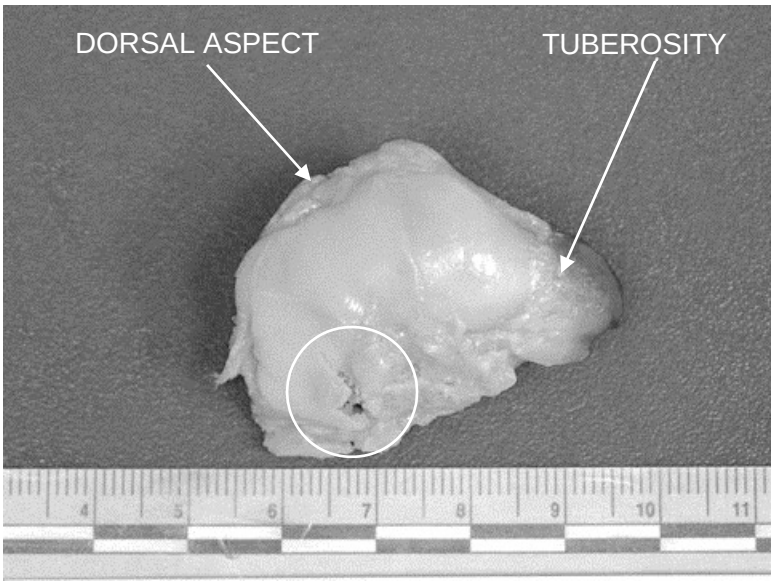

Figure E-34. Fracture through the articular surface for the third cuneiform of the right navicular of S5C1 (anterior view showing articular surface for cuneiforms)

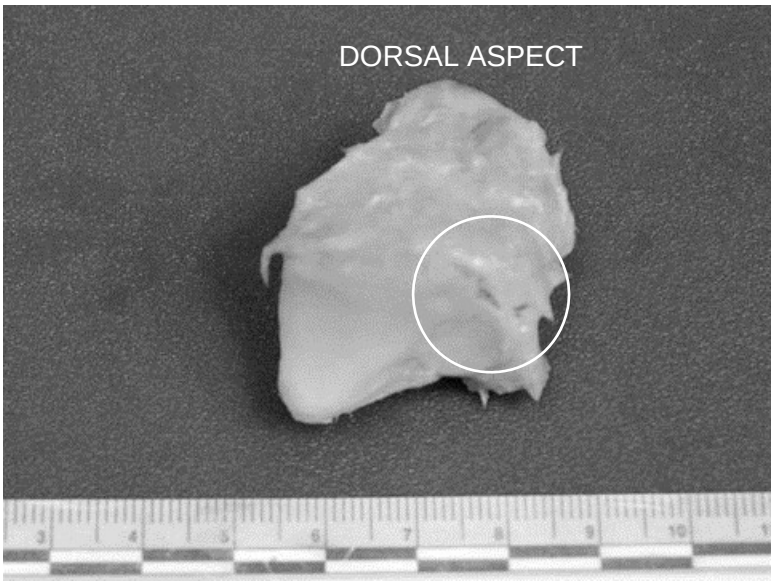

Figure E-35. Fracture to the lateral portion of the posterior surface of the right cuboid of S5C1 (posterior view showing articular surface for the calcaneus)

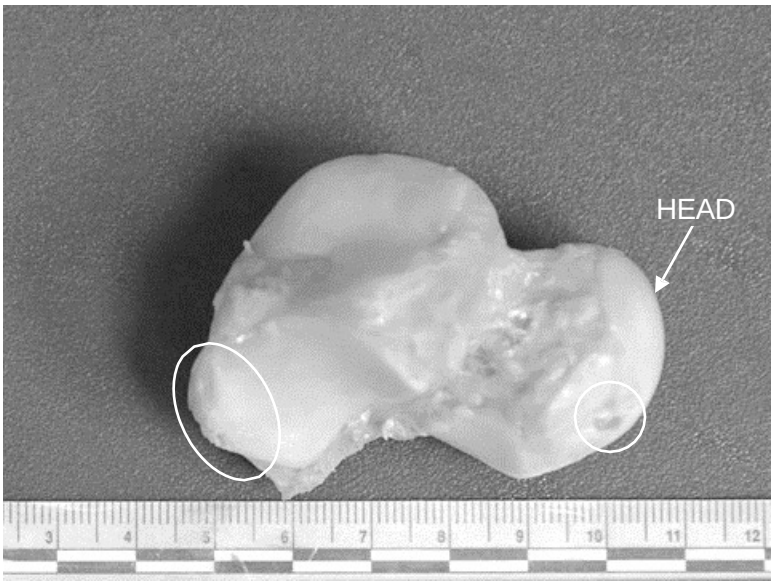

Figure E-36. Chip fractures to the posterolateral tubercle and articular surface—facies articularis navicularis of the right talus of S5C1 (inferolateral view)

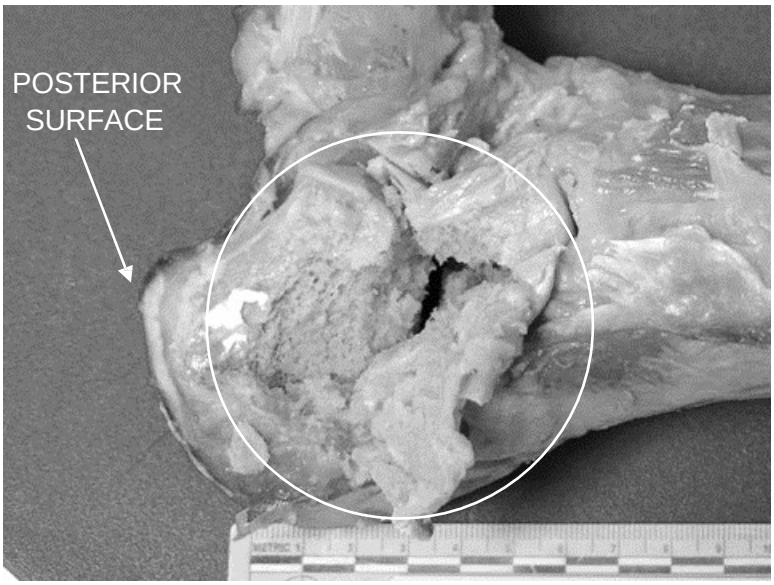

Figure E-37. Crushed right calcaneus of S5C1 (lateral view)

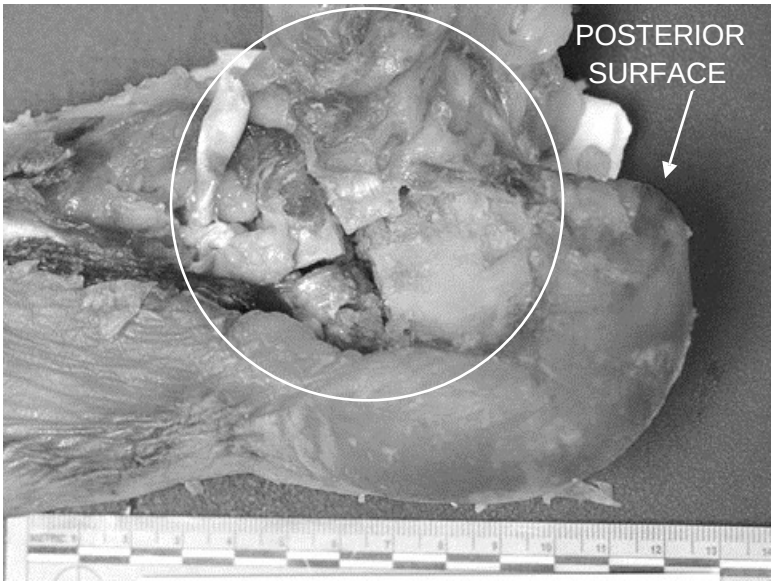

Figure E-38. Crushed right calcaneus of S5C1 (medial view)

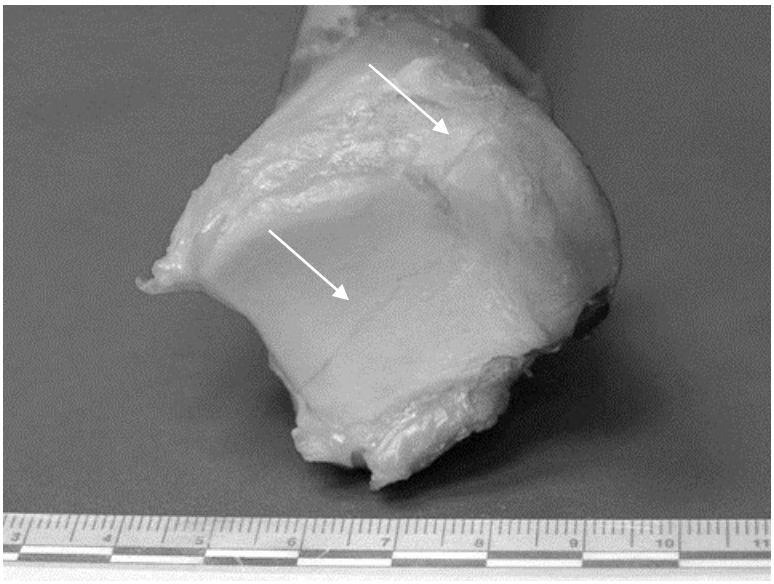

Figure E-39. Pilon fracture originating at the tibial plafond oriented from the lateral aspect to the anterior colliculus of the right tibia of S5C1 (inferior view)

Figure E-40. Fracture of the left 5th proximal phalange of S5C1 (posterior view of articular surface for 5th metatarsal; 4th and 5th metatarsals are removed)

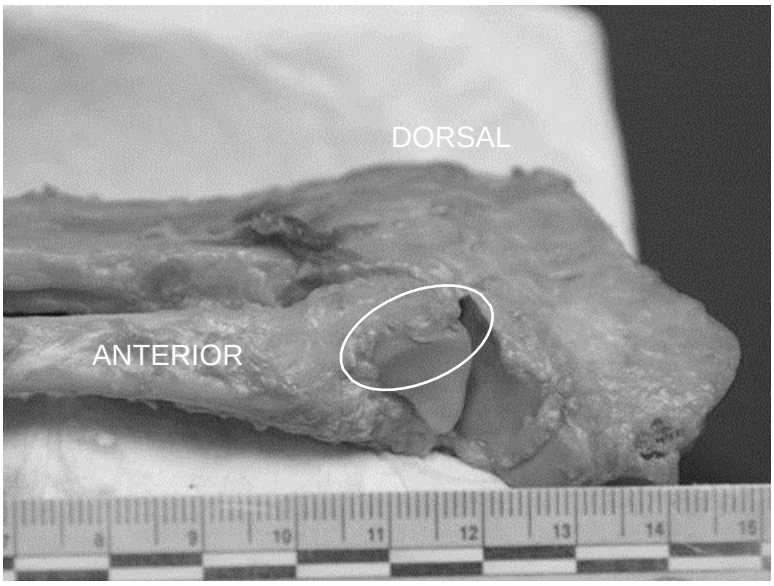

Figure E-41. Fracture of the superior edge of the articular surface for the 5th metatarsal on the left 4th metatarsal of S5C1 (lateral view, 5th metatarsal is removed)

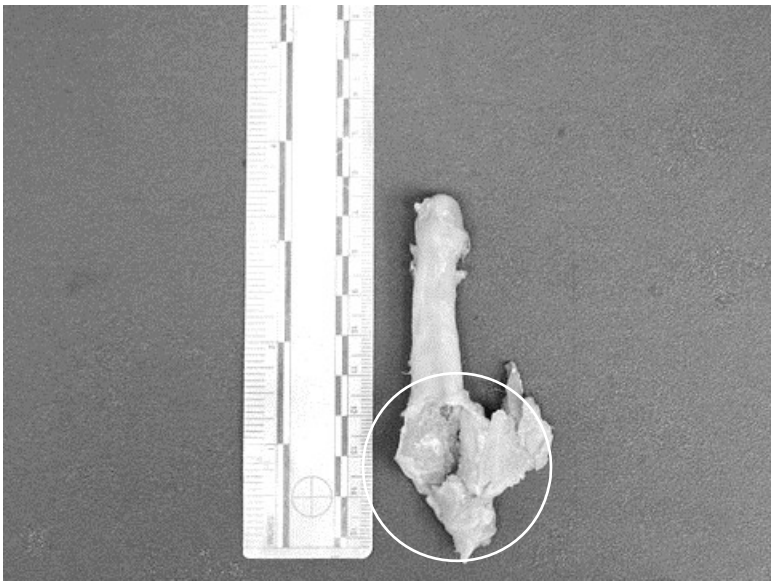

Figure E-42. Crushing of the proximal end of the left 5th metatarsal of S5C1 (superior view)

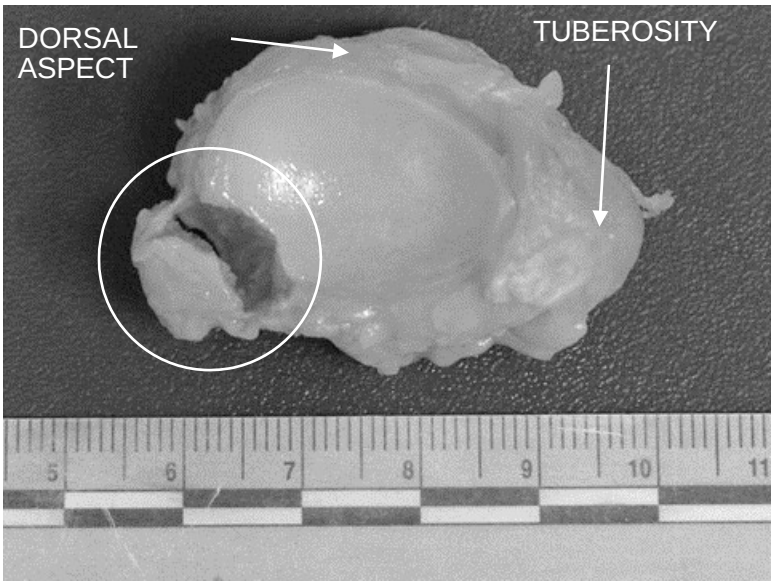

Figure E-43. Fracture of the beak of the left navicular of S5C1 (posterior view of the talar articular surface)

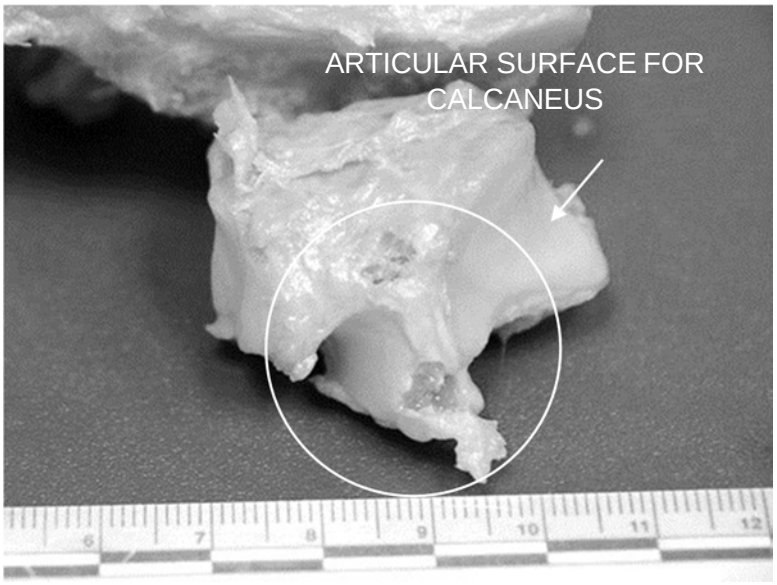

Figure E-44. Fracture to the posterior border of the dorsal surface left cuboid of S5C1 (superior/lateral view)

Figure E-45. Shattered left distal tibia of S5C1 (lateral view; fibula is also shown)

Figure E-46. Compression fracture of the left distal tibia of S5C1 (anterior view)

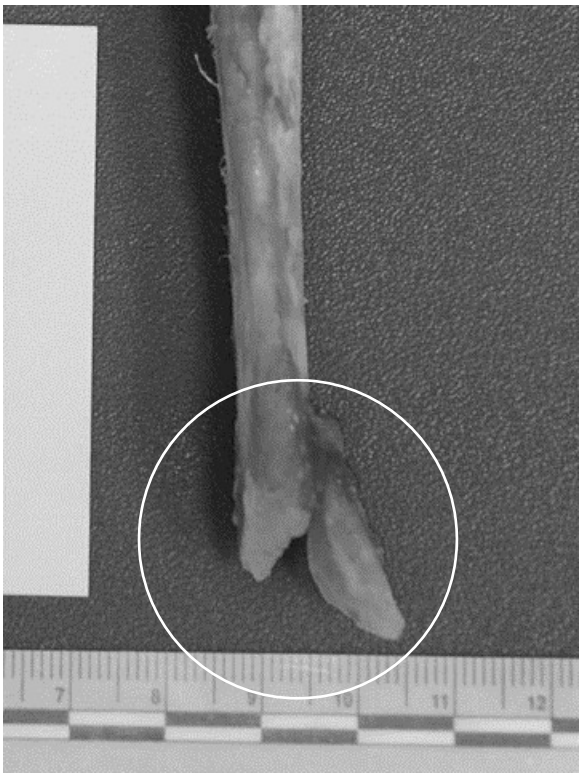

Figure E-47. Vertical fracture originating from the articular surface of the lateral malleolus of the left fibula of S5C1 (anterior view)

E.12 Female Shot 5 Crew 2: 5th percentile female

Thorax

- Rib Fractures
  - *AIS 450203.3 fracture(s) without flail, any location unilateral or bilateral NFS ≥3 ribs*
  - Right rib 2, fx (11 cm)*
  - Right rib 3, fx (15.8 cm)*
  - Right rib 4, fx (17.5 cm)*
  - Right rib 5, fx (18 cm)*
  - Right rib 6, fx (22 cm)*
  - Right rib 7, fx (17 cm)**
  - Left rib 2, fx (9.5 cm)*
  - Left rib 3, fx (15.2 cm)*
  - Left rib 4, fx (16 cm)*
  - Left rib 5, fx (16.2 cm)*
  - Left rib 6, fx (21.8 cm)*
  - Left rib 7, fx (16.5 cm)**

    - * Measured from centerline of sternum
    - ** measured from sternum attachment

Spine

- T4, burst fx (check pre- and posttest CT) – checked and it was not pre-existing in instrumentation scan, approximately 40% loss of height based on surrounding vertebral body heights
    - *AIS: 650434.3 major compression (>20% loss of anterior height)*
    - *BioPT- no bin for T-spine injury*
- L4, right. Transverse process, fx
    - *AIS: 650620.2 Lumbar spine transverse process fracture*
    - *BioPT bin 2: Posterior vertebra (simple fx; no canal compromise)*

Pelvis

- Pelvis – coccyx, 2 fx
    - *AIS 856151.2 Pelvic ring fracture, posterior arch intact; isolated fracture not destroying the integrity of the pelvic ring*
    - *BioPT bin 61-A3.1 (row 23)*
    - *OTA Pelvis 61-A3.1*

Lower Extremity

- Talus, right – transected
    - *AIS: 857261.2 fracture line into one joint surface; talus body*
    - *BioPT Bin 2: Talus fracture (fx nondisplaced or simple displacement; Hawkins Type I and II)*
    - *Hawkins Type I - nondisplaced fracture of the talar neck*
- Calcaneus, right - crushed
    - *AIS: 857371.2 fracture line into ≥2 joint surfaces*
    - *BioPT Bin 5: Calcaneus fracture (comminuted crush, comminuted, Sanders Type III and Type IV)*
    - *Sanders Type IV, 3 or more fracture lines*
- Femur, left - segmented bending fx
    - *AIS: 853271.3 complex; comminuted; segmental; Winquist IV*
    - *BioPT Bin 3: Femur shaft fracture (complex; OTA Type 32-C; Winquist IV)*
    - *OTA 32-C2: complex- segmental*
    - *Winquist IV*
- Tibia, left - pilon fx
    - *AIS: 854361.2 distal tibia, partial articular*

    - *BioPT Bin 6: Distal tibia fracture (partial articular; simple pilon; OTA Type 43-B)*
    - *OTA 43-B1 pure split*
- Calcaneus, left - crushed
    - *AIS: 857371.2 fracture line into ≥2 joint surfaces*
    - *BioPT Bin 5: Calcaneus fracture (comminuted crush, comminuted, Sanders Type III and Type IV)*
    - *Sanders Type IV, 3 or more fracture lines*
- Navicular, left - fx
    - *AIS: 857461.2 navicular fracture, fracture line into one joint surface*
    - *BioPT bin 1 Tarsal bone fracture (navicular, cuboid, and cuneiforms)*
    - Proximal 5th metatarsal, left - fx
    - *AIS 858163.2 partial articular*

Detailed damage description and photos

S5C2 sustained several rib fractures (Figures E-48 and E-49); a burst fracture of the fourth thoracic vertebra with 40% loss of height (Figure E-50); a fracture of the right transverse process of the fourth lumbar vertebra (Figure E-51); and two fractures of the coccyx (Figure E-52). The right lower extremity sustained a crushed calcaneus (Figure E-53) and transection of the body of the talus (Figure E-54). The left lower extremity sustained a fracture through the proximal end of the 5th metatarsal (Figure E-55), a fracture through the inferior and lateral corner of the navicular (Figure E-56), a crushed calcaneus (Figure E-57), a pilon fracture of the distal tibia (Figures E-58 and E-59), and a segmented bending fracture of the femur (Figure E-60).

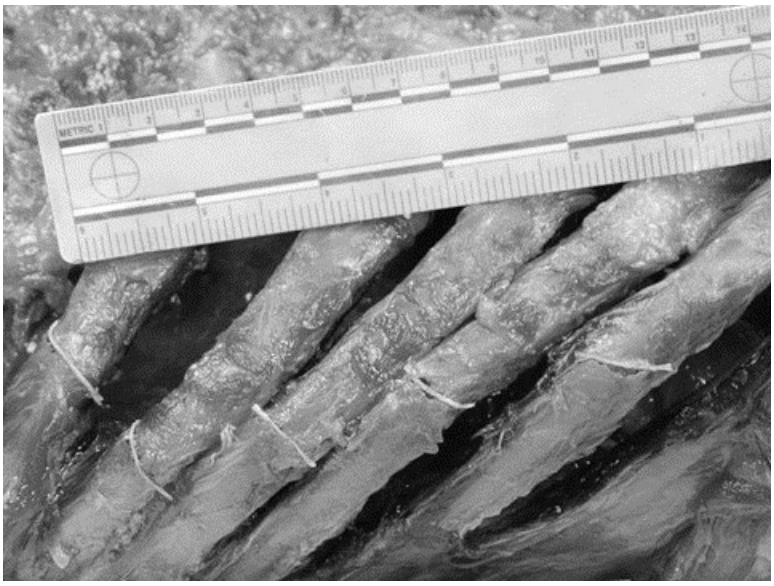

Figure E-48. Right rib fractures of S5C2. Right rib 2, 11 cm*; right rib 3, 15.8 cm*; right rib 4, 17.5 cm*; right rib 5, 18 cm*; right rib 6, 22 cm*; right rib 7, 17 cm (*, measured from centerline of sternum; **, measured from sternum attachment)**

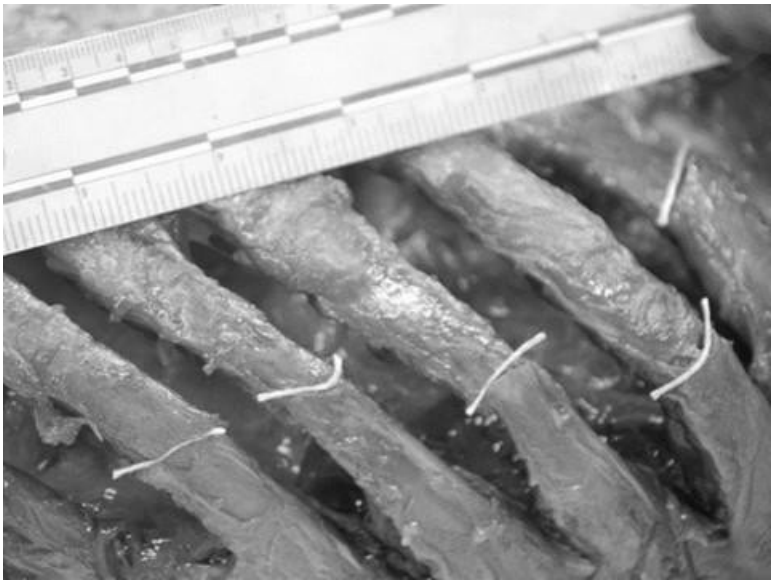

Figure E-49. Left rib fractures of S5C2. Left rib 2, 9.5 cm*; left rib 3, 15.2 cm*; left rib 4, 16 cm*; left rib 5, 16.2 cm*; left rib 6, 21.8 cm*; left rib 7, 16.5 cm (*, measured from centerline of sternum; **, measured from sternum attachment)**

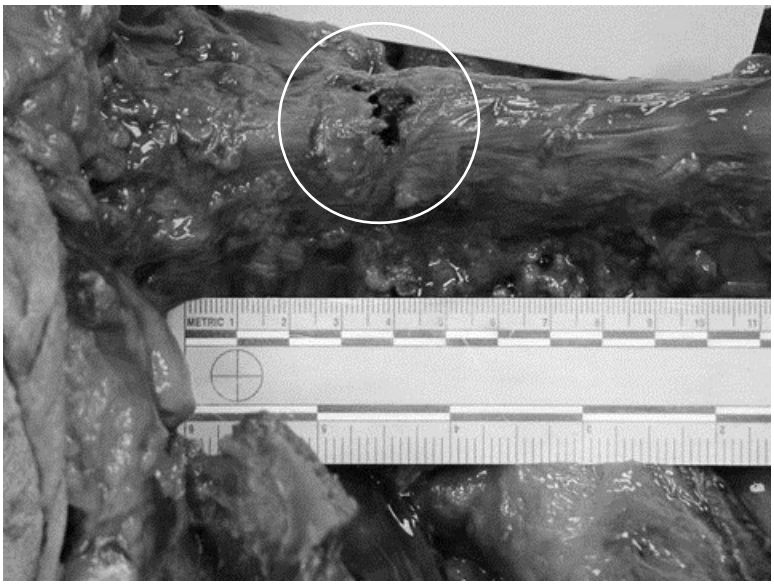

Figure E-50. Burst fracture of the fourth thoracic vertebra of S5C2

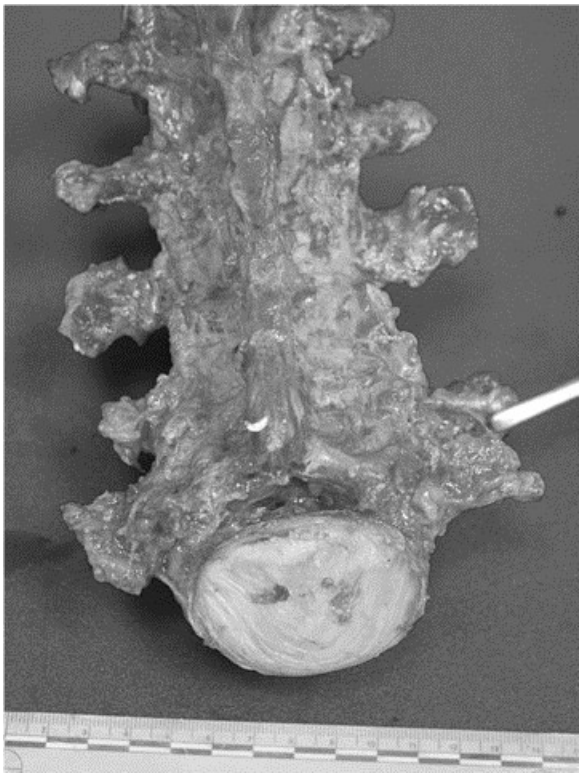

Figure E-51. Fracture of the right transverse process of the fourth lumbar vertebra of S5C2

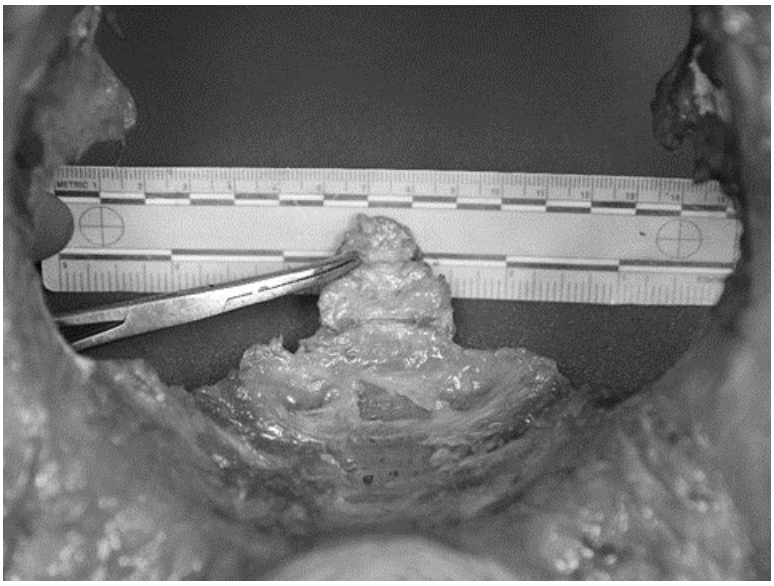

Figure E-52. Fractures of the coccyx of S5C2

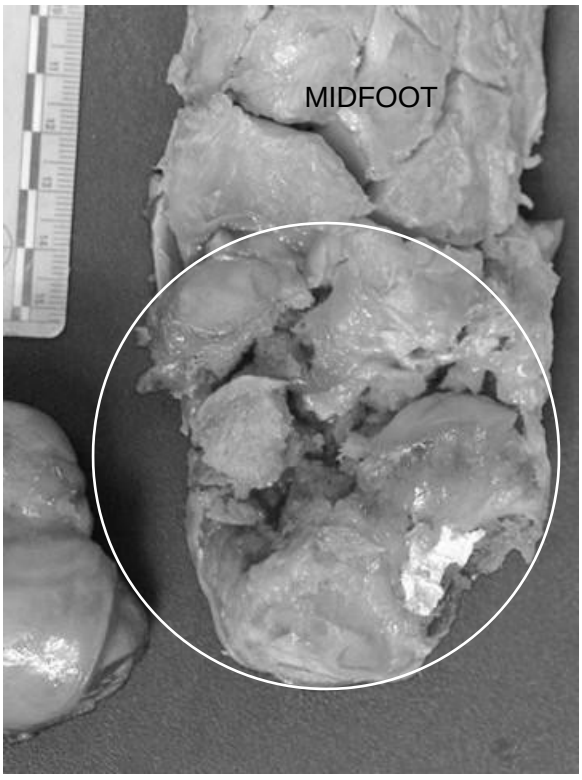

Figure E-53. Crushed right calcaneus of S5C2 (superior view; talus is also shown on bottom left)

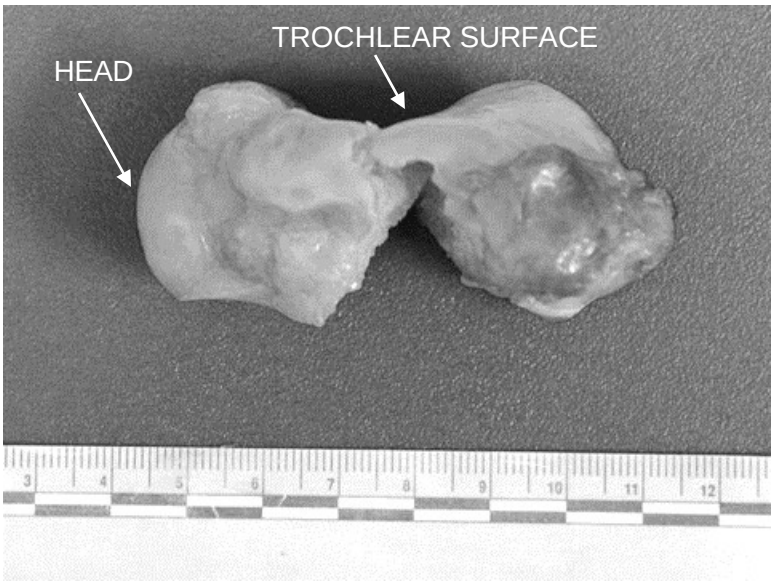

Figure E-54. Transection through body of right talus of S5C2 (medial view)

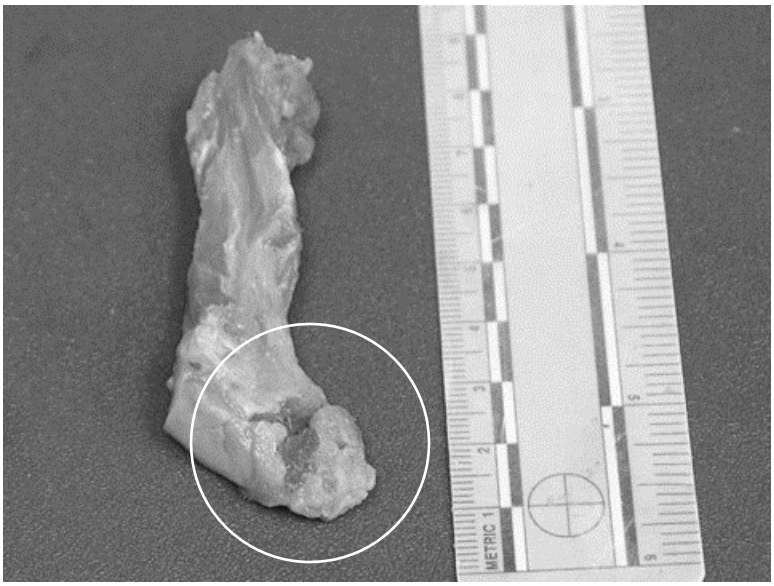

Figure E-55. Crushing fracture of the proximal end of left 5th metatarsal of S5C2 (medial view)

Figure E-56. Fracture of the beak of the left navicular of S5C2 (posterior view, talus removed)

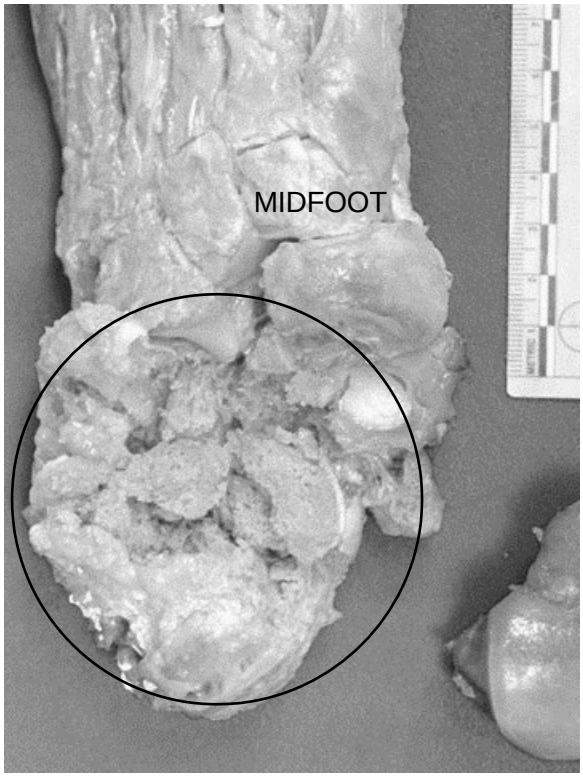

Figure E-57. Crushed left calcaneus of S5C2 (anterior view; talus is also shown on bottom right)

Figure E-58. Compression fracture of the left distal tibia of S5C2 (anterior view)

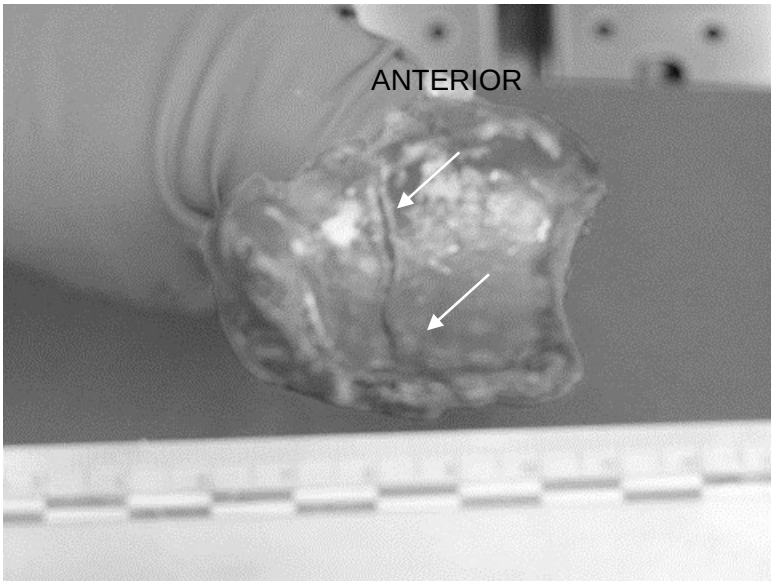

Figure E-59. Pilon fracture originating at the tibial plafond oriented from anterior to posterior of the left tibia of S5C2 (inferior view)

Figure E-60. Fracture of left femur of S5C2 (anterior view, with the left side of the photo being proximal)

E.13 Female Shot 6 Crew 1: 50th percentile male

Thorax

- Rib Fractures:
  - *AIS 450203.3 fracture(s) without flail, any location unilateral or bilateral NFS ≥3 ribs*
  - Right rib 3, fx (8.5 cm)*
  - Right rib 4, fx (9.1 cm)*
  - Right rib 5, fx (3.6 cm)*
  - Right rib 6, fx (3.8, 10.2 cm)*
  - Left rib 4, fx (at sternum attachment, 5.8 cm)*
  - Left rib 5, fx (9.7 cm)*
  - Left rib 6, fx (11.3 cm)*

  * Measured from midline of sternum

Spine

- L1–L3 bilateral transverse process, fx
  - *AIS: 650620.2 Lumbar spine transverse process fracture*
  - *BioPT bin 2: Posterior vertebra (simple fx; no canal compromise)*

Pelvis

- Pelvis – coccyx, fx
    - *AIS 856151.2 Pelvic ring fracture, posterior arch intact; isolated fracture not destroying the integrity of the pelvic ring*
    - *BioPT bin 61-A3.1 (row 23)*
    - *OTA pelvis 61-A3.1*

Lower Extremity

- Calcaneus, right - crushed
    - *AIS: 857371.2 fracture line into ≥2 joint surfaces*
    - *BioPT Bin 5: Calcaneus fracture (comminuted crush, comminuted, Sanders Type III and Type IV)*
    - *Sanders Type IV, 3 or more fracture lines*
- Femur, left - spiral wedge fx
    - *AIS: 853261.3 wedge; "butterfly"; Winquist II or III*
    - *BioPT Bin 2: Femur shaft fracture (wedge; OTA Type 32-B; Winquist II/III)*
    - *OTA Bin 32-B1 spiral wedge*
- Calcaneus, left - crushed
    - *AIS: 857371.2 fracture line into ≥2 joint surfaces*
    - *BioPT Bin 5: Calcaneus fracture (comminuted crush, comminuted, Sanders Type III and Type IV)*
    - *Sanders Type IV, 3 or more fracture lines*
- Proximal 4th metatarsal, left - fx

Detailed damage description and photos

S6C1 sustained several rib fractures (Figure E-61), bilateral transverse process fractures of the first through third lumbar vertebrae (Figure E-62), and a fracture of the coccyx (Figure E-63). The right lower extremity sustained a crushed calcaneus (Figure E-64), whereas the left lower extremity sustained 2 fractures through the proximal end of the fourth metatarsal (Figure E-65), a crushed calcaneus (Figure E-66), and a spiral wedge fracture of the femur (Figures E-67, E-68, and E-69).

Figure E-61. Rib fractures of S6C1. Right rib 3, 8.5 cm*; right rib 4, 9.1 cm*; right rib 5, 3.6 cm*; right rib 6, 3.8 and 10.2 cm*; left rib 4, 5.8 cm; left rib 5, 9.7 cm*; left rib 6, 11.3 cm* (*, measured from midline of sternum; **, measured from sternum attachment)**

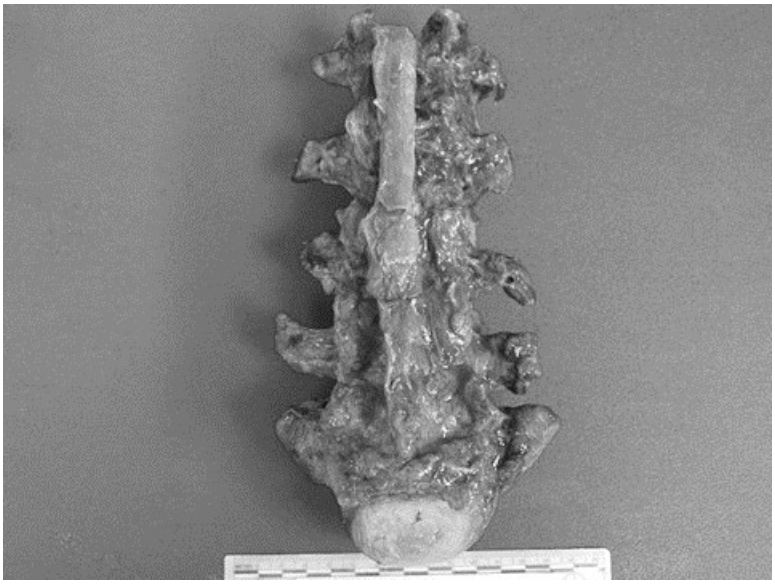

Figure E-62. Transverse process fractures of S6C1 (L1–L3, bilateral)

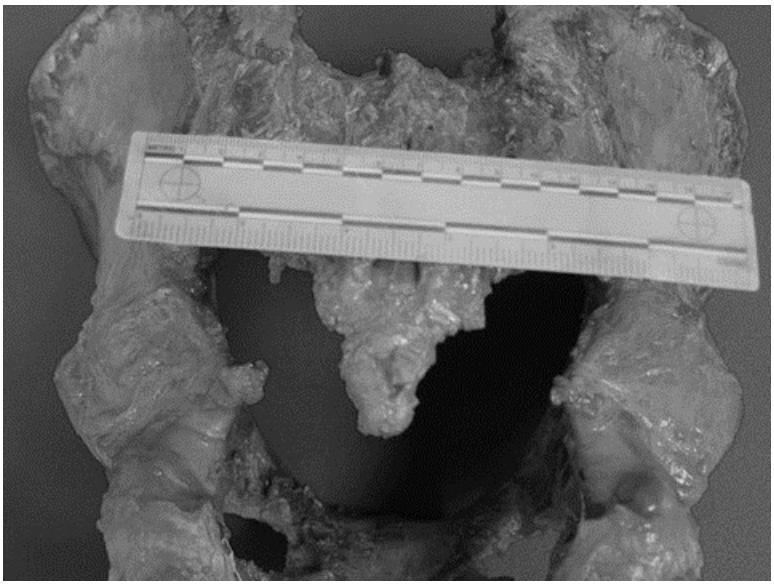

Figure E-63. Fracture to the coccyx of S6C1

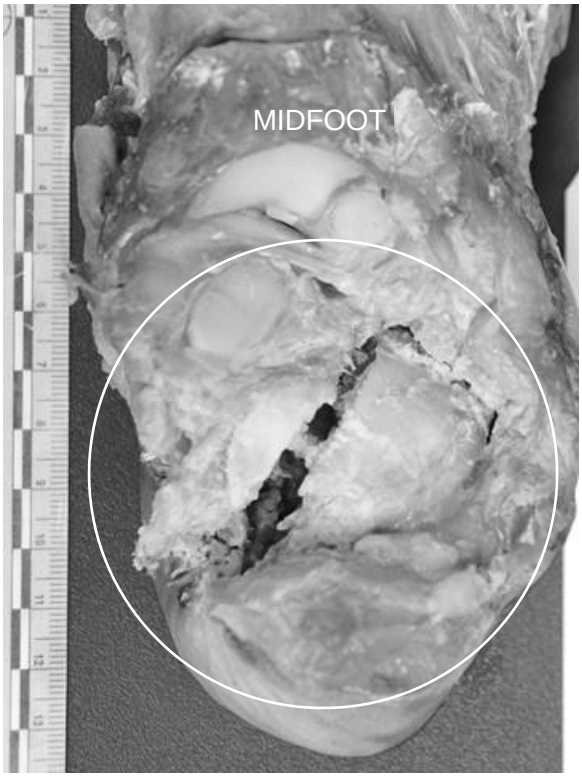

Figure E-64. Crushed right calcaneus of S6C1 (superior view)

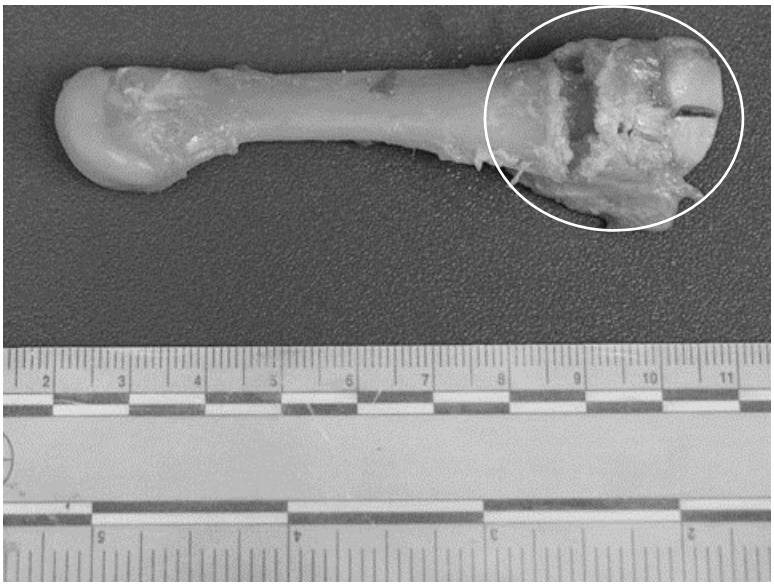

Figure E-65. Fracture of the proximal 4th metatarsal of S6C1 (superior view)

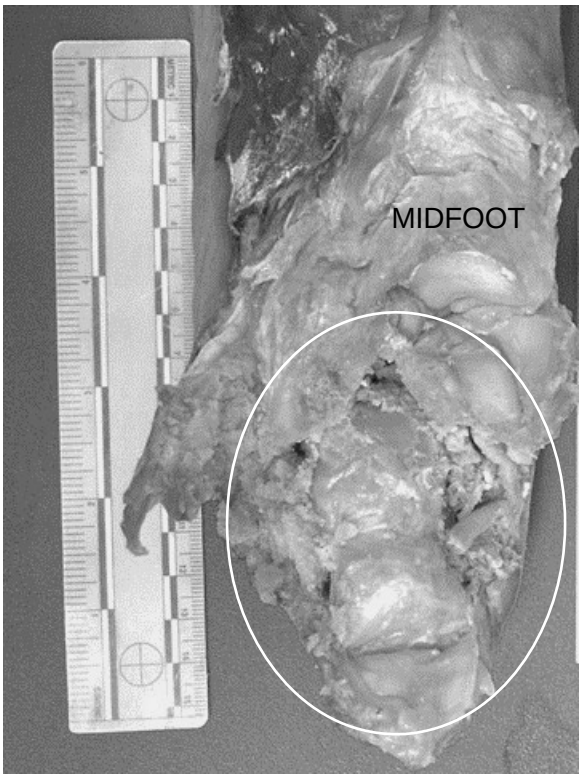

Figure E-66. Crushed left calcaneus of S6C1 (superior view)

Figure E-67. Fracture of the left femur of S6C1 (anterior view, left side of photo is distal)

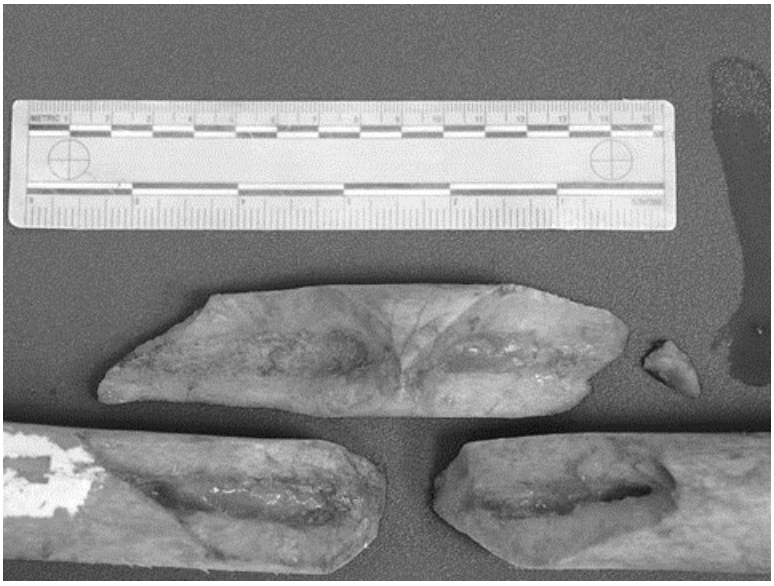

Figure E-68. Fracture of the left femur of S6C1 with fragment removed (anterior view, left side of photo is distal)

Figure E-69. Fracture of the left femur of S6C1 (right lateral view, left side of photo is proximal)

E.14 Female Shot 6 Crew 2: 5th percentile female

Thorax

- Left rib 5, fx (15.7 cm) (measured from midline of sternum)
  - *AIS: 450201.1 one rib [OIS I], fracture(s) without flail, any location*

Spine

- L1 right. Transverse process, fx
  - *AIS: 650620.2 Lumbar spine transverse process fracture*
  - *BioPT bin 2: Posterior vertebra (simple fx; no canal compromise)*

Pelvis

- Pelvis – coccyx, fx
  - *AIS 856151.2 Pelvic ring fracture, posterior arch intact; isolated fracture not destroying the integrity of the pelvic ring*
  - *BioPT bin 61-A3.1 (row 23)*
  - *OTA pelvis 61-A3.1*

Lower Extremity

- Calcaneus, right - crushed
  - *AIS: 857371.2 fracture line into ≥2 joint surfaces*

    - *BioPT Bin 5: Calcaneus fracture (comminuted crush, comminuted, Sanders Type III and Type IV)*
    - *Sanders Type IV, 3 or more fracture lines*
- Navicular, right - fx
    - *AIS: 857451.2 extra articular [coronal body split, no joint involvement]*
    - *BioPT Bin 1: Tarsal bone fracture (navicular, cuboid, and cuneiforms)*
- Talus, left - fx
    - *AIS: 857261.2 fracture line into one joint surface; talus body*
    - *BioPT Bin 2: Talus fracture (fx nondisplaced or simple displacement; Hawkins Type I and II)*
    - *No Hawkins classification, not a neck fracture*
- Calcaneus, left - crushed
    - *AIS: 857371.2 fracture line into ≥2 joint surfaces*
    - *BioPT Bin 5: Calcaneus fracture (comminuted crush, comminuted, Sanders Type III and Type IV)*
    - *Sanders Type IV, 3 or more fracture lines*

Detailed damage description and photos

S6C2 sustained one rib fracture (Figure E-70), a fracture of the right transverse process of the first lumbar vertebra (Figure E-71), and a fracture of the coccyx (Figure E-72). The right lower extremity sustained a crushed calcaneus (Figure E-73) and some damage to the inferior and lateral aspect of the articular surface for the calcaneus on the navicular (Figure E-74). The left lower extremity sustained a crushed calcaneus (Figure E-75) and a fracture of the lateral aspect of the posterior facet of the talus (Figure E-76).

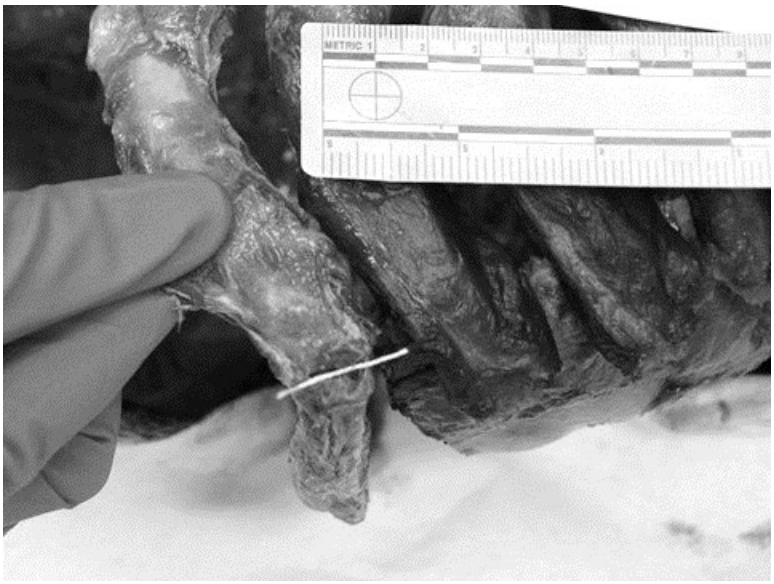

Figure E-70. Fracture of rib of S6C2. Left rib 5, 15.7 cm measured from midline of sternum

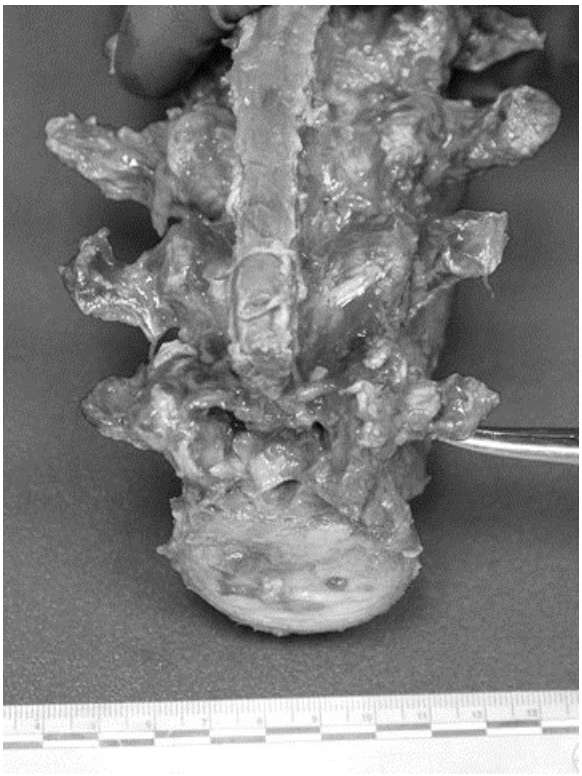

Figure E-71. Fracture of the right transverse process of the first lumbar vertebra of S6C2

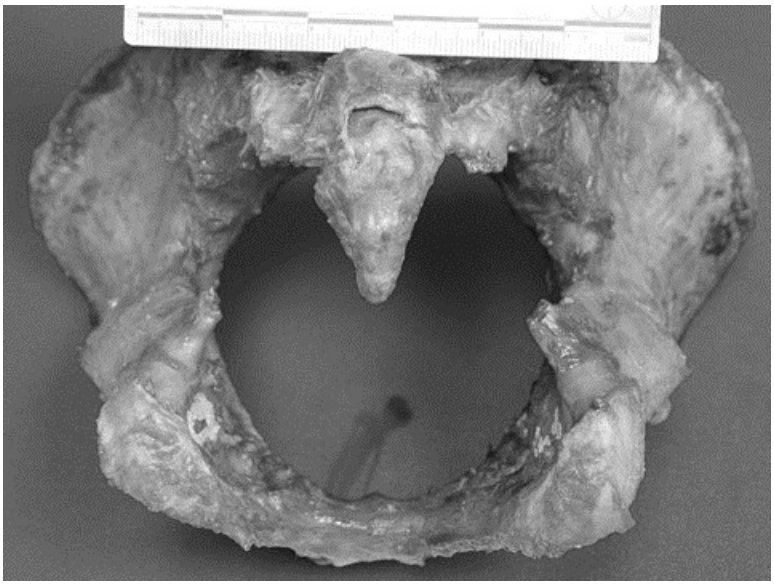

Figure E-72. Fracture of the coccyx of S6C2

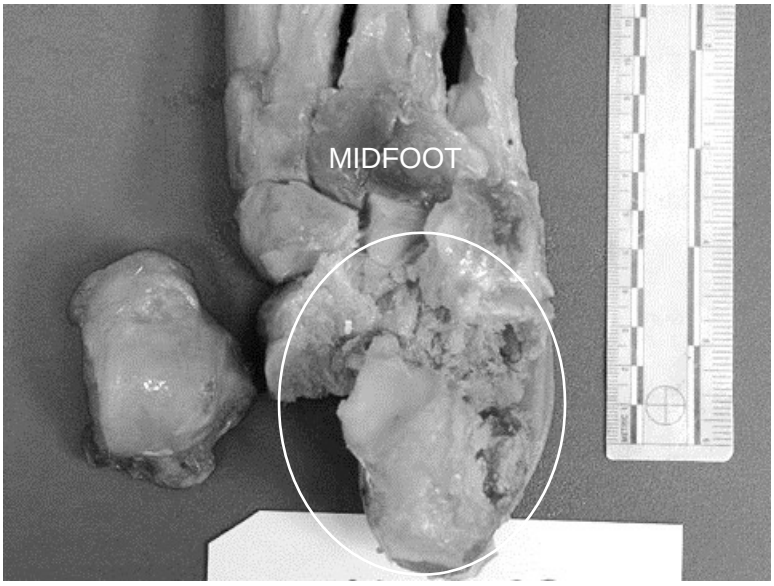

Figure E-73. Crushed right calcaneus of S6C2 (superior view, right talus is included)

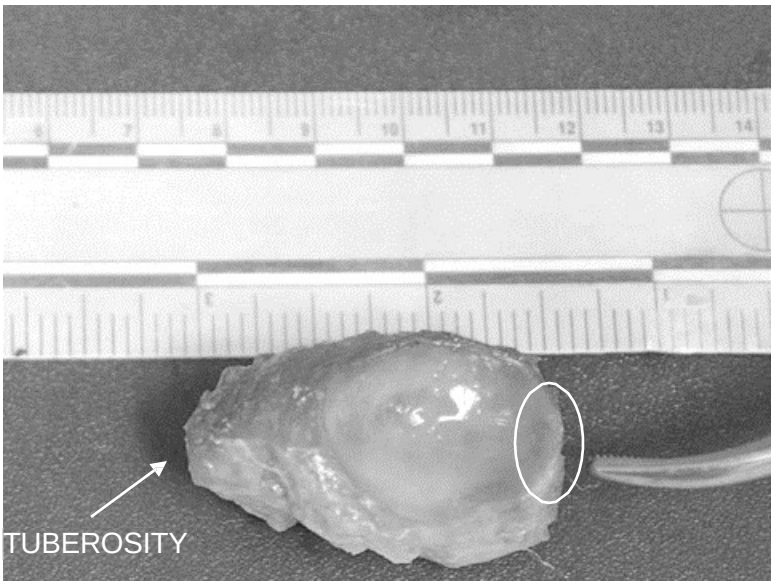

Figure E-74. Damage to the lateral border of the dorsal surface of the right navicular of S6C2 (posterior view of articular surface for talus)

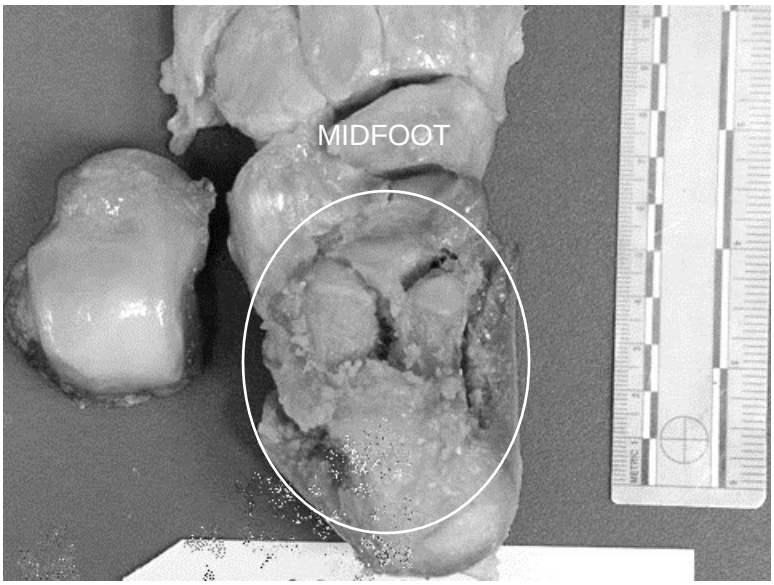

Figure E-75. Crushed left calcaneus of S6C2 (superior view)

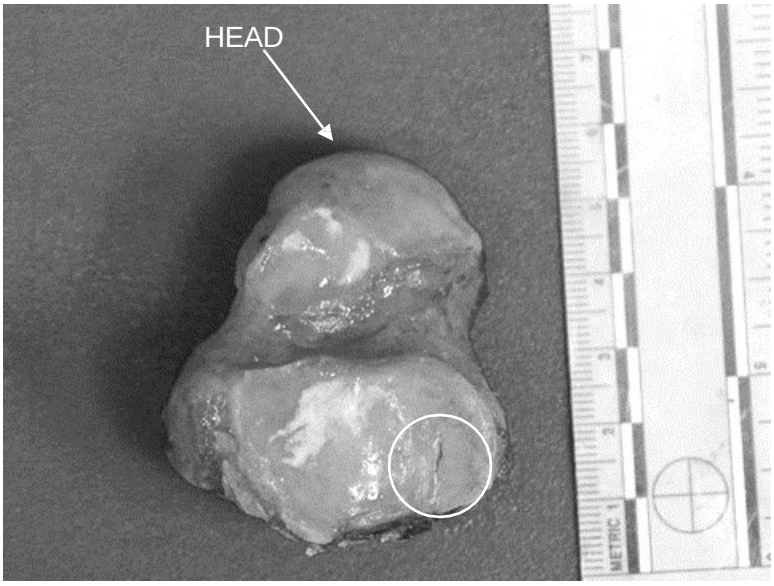

Figure E-76. Fracture to the lateral aspect of the posterior calcaneal articular surface of the talar body of the left talus of S6C2 (inferior view)

E.15 Female Shot 7 Crew 1: 50th percentile male

Thorax

- None

Spine

- L1 right. transverse process, fx
  - *AIS: 650620.2 Lumbar spine transverse process fracture*
  - *BioPT bin 2: Posterior vertebra (simple fx; no canal compromise)*
- L4, burst fx- not substantial loss of height
  - *AIS: vertebral body fx: 650632.2 minor compression (≤20% loss of anterior height)*
  - *BioPT bin 1: VB (simple fx; no canal compromise)*

Pelvis

- Pelvis – coccyx, fx
  - *AIS 856151.2 Pelvic ring fracture, posterior arch intact; isolated fracture not destroying the integrity of the pelvic ring*
  - *BioPT bin 61-A3.1 (row 23)*
  - *OTA pelvis 61-A3.1*

Lower Extremity

- Calcaneus, left - sectioned
    - *AIS: 857371.2 fracture line into ≥2 joint surfaces*
    - *BioPT Bin 5: Calcaneus fracture (comminuted crush, comminuted, Sanders Type III and Type IV)*
    - *Sanders Type IV, 3 or more fracture lines*

Detailed damage description and photos

S7C1 sustained a fracture of the right transverse process of the first lumbar vertebra (Figure E-77), a burst fracture of the body of the fourth lumbar vertebra without a substantial loss of height (Figures E-78, E-79, E-80, and E-81), and a fracture of the coccyx (Figure E-82). The left calcaneus was sectioned, showing crush fractures (Figure E-83).

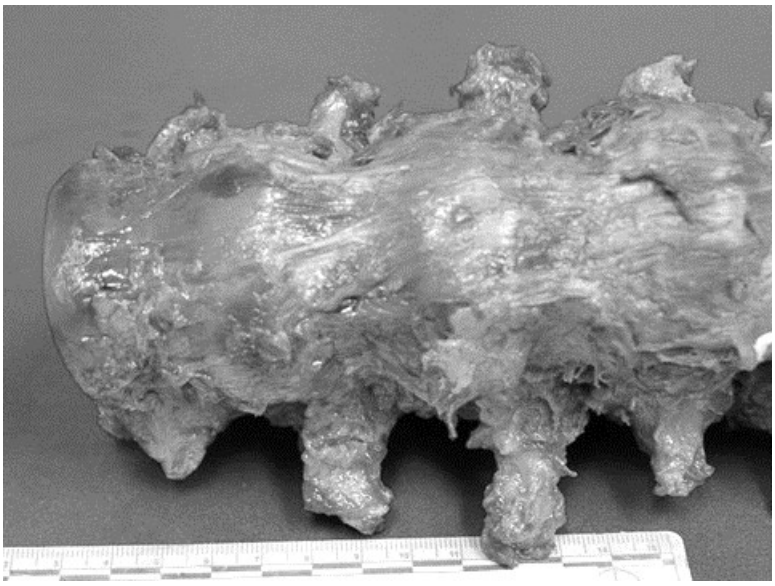

Figure E-77. Facture of the right transverse process of the first lumbar vertebra of S7C1

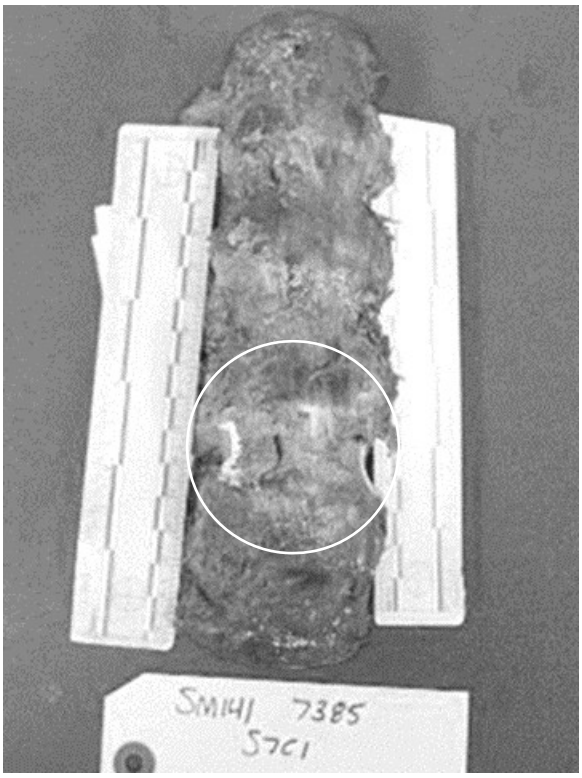

Figure E-78. Burst fracture of the body of L4 of S7C1 (anterior view)

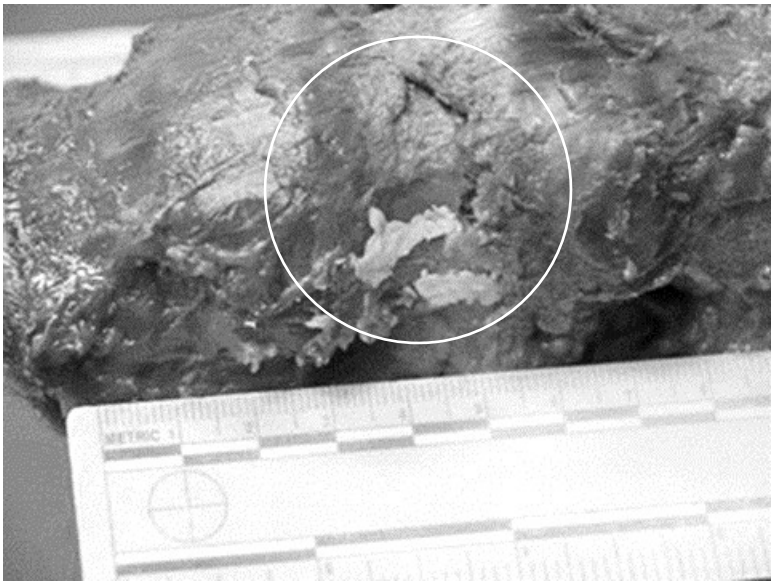

Figure E-79. Burst fracture of the body of L4 of S7C1 (left lateral view, close-up)

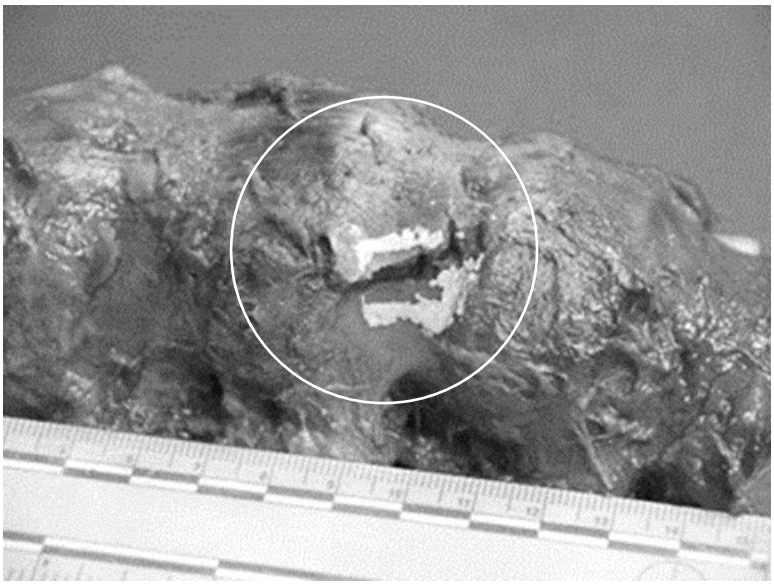

Figure E-80. Burst fracture of the body of L4 of S7C1 (right lateral view, close-up)

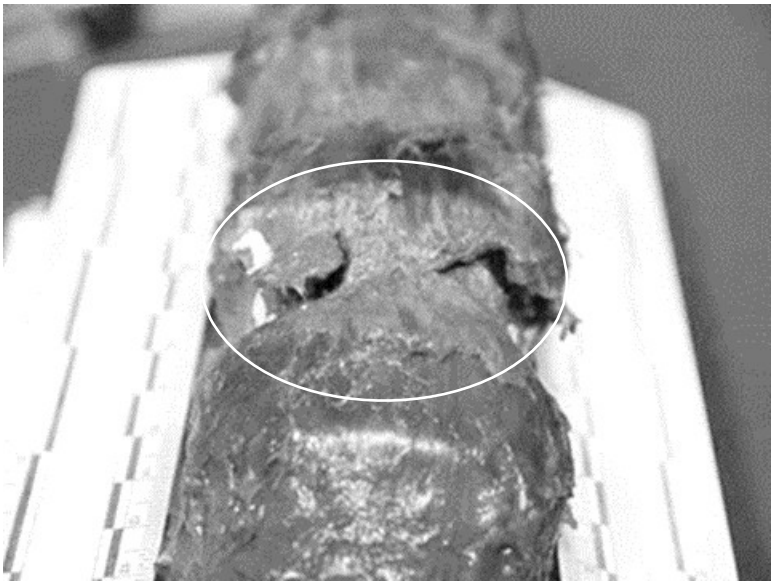

Figure E-81. Burst fracture of the body of L4 of S7C1 (inferior view, close-up)

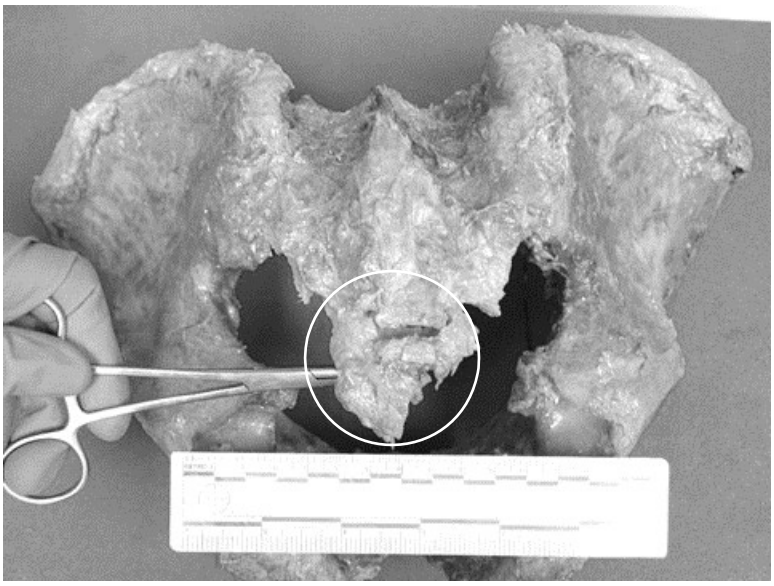

Figure E-82. Fracture of the coccyx of S7C1

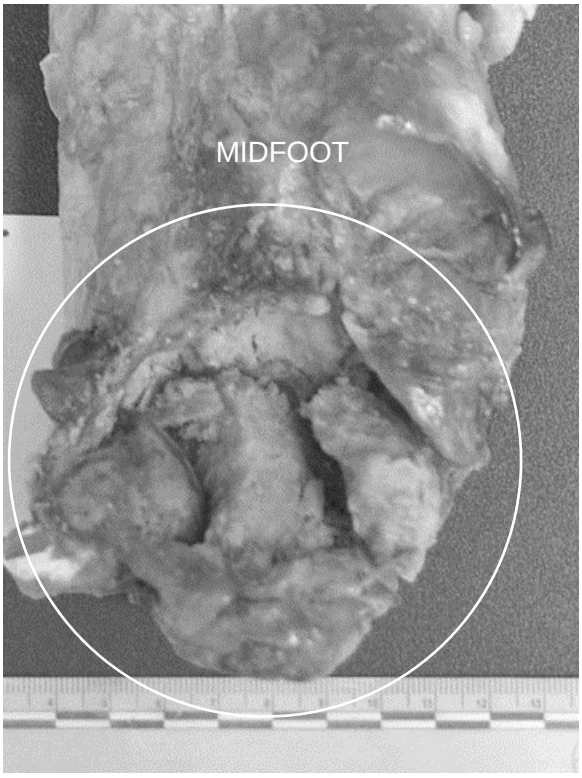

Figure E-83. Crushed left calcaneus of S7C1 (superior view)

E.16 Female Shot 7 Crew 2: 75th percentile female

Thorax

- None

Spine

- L1 bilateral transverse process, fx
  - *AIS: 650620.2 Lumbar spine transverse process fracture*
  - *BioPT bin 2: Posterior vertebra (simple fx; no canal compromise)*
- L2, burst fx- less than 20% loss of height
  - *AIS: vertebral body fx: 650632.2 minor compression (≤20% loss of anterior height)*
  - *BioPT bin 1: VB (simple fx; no canal compromise)*

Pelvis

- Pelvis – bilateral ischial tuberosity, chip fx
  - *AIS 856151.2 Pelvic ring fracture, posterior arch intact; isolated fracture not destroying the integrity of the pelvic ring (but this would not be coded separately from below)*
  - *BioPT bin 61-A1.3 (row 11)*
  - *OTA pelvis 61-A1.3*
- Pelvis – coccyx, fx
  - *AIS 856151.2 Pelvic ring fracture, posterior arch intact; isolated fracture not destroying the integrity of the pelvic ring*
  - *BioPT bin 61-A3.1 (row 23)*
  - *OTA pelvis 61-A3.1*
  - *Not coded separately from above (AIS)*

Lower Extremity

- Talus, right - 2 fx
  - *AIS: 857261.2 fracture line into one joint surface; talus body*
  - *BioPT Bin 2: Talus fracture (fx nondisplaced or simple displacement; Hawkins Type I and II)*
  - *No Hawkins classification, not a neck fracture*
- Calcaneus, right - crushed
  - *AIS: 857371.2 fracture line into ≥2 joint surfaces*
  - *BioPT Bin 5: Calcaneus fracture (comminuted crush, comminuted, Sanders Type III and Type IV)*

    - *Sanders Type IV, 3 or more fracture lines*
- Navicular, right - fx
    - *AIS: 857451.2 extra articular [coronal body split, no joint involvement]*
    - *BioPT Bin 1: Tarsal bone fracture (navicular, cuboid, and cuneiforms)*
- Distal tibia, left - shattered
    - *AIS: 854371.2 distal tibia complete articular*
- *BioPT Bin 7: Distal tibia fracture (complete articular; comminuted pilon; OTA Type 43-C)*
    - *OTA Type 43-C3 articular multifragmentary*
- Fibula, left - 2 fx
    - *AIS: 854471.2 fibula above joint (suprasyndesmotic); isolated shaft, head or neck; Weber C*
    - *BioPT Bin- no bin*
    - *OTA 44-C1 fibular diaphyseal fracture, simple*
    - *Weber C*
- Talus, left - cartilage damage
    - *AIS- no code for cartilage damage*
- Calcaneus, left - sectioned
    - *AIS: 857371.2 fracture line into ≥2 joint surfaces*
    - *BioPT Bin 5: Calcaneus fracture (comminuted crush, comminuted, Sanders Type III and Type IV)*
    - *Sanders Type IV, 3 or more fracture lines*

Detailed damage description and photos

S7C2 sustained fractures to both transverse processes of the first lumbar vertebra (Figure E-84), a burst fracture of the body of the second lumbar vertebra with less than 20% loss of height (Figures E-85 and E-86), bilateral chip fractures of the ischial tuberosities (Figures E-87 and E-88), and a fracture of the coccyx (Figure E-89). The right lower extremity sustained a crushed calcaneus (Figure E-90), fractures of the talus on the posterior facet and the trochlea (Figures E-91, E-92, and E-93), and a fracture through the inferior aspect of the navicular (Figure E-94). The left lower extremity sustained a shattered distal tibia (Figure E-95), an oblique fracture of the distal diaphysis of the fibula (Figure E-96), a partial separation of the head of the fibula (Figure E-97), and a sectioned calcaneus (Figure E-98).

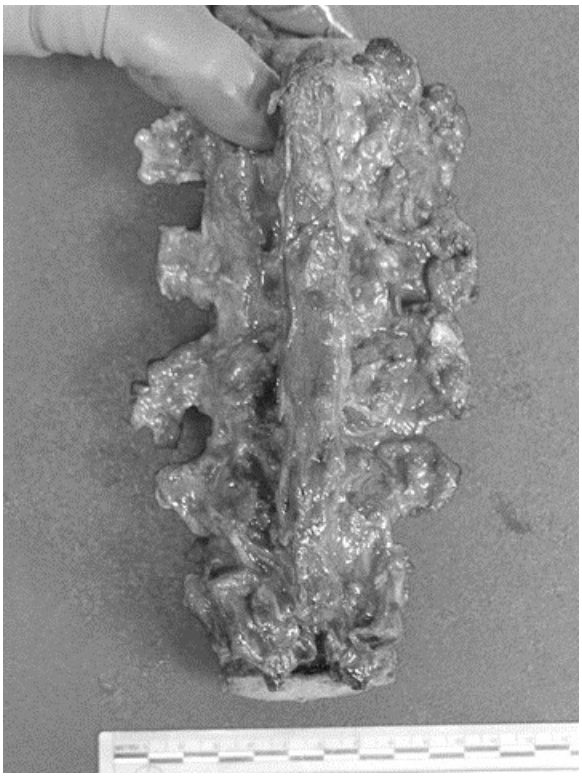

Figure E-84. Bilateral fractures of the transverse processes of the first lumbar vertebra of S7C2

Figure E-85. Burst fracture of L2 of S7C2 (left lateral view)

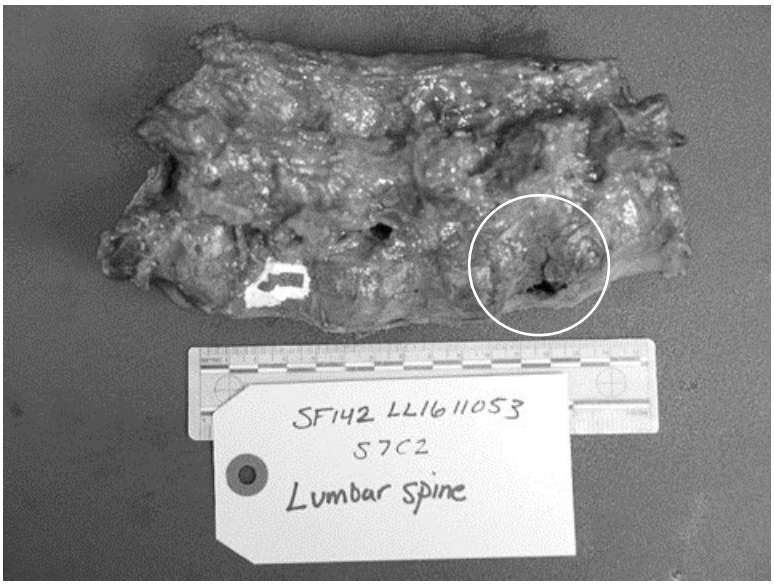

Figure E-86. Burst fracture of L2 of S7C2 (right lateral view)

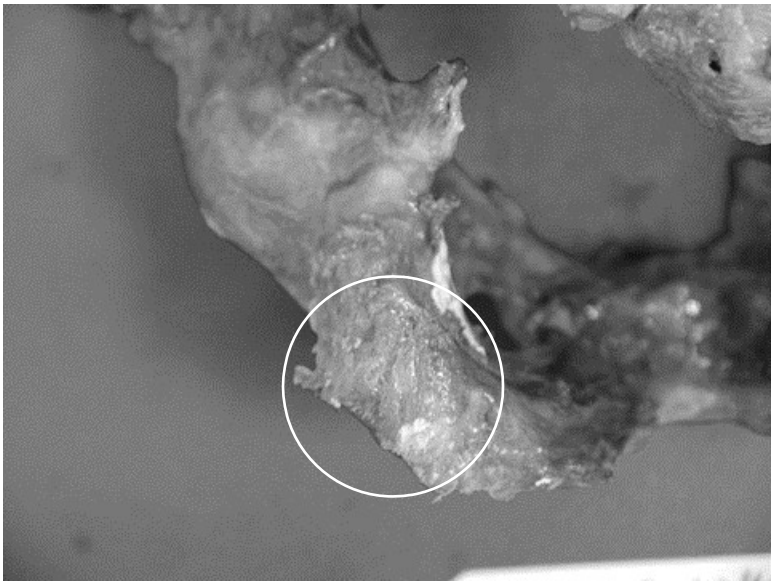

Figure E-87. Chip fracture of the left ischial tuberosity of S7C2

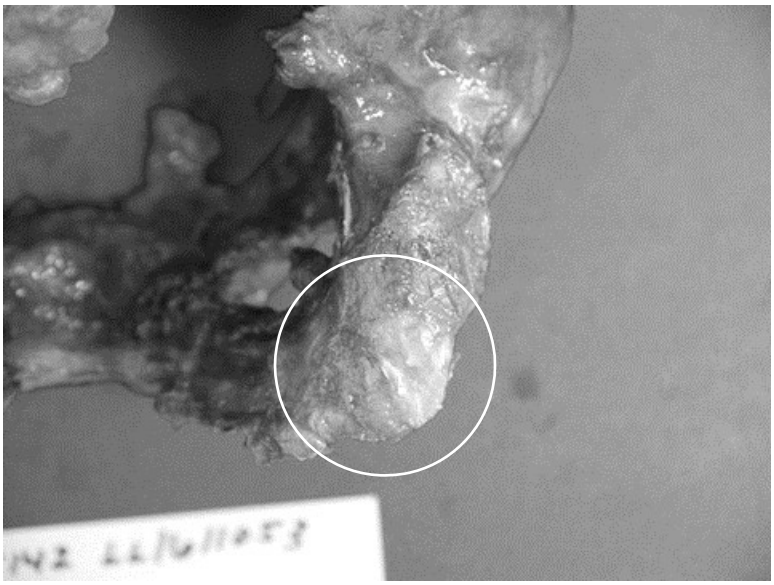

Figure E-88. Chip fracture of the right ischial tuberosity of S7C2

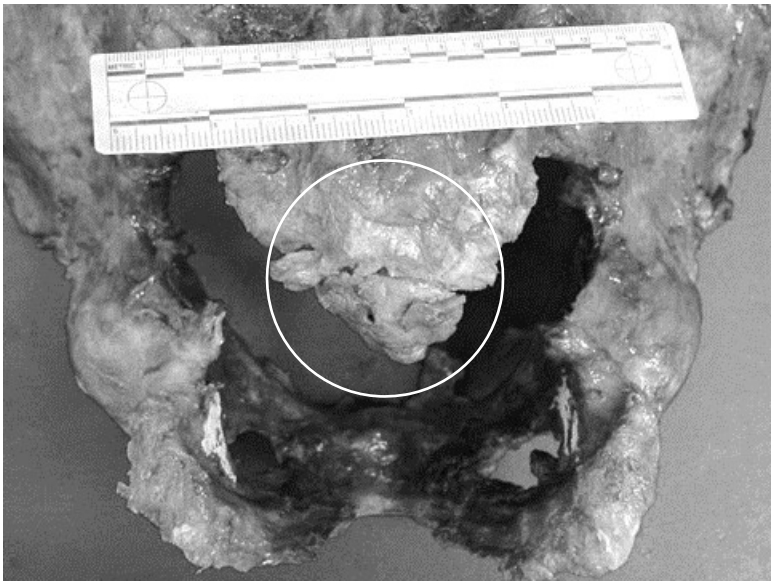

Figure E-89. Coccyx fracture of S7C2

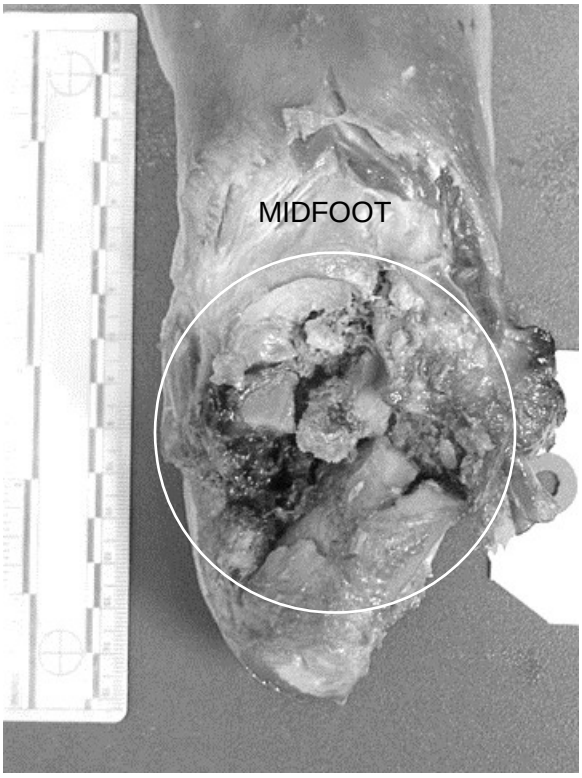

Figure E-90. Crushed right calcaneus of S7C2 (superior view)

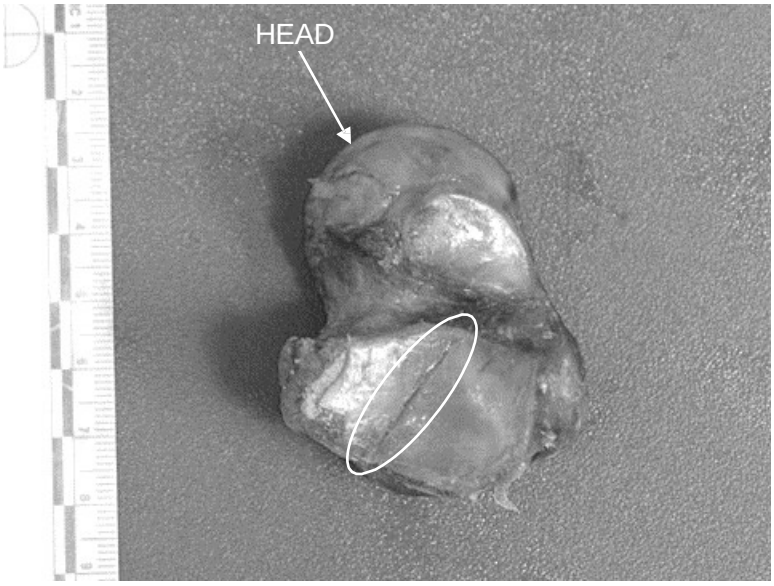

Figure E-91. Fracture to the posterior calcaneal articular surface of the talar body of the right talus of S7C2 (inferior view)

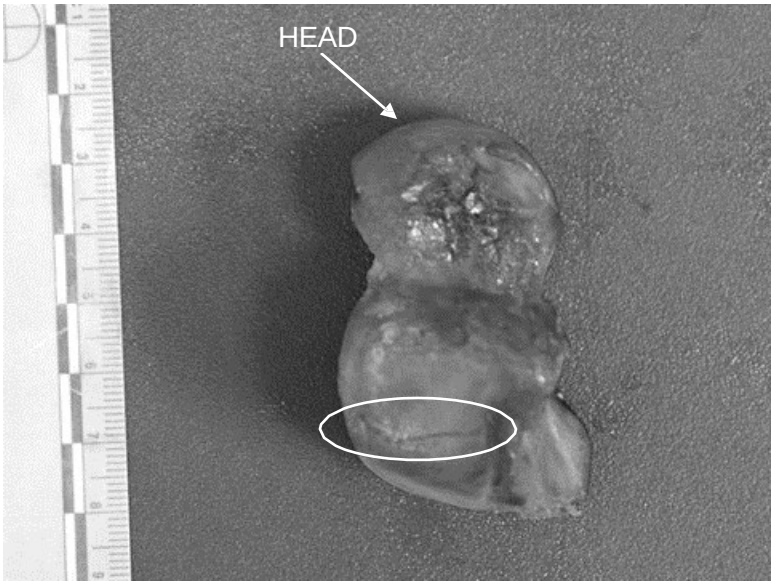

Figure E-92. Fracture of the articular surface—facies malleolus lateralis of the right talus of S7C2 (lateral view)

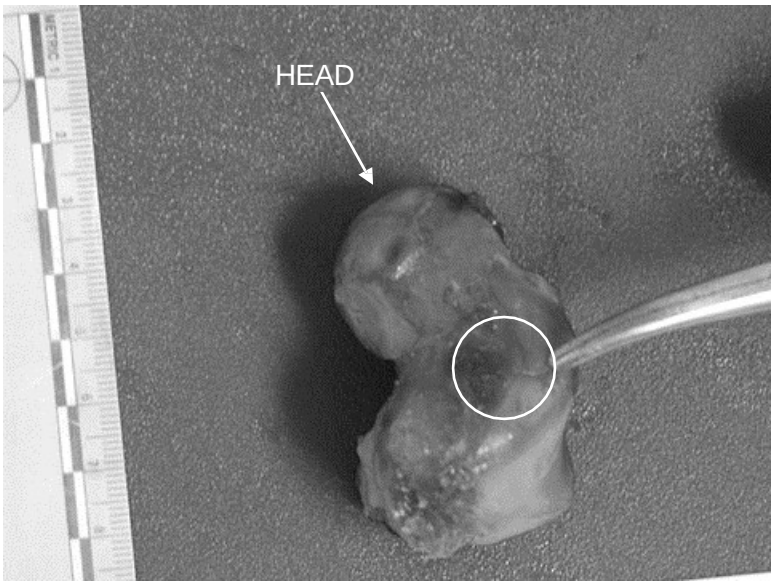

Figure E-93. Fracture to the articular surface—facies malleolaris medialis of the right talus of S7C2 (medial view)

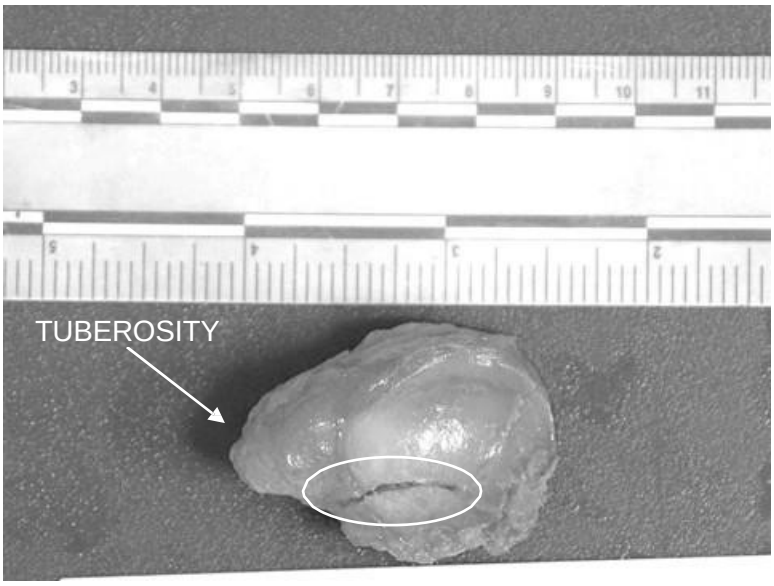

Figure E-94. Fracture of the beak of the right navicular of S7C2 (posterior view of talar articular surface)

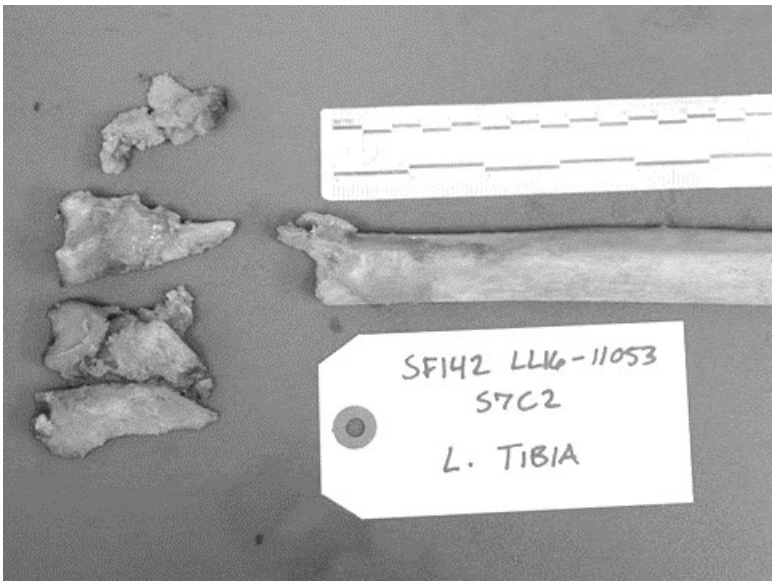

Figure E-95. Shattered left distal tibia of S7C2 (anterior view)

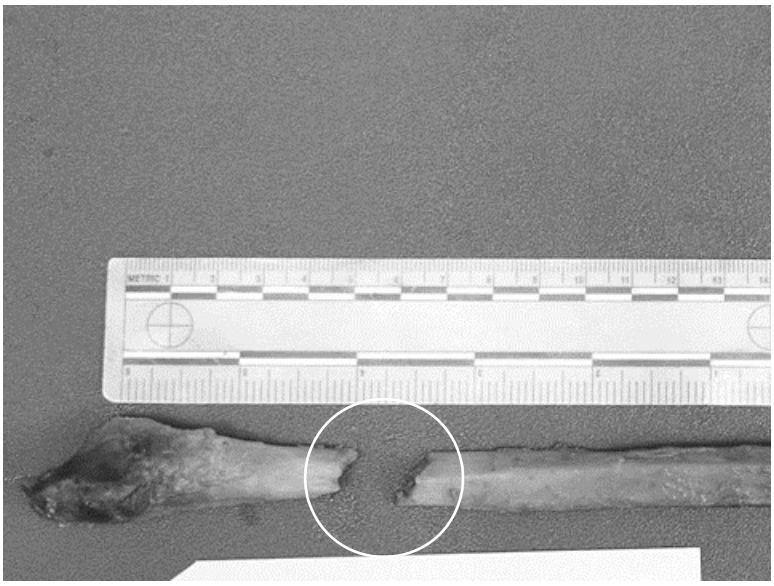

Figure E-96. Oblique fracture of the left distal fibula of S7C2 (anterior view)

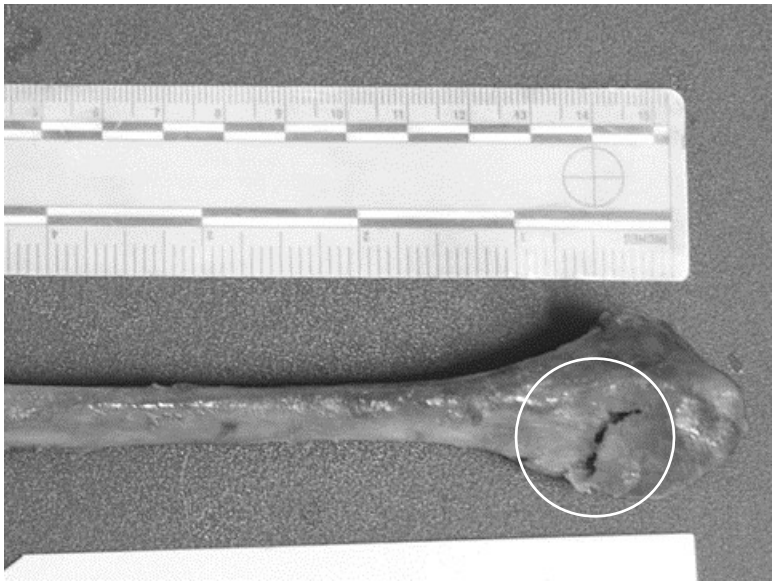

Figure E-97. Fracture of the head of the left fibula of S7C2 (lateral view)

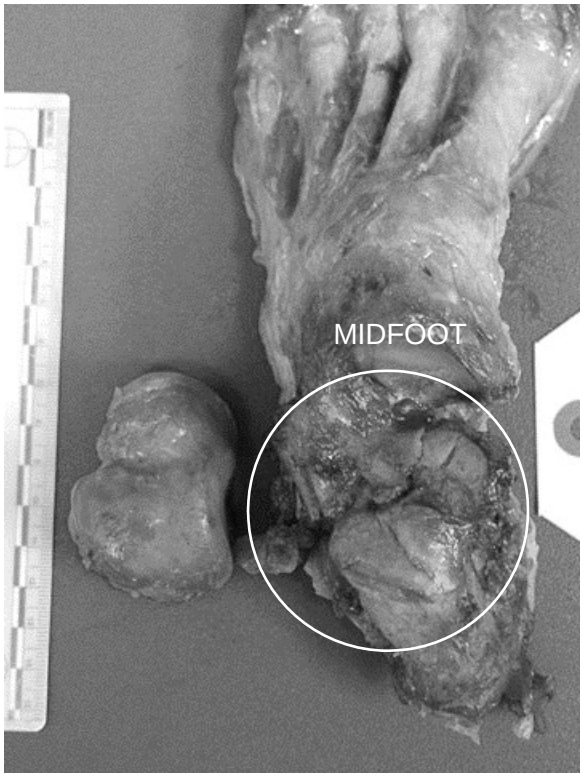

Figure E-98. Crushed left calcaneus of S7C2 (superior view)

E.17 Female Shot 8 Crew 1: 50th percentile male

Thorax

- None

Spine

- L4 Mild anterior wedge fx proximal to superior endplate (flexion)
  - *AIS 650630.2: Vertebral body NFS (until verified with radiology; if mild wedge, it will be 650632.2: vertebral body, minor compression (20% loss of anterior height)*
  - *BioPT bin 1: VB (simple fx; no canal compromise)*

Pelvis

- Coccyx - First, second, and third joint from caudal fx/dislocation; fx/dislocation of coccyx from sacrum
  - *AIS 856151.2 Pelvic ring fracture, posterior arch intact; isolated fracture not destroying the integrity of the pelvic ring (but this would not be coded separately from below)*

- *BioPT bin 61-A3.1 (row 23)*
- *OTA pelvis 61-A3.1*

Lower Extremity

- Tibia, right - minor damage to the anterior and posterior margins of the plafond. Posterior damage corresponds to posterior damage on the talus (plantar flexion)
  - *AIS: 854361.2 distal tibia, partial articular*
  - *BioPT Bin 6: Distal tibia fracture (partial articular; simple pilon; OTA Type 43-B)*
  - *OTA 43-B1 pure split*
- Talus, right - cartilage damage to posterolateral portion of articular surface for tibia; fx of posterior process
  - *AIS: 857261.2 fracture line into one joint surface; talus body*
  - *BioPT Bin 2: Talus fracture (fx nondisplaced or simple displacement; Hawkins Type I and II)*
  - *No Hawkins classification, not a neck fracture*
- Calcaneus, left - separation of sustentaculum tali and general anterior-posterior segmentation resulting in four large pieces and associated chips
  - *AIS: 857371.2 fracture line into ≥2 joint surfaces*
  - *BioPT Bin 5: Calcaneus fracture (comminuted crush, comminuted, Sanders Type III and Type IV)*
  - *Sanders Type IV, 3 or more fracture lines*

Detailed damage description and photos

S8C1 sustained a mild anterior wedge fracture of the fourth lumbar vertebra that was located proximal to the superior endplate (Figures E-99, E-100, and E-101) and a fracture/dislocation of the coccyx at the first, second, and third joints from caudal (Figure E-102). The right talus sustained cartilage damage to posterolateral portion of articular surface for tibia (Figure E-103), as well as a fracture of the posterior process (Figure E-104). The right tibia sustained minor damage to the anterior (Figure E-105) and posterior (Figure E-106) margins of the plafond. The posterior damage corresponds to posterior damage on the talus (plantar flexion). The left calcaneus sustained separation of sustentaculum tali and general anterior-posterior segmentation resulting in four large pieces and associated chips (Figures E-107 and E-108).

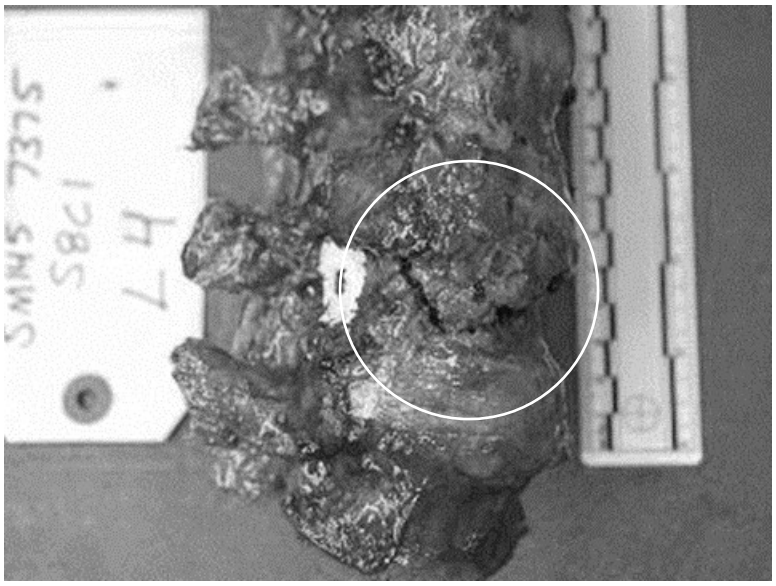

Figure E-99. Anterior wedge fracture of L4 of S8C1 (right lateral view)

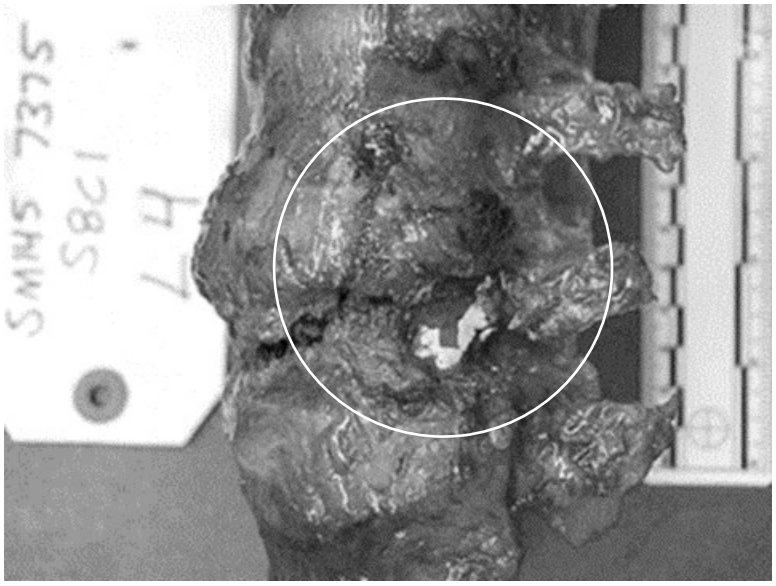

Figure E-100. Anterior wedge fracture of L4 of S8C1 (left lateral view)

Figure E-101. Anterior wedge fracture of L4 of S8C1 (anterior view)

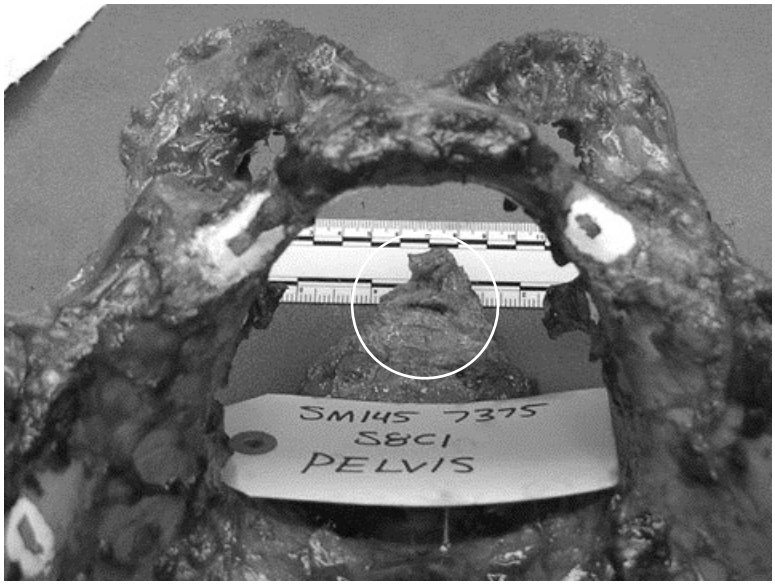

Figure E-102. Fracture of the coccyx of S8C1

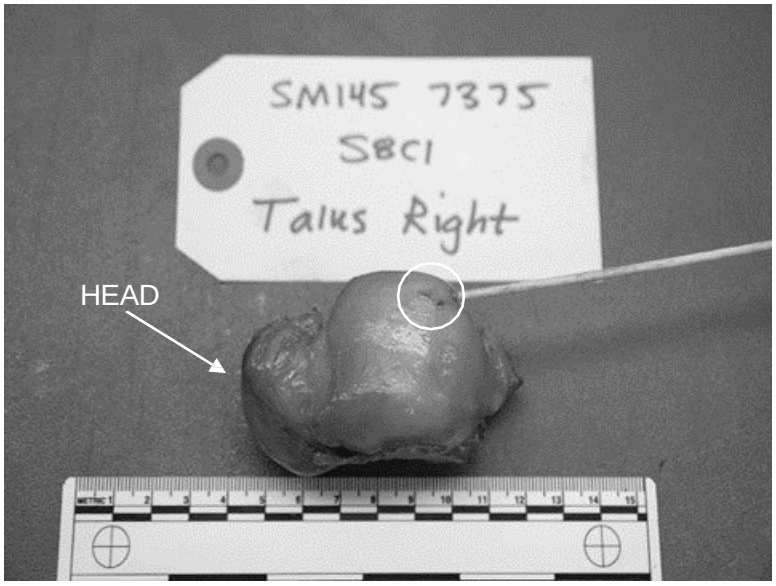

Figure E-103. Cartilage damage to the trochlear surface of the right talus of S8C1 (superior view)

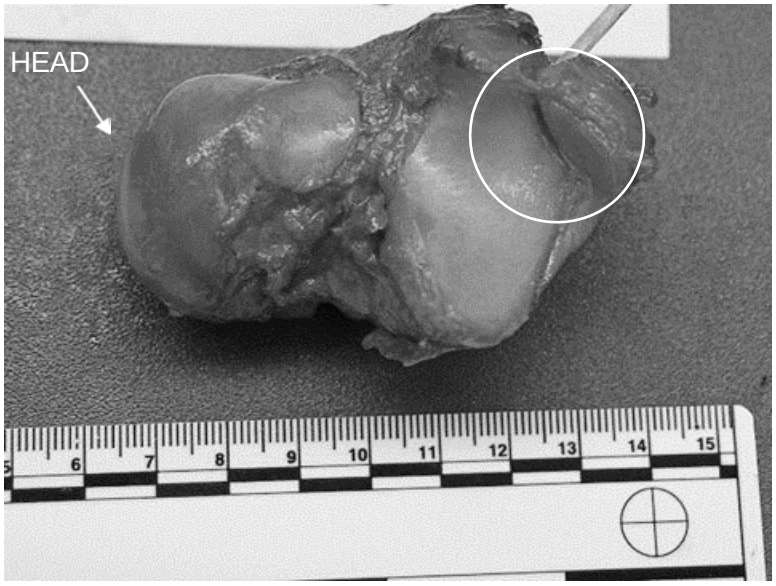

Figure E-104. Fracture to the posterolateral tubercle of the right talus of S8C1 (inferior view)

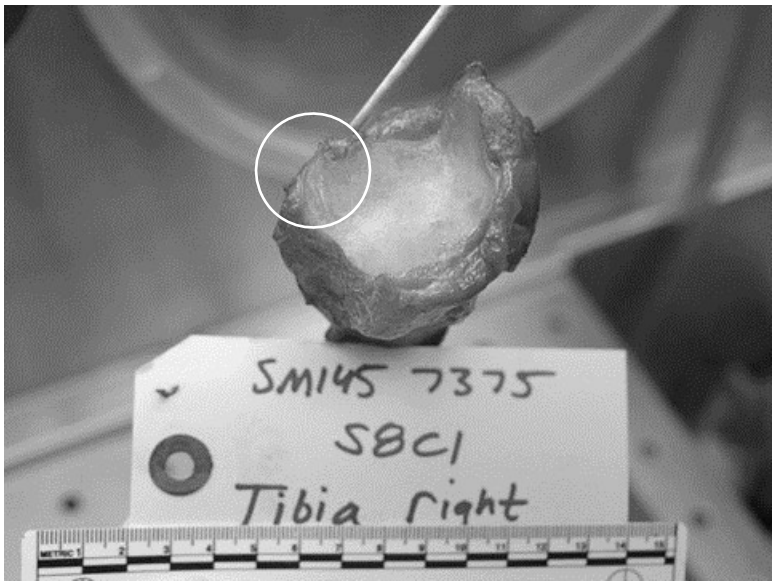

Figure E-105. Damage to the tibial plafond of the right tibia of S8C1 (inferior view)

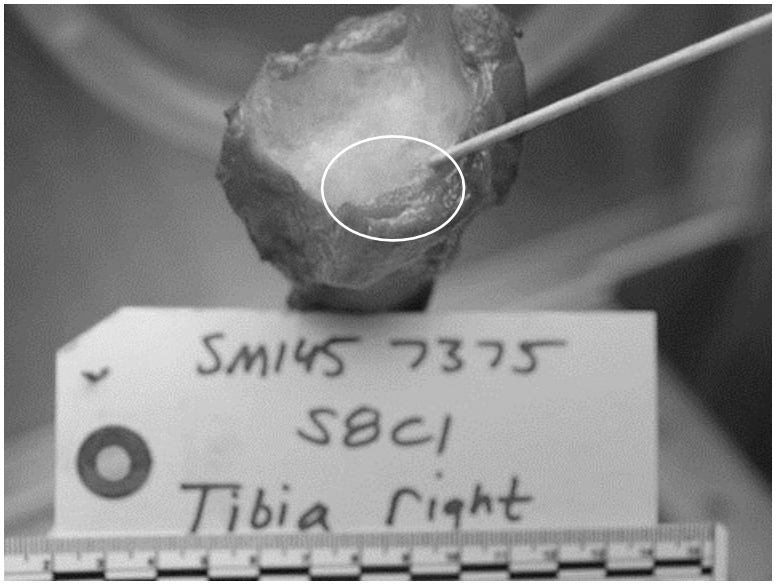

Figure E-106. Damage to the tibial plafond of the right tibia of S8C1 (inferior view)

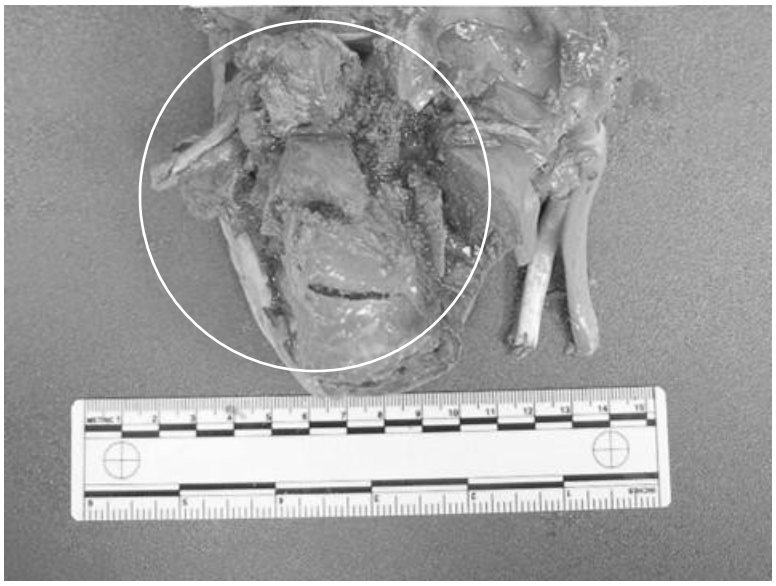

Figure E-107. Crushed left calcaneus of S8C1 (superior view)

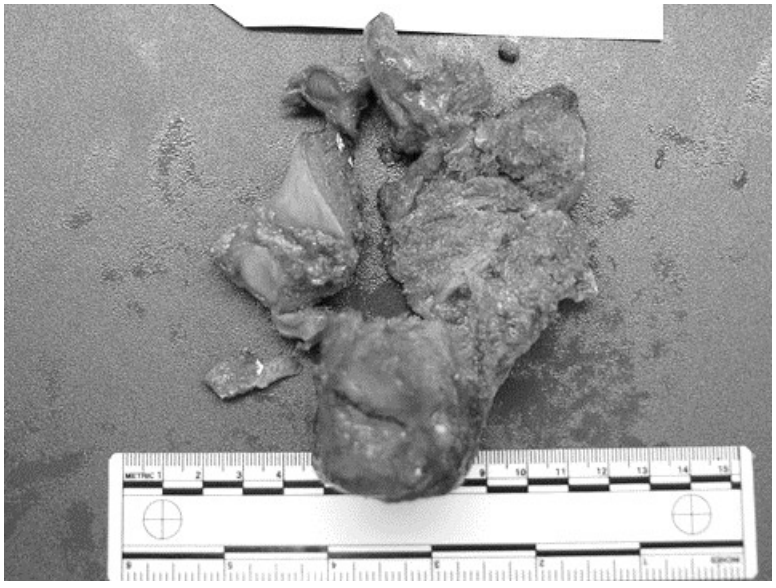

Figure E-108. Crushed left calcaneus of S8C1, dissected out (superior view)

E.18 Female Shot 8 Crew 2: 75th percentile female

Thorax

- Ribs (measured on deep surface of ribs)
    - *AIS 450203.3 fracture(s) without flail, any location unilateral or bilateral NFS ≥3 ribs*
    - Right rib 3 (9.2 cm from sternum and 22.5 cm from spine)
    - Right rib 4 (10 cm from sternum and 25.1 cm from spine)
    - Right rib 5 (18 cm from sternum and 25.3 cm from spine)
    - Right rib 7 (17 cm from sternum and 29.5 cm from spine)
    - Left rib 2 (4.5 cm from sternum and 18.2 cm from spine)
    - Left rib 3 (5.4 cm from sternum and 25.5 cm from spine)
    - Left rib 4 (6.5 cm from sternum and 28 cm from spine)
    - Left rib 5 (12.5 cm from sternum and 24.5 cm from spine)
    - Left rib 6 (11 cm from sternum and 28.7 cm from spine)

Spine

- Lumbar spine
    - *AIS: 650620.2 Lumbar spine transverse process fracture*
    - *BioPT bin 2: Posterior vertebra (simple fx; no canal compromise)*
    - L1 transverse process left fx (medial)
    - L1 transverse process right fx (medial)
    - L2 transverse process right fx (lateral)
    - L2 transverse process left fx (lateral)
    - L3 transverse process right chip
    - L4 transverse process right chip
    - L5 transverse process left fx (lateral)
- L5 body compression fx minimal height loss
    - *AIS 650632.2: vertebral body, minor compression (≤20% loss of anterior height) BioPT bin 1: VB (simple fx; no canal compromise)*

Pelvis

- Coccyx - fx/dislocation second joint from caudal
    - *AIS 856151.2 Pelvic ring fracture, posterior arch intact; isolated fracture not destroying the integrity of the pelvic ring (but this would not be coded separately from below)*
    - *BioPT bin 61-A3.1 (row 23)*
    - *OTA pelvis 61-A3.1*

Lower Extremity

- Tibia, right - distal tibia fx of cartilage on posterior lateral aspect. Reaches bone, but there is negligible bone damage (12-mm length)
    - *AIS: 854361.2 distal tibia, partial articular*
    - *BioPT Bin 6: Distal tibia fracture (partial articular; simple pilon; OTA Type 43-B)*
    - *OTA 43-B1 pure split*
- Calcaneus, right - sectioning of the dorsal half and crushing of the plantar half
    - *AIS: 857371.2 fracture line into ≥2 joint surfaces*
    - *BioPT Bin 5: Calcaneus fracture (comminuted crush, comminuted, Sanders Type III and Type IV)*
    - *Sanders Type IV, 3 or more fracture lines*
- Tibia, left - stellate fx pattern beginning at tibia plafond (articular surface) propagating 6 cm with general crushing of the distal tibia generating several fragments ranging from 15 mm to 4 cm in length with multiple small chips. Largest segments were both medial and lateral
    - *AIS: 854361.2 distal tibia, partial articular*
    - *BioPT Bin 6: Distal tibia fracture (partial articular; simple pilon; OTA Type 43-B)*
    - *OTA 43-B1 pure split*
- Fibula, left - transverse fx 9 cm from distal end. Slight angulation from medial distal to lateral proximal. Possibly from lateral motion of the malleolus
    - *AIS: 854471.2 above joint (suprasyndesmotic); isolated shaft, head or neck; Weber C*
    - *BioPT Bin 10: Distal fibula fracture (simple, complex bimalleolar)*
    - *Weber classification: C*
    - *OTA 44-C1: fibular diaphyseal fracture, simple*
- Talus, left - two lateral evulsions, both triangular: one at anterior portion of superior articular surface (12 mm on a side); One at lateral process (junction between lateral and inferior articular surfaces) (15 mm on a side)
    - *AIS: 857261.2 fracture line into one joint surface; talus body*
    - *BioPT Bin 2: Talus fracture (fx nondisplaced or simple displacement; Hawkins Type I and II)*
    - *No Hawkins classification, not a neck fracture*
- Calcaneus, left - one primary anterior-posterior fx through calcaneal sulcus (4 cm) producing two anterior-medial chips (2.5 cm and 1.5 cm) involving the middle articular surface and separating the anterior articular surface; posterior cortical chip on dorsal surface located 1 cm from posterior aspect (7 mm wide)
    - *AIS: 857371.2 fracture line into ≥2 joint surfaces*

    - *BioPT Bin 5: Calcaneus fracture (comminuted crush, comminuted, Sanders Type III and Type IV)*
    - *Sanders Type IV, 3 or more fracture lines*
- Third metatarsal, left - proximal articular surface crushed. Dominant horizontal fracture (18 mm). Dorsal part separated from ventral
    - *AIS 858163.2 partial articular*
    - Fourth metatarsal, left - proximal articular surface crushed; horizontal fx propagating to mid- diaphysis
    - *AIS: 858173.2 complete articular*
- Fifth metatarsal, left - proximal lateral chip. Triangular with base being 5 mm and sides being 3 mm
    - *AIS 858163.2 partial articular*

Detailed damage description and photos

S8C2 sustained several rib fractures (Figures E-109 and E-110), several transverse process fractures of the lumbar spine (Figure E-111), a compression fracture of the body of the fifth lumbar vertebra with minimal height loss (Figures E-112, E-113, and E-114), and a fracture/dislocation of the coccyx at the second joint from caudal (Figure E-115). The right calcaneus sustained sectioning of the dorsal half and crushing of the plantar half (Figures E-116, E-117, and E-118). The right tibia sustained cartilage damage on the posterior lateral aspect (Figure E-119). The fracture reaches the bone, but there is negligible bone damage (12-mm length). The left third metatarsal sustained a crushing fracture of the proximal articular surface (Figure E-120). There was a dominant horizontal fracture (18 mm), and the dorsal part was separated from ventral part. The left fourth metatarsal sustained a crushing fracture of the proximal articular surface and a horizontal fracture propagating to the mid-diaphysis (Figures E-121 and E-122). The left fifth metatarsal sustained a proximal lateral chip that was triangular in shape with base being 5 mm and sides being 3 mm (Figures E-121 and E-123). The left calcaneus sustained one primary anterior-posterior fracture through calcaneal sulcus (4 cm), producing two anterior-medial chips (2.5 cm and 1.5 cm) involving the middle articular surface and separating the anterior articular surface (Figures E-124 and E-125). The left talus sustained two lateral evulsions that were both triangular. One was located at anterior portion of superior articular surface (12 mm on a side) (Figures E-126 and E-127), whereas the other was located at the lateral process (junction between lateral and inferior articular surfaces) (15 mm on a side) (Figure E-127). The left tibia sustained a crushing fracture of the distal end with a stellate fracture pattern beginning at tibia plafond (articular surface) and propagating 6 cm generating several fragments ranging from 15 mm to 4 cm in length with multiple small chips (Figures E-128 and E-129). The largest segments were both medial and lateral. The left fibula sustained a

transverse fracture that was located 9 cm from distal end (Figure E-130). There was slight angulation from medial distal to lateral proximal (possibly from lateral motion of the malleolus).

Figure E-109. Fractures of the right ribs of S8C2: right rib 3 (9.2 cm from sternum and 22.5 cm from spine); right rib 4 (10 cm from sternum and 25.1 cm from spine); right rib 5 (18 cm from sternum and 25.3 cm from spine); right rib 7 (17 cm from sternum and 29.5 cm from spine)

Figure E-110. Fractures of the left ribs of S8C2: left rib 2 (4.5 cm from sternum and 18.2 cm from spine); left rib 3 (5.4 cm from sternum and 25.5 cm from spine); left rib 4 (6.5 cm from sternum and 28 cm from spine); left rib 5 (12.5 cm from sternum and 24.5 cm from spine); left rib 6 (11 cm from sternum and 28.7 cm from spine)

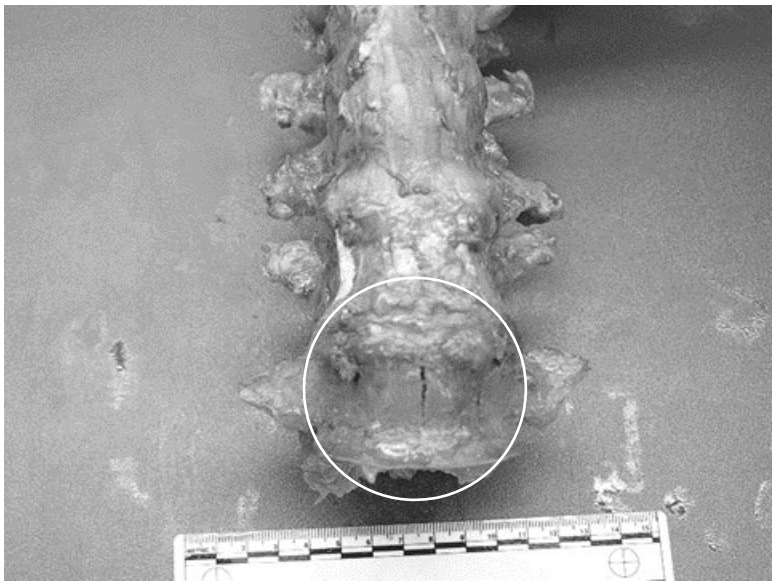

Figure E-111. Transverse process fractures of S8C2: L, bilateral; L2, bilateral; L3, right; L4, right; L5, left

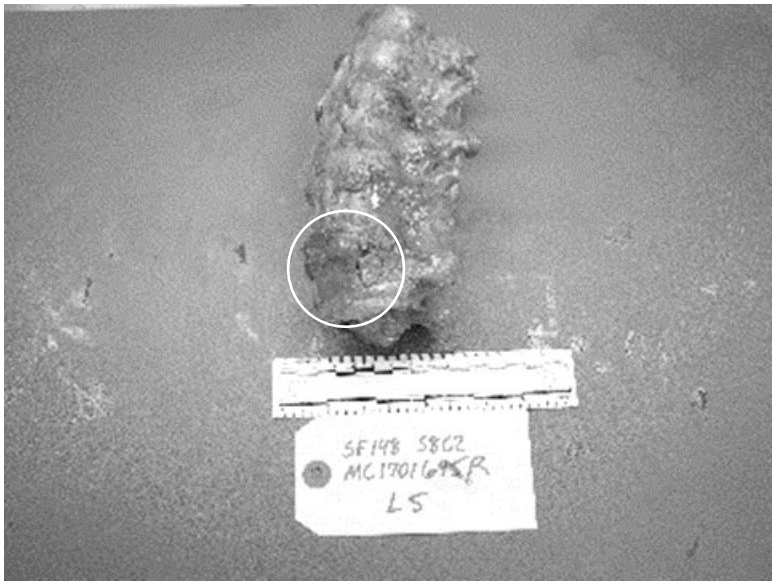

Figure E-112. Compression fracture of L5 of S8C2 (anterior/left lateral view)

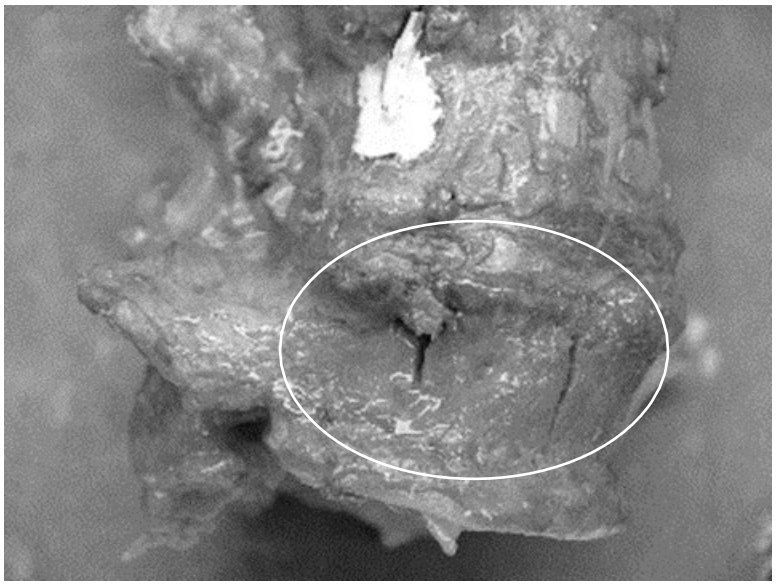

Figure E-113. Compression fracture of L5 of S8C2 (anterior/right lateral view)

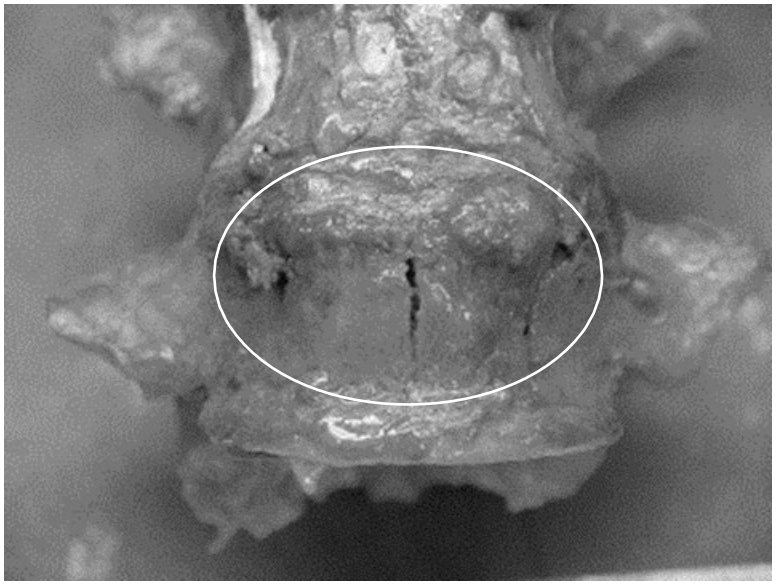

Figure E-114. Compression fracture of L5 of S8C2 (anterior view)

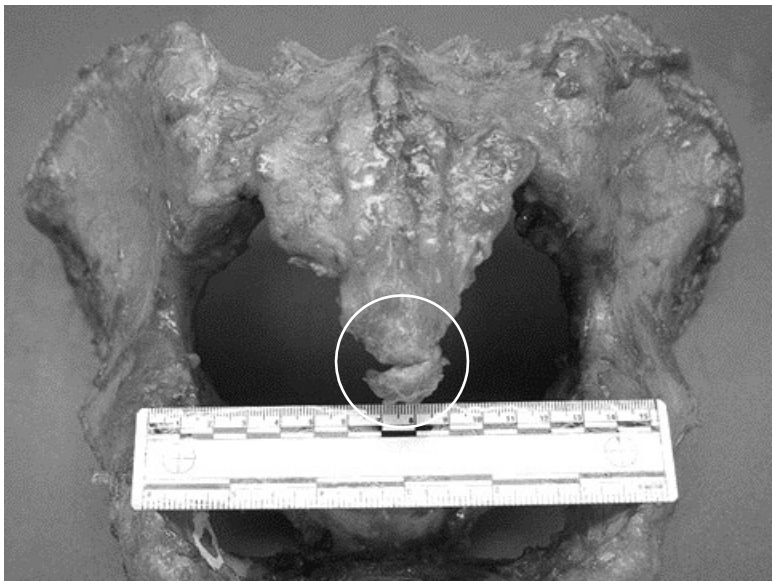

Figure E-115. Fracture of the coccyx of S8C2

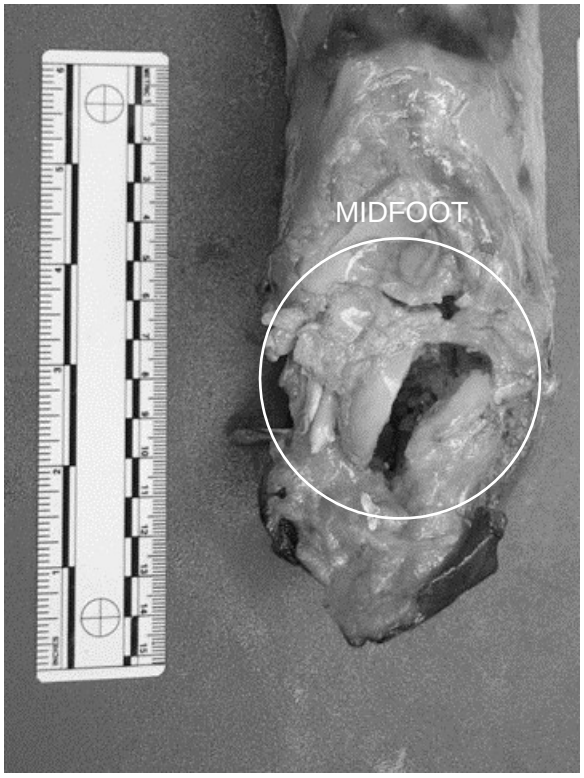

Figure E-116. Crushed right calcaneus of S8C2 (superior view)

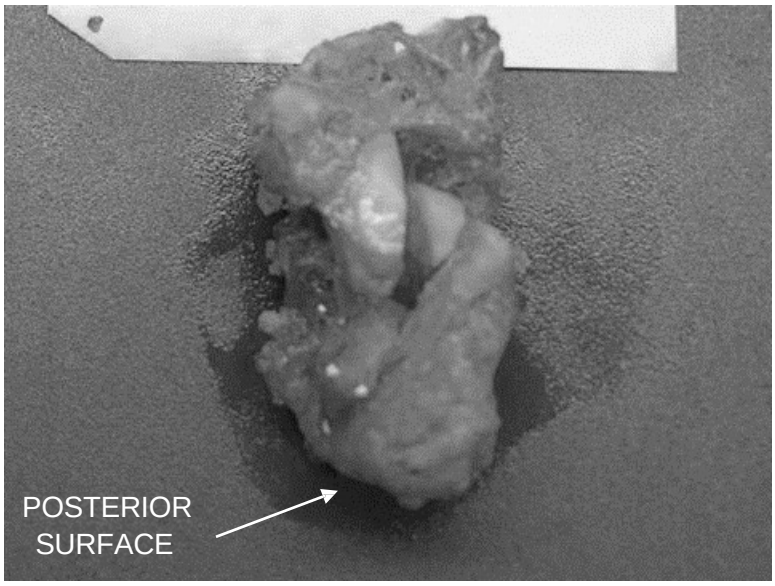

Figure E-117. Crushed right calcaneus of S8C2, dissected out (superior view)

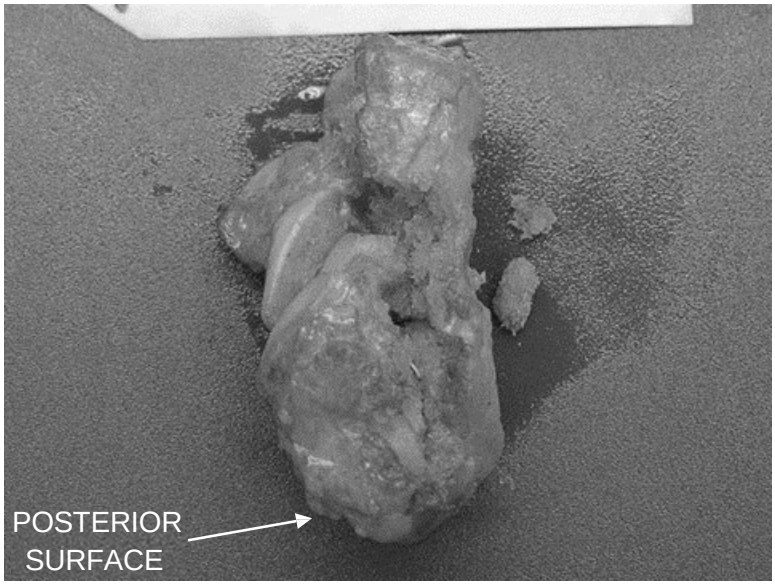

Figure E-118. Crushed right calcaneus of S8C2, dissected out (lateral view)

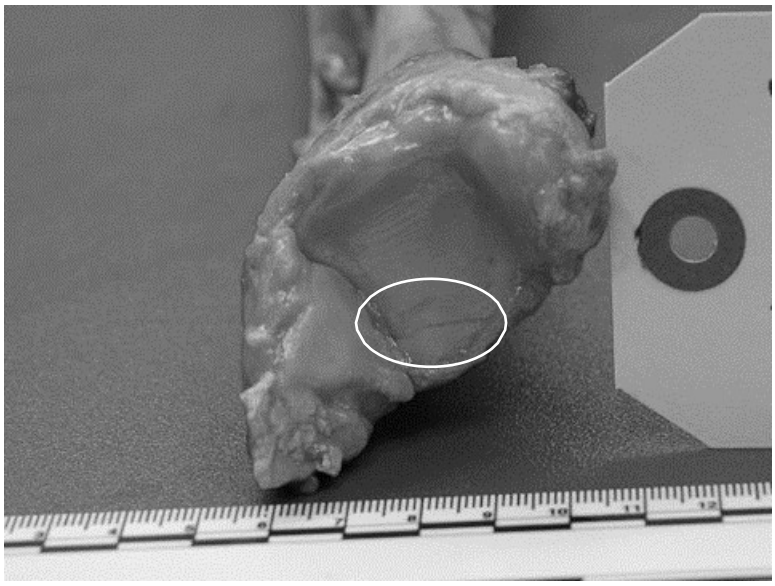

Figure E-119. Fracture of the plafond of the right distal tibia of S8C2 (inferior view)

Figure E-120. Fracture of the 3rd metatarsal of S8C2 (lateral view)

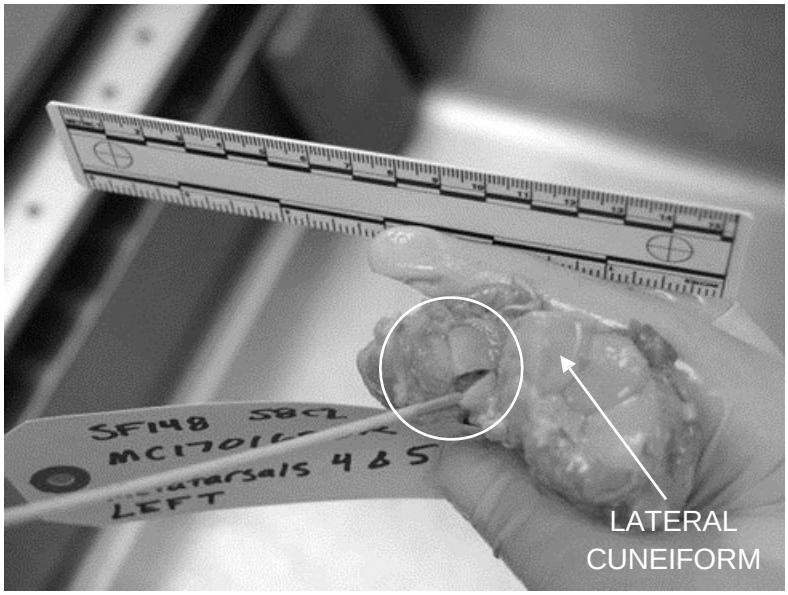

Figure E-121. Fractures of the left 4th and 5th metatarsals of S8C2 (posterior view)

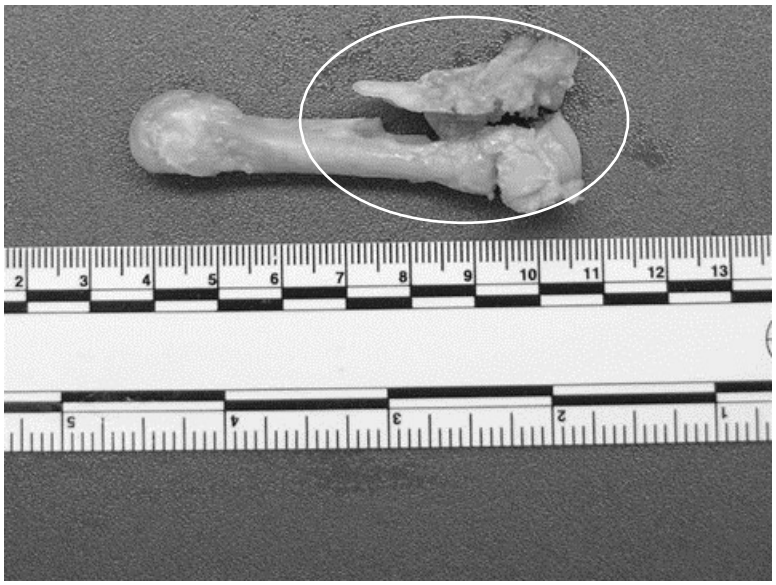

Figure E-122. Fracture of the proximal end of the 4th metatarsal of S8C2 (inferior view)

Figure E-123. Fracture of the proximal end of the left 5th metatarsal of S8C2 (inferior view)

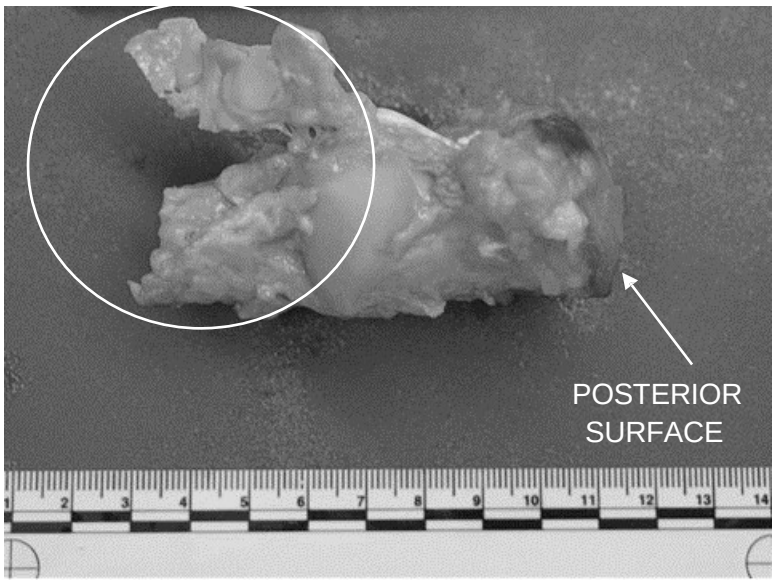

Figure E-124. Fracture of left calcaneus of S8C2 (superior view)

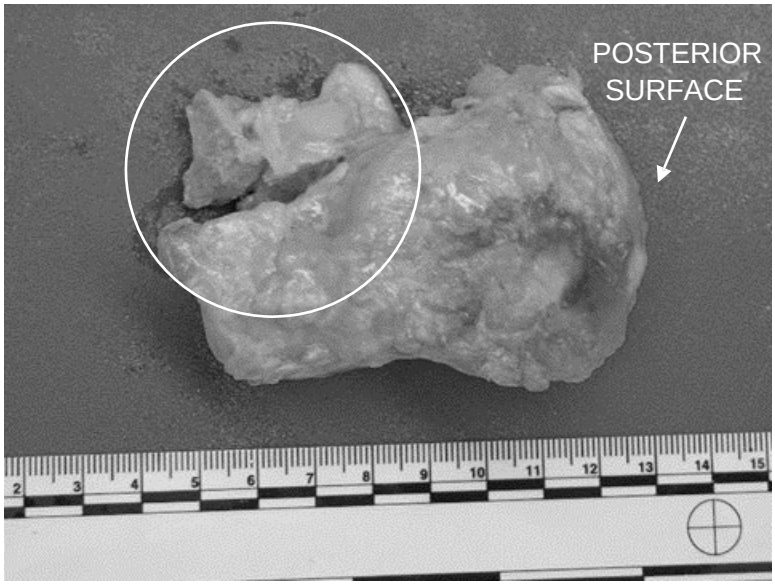

Figure E-125. Fracture of left calcaneus of S8C2 (lateral view)

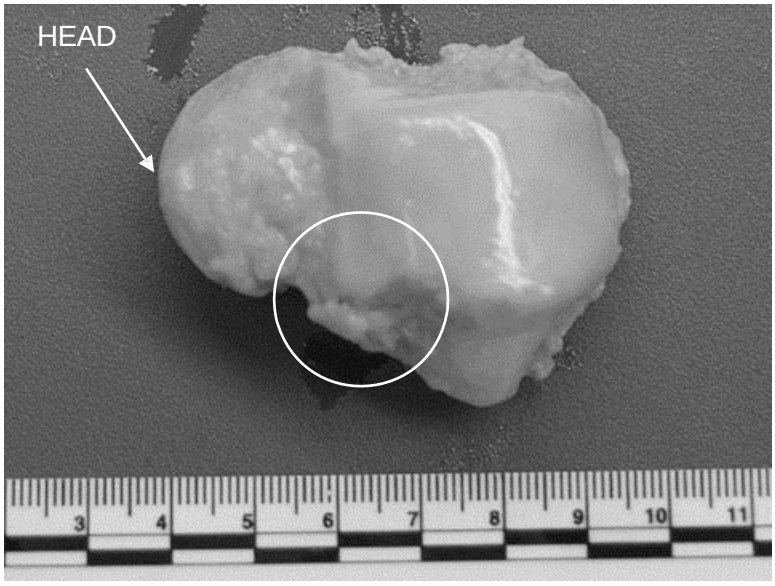

Figure E-126. Fracture to the anterolateral aspect of the trochlear surface of the left talus of S8C2 (superior view)

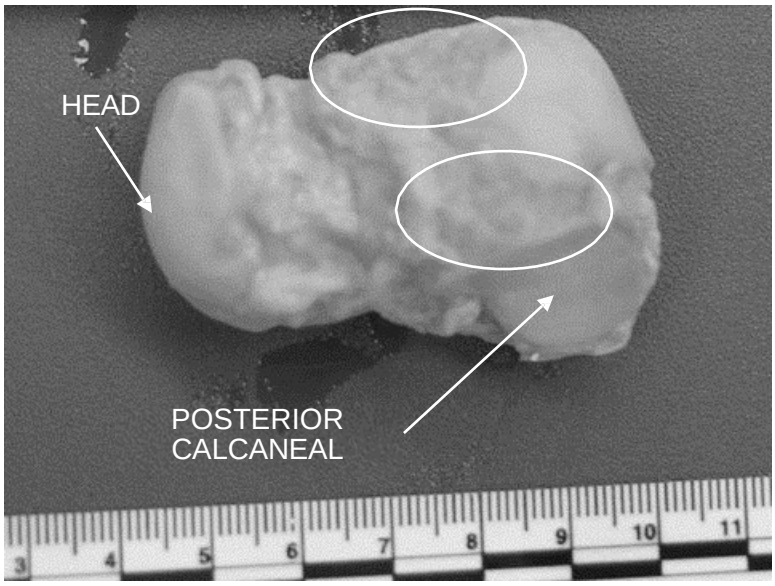

Figure E-127. Damage to the lateral process and articular surface—facies malleolus lateralis of the left talus of S8C2 (inferolateral view)

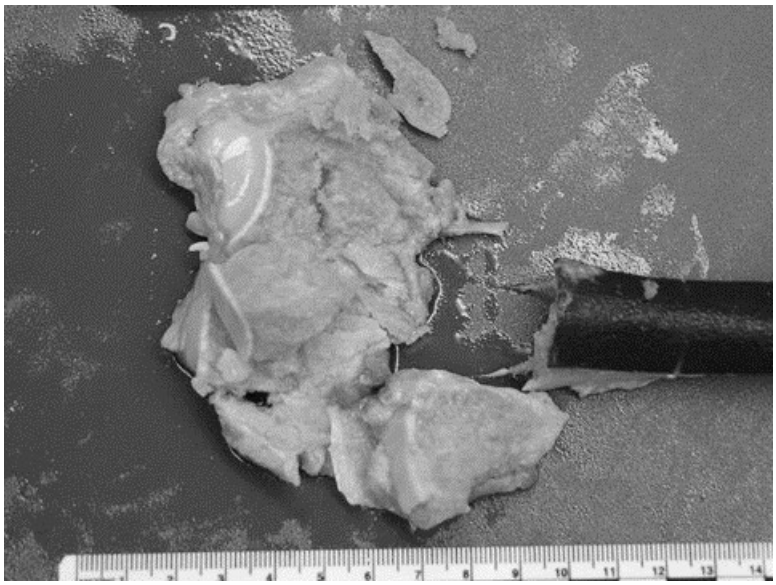

Figure E-128. Shattered left distal tibia of S8C2, sandpaper not removed (anterior view)

Figure E-129. Shattered left distal tibia of S8C2 (posterior view)

Figure E-130. Fracture of the left distal fibula of S8C2 (lateral view)

E.19 Female Shot 9 Crew 1: 50th percentile male

Thorax

- None

Spine

- None

Pelvis

- Coccyx fx/dislocation third joint from caudal. Posterior chip (8 × 5 × 3 cm)

Lower Extremity

- Femur, left – shaft fracture fragmented wedge fx

Detailed damage description and photos

S9C1 sustained a fracture/dislocation of the coccyx at the third joint from caudal (Figure E-131). The left femur sustained a fragmented wedge fracture of the shaft (Figures E-132, E-133, E-134, E-135, E-136, and E-137).

Figure E-131. Fracture of the coccyx of S9C1

Figure E-132. Fracture of the left femur of S9C1 (anterior view, right is proximal)

Figure E-133. Fracture of the left femur of S9C1 (lateral view, right is proximal)

Figure E-134. Fracture of the left femur of S9C1 (posterior view, right is proximal)

Figure E-135. Fracture of the left femur of S9C1 (medial view, right is proximal)

Figure E-136. Fracture of the left femur of S9C1, dissected out (anterior view, right is proximal)

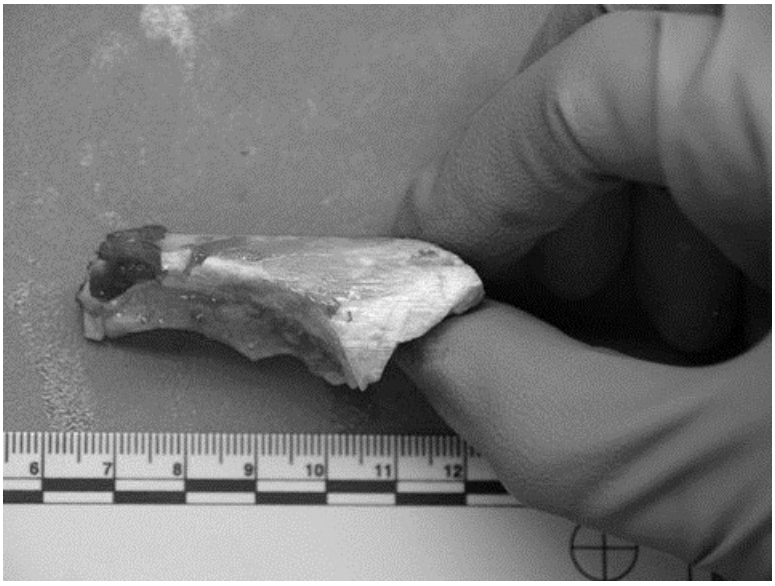

Figure E-137. Anterior fragment of the fractured left femur of S9C1 (lateral view, right is proximal)

E.20 Female Shot 9 Crew 2: 5th percentile female

Thorax

- None

Spine

- None

Pelvis

- Coccyx fx/dislocation second joint from caudal

Lower Extremity

- Talus, right - Posterior chip on articular surface for calcaneus (4 pieces approximately 5 mm each)
- Calcaneus, right - General crushing of plantar half and sectioning of dorsal half. Large posterior chip (5 × 2 × 3 cm). Several smaller chips ranging from 2 to 4 cm in length from superolateral and superomedial aspect.
- Calcaneus, left - General crushing of plantar half and sectioning of dorsal half. Large posterior chip (5 × 3 × 3 cm). Several smaller chips ranging from 1 to 3 cm in length from superolateral and superomedial aspect. Splitting of the articular surface for the cuboid (articular surface of cuboid was intact)

Detailed damage description and photos

S9C2 sustained a fracture/dislocation of the coccyx at the second joint from caudal (Figure E-138). The right calcaneus sustained general crushing of plantar half and sectioning of dorsal half (Figures E-139 and E-140). There was a large posterior chip (5 × 2 × 3 cm) and several smaller chips ranging from 2 to 4 cm in length from superolateral and superomedial aspect. The right talus sustained a posterior chip on the articular surface for calcaneus (4 pieces approximately 5 mm each) (Figure E-141). The left calcaneus sustained general crushing of plantar half and sectioning of dorsal half (Figures E-142 and E-143). There was a large posterior chip (5 × 3 × 3 cm) and several smaller chips ranging from 1 to 3 cm in length from superolateral and superomedial aspect. There was splitting of the articular surface for the cuboid, but the articular surface of cuboid was intact.

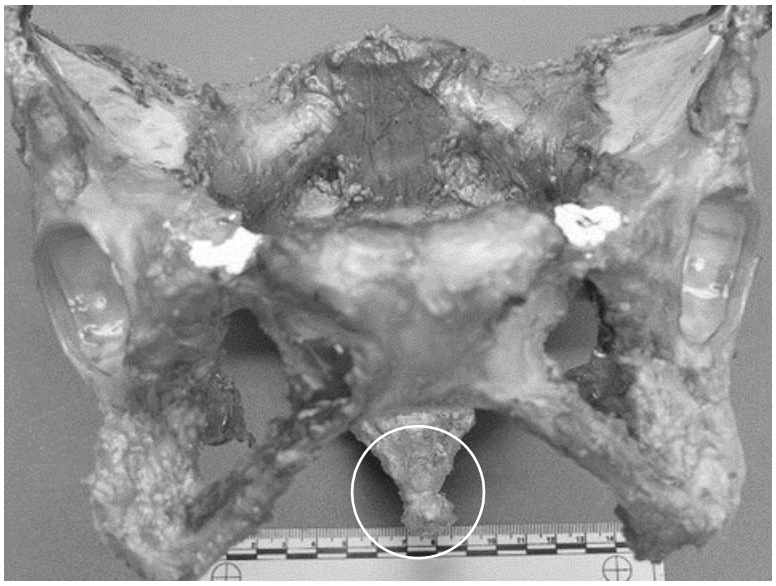

Figure E-138. Fracture of the coccyx of S9C2

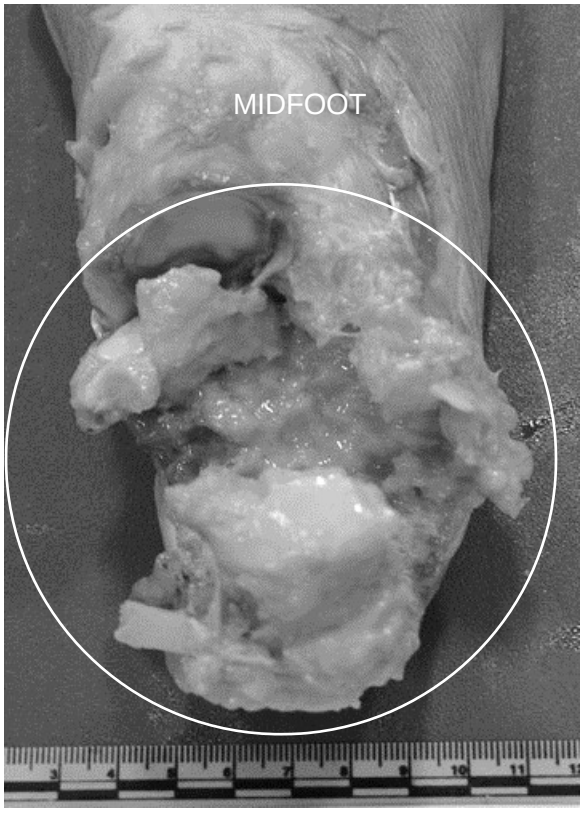

Figure E-139. Crushed right calcaneus of S9C2 (superior view)

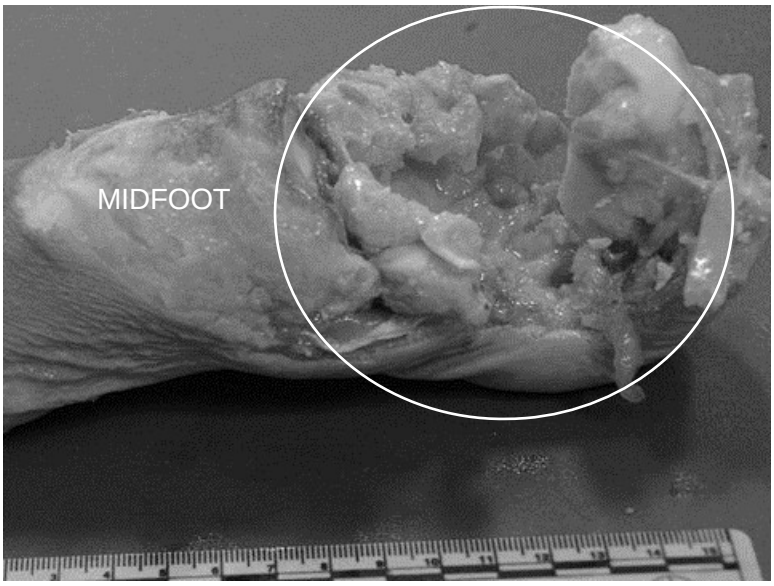

Figure E-140. Crushed right calcaneus of S9C2 (medial view)

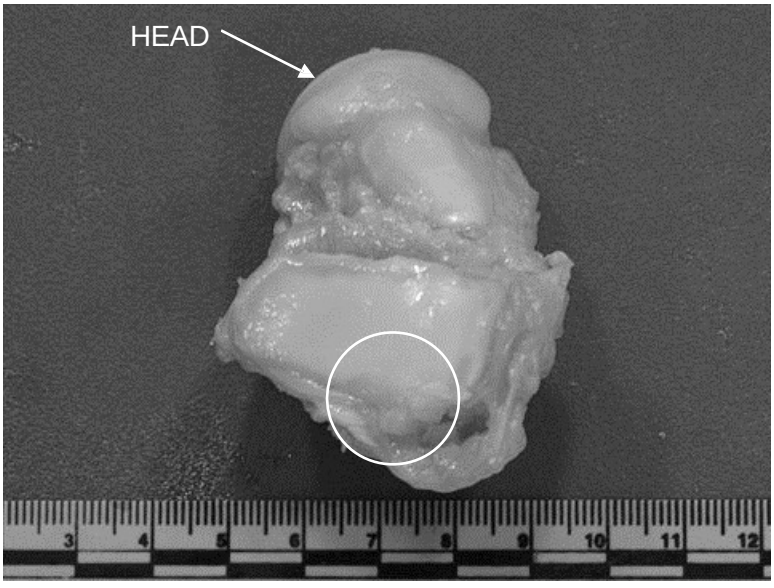

Figure E-141. Fracture of posterolateral tubercle of right talus of S9C2 (inferior view)

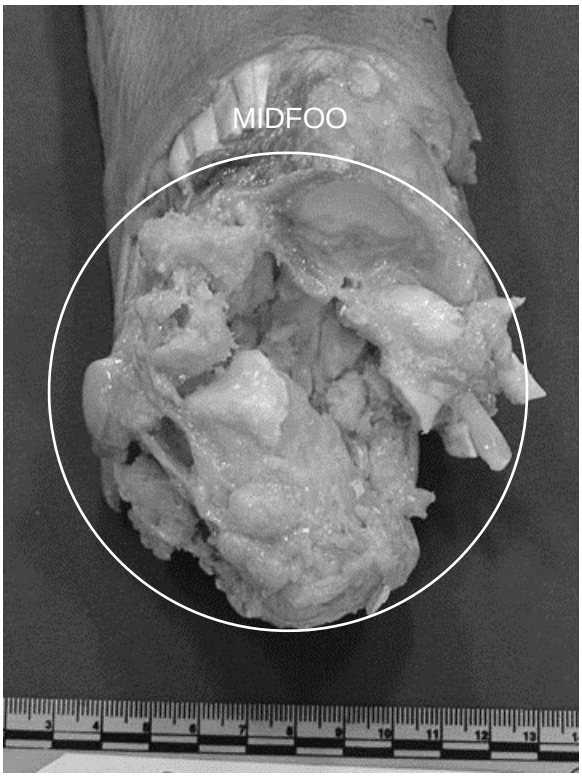

Figure E-142. Crushed left calcaneus of S9C2 (superior view)

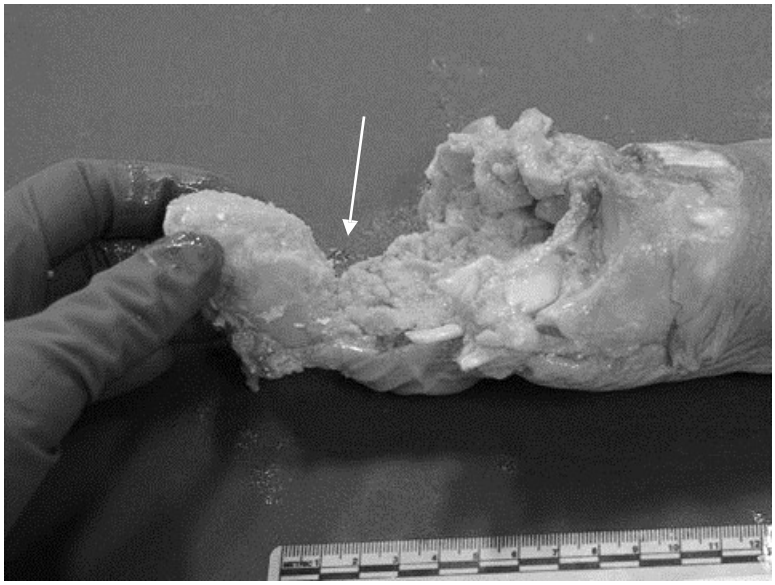

Figure E-143. Crushed left calcaneus of S9C2 (medial view)

LIST OF ACRONYMS

6-DoF	six-degrees-of-freedom
ALF	accelerative loading fixture
APG	Aberdeen Proving Ground
ARL	Army Research Laboratory
ASIS	anterior superior iliac spine
ATC	Aberdeen Test Center
ATD	anthropomorphic test device
BMD	bone mass density
BMI	body mass index
CAD	computer-aided design
CORA	correlation and analysis
CT	computed tomography
DEVCOM	U.S. Army Combat Capabilities Development Command
ISO	International Organization for Standardization
L-C	less-censored
NFS	not further specified
PMHS	postmortem human surrogates
PPE	personal protective equipment
ScoTT	Signal Conversion Tiger Team
TTP	time to peak
UBB	underbody blast
VALTS	Vertically Accelerated Load Transfer System
VertAc	Vertical Accelerator
WIAMan	Warrior Injury Assessment Manikin

DISTRIBUTION LIST

DEVCOM Analysis Center
FCDD-DAG-S/K. Loftis
FCDD-DAG-S/M. Wassick
FCDD-DAG-S/D.R. Barnes
FCDD-DAG-S/K. Sandora
FCDD-DAG-S/G. Steiger
FCDD-DAG-S/B. Vanamburg
6896 Mauchly Street
Aberdeen Proving Ground, MD 21005-5071

U.S. Army Evaluation Center
Survivability Evaluation Directorate
S. Swann
A Taylor
6617 Aberdeen Blvd.
Bldg 2202, 2nd Floor
Aberdeen Proving Ground, MD 21005-5071

U.S. Army DEVCOM Ground Vehicle Systems Center
FCDD-GVR-VMT/D. Weyland
FCDD-GVR-VMT/R. Scherer
6501 E. 11 Mile Rd
Detroit Arsenal, MI 48397-5000

Office of the Director, Operational Test and Evaluation
OSD DOT&E
LFT&E/J. Ivancik
1700 Defense Pentagon 1D548
Washington, DC 203

DEVCOM Army Research Laboratory
FCDD-RLB-CI/Tech Library
2800 Powder Mill Rd.
Adelphi, MD 20783

Defense Technical Information Center
ATTN: DTIC-O
8725 John J. Kingman Rd.
Fort Belvoir, VA 22060-6218